MATHEMATICAL MODELLING OF DIFFUSION-DRIVEN OXIDATION IN METALS

A thesis submitted to The University of Manchester
for the degree of Doctor of Philosophy
in the Faculty of Science and Engineering

2020

Monisha Natchiar Subbiah Renganathan

Mathematics

Contents

Word Count: 73690

List of Tables

List of Figures

Abstract

MATHEMATICAL MODELLING OF DIFFUSION-DRIVEN OXIDATION IN METALS
Monisha Natchiar Subbiah Renganathan
A thesis submitted to The University of Manchester
for the degree of Doctor of Philosophy, 2020.

Corrosion (or oxidation) of metals in ambient air produces metal oxide that is undesirable in most cases. In the case of uranium, a solid corrosion product consisting of uranium dioxide and uranium hydride is produced. Uranium hydride is pyrophoric in air and can therefore self-ignite leading to operational safety issues in nuclear waste storage facilities. In addition, hydrogen gas that is produced when uranium reacts with water vapour is potentially hazardous when it accumulates and leads to deterioration of the material. In this study, we investigate the oxidation kinetics of uranium in environments that contain oxygen or water vapour. Uranium dioxide is produced as the main corrosion product in such environments, with uranium hydride formed as a reaction intermediate in the presence of water vapour. The corrosion product is less dense than the parent metal (uranium), resulting in expansion of the material when the metal is converted to oxide or hydride. Experimental evidence indicates that the oxidation rate in water vapour is at least 5000 times larger than the rate in dry air or oxygen, suggesting different mechanisms or diffusing species. Uranium oxidation is thus a complex process involving several physicochemical processes (including advection, adsorption, diffusion, reaction and desorption), where diffusion of the oxidising species through the oxide layer adhering to the metal or hydride largely determines the overall oxidation rate. Here oxygen ions in dry air and hydroxide ions in water vapour constitute the oxidising species.

In the oxidation of uranium by dry air, a self-induced electric field contributes to the diffusing flux of oxygen ions, in addition to a concentration gradient. The dry-air oxidation is modelled as a Stefan (discrete-layer) problem, where a Stefan condition provides the velocity of the moving interface (or phase boundary) that separates different homogeneous phases. The Stefan model allows for unsteady development of the concentration profile of the diffusing species in the oxide layer, which forms the novel aspect of this problem.

As the underpinning chemistry becomes substantially more complex in a water-vapour environment, it is unclear how to construct an analogous Stefan problem (or even if one exists). For the water-vapour corrosion of uranium, a one-dimensional reaction-advection-diffusion (RAD) problem is formulated as a new model based on a proposed reaction scheme involving at least two diffusing and three static components. A distinguishing feature in the RAD model compared to the Stefan model is the presence of “reaction fronts” which are transition (or mixed-phase) regions. The RAD model is tackled using both numerical and asymptotic approaches, wherein two diffusion layers and two reaction fronts are found in the large-time asymptotic solution. Asymptotic matching across the different regions (or layers) provides analytical predictions for the thickness of the diffusion layers, locations of the propagating reaction fronts and concentration profiles in the diffusion layers. The numerical solution strategy utilises a Howarth-Dorodnitsyn transformation to allow for volumetric expansion during corrosion. The full numerical solution is found to be consistent with the asymptotic predictions, showing that a few-nanometres-thick propagating hydride layer that is bounded by a pair of coupled reaction fronts is possible in the RAD model. A “parabolic” (square-root time dependence) oxidation regime is found at the early stages of oxidation, whereas the late stages (i.e. after cracking or spalling of the surface oxide) follow linear kinetics in both dry air and water vapour environments. The influence of parameters associated with the diffusion coefficients, material properties and the external gas state on the oxidation kinetics is investigated. For the water-vapour oxidation of uranium, even though the oxide formation relies on the presence of an intermediate hydride phase, its thickness is found to be dependent only on the material properties and the external water vapour state. The RAD model is a first mechanistic model of uranium oxidation in water vapour and gives qualitative predictions that are consistent with the recent experimental observations using atom-probe tomography.

Keywords: uranium corrosion, moving boundary problem, reaction-diffusion fronts, partial differential equations, matched-asymptotic analysis.

Declaration

No portion of the work referred to in this thesis has been submitted in support of an application for another degree or qualification of this or any other university or other institute of learning.

Copyright

i. The author of this thesis (including any appendices and/or schedules to this thesis) owns certain copyright or related rights in it (the "Copyright") and she has given The University of Manchester certain rights to use such Copyright, including for administrative purposes.

ii. Copies of this thesis, either in full or in extracts and whether in hard or electronic copy, may be made **only** in accordance with the Copyright, Designs and Patents Act 1988 (as amended) and regulations issued under it or, where appropriate, in accordance with licensing agreements which the University has from time to time. This page must form part of any such copies made.

iii. The ownership of certain Copyright, patents, designs, trade marks and other intellectual property (the "Intellectual Property") and any reproductions of copyright works in the thesis, for example graphs and tables ("Reproductions"), which may be described in this thesis, may not be owned by the author and may be owned by third parties. Such Intellectual Property and Reproductions cannot and must not be made available for use without the prior written permission of the owner(s) of the relevant Intellectual Property and/or Reproductions.

iv. Further information on the conditions under which disclosure, publication and commercialisation of this thesis, the Copyright and any Intellectual Property and/or Reproductions described in it may take place is available in the University IP Policy (see `http://documents.manchester.ac.uk/DocuInfo.aspx?DocID=24420`), in any relevant Thesis restriction declarations deposited in the University Library, The University Library's regulations (see `http://www.library.manchester.ac.uk/about/regulations/`) and in The University's policy on presentation of Theses

Acknowledgements

I am immensely grateful to my supervisor Prof. Richard E. Hewitt for his guidance, support, patience and understanding. Richard has introduced me to mathematical thinking and has taught me the methods of scientific inquiry to approach a range of problems. He has been patient throughout my learning process whilst also instrumental in developing my self-confidence. I have benefited enormously from numerous discussions with him. Richard has been a knowledgeable and dedicated mentor, without whom this project would not have reached this stage. We have benefited from a number of discussions with Dr. Phil D.D. Monks, Dr. Peter Morrall, Dr. J. Petherbridge and Dr. R. Harker (AWE plc.), and I extend my gratitude to them. I also thank Dr. Gareth Wyn Jones, Dr. Raphael Assier and Prof. Jitesh Gajjar for valuable comments on my yearly transfer reports.

I thank AWE plc. and UK Engineering and Physical Sciences Research Council (EPSRC) for the funding provided. I also thank the Department of Mathematics in The University of Manchester, UK for providing the necessary resources for the successful completion of this project. I extend my thanks to my colleagues and friends, especially Jack Mckenzie, Holly Barker, Thomas Barker (Tom), Massimiliano Fasi (Max), Amritha, Ashish, Alexander Erlich, Mónica, Yuqing Zhang (Mila), Rudradip, Alex Batsis, Anthony Williams and my other office mates for all the academic and non-academic discussions.

Lastly, I thank my family and my longtime friends for their constant support, love and encouragement through all these years. I am very grateful to my parents, Padmavathy and Renganathan, my sister Sruthi and my partner Vijay who have been a vital part of my academic journey. They have been a constant source of inspiration and motivation, with my mom playing a predominant role in shaping me into the person I am today. Many thanks to my friends Rami, Kate and Andy who have made my stay in Manchester enjoyable and memorable.

Chapter 1

Introduction

Metal oxidation/corrosion is a process in which the metal (solid) reacts with an oxidising species (gas/liquid) such as oxygen (O_2) or water vapour (H_2O) to form a metal oxide product which in most cases is undesirable. A common feature in such a system is a corroded layer (largely oxide) that forms at the solid-gas interface and grows into the solid/metal. In this study, we focus on uranium (U) which forms uranium dioxide (UO_2) as the dominant corrosion product. We aim to model the oxidation of uranium under different environments and investigate the factors that influence the kinetics of the oxidation process. Oxidation involves several physicochemical processes that include diffusion and reaction among others. In cases of interest, the reaction is internal to the solid, and diffusion is important in the transport of the reacting species into the metal. The density of the corrosion product usually differs from that of the metal, resulting in advection of the material. Therefore the overall oxidation process can be described by one or more reaction-diffusion-advection partial differential equations. The overall reactions in three different environments are given below:

$$\begin{gathered}
\mathrm{U} + \mathrm{O_2} \longrightarrow \mathrm{UO_2} \quad \text{oxygen/dry air} \\
\mathrm{U} + 2\,\mathrm{H_2O_{(v)}} \longrightarrow \mathrm{UO_2} + 2\,\mathrm{H_2} \quad \text{pure water vapour} \\
\mathrm{U} + \mathrm{H_2O_{(v)}} + 0.5\,\mathrm{O_2} \longrightarrow \mathrm{UO_2} + \mathrm{H_2} \quad \text{moist air}\,.
\end{gathered}$$

We study the kinetics of uranium oxidation in dry air (or oxygen) and water vapour, although some of the literature on moist air ($H_2O_{(v)}$ + O_2) oxidation is also reviewed.

1.1 Motivation

In this thesis, the kinetics of uranium oxidation under different environmental conditions is discussed. Although there are several empirical models for oxidation/corrosion of uranium under dry air (atmospheric air without water vapour) or moist air (air containing water vapour) (see for example Cubicciotti, 1952; Colmenares, 1984; Ritchie, 1984; Lin et al., 2008; Chernia, 2009; Baker, Less, and Orman, 1966a; Baker, Less, and Orman, 1966b; Martin et al., 2016), there is a dearth of physically motivated mathematical models that explain the underlying mechanisms of uranium oxidation in these environments.

Uranium is highly reactive in both dry (O_2) and moist (O_2 + $H_2O_{(v)}$) air, where nitrogen in air acts as an inert species (i.e. unreactive towards uranium) and the influence of other trace gases such as CO_2 on the oxidation process is insignificant. We therefore use the terms *dry air* and *oxygen* interchangeably in the context of uranium oxidation. Uranium oxidation is a complex process that involves several physical and chemical processes such as adsorption, surface reaction, diffusion of the oxidising species and reaction with the underlying metal, and finally desorption of the gaseous by-products. We mainly focus on the oxidation of uranium by oxygen (or dry air) and pure water vapour in this thesis. The mechanisms are different in dry air and water vapour on account of the different diffusing species in these environments which will be discussed in the forthcoming sections.

Uranium reacts with oxygen and water vapour to form uranium dioxide (UO_{2+x})[a] and uranium hydride (UH_3), with the latter formed only in the presence of water vapour (which is another feature that distinguishes dry-air oxidation from water-vapour oxidation). Uranium hydride present in significant quantities (in high mass and surface area) is pyrophoric in air and leads to operational safety issues in nuclear facilities (Totemeier, 2000; also see Banos, Harker, and Scott, 2018). Uranium hydride deteriorates the material quality of uranium and hence is undesirable. It will be seen later that uranium hydride is formed as an intermediate in the water vapour oxidation of uranium, with uranium dioxide and hydrogen gas produced as the main products. The deterioration of material quality is caused by both uranium hydride and hydrogen gas (H_2) as the latter can further react

---

[a] Here, x represents the hyper-stoichiometry of the uranium dioxide formed. For oxides formed in O_2/dry air, $x = 0.09$, and $x = 0{-}0.18$ for oxides formed in a water vapour environment (see Gharagozloo and Kanouff, 2013 and Banos and Scott, 2020).

with uranium to form uranium hydride (Banos and Scott, 2020).

Although a majority of the studies on uranium oxidation are experimental, there exist some theoretical models for metal oxidation in general (that can be applied to uranium oxidation), such as Wagner's theory (see reviews by Atkinson, 1985; Ritchie, 1984) for 'thick' films[b] ($\sim 1\,\mu$m) and Cabrera-Mott theory (Cabrera and Mott, 1949) for 'thin' films (< 100 Å). However, these models do not provide a mechanistic link of the oxidation kinetics to the physical and/or chemical processes that occur during oxidation. Similarly, the theoretical model of Haycock (1959), which models the transition from 'parabolic' (thickness of oxide $\propto \sqrt{\text{time}}$) to linear kinetics in the formation of *scales*[c] in metal oxidation is based on empirical data fitting, and has limited connection with the underlying physical/chemical processes. With this in mind, we aim to formulate a set of models that relate the observable kinetic quantities such as thickness or weight of the oxide formed per unit time with the physical/chemical processes that occur during uranium oxidation.

1.2 Literature review

Our review of the current literature on metal/uranium oxidation is organised as follows. The general theories and empirical models on metal oxidation are first reviewed, which also encompass uranium oxidation in dry air (oxygen gas). Subsequently, the literature on water vapour oxidation of uranium is reviewed. A brief overview of the limitations/gaps in the current literature on metal oxidation is then presented, and the chapter is ended with an overview of the content of this thesis and its organisation. The focus of this review is on the existent theories and models of uranium/metal oxidation rather than on the mathematical literature on phase transition phenomena (for example). However, adequate and appropriate mathematical literature will be reviewed in the respective chapters.

---

[b] Here, the term *film* refers to the oxide layer formed during metal oxidation.

[c] Films thicker than $\sim 10\,\mu$m are generally referred to as *scales* (Atkinson, 1985).

1.2.1 General theories on metal oxidation (including uranium oxidation in dry air/oxygen)

According to the early empirical models of metal oxidation (e.g. empirical models of Tammann (1920) and Pilling and Bedworth (1923); see review by Atkinson, 1985), the oxide growth (increase in weight/thickness of the oxide) in most metals is proportional to the square-root of time (called the 'parabolic' growth law, $L^{*^2} = k_p^* t^*$,[d] where L^* is the (dimensional) oxide/film thickness at the (dimensional) time t^* and k_p^* is the parabolic rate constant). In other words, the rate of oxide growth is inversely proportional to the thickness of the oxide formed. This growth law assumes the diffusion of uncharged oxidising species to be the rate-limiting step (see Fromhold, 1972). However, several authors (see reviews by Ritchie, 1981; Ritchie, 1984) report that simple chemical diffusion (or diffusion due to a chemical potential gradient) does not account for the rate of oxidation observed experimentally; available estimates of the relevant diffusion coefficient are too small to account for the observed rate of oxidation.

Migration of ions due to an additional driving force caused by a self-induced electric field has been suggested as an additional mechanism that may explain the observed oxidation rate. The main theories of charged particle transport in metal oxidation has been developed by Cabrera and Mott (1949) and Fromhold and Cook (1967). The continuum model of Fromhold and Cook (1967) has been recently applied to uranium oxidation via a quasi-steady assumption by Gharagozloo and Kanouff (2013). We aim to develop a formal Stefan model (explained later) based on the approach by Fromhold and Cook (1967), accounting for unsteady effects. In what follows, we discuss some of the key ideas, history and development of literature that led to the continuum model by Fromhold and Cook (1967).

Ionic diffusion as the rate-limiting step in metal oxidation was first proposed by Wagner in 1933 for thick ($\sim 1\,\mu m$) film growth (see Ritchie, 1984). Here, diffusion of metal or oxygen ions due to the combined driving influences of chemical and a self-induced electric potential gradient is considered. Whether metal or oxygen ions form the diffusing species depends on the nature of the point defects[e]

---

[d] Throughout this thesis, the superscript asterisk (*) denotes dimensional quantities, and nondimensional quantities are represented without an asterisk.

[e] Point defects are where there are missing, insterstitial or substitutional atoms in an otherwise regular crystal lattice structure.

in the oxide (Atkinson, 1985). In uranium oxidation for example, the oxygen ions form the diffusing species rather than metal ions, as has been evidenced from marker experiments in uranium oxidation (Schnizlein et al., 1960, also see Ritchie, 1984). This may be due to uranium ions being much larger and therefore substantially less mobile than oxygen ions. Nevertheless, Wagner's theory of metal oxidation is applicable for diffusion of either oxygen or metal ions. The theory of metal oxidation in general considers that the metal ions (in most cases) diffuse through an already formed surface oxide layer, due to the combined influences of chemical and a self-induced electric potential gradient, and react with the adsorbed oxygen to form new oxide at the surface/gas-oxide interface. Diffusion (or migration) of metal ions is considered to be rate-limiting in such mechanisms. For any diffusing species i, the ionic (or defect) current in a self-induced electric field is then given by (see Atkinson, 1985)

$$J_i^* = \frac{D_i^* C_i^*}{k_b^* T^*} \left(-\frac{\mathrm{d}\mu_i^*}{\mathrm{d}x^*} + q_i^* E^* \right) , \tag{1.1}$$

where C_i^* is the (number) concentration of the diffusing species i, μ_i^* is their chemical potential ($= k_b^* T^* \ln(C_i^*) + \text{constant}$ with k_b^* the Boltzmann constant), D_i^* is their diffusion coefficient, q_i^* is the effective charge on the diffusing species and E^* is the electric field strength. Equation (1.1) assumes that the electric field is small and satisfies $q^* E^* a^* \ll k_b^* T^*$[f] (i.e. the energy of thermal motion is much greater than the energy provided by the electric field), where a^* is the lattice parameter (or the ionic jump distance), k_b^* is the Boltzmann constant, and T^* is the absolute temperature. However, Wagner assumed no net electrical current across the film and that local chemical equilibrium exists throughout the oxide film. Thus he was able to eliminate all the coupled ionic transport equations of type (1.1) across the film, and reduced the set of coupled equations to a single transport equation for the chemical potential of oxygen.

Wagner's theory gives a 'parabolic' ($L^* \propto \sqrt{t^*}$) growth law for thick films or oxide films formed at sufficiently high temperatures. Here, the rate of film growth is related to the transport properties of the oxide (e.g. the diffusion coefficients) through the Nernst-Einstein relation.

Mott (1940) later postulated his theory for the formation of 'protective' oxide

---

[f] The consideration of a small electric field for the validity of (1.1) comes from the Nernst-Einstein relation (for more details, see Atkinson, 1985).

films on metals based on Wagner's theory, and suggested that electrons from the metal atoms pass through the oxide layer either by thermionic emission (if the temperature is large enough for the electrons in the metal to overcome the work function[g] of the metal with an overlying oxide layer) or quantum mechanical tunnelling (if the thickness of the oxide layer is less than 40 Å). In metals such as aluminium and chromium, the oxide grows according to a parabolic law up to a certain critical thickness and then the growth becomes negligible. The author based his theory for the formation of 'protective' oxides upon the energy required for the transfer of an electron from the metal into the conduction band of the oxide (ϕ^*) and that required to bring a metal ion into an interstitial position in the oxide (W^*). Mott's theory is applicable only for cases where the metal ions are dissolved in the oxide and migrate towards the gas-oxide interface (i.e. the metal ions form the diffusing species).

According to Mott's theory, the (number) concentration of dissolved metal ions near the oxide-metal interface is given by

$$n_i^{*2} = A^{*2} \exp\left(-\frac{\phi^* + W^*}{k_b^* T^*}\right) , \tag{1.2}$$

where A^* is related to the volume of a unit cell in the oxide lattice and T^* is the absolute temperature. He surmised that if $\phi^* > W^*$, then the electrons cannot pass to the conduction band of the oxide at room temperatures unless via quantum mechanical tunnelling; hence for oxides of metals such as aluminium, the number of electrons passing into the conduction band of the oxide via thermionic emission given by

$$\frac{120\, T^{*2}}{e^*} e^{-\phi^*/k_b^* T^*} \ \mathrm{cm}^{-2}\mathrm{s}^{-1} \tag{1.3}$$

is negligible, where e^* is the electronic charge in Coulombs. Mott noted that thermionic emission would be impossible at room temperatures in metals with work functions greater than 1 eV. Therefore, the growth of such oxides is limited by quantum mechanical tunnel effect, with the thickness limited to about 40 - 50

---

[g] Work function of a 'clean' metal is the energy required to remove an electron from the highest occupied electron level in the metal to a point in vacuum (field-free zone) immediately outside the metal, at absolute zero temperature. It should be noted that the work function depends on the configuration of atoms on the surface of the metal rather than the bulk properties of the metal.

Å (Mott, 1940; Mott, 1947) at room temperatures. The assumptions involved in this theory in addition to metal ions forming the diffusing species are that the oxide is stoichiometric[h] and in equilibrium with the oxygen gas.

However for oxides with limiting thicknesses that depend on temperature, Mott hypothesised another mechanism[i] for the formation of protective films. He proposed that if the work function ϕ^* of the metal is small enough (say, $\phi^* < 1$ eV) to allow thermionic emission of electrons to the conduction band of the oxide, then a potential gradient (now referred to as the Mott potential V_M^*) is set up across the oxide upon rearrangement of charges, resulting in an electric field that causes the metal ions to migrate towards the adsorbed anions (oxygen ions) at the gas-oxide interface. The migration of the metal ions under such conditions is then the rate-limiting step. Based on this theory, Mott proposed the existence of a limiting thickness (for 'protective' oxides) that depends on temperature.

In his paper, Mott (1947) assumed that no space charge is set up in the oxide[j], and for small (or moderate) electric fields ($E_0^* < 10^6$ V/cm), the ionic current (in A/m^2) would then be proportional to the field strength E_0^*:

$$J_{ion}^* = pN_0^* e^* \mu^* E_0^* \,, \tag{1.4}$$

where N_0^* is the (number) concentration of the interstitial positions in the oxide, p is the probability that an interstitial position near the oxide-metal interface is occupied by a metal (diffusing) ion (assuming Boltzmann statistics, $p = e^{-W^*/k_b^* T^*}$)[k] and μ^* is the mobility of a diffusing ion.

In the case of strong fields ($E_0^* > 10^6$ V/cm), a nonlinear dependence of the drift velocity (v_d^*) of a metal ion on the electric field strength was given by Verwey (1935):

$$v_d^* = 4\nu^* a^* e^{-U^*/k_b^* T^*} \sinh(a^* e^* E_0^* / k_b^* T^*) \,, \tag{1.5}$$

---

[h] Stoichiometric oxide refers to an oxide that is formed with its constituent elements present in the same proportion as indicated by the elementary reaction.

[i] For quantum mechanical tunnelling to explain the formation of protective oxide films, the limiting thickness should be independent of temperature.

[j] If no space charge is set up in the oxide, then the electric field is *homogeneous* (denoted as E_0^*) and given by the surface charge distribution.

[k] Boltzmann probability (p) gives the probability that an ion in thermal equilibrium at a temperature T^* can cross the potential barrier W^*.

where $2a^*$ is the distance between two interstitial positions (or potential minima) in the oxide lattice, ν^* is the frequency of atomic vibrations, U^* is energy barrier that has to be overcome in order to reach the adjacent interstitial position.

Mott (1947) replaced the 'sinh' term with an exponential term, and also took into account the modification to p as a result of the field to describe the ionic current (in A/m^2) in strong fields and/or low temperatures as

$$J^*_{ion} = e^* b^* \nu^* n^*_i e^{-(W^*+U^*)/k^*_b T^*} e^{(b^* e^* E^*_0)/k^*_b T^*} , \tag{1.6}$$

where n^*_i is the number concentration of (metal) ions at (or near) the oxide-metal interface and b^* is the distance between the position of a metal ion at the oxide-metal interface and an adjacent interstitial position in the oxide lattice. Thus an exponential dependence of the ionic current on the electric field strength was proposed by Mott (1947), whilst a linear dependence on the field was given for the ionic current/flux (in A/m^2) in moderate fields and/or high temperatures:

$$J^*_{ion} = \frac{N^*_0 e^{*2} a^{*2} E^*_0 \nu^*}{k^*_b T^*} e^{-(W^*+U^*)/k^*_b T^*} . \tag{1.7}$$

It is to be noted that the electrons pass from the metal atoms to the adsorbed oxygen atoms at the surface through the oxide layer. This process continues until a quasi-equilibrium is reached, that is, until the electron energy levels of the adsorbed oxygen ions (O^{2-}) at the surface is raised to the Fermi level of the metal, resulting in a self-induced electric field. Although a steady-state ionic flux is assumed, Fickian diffusion was not rigorously modelled by Mott.

Cabrera and Mott (1949)[1] then proposed their theory for the formation of thin oxide films (< 100 Å) based on Mott's hypothesis (Mott, 1947). They studied ionic diffusion for different oxide thickness and temperature regimes. For high temperatures and thick films, they suggested that the metal oxidation can be modelled by a parabolic law. For low temperatures and thin films, however, the oxide growth is assumed to have an exponential dependence on the field. A 'homogeneous field approximation' (i.e. a constant electric field across the oxide film) is made for sufficiently thin films, based on the assumption that no appreciable space charge is set up for this thickness. This approximation allows one to model

---

[1] Their theory is notably called the Cabrera-Mott theory of metal oxidation.

the movement of ions and electrons separately. Therefore the more mobile electrons can easily set up a potential difference (also called the 'Mott potential'). A rough estimate of the Mott potential (V_M^*) was given by Cabrera and Mott (1949) as

$$V_M^* = -\frac{EA^* + W_{\text{bind}}^* - \phi_0^*}{e^*}\,, \tag{1.8}$$

where EA^* is the electron affinity of O, W_{bind}^* is the adsorption energy of an oxygen ion on the oxide surface and ϕ_0^* is the work function of the metal against vacuum. The electric field set up can then lower the energy barrier for the metal ions to diffuse across the oxide layer, thereby contributing to the ionic current and increasing the rate of oxidation compared to simple chemical diffusion. Cabrera and Mott also analysed several experimental results and verified their theoretical model. They found that all the metals investigated (e.g. Al, Cu, Ag) exhibited similar behaviour at low temperatures, wherein the rate of growth slows down after a rapid initial growth and finally becomes negligible. They found this behaviour to be insensitive to the oxygen pressure to which the metal (or metal/metal oxide) sample is exposed. It is to be noted that Mott assumed that the metal ions (cations/positive ions) diffused through the oxide, owing to the difficulty of the relatively large oxygen ions (anions)[m] diffusing through the interstitial positions and/or vacancies in the oxide lattice. Whether metal ions or oxygen ions diffuse through the oxide lattice is mainly attributed to the electrical/semi-conductor properties of the oxide[n].

Cabrera and Mott (1949) proposed that strong fields of the order of 10^7 V/cm may be set up in an oxide layer of thickness about 50 Å, in which case the diffusion (or drift) velocity is no longer proportional to the field strength. For v_d^* to be proportional to the field strength, the condition $q^* a^* E_0^* \ll k_b^* T^*$ should be satisfied, where q^* is the charge on the ion, a^* is the lattice parameter. Thus they derived a parabolic law when this condition is satisfied to explain the rate of oxidation for aluminium between 350°and 450°C observed by Gulbransen and

---

[m] Note that the effective ionic radius of O^{2-} is 140 pm, whilst that of Ag^+ (for example) is 115 pm (Shannon, 1976); thus oxygen anions are larger than the cations considered, even though the atomic radius of O is smaller than those of the metal atoms.

[n] Mott predominantly studied the oxidation of *d-block* metals such as aluminium(Al), chromium(Ch) and zinc(Zn). However, Mott (1947) also noted that metals such as copper (Cu) form oxides which dissolve excess oxygen; that is, oxygen ions form the diffusing species.

Wysong (1947). However, Cabrera and Mott did not adequately explain the linear rate observed by Gulbransen and Wysong (1947) for Al at 500°C.

For oxides of Cu and Fe, for example, Cabrera and Mott (1949) proposed that vacant cation sites form the diffusing species, the number (n_i^*) of which depends on the oxide thickness, unlike the previous case (metal ions forming the diffusing species) where it was solely dependent on the oxide-metal equilibrium (Cabrera and Mott, 1949). Here, n_i depends on the number concentration of the adsorbed oxygen ions (N^*) which in turn is related to the field $E_0^* = -V_M^*/L^*$ via

$$N^* = \frac{\kappa V_M^*}{4\pi e^*} \frac{1}{L^*} \,, \tag{1.9}$$

from which Cabrera and Mott (1949) obtained a 'cubic' growth law for the oxide thickness:

$$L^{*3} = A^* t^* \,. \tag{1.10}$$

Here, A^* is some parameter that is proportional to $\exp(-(W^* + U^*)/k_b^* T^*)$, with W^* being the energy to form a vacant cation site and U^* the activation energy for its diffusion in the oxide. It is interesting to note that Cabrera and Mott (1949) derived their formula for the number of oxygen ions (or anions) adsorbed at the surface based on the Coulomb formula (1.9) which implies that for a fixed electric field (or Mott potential), a fixed number of oxygen ions are adsorbed at the surface (that is, the rate of oxide growth will be independent of the external oxygen/gas pressure). Cabrera and Mott then validated their theory based on some experimental observations.

In the case of 'very thin' (order of nm) films, Cabrera and Mott (1949) derived the drift velocity as given by

$$v_d^* = \nu^* a^* \exp(-U^*/k_b^* T^*) \left[\exp\left(\frac{q^* a^* E_0^*}{2 k_b^* T^*} \right) - \exp\left(-\frac{q^* a^* E_0^*}{2 k_b^* T^*} \right) \right] . \tag{1.11}$$

The authors suggested that for very strong fields (i.e. $E_0^* > 10^7$ V/cm), the growth rate is determined by the rate at which the ions leave the metal lattice (for cases where metal ions form the diffusing species). They then derived the growth rate of oxide to be

$$\frac{\mathrm{d}L^*}{\mathrm{d}t^*} = n_i^* \Omega^* \nu^* \exp(-(W^* + U^*)/k_b^* T^*) \exp\left(\frac{q^* b^* E_0^*}{k_b^* T^*} \right) , \tag{1.12}$$

where n_i^* is the number concentration of the metal ions at the oxide-metal interface, Ω^* is the volume of oxide formed per metal ion. The exponential dependence is applicable only for very strong electric fields (i.e. for 'very thin' films where $L^* \ll L^*_{\text{crit}}$, L^*_{crit} being $|q^* b^* V_M^*/(k_b^* T^*)|$).

Based on Cabrera-Mott theory of thin-film oxidation of metals, Fromhold and Cook (1967) formulated their ionic diffusion model for discrete lattices. If J_f^* and J_r^* (in units of number of ions per m^2 per second) represent the forward and reverse ionic currents at a lattice site k, then in the presence of an electric field, J_f^* and J_r^* are given by

$$J_f^* = n_{k-1}^* \nu^* \exp\{-(W^* - Z^* e^* E_k^* a^*)/k_b^* T^*\}\,, \tag{1.13a}$$

$$J_r^* = n_k^* \nu^* \exp\{-(W^* + Z^* e^* E_k^* a^*)/k_b^* T^*\}\,, \tag{1.13b}$$

where n_{k-1}^* and n_k^* are the number of ions (of charge $Z^* e^*$ per ion) per unit area at the $(k-1)$th and kth potential minima respectively, ν^* is the frequency with which the ion attempts to cross the barrier W^* and a^* is the lattice constant. We can see that the activation barrier is decreased (in the presence of a forward electric field E_k^*) for the ion to move from $(k-1)$th to kth potential minima, thereby contributing to the forward ionic current, whereas the barrier is increased for an ion to move from kth to $(k-1)$th minima. This leads to a unidirectional net ionic current given by $J_k^* = J_f^* - J_r^*$.

Fromhold and Cook (1967) also derived the ionic current in the continuum limit under steady-state by averaging the number of diffusing species at position x^* [o] as the bulk concentration. The steady-state ionic current under a homogeneous electric field is then

$$J_i^*(x^*) = \mu'^* E_0^* C^*(x^*) - D'^* \frac{\mathrm{d}C^*(x^*)}{\mathrm{d}x^*}\,, \tag{1.14a}$$

where

$$\mu'^* = \mu^* \frac{k_b^* T^*}{Z^* e^* E_0^* a^*} \sinh\left(\frac{Z^* e^* E_0^* a^*}{k_b^* T^*}\right)\,, \tag{1.14b}$$

---

[o] Note that the electric field (E_k^*) independent of the position x_k^* is a homogeneous field given by E_0^* (i.e. no space charges).

and,

$$D^{'*} = D^* \cosh\left(\frac{Z^* e^* E_0^* a^*}{k_b^* T^*}\right) . \tag{1.14c}$$

Here, $Z^* e^*$ is the '*effective charge*' of the diffusing species, instead of q_i^* in Mott's equation which is the actual electric charge per particle of the diffusing species; μ^* and D^* are the mobility and the diffusion coefficient of the ions that are related via the Sutherland-Einstein relation (also called the Einstein–Smoluchowski relation) given by

$$\mu^* = \left(\frac{Z^* e^*}{k_b^* T^*}\right) D^* . \tag{1.14d}$$

In (1.14), $\mu^{'*}$ and $D^{'*}$ correspond to the enhanced mobility and diffusivity as a result of the electric field. The effective charge takes into account the partial covalent bonding and hence is not equal to the actual charge on the diffusing species. In (1.14a), the second term represents the contribution to the flux due to a concentration gradient (i.e. from Fick's I law), whilst the first term gives the additional contribution to the flux due to the self-induced electric field. As previously discussed, the contribution due to a concentration gradient alone does not account for the oxidation rate observed in experiments, hence the interest in the additional electric field contribution to the ionic flux.

Equation (1.14a) is based on the discrete model of the oxide lattice and its derivation makes use of the homogeneous field approximation and the field due to space charges is neglected. This approximation is valid in the continuum limit and for small space charge concentrations. Fromhold and Cook (1967) show that the equations for both the discrete and continuum models reduce to the simple chemical diffusion case for electric fields below 10^4 V/cm. However, for electric fields in the range $E_0^* = 10^4 - 10^6$ V/cm, equation (1.14) reduces to the following form at steady-state:

$$J_i^* \approx \mu^* E_0^* \frac{[C^*(L^*) - C^*(0)\exp(Z^* e^* E_0^* L^*/k_b^* T^*)]}{[1 - \exp(Z^* e^* E_0^* L^*/k_b^* T^*)]} , \tag{1.15}$$

with the appropriate approximations made for small E_0^*; here J_i^* is the constant ionic flux in the oxide, $C^*(L^*)$ is the concentration of the diffusing species at the oxide-gas interface and $C^*(0)$ is the concentration at the oxide-metal interface. According to Fromhold and Cook (1967), this equation is valid when $|Z^* e^* E_0^* a^*/(2k_b^* T^*)| \ll 1$.

Fromhold and Cook (1967) performed numerical computations of the ionic current and compared the results with analytical calculations and experimental observations. They found that their discrete model in all cases (and their continuum model in some cases) showed consistency with available data.

Building upon Fromhold and Cook (1967)'s continuum model for metal oxidation, Gharagozloo and Kanouff (2013) (henceforth abbreviated as GK) studied the low-temperature oxidation kinetics specific to uranium. Their model is based on the diffusion of oxygen ions (ionic diffusion model) rather than metal ions (owing to the large size of uranium ions), which is supported by several authors (Auskern and Belle, 1961; Kim and Olander, 1981; Colmenares, 1975). Though there have thus far been several empirical models for the uranium oxidation kinetics (Chernia, 2009; Colmenares, 1984; Cubicciotti, 1952; Lin et al., 2008; Ritchie, 1984), Gharagozloo and Kanouff (2013)'s model is the first theoretical treatment of the problem. They modelled the oxidation of uranium in dry air (i.e. pure O_2) and compared their numerical results with several published experimental results. They reported good agreement with the experimental results with only a few deviations.

GK applied Fromhold and Cook's continuum formulation to uranium oxidation. They assumed the following form of the ionic current from equation (4.1) of Fromhold and Cook (1967) (p. 1550):

$$J_i^* = 4a^* \nu^* \exp\left(-W^*/k_b^* T^*\right) \sinh\left(\frac{Z^* e^* E_0^*}{k_b^* T^*}\right) \frac{\left[C^*(L) - C^*(0)\exp(\frac{Z^* e^* E_0^* L^*}{k_b^* T^*})\right]}{\left[1 - \exp(Z^* e^* E_0^* L^*/k_b^* T^*)\right]}, \tag{1.16}$$

where the diffusivity $D^* = 4a^{*2}\nu^* \exp(-W^*/(k_b^* T^*))$. Here, the model assumes quasi-steady diffusion and therefore time only appears implicitly through the oxide thickness $(L^*(t^*))$.

Gharagozloo and Kanouff (2013) make the following assumptions:

G1. A linear concentration gradient of the oxide ions across the oxide layer (corresponding to a quasi-steady assumption).

G2. Space charges are assumed to be negligible and therefore a homogeneous field approximation is made.

G3. The initial oxide thickness is taken as one lattice constant ($a^* = 3.8682$Å).

G4. Oxygen is said to adsorb on the uranium oxide surface as a O radical instead of O^-,O^{2-} or O_2 due to the smaller size of O compared to the other species.

G5. All adsorbed oxygen gets ionised; this assumption is supported by the claim that uranium ions in the oxide lattice increase their oxidation states from +4 to +5 or +6 as additional oxygen atoms get adsorbed onto the oxide surface (Grønvold and Haraldsen, 1948; Yasutoshi, 1974), which implies that the electrons from the uranium metal (or ion) ionise the adsorbed oxygen atoms.

The assumptions G4 and G5 could have implications on the Mott potential (V_M^*) considered by GK through W_{bind}^* and EA^* (cf. equation (1.8)) and therefore on the electric field strength E_0^*. Gharagozloo and Kanouff (2013) cite an 'inverse logarithmic'[p] growth for oxidation at low temperatures and a parabolic growth at high temperatures. The transition temperature is reported as 50°C. The authors report the model results to be in good agreement with the published experimental results in the temperature range up to 200°C and thicknesses smaller than 300 nm, whilst above this range, the model performs poorly in the prediction of the experimental results. GK attribute the mismatch to the change in the mechanism of oxidation caused due to the cracking and spalling of the oxide film above 300 nm.

1.2.2 Limitations/gaps in the current literature on dry-air oxidation

As noted at the start of this introduction, there is a sparsity of theoretical investigations of the physical mechanisms of uranium oxidation in dry air (and in water vapour, similarly for "moist air" which is a combination of the two, i.e. $H_2O + O_2$). The growth laws discussed above are at best an order of magnitude prediction, whilst the ionic flux expressions above have yet to be discussed in

---

[p] The 'inverse-logarithmic' equation (dimensional) given by Ritchie (1984) describing the oxide thickness (y) for low temperatures (and during the initial stages) at a time t is $1/y = 1/y_0 - K' \ln(1 + a(t - t_0))$, where y_0 is the oxide thickness at time t_0 and K' is some parameter that depends on temperature.

the context of a governing diffusion equation, instead relying on simplistic quasi-static theories, some of which will be put into the context of the 'full' unsteady problem in Chapter 2 and Chapter 3 of this work.

1.2.3 Objectives of our study of the U-O_2 system

We consider that oxygen ions diffuse through the surface oxide rather than the metal (U^{4+}) ions. We assume that diffusion occurs via lattice defects in the oxide, the number or concentration of which may depend on the stoichiometry of the oxide under consideration. The influence of stoichiometry is largely via the theoretical diffusion coefficient, although (a small) influence of the (hyper-) stoichiometry appears via a Stefan parameter that will be discussed in Chapter 2 of this thesis. Similarly, we will not consider the orientation of the crystal lattice, that is if the oxide formed is a single-crystal or a polycrystalline lattice. Therefore, distinction between diffusion via grain boundaries and the lattice will not be considered.

In our present work, we extend the continuum model by Fromhold and Cook (1967) to solve the full diffusion equation (using Fick's second law) without making a priori assumptions regarding the concentration distribution within the oxide layer. That is, we include the unsteady effects of the ionic current to eliminate the approximation of a linear concentration gradient of the oxygen (O^{2-}) ions across the film. Our dry-air model will address the early-stage oxidation before cracking/spalling, where the oxide growth shows a square-root dependence on time (called 'parabolic' oxidation in chemistry parlance). We model the system using a Stefan/discrete-layer model (in Chapter 2) which is commonly used to model phase-transition phenomena (e.g. melting/freezing) in heat transfer. We later model the same system using a mixed-phase/diffuse-interface model in Chapter 3.

1.2.4 Oxidation studies of uranium by pure water vapour

Uranium oxidation in a water vapour environment is different and more complex than that in dry air/oxygen. The oxidation rate in pure water vapour ($U+H_2O_{(v)}$) is at least 5000 times larger than in dry air (Baker, Less, and Orman, 1966a) suggesting distinct mechanisms. Also note that the oxidation rate in moist air ($U+O_2+H_2O_{(v)}$) is less than that in pure water vapour. We will only address the pure water vapour case as being entirely distinct from that of dry-air oxidation, although some of the literature on moist air oxidation of uranium is also reviewed.

Different mechanisms by various authors have been proposed for the water vapour oxidation of uranium. We however use the reaction mechanism proposed by Glascott and Findlay (2019), AWE plc and find support for the reaction scheme which is outlined in § 1.2.6 through the surface science and kinetic studies reported in the literature.

According to the proposed scheme, hydroxide ions (OH^-) form the diffusing species in a water vapour environment. Here, a uranium hydride (UH_3) reaction intermediate is formed that further reacts to produce the final products uranium dioxide (UO_2) and hydrogen gas (H_2). Although, a slightly hyper-stoichiometric product UO_{2+x}, with $x = 0 - 0.18$ is observed (see Banos and Scott, 2020) in a water vapour environment, we will consider that the uranium dioxide formed is stoichiometric (UO_2). The formation of H_2 and UH_3 makes corrosion in water vapour more detrimental (by degrading the material (U) quality) than that in oxygen/dry air.

We organise our review and analyses of the literature on uranium-water vapour corrosion into two sections: the first section deals with the surface science studies of the uranium and water vapour system, the second section with the diffusing species and the possible reaction mechanisms resulting in the formation of uranium hydride (UH_3) and uranium dioxide (UO_2). We mainly perform these studies to corroborate our reaction mechanism for the oxidation of uranium in a water vapour environment (see § 1.2.6), which has been proposed by Glascott and Findlay (2019). We also briefly review some of the studies on oxidation of U in moist air ($O_2 + H_2O$).

1.2.4.1 Surface science studies

It has to be noted that most of the studies on the reaction of pure water vapour with the surface of stoichiometric or non-stoichiometric uranium dioxide were performed on single-crystal surfaces. Some studies used poly-crystalline UO_{2+x} surfaces, which may represent a more realistic scenario. However, since the (111) surface is the natural cleavage plane of the fluorite-type structure (Castell et al., 1996), we place more importance on the studies involving $UO_2(111)$. Our choice is also aided by the fact that $UO_2(111)$ is the most stably oriented surface among (110), (111) and (100) (i.e. low index) surfaces, with a surface energy of 1.07

J/m^2 (Tasker, 1979).

Hedhili, Yakshinskiy, and Madey (2000) studied the interaction of water vapour with stoichiometric $UO_2(001)$. Techniques such as electron stimulated desorption (ESD) and X-ray photoelectron spectroscopy (XPS) among others were employed to characterise the oxide surface, where the presence of both H^+ and O^+ (O^+ being the dominant signal) has been observed. However, since the authors did not observe any OH^+ on the surface, they concluded that hydroxyl species were not adsorbed. They suggested that oxygen as O^- or O^{2-} diffuses into the bulk which is then responsible for the oxidation of uranium. In another experiment involving heavy water ($D_2{}^{18}O$), they exposed a sample $UO_2(001)$ surface to 1000 L[q] of $D_2{}^{18}O$ and concluded that the surface chemistry of UO_2 remains unaffected, basing their conclusion on a lack of evidence for the presence of D_2O or any OD species on the surface. Observance of an ^{18}O peak only after 8 L of $D_2{}^{18}O$ exposure has been reported, but again no evidence for an OD^+ (mass-to-charge ratio, $m/e = 20$), $^{18}OH^+$ ($m/e = 19$) or $^{16}OH^+$ ($m/e = 17$) signal was found, thereby leading to the conclusion that no adsorbed hydroxyl species were present. The work by Henrich and Cox (1996) was cited by the authors to infer that the presence of lattice defects or vacancies appear to be important in determining the adsorbate and therefore the diffusing species in water vapour environments.

Hedhili, Yakshinskiy, and Madey (2000) also cite Winer et al. (1987) who investigated the interaction of D_2O with clean U at room temperature. Winer et al. (1987) found the presence of strongly chemisorbed[r] OD^- on U from their XPS results. This result has also been confirmed by Secondary Ion Mass Spectrometry (SIMS)[s] which showed a substantial relative amount of OD^-after D_2O exposure. They also conducted temperature programmed desorption (TPD) studies and

---

[q] Langmuir(L) is a unit to define the exposure of a solid surface to gases and is used in adsorption studies. $1\ L = 10^{-6}$ Torr s, which is equivalent to an exposure of the surface to a pressure of 10^{-6} Torr of the gas for 1 second.

[r] Chemisorption refers to adsorption wherein there is occurrence of chemical reaction between the absorbent and absorbate molecules, thereby involving exchange of electrons between them.

[s] Secondary Ion Mass Spectrometry (SIMS) is a surface analytical technique wherein a primary ion beam (high energy ions) is made to bombard the sample surface, leading to an ejection of the surface ions in the sample (‘*secondary ions*’) which is called sputtering. The masses of the secondary ions ejected can then be determined by measuring their times of flight in a detector from which the ion species are identified. Depth profiling can be done by recording the sequential SIMS spectra by the bombardment of the exposed surface.

monitored the desorbing species by carefully heating the surface from 85 to 298 K. They found that D_2O strongly chemisorbed to the surface at 85 K, which formed a first layer, covered by multilayer ice. They also found significant differences in binding energies of oxygen 1s spectra[t] between water vapour adsorption on clean and oxygen-covered uranium, and concluded that oxygen inhibition of $U - H_2O$ reaction was due to a surface mechanism. This conclusion may have possibly been misinterpreted by Hedhili, et al. who reported the differences in binding energy spectra between the pure and oxygen-covered surfaces to be sufficient evidence for no hydroxyl groups to form on the oxide surface. This has also been pointed out by Stultz, Paffett, and Joyce (2004), who suggested that water dissociation must take place for oxygen to be incorporated into the surface and also pointed to the fact that hydrogen has not been monitored in the experiments conducted by Hedhili, Yakshinskiy, and Madey (2000).

Further supporting evidence for the chemisorption of water on the oxide surface, and its dissociation into H^+ and OH^- can be found in Colmenares (1984) who investigated the corrosion of U by $H_2O_{(v)}$ in the temperature range 333 - 453 K, with a $H_2O_{(v)}$ pressure from 7×10^{-3} to 20 kPa. He suggested that the transport of OH^- through the oxide layer occurs via an 'interstitialcy' mechanism to then react with the metal. The study by Catlow (1977) has been cited, according to which the transport of OH^- is energetically favoured over the transport of O^- or O^{2-} through the oxide layer, owing to the large Coulomb energy[u] opposing the displacement of O^- or O^{2-} from their lattice positions.

Senanayake and Idriss (2004) investigated the interactions of water vapour on $UO_2(111)$ surfaces by deliberately creating defects on the UO_2 surface and monitoring the amount of H_2 evolved (or desorbed) as a function of the defect concentration. The study was thus focused on hypo-stoichiometric (UO_{2-x}) or O-defected crystals (UO_2 crystals with oxygen vacancies). The authors observed that the adsorption of H_2O molecules at 300 K on stoichiometric surfaces (no defects) was mostly reversible ($> 80\%$) implying that the stoichiometric oxide surface was largely non-reactive (i.e. no dissociative adsorption), whereas dissociative adsorption of water vapour was found to occur in the presence of defects. This study further confirms that defects play an important role in the adsorption

---

[t] Here, oxygen 1s spectra refers to the X-ray photoelectron spectra of the core electron energy levels in the oxygen species.

[u] Coulomb energy is the energy associated with the electrostatic forces within atoms or molecules, such as between electrons, or between the nucleus and the electrons.

of water vapour and in the subsequent diffusion of OH^- through the oxide layer. The evolution of hydrogen (H_2) occurred only in cases where the surface was O-defected (through Ar^+ sputtering), while no H_2 was formed in purely stoichiometric UO_2 crystals, leading the authors to conclude that H_2 was desorbed only from O-defected sites.

The study of water adsorption on defective $UO_2(100)$ by Stultz, Paffett, and Joyce (2004) lends further support to Senanayake and Idriss's hypothesis that H_2 was primarily desorbed from the surface defects (O vacancies). Stultz et al. observed significant amount of H_2 evolution from highly defected oxide surfaces at ~ 400 K.

One of the pioneering studies on U oxidation by water vapour was conducted by Baker, Less, and Orman (1966a). They proposed a mechanism involving dissociation of water vapour to produce OH^-, and the formation of UH_3 as an intermediate in the oxidation reaction, where the amount of UH_3 formed was indirectly estimated based on the hydrogen gas deficit. The involvement of OH^- in the oxidation of U in water vapour environments has been confirmed by the recent advanced study using atom probe tomography (APT) technique[v] by Martin et al. (2016).

In our study, we consider OH^- to be the diffusing species in a pure water vapour environment, as it has been established from several studies in the literature. We will, however, not take into account the influence of deviation from stoichiometry on the oxidation kinetics. The influence of hyper-stoichiometry is assumed to be only via the lattice parameter appearing in the diffusion coefficient.

1.2.4.2 Studies on diffusion and reaction kinetics

Baker, Less, and Orman (1966a) proposed a mechanism involving diffusion of OH^- ions through an initially formed layer of oxide, which then react with the metal underneath. Uranium hydride is formed as a reaction intermediate, and diffusion of OH^- ions was suggested as the rate-limiting step.

The influence of oxygen on the uranium and water vapour reaction was also

---

[v] APT is an analytical technique to determine the material composition, wherein a sharp tip (thickness of the order of nm) of the material sample is subjected to a focused ion beam that vaporises and ionises the atoms one by one and then detects them using a Position Sensitive Detector (PSD). The individual time of flight of the ions are then measured to identify the ions. The atom probe microscope provides a 3D reconstruction of the sample tip analysed.

studied by Baker, Less, and Orman (1966b) and they found that oxygen had an inhibitory effect on the U+$H_2O_{(v)}$ reaction, which has also been confirmed by other studies (Draley and Ruther, 1957; Kondo et al., 1964). The effect of parameters such as temperature, hydrogen pressure and relative humidity on the corrosion rate were investigated by Baker, Less, and Orman (1966a) and the results were reported. The authors also reported that the growth (thickness) of the oxide layer and hydrogen evolution have a linear dependence on time. It will be seen in the later chapters that whilst the initial stage of oxidation is parabolic, the late stage is linear. Late stage is defined as the period after cracking and spalling of the surface oxide, wherein a portion of the oxide adhering to the metal is coherent whilst the remaining non-adherent portion is porous as a result of cracking/spalling of the surface oxide (see Figure 1.2). The porous layer allows the diffusion of water vapour molecules, and the dissociation of water vapour into H^+ and OH^- occurs at the surface of the adherent oxide (beneath the non-adherent surface layer) having constant width/thickness; the thickness of the adherent layer is dependent on temperature. The late-stage oxidation of uranium in water vapour ($H_2O_{(v)}$) thus shows a linear growth according to our models and will be presented in Chapter 5 after an investigation of the early-stage oxidation of uranium by water vapour in Chapter 4.

The major findings of Baker et al. (Baker, Less, and Orman, 1966a; Baker, Less, and Orman, 1966b) that are relevant to our present study are:

i Hydroxyl anion (OH^-) is the diffusing species in both pure water vapour and moist air (O_2 + H_2O).

ii The oxide layer is not protective enough to prevent the evolved hydrogen at the surface formed from the reaction of U with $H_2O_{(v)}$ to re-diffuse through the surface oxide and react with the underlying uranium metal. Cracking/spalling of the oxide which makes it non-protective may be attributed to the build-up of stress due to the difference in the densities of uranium and uranium dioxide. Nevertheless, the oxide layer retards the rate of formation of uranium hydride that may form from the reaction of the evolved H_2 with uranium. Our study will however not focus on the diffusion of the evolved hydrogen and its reaction with the metal. Baker, Less, and Orman (1966a) (among other authors) reported that a build up of hydrogen gas up to a pressure of 6 atm did not alter the rate of oxidation, and hence we can safely neglect it.

iii The uranium dioxide formed is hyper-stoichiometric i.e. $UO_{2.06\pm0.02}$ in a uranium and moist air ($U + O_2 + H_2O_{(v)}$) system and stoichiometric (UO_2) in a pure water vapour ($U + H_2O_{(v)}$) system. Baker, Less, and Orman (1966b) attributed the hyper-stoichiometry of the oxide in a moist air environment to the oxidation of the already formed layer of uranium dioxide by O_2.

iv The uranium hydride (UH_3) that is formed as an intermediate product further reacts with water vapour to form uranium dioxide and hydrogen; the amount of UH_3 formed depends on the relative humidity and pore size distribution of the oxide (which we presume relates to the properties of the porous oxide) among other factors (Baker, Less, and Orman, 1966b). The authors report that a greater quantity (i.e. more mass at a fixed dimensional time) of hydride at a higher relative humidity (in the case of moist air) is due to the blockage of the diffusion path for water vapour ($H_2O_{(v)}$) by condensed water ($H_2O_{(l)}$) in the pores of the oxide layer, which prevents the reaction of uranium hydride with water vapour to form uranium dioxide. This statement however needs further experimental verification and is out of the scope of our work.

Jones et al. (2013) suggested that the hydride nucleation sites occur at the metal-oxide interface instead of the metal subsurface (i.e. within the metal). Banos, Harker, and Scott (2018) proposed point defect sites on the surface of the metal as one of the hydride nucleation sites apart from carbide inclusions and grain boundaries. The formation of UH_3 between the metal and the oxide layers has also been irrefutably shown by the recent high spatial-resolution atom probe tomography (APT) studies conducted by Martin et al. (2016). A discrete hydride layer of near constant thickness of 3 - 5 nm (during the time period of the experiments of approximately 1-2 hours) is shown to exist between the metal and oxide layers. It is noteworthy to mention that the formation of uranium hydride (UH_3) during ambient air oxidation was first explicitly observed in the atom probe tomography studies of Martin et al. (2016). This study confirms Baker, Less, and Orman (1966a)'s hypothesis that UH_3 forms as a reaction intermediate, which has been previously disputed by several authors. Our reaction mechanism is largely based on the reaction mechanism proposed by Baker, Less, and Orman (1966a).

1.2.5 Oxidation studies in moist air ($U + O_2 + H_2O_{(v)}$)

McGillivray, Geeson, and Greenwood (1994) studied uranium oxidation in both dry and moist air. They proposed that different diffusing species, viz., hydroxide (OH^-) and oxide (O^{2-}) ions were produced in moist and dry air respectively. The influence of water vapour pressure on the oxidation rate among other factors has been studied under moist air conditions. Depth profiling of the oxide formed has been performed using SIMS (Secondary Ion Mass Spectrometry) and the oxide layer in a moist air environment was speculated to be formed from both O_2 and H_2O. A linear rate of oxidation even at small times has been observed in the temperature range 150 to 350°C and Langmuir adsorption isotherm[w] has been used to fit the data.

Haschke, Allen, and Martz (1998) and Haschke, Allen, and Morales (2001) compared uranium(U) and plutonium(Pu) systems and proposed a mechanism in which Pu or U reacts chemically with pure water vapour ($H_2O_{(v)}$) whilst catalytically with $O_2 + H_2O$ mixture wherein the hydride formed acts as a catalyst. Haschke et al. dismissed OH^- to be the diffusing species and instead proposed oxygen ions (O^{2-}) to be the sole diffusing species in the moist air environment, which can be proved to be flawed based on the recent atom probe tomography (APT) study by Martin et al. (2016) (refer figure 1.1(c) where UH molecular ions are detected).

All the above discussed studies (Baker, Less, and Orman, 1966a; Baker, Less, and Orman, 1966b; McGillivray, Geeson, and Greenwood, 1994; Haschke, Allen, and Morales, 2001) proposed the uranium oxidation mechanisms based on experimental results and empirical data-fitting. The rate of oxidation was determined to be mostly linear even at small times in the temperature range studied.

1.2.6 Objectives of our study of the U-$H_2O_{(v)}$ system

Our work follows from the reaction mechanism proposed by Glascott and Findlay (2019) in an internally published report within AWE plc., on uranium corrosion in water vapour environments. They suggested that the diffusing species in water

---

[w] Adsorption isotherm gives the variation of the amount of adsorbate on the absorbent surface with the partial pressure of the gaseous absorbate molecules, at a constant temperature. The Langmuir adsorption isotherm is given by $\theta = \frac{K_{\text{eq}}p}{1+K_{\text{eq}}p}$ where θ is the fractional occupancy of the adsorption sites by the adsorbate molecules or ions or radicals, p is the partial pressure of the gas (adsorbate) and K_{eq} is the equilibrium constant for adsorption.

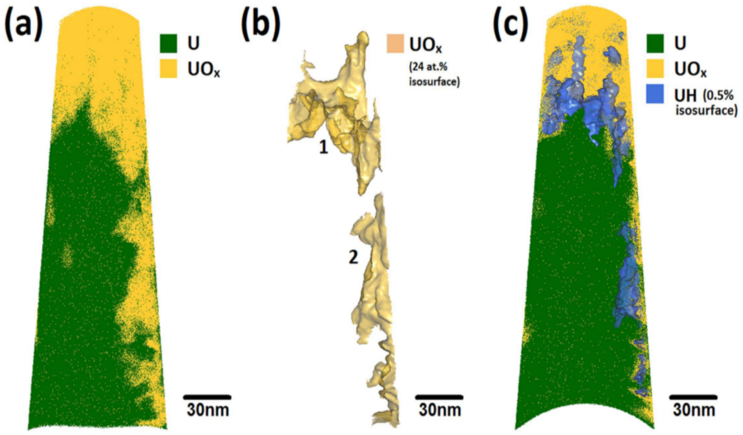

Figure 1.1: (a) An atom probe map of a tip from a uranium sample exposed to air, showing U and UO$_x$ ions in green and yellow respectively. (b) A 24 atomic % UOx isosurface showing two oxide regions that indicates the percentage of UOx atoms to the total amount of atoms present in that location. (c) An atom probe map showing a 0.5 atomic % UH in blue indicating the location of the hydride ions. Image reproduced with permission from Martin et al. (2016).

vapour environments are the hydroxide ions (OH$^-$) which is adequately supported by the recent research using the high spatial resolution atom probe tomography (APT) technique by Martin et al. (2016), wherein the authors infer that hydroxyl (OH$^-$) containing species are distributed throughout the oxide. These hydroxyl species are observed to disappear at the location where the hydride (H$^-$) molecular ions are observed, thereby suggesting a mechanistic link for the formation of UO$_2$ through the reaction of UH$_3$ with the hydroxide species. Glascott and Findlay proposed that the diffusing OH$^-$ ions react with UH$_3$ to form UO$_2$ and hydrogen radicals (H$^\bullet$), the latter reacting further with the metal to form UH$_3$. This mechanistic link of UH$_3$ in the formation of UO$_2$ is also supported by the fact that there is no UO$_2$ layer observed between the metal (U) and the hydride layers, suggesting that the oxide is not formed directly from the metal once a layer of UH$_3$ is formed. It has been suggested in several studies (see reviews by Banos, Harker, and Scott, 2018; Banos and Scott, 2020) that the oxide (UO$_2$) is immediately formed on a freshly polished or clean U surface under ambient conditions such that an initial oxide layer is always observed regardless of the method of preparation. A hydride layer has not been reported in such studies, possibly due to the high resolution needed to detect a few nanometers thick hydride layer, which was only recently confirmed using the atom probe tomography technique (Martin et al., 2016).

In our model, we therefore consider an initial thin (a few atomic layers) oxide layer. Also, we consider an initial relatively thinner hydride layer in order to initiate the reaction in accordance with the mechanism proposed. The reaction mechanism proposed by Glascott and Findlay (2019) for the water vapour corrosion of uranium is given in the form of the following elementary reaction steps.

Proposed reaction for oxidation in water vapour

R1. Adsorption of water vapour molecules ($H_2O_{(v)}$) onto the surface of uranium dioxide lattice to form two mobile hydroxide ions (OH^-):

$$2\,H_2O_{(v)} + \underset{\text{surface/lattice}}{2\,O^{2-}} \xrightarrow{k_s^*} \underset{\text{surface/lattice}}{2\,OH^-} + \underset{\text{mobile}}{2\,OH^-}.$$

There is diffusion of the mobile OH^- through the bulk medium.

R2. The diffusing OH^- reacts with uranium hydride (UH_3) to produce uranium dioxide (UO_2) and hydrogen radicals ($H^\bullet$), via

$$UH_3 + 2\,OH^- \xrightarrow{k_{cH}^*} UO_2 + 5\,H^\bullet + 2\,e^- \ .$$

Therefore UH_3 acts as an intermediate to form UO_2 from uranium and water vapour and this reaction is a source of $H^\bullet$, which diffuse through the bulk medium.

R3. The diffusing hydrogen radicals generated in R2 then react with uranium to produce more UH_3 via

$$3\,H^\bullet + U \xrightarrow{k_{hM}^*} UH_3\,.$$

R4. The hydrogen radicals may also react with each other at the surface (gas-oxide interface) after diffusing through the oxide layer, subject to

$$2\,\mathrm{H}^{\bullet} \xrightarrow{k_H^*} \mathrm{H}_2\,.$$

R5. The electrons produced recombine with the lattice OH^- at the surface to reproduce the uranium dioxide lattice:

$$2\,\mathrm{e}^- + \underset{\text{lattice}}{2\,\mathrm{OH}^-} \xrightarrow{k_e^*} \underset{\text{lattice}}{2\,\mathrm{O}^{2-}} + \mathrm{H}_2\;.$$

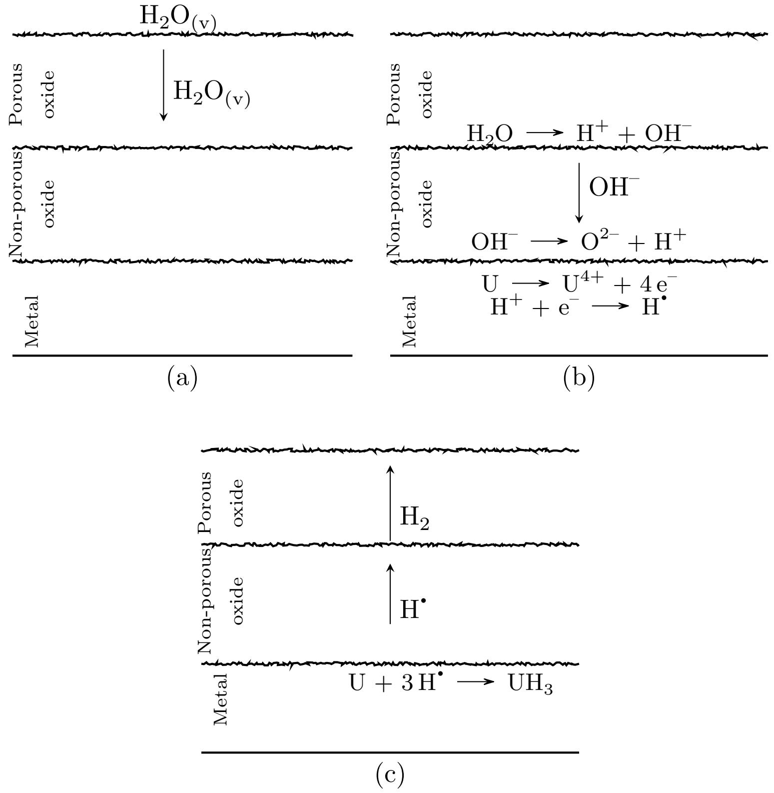

Figure 1.2: The various processes occurring during uranium oxidation in a pure water vapour ($H_2O_{(v)}$) environment, where (a) represents diffusion of water vapour through the porous oxide, (b) dissociation of water vapour molecules at the surface of the adherent (or non-porous) oxide, diffusion of OH^- ions through the non-porous oxide and reaction of OH^- with U to form UO_2, (c) formation of UH_3 and diffusion of $H^\bullet$ to the surface of the adherent oxide to form H_2. The formation of porous/non-adherent oxide occurs after cracking/spalling of the surface oxide and leads to a linear oxidation regime.

The overall reaction of uranium with pure water vapour is represented as follows:

$$U + 2\,H_2O_{(v)} \longrightarrow UO_2 + 2\,H_2 \ .$$

Figure 1.2 shows the reaction mechanism proposed by Glascott and Findlay (2019) in different stages. They suggested that $H_2O_{(v)}$ molecules diffuse through a porous (non-coherent) oxide, formed as a result of cracking and spalling at the late stages of corrosion when the oxide layer has reached a thickness of 500 Å (Harker, 2006) at room temperatures (thickness of the coherent oxide being a function of temperature). In the schematic, we do not explicitly represent an initial hydride layer that is considered in the model.

1.2.7 Assumptions in our $U + H_2O_{(v)}$ models

In this section, we discuss the assumptions made before we venture into mathematically modelling uranium corrosion in water vapour.

A1. The surface reactions represented in R1, R4 and R5 are neglected. The justification for this assumption will be provided in Chapter 4.

A2. The hydrogen radicals coming in contact with the metal atoms (or ions) spontaneously react to form UH_3 and therefore the solubility of hydrogen (as radicals or H_2) in the metal is neglected.

A3. The amount of uranium hydride (UH_3) formed is assumed to be not sufficient to rupture the overlying oxide layer during the initial stages of uranium corrosion. This assumption is also supported by the fact that we do not observe a non-coherent oxide layer in these early stages, when the thickness of the overlying oxide is less than 500 Å (Harker, 2006; Banos, Harker, and Scott, 2018) at room temperatures.

A4. The effects of stress due to volume expansion on the kinetics of uranium corrosion are neglected.

A5. Radiolysis of H_2O (i.e. dissociation of water molecules by radiation) on the surface of the oxide is not considered.

The other assumptions underpinning our mathematical models will be discussed in the respective chapters.

1.3 Thesis overview

The remaining chapters in this thesis are organised as follows.

- In Chapter 2, we present discrete-layer (Stefan) formulations of simple chemical diffusion and ionic diffusion (in the presence of a self-induced electric field) problems for the dry-air oxidation of uranium. The models are solved using numerical approaches, whilst analytical and/or asymptotic solutions are also derived for some problems. We compare our unsteady model with the quasi-steady model of GK and discuss the range of validity for the quasi-steady approximation. The influence of different parameters on the dry-air oxidation rate are discussed.

- In Chapter 3, a mixed-phase/diffuse-interface formulation for dry-air oxidation is presented. This chapter provides a link between the work of Chapter 2 and the approach taken in chapters 4 and 5. Here we validate the mixed-phase formulation, before it is extended to model the more complex water-vapour oxidation in Chapter 4.

- Chapter 4 discusses the early-stage oxidation of uranium in water vapour. A reaction-advection-diffusion (RAD) model is formulated using a diffuse-interface approach for which both numerical and asymptotic solutions are presented. A matched asymptotic analysis is performed in the limit of a large reaction rate constant or equivalently in the large-time limit. The numerical simulation results are compared with the leading-order asymptotic solution to validate the numerical formulation. The influence of different diffusivity parameters, rate constants and initial conditions on the water-vapour oxidation kinetics are explored. This chapter forms the basis of material published in the paper, "Asymptotics of coupled reaction-diffusion fronts with multiple static and diffusing reactants: uranium oxidation in water vapor" by Natchiar, Hewitt, Monks and Morall in SIAM Journal on Applied Mathematics (Monisha Natchiar et al., 2020).

- In Chapter 5, we discuss the late-stage oxidation of uranium in water vapour that comprises the linear regime after cracking and spalling of the surface oxide. For the same reaction RAD model presented in the previous chapter, constant-flux solutions are explored; the motivation for this can be found within the chapter.

- Discussion on the different models for dry-air and water-vapour oxidation and their comparisons with published results are presented in Chapter 6, and we end the chapter with conclusions and future work.

Chapter 2

Dry-air oxidation of uranium

When uranium is oxidised by dry air or oxygen, uranium dioxide (UO_{2+x}) is produced at room temperatures; the formation of U_3O_8 that occurs at higher temperatures will not be studied or discussed in this work. In this chapter, we investigate the kinetics of uranium oxidation by dry air/oxygen to form UO_{2+x} using a range of modelling approaches. Nitrogen in dry air acts as an inert species in the corrosion/oxidation of uranium (refer § 1.1); hence the terms *dry air* and *oxygen* will be used interchangeably for the kinetic study in this chapter. It is well-known that diffusion is the rate-determining step in the oxidation of uranium by dry air/oxygen and the diffusing species in this case are oxygen ions (O^{2-}). Although the study of water vapour oxidation of uranium is more significant/relevant in a practical setting (pertaining to nuclear waste storage applications), there is a dearth of mathematical models for the study of uranium oxidation per se, and the study of dry air oxidation of uranium provides a context for the subsequent study of the more complicated water-vapour oxidation in Chapter 4.

Uranium dioxide is less dense than the parent metal (U) (refer Table A.1), and can lead to deterioration of the material (U) quality after a prolonged storage period. Motivated by these applications, we investigate the uranium oxidation kinetics in dry air. Figure 2.1 depicts our workflow in the modelling and investigation of dry air-uranium oxidation kinetics; the detailed modelling approaches are not depicted for the sake of brevity, and can be found in the respective sections.

2.1 Quasi-steady chemical diffusion

We begin our investigation of uranium oxidation in dry air by considering the quasi-steady diffusion model of Gharagozloo and Kanouff (2013). Gharagozloo and Kanouff (henceforth abbreviated as GK) have modelled the uranium oxidation process using two mechanisms, viz. chemical and ionic diffusion.

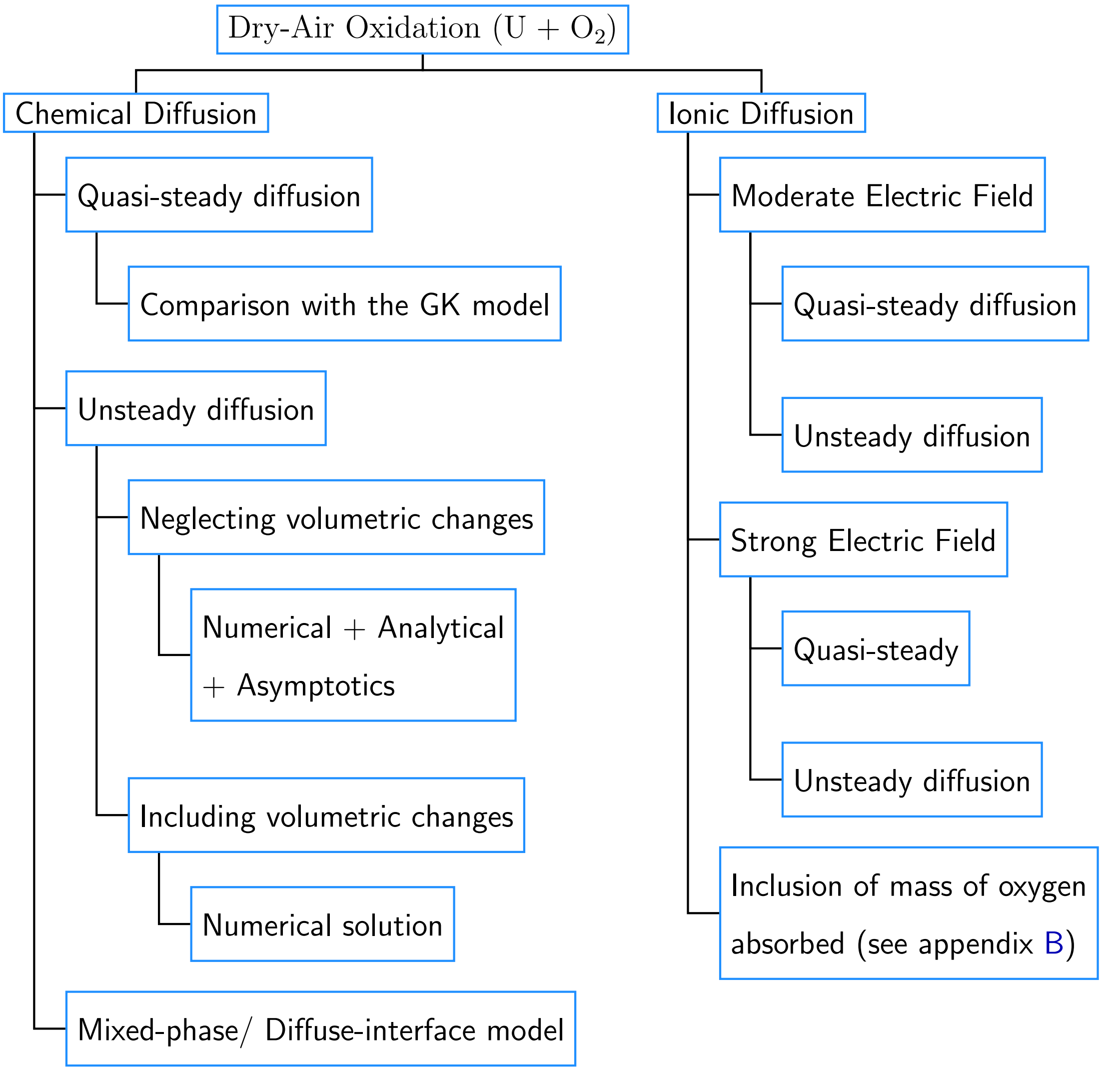

Figure 2.1: Workflow for dry-air oxidation modelling.

When a quasi-steady approximation is made, the flux of oxygen in the oxide layer is independent of the position in the layer; in other words, the concentration gradient of the diffusing species is linear. We compare the results of our quasi-steady formulation with that of GK, and then finally compare with the unsteady solution in §§§ 2.2.1.6 (also see § 2.3) to analyse the validity of this approach (or to find the range of parameters for which the quasi-steady approximation is valid).

We begin by modelling the dry-air oxidation process as a simple chemical diffusion model that is further subdivided into quasi-steady and unsteady formulations. We then model the process using an ionic diffusion model, again subdivided into quasi-steady and unsteady formulations. Both the quasi- and unsteady models are formulated as a Stefan problem in this chapter. The classical Stefan problems typically describe phase-transition phenomena involved in heat transfer (for e.g. melting/solidification). The characteristic feature of a Stefan problem is the existence of one/more *free boundaries* (also called moving/phase boundaries) that are unknown a priori and the evolution of which is described by the "Stefan condition". Here, we define a Stefan problem as a discrete-layer model consisting of sharp interfaces (i.e. phase boundaries) that separate the different homogeneous (or pure) phases. The distinction between the quasi- and unsteady Stefan models is based on a nondimensional parameter called the Stefan number. Detailed discussion of the models are provided in the respective sections.

Generally a quasi-steady-state approximation can be applied to systems in which the time taken for diffusion is much less than the time that is required to change the bulk concentration of the material phase by the diffusing species.

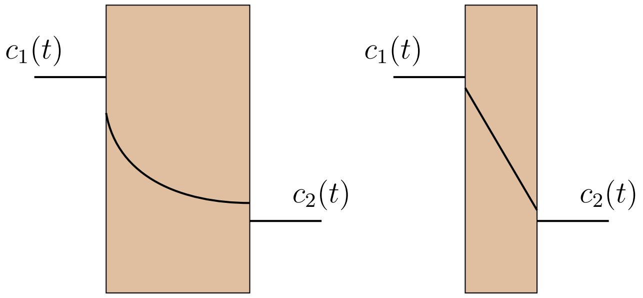

(a) (b)

Figure 2.2: Schematic of (a) unsteady/transient diffusion across a thick slab or layer (b) quasi-steady diffusion across a thin layer. The concentrations of an arbitrary diffusing species at the two boundaries of the slabs are denoted as $c_1(t)$ and $c_2(t)$.

For example, in the case of diffusion occurring through a thin slab or layer as shown in subfigure 2.2(b), the diffusion is quasi-steady wherein the diffusive flux inside the slab is constant and the concentration profile is linear. In more general problems, although the thickness of the layer through which diffusion occurs does not in itself determine whether the diffusion is quasi-steady, it determines the timescale over which quasi-steady behaviour is found.

2.1.1 The reduced model of GK

A one-dimensional model for the diffusion of oxygen ions (O^{2-}) that is the rate-determining step in the oxidation kinetics of uranium has been considered. From Fick's first law of diffusion, the chemical diffusive flux of oxygen ions is proportional to their concentration gradient and the proportionality constant is called the diffusion coefficient or diffusivity of oxygen (O^{2-}) in uranium dioxide ($UO_{2.09}$)[a]. The diffusivity can be determined either theoretically or from empirical data. The chemical diffusive flux is then mathematically written (using Fick's first law) as

$$J_c^* = -D_c^{O*} \frac{\partial c^*}{\partial z^*}, \tag{2.1}$$

where J_c^* is the chemical diffusive flux in the z^* direction, D_c^{O*} is the diffusivity of oxygen ions in uranium dioxide and $c^*(z^*, t^*)$ represents the (number) concentration of oxygen ions as a function of z^* and time t^*. For a quasi-steady approach, the governing equation for the diffusion of oxygen ions in the oxide layer is given by $\partial J_c^* / \partial z^* = 0$, with an initial state consisting of both the metal layer and an oxide layer of thickness δ_O^*[b].

A schematic of the configuration is shown in Figure 2.3, where we choose to measure z^* relative to an initial oxide surface, $z_s^*(t^* = 0) = 0$. Interfaces define locations that separate one phase from the other. For example, a metal-oxide interface separates the pure metal and oxide phases and is denoted by $z^* = z_1^*(t^*)$. As can be seen in the figure, the oxide surface $z_s^*(t^*)$ is not stationary and advects 'upwards' ($t^* > 0$) to accommodate the increased volume resulting from phase conversion or density change (as the more dense metal is converted to less dense oxide). The oxide-metal interface ($z_1^*(t^*)$) in turn moves 'downwards' as the reaction progresses. Here, the material expansion due to the phase changes is considered to be only in the upward direction.

---

[a] A slight hyper-stoichiometry of $x = 0.09$ is considered for uranium dioxide, i.e. $U + \frac{(2+x)}{2} O_2 \rightarrow UO_{2+x}$ where $x = 0.09$ is in accordance with the experimental data of Colmenares (1984) (see Gharagozloo and Kanouff, 2013).

[b] From the experimental studies, a 'clean' uranium sample without an initial oxide layer has not been observed as the uranium metal is highly reactive with oxygen or water vapour (Gharagozloo and Kanouff, 2013; Banos and Scott, 2020).

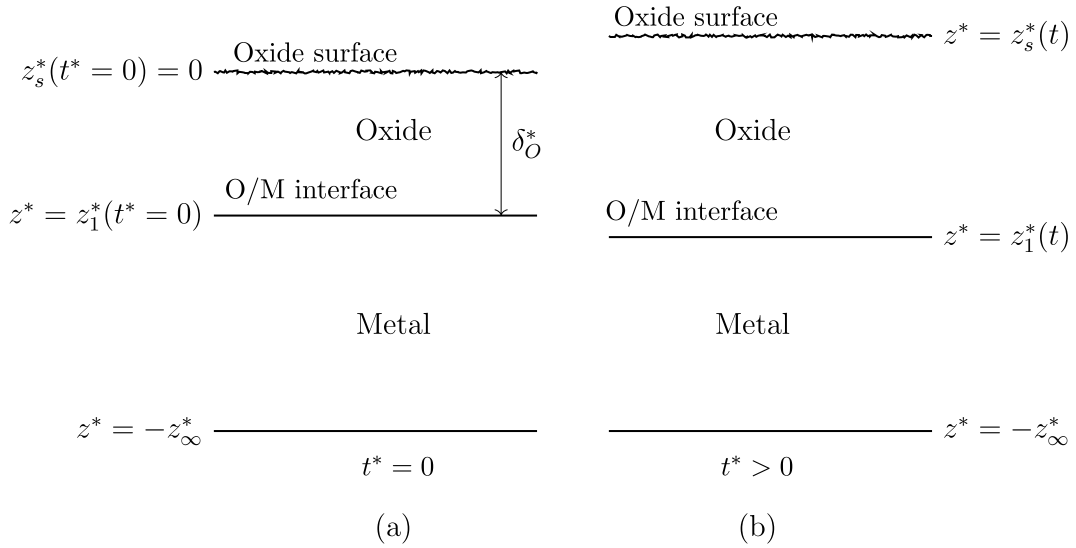

Figure 2.3: Schematic of the (a) initial state and (b) later state of the metal (U) + metal oxide ($UO_{2.09}$) system, with two moving interfaces at the locations $z^* = z_1^*(t^*) < 0$ and $z^* = z_s^*(t^*) > 0$. Here the O/M interface represents the interface that separates the pure metal and oxide phases, and the oxide surface represents the gas-oxide interface.

The oxide surface is exposed to an ambient concentration of oxygen gas (O_2). We neglect the details of the surface reactions, where it is assumed that the timescale for achieving the surface equilibrium concentration of the adsorbed oxygen ions (O^{2-}) is much less than the timescale for the diffusion of O^{2-} through the surface oxide to react with the metal (Gharagozloo and Kanouff, 2013). We therefore consider a constant surface concentration of the oxygen ions equal to C_a^* ions/m^3 in order to compare our quasi-steady results with that of GK. Furthermore, we assume that the rate of reaction at the oxide-metal interface is much faster (i.e. instantaneous reaction) than the rate of diffusion of oxygen, leading to $c^*|_{(z^*=z_1^*(t^*))} = 0$. The boundary conditions are thus $c^*(z_1^*) = 0$ and $c^*(z_s^*) = C_a^*$.

Assuming a quasi-steady solution implies that the diffusion equation,

$$\frac{\partial^2 c^*}{\partial z^{*2}} = 0 \tag{2.2}$$

gives a concentration profile that is a linear function of depth,

$$\frac{\partial c^*}{\partial z^*} = \frac{c^*|_{(z^*=z_s^*)} - c^*|_{(z^*=z_1^*)}}{z_s^*(t^*) - z_1^*(t^*)} = \frac{C_a^*}{z_s^*(t^*) - z_1^*(t^*)}\,, \tag{2.3}$$

where $z_1^*(t)$ is the location of the oxide-metal interface and $z_s^*(t)$ is the location of the surface.

Using this quasi-steady approach, (2.1) can be simplified to a constant flux of

$$J_c^* = -D_c^{O*} \frac{C_a^*}{z_s^* - z_1^*} \,. \tag{2.4}$$

The chemical diffusivity D_c^{O*} is defined in Gharagozloo and Kanouff (2013) as

$$D_c^{O*} = 4a^{*2}\nu^* \exp\left(\frac{-W^*}{k_b^* T^*}\right), \tag{2.5a}$$

with the lattice constant (length of a unit cell in the uranium dioxide lattice), $a^* = 5.4713\,\text{Å}$ (Leinders et al., 2015)[c]; vibrational frequency of oxygen atoms in uranium dioxide, $\nu^* = 19 \cdot 10^{12}$ Hz; energy barrier height, $W^* = 1.98 \cdot 10^{-19}$ J (Gharagozloo and Kanouff, 2013); and the Boltzmann constant, $k_b^* = 1.3806 \cdot 10^{-23}$ J/K. Substituting these constants in (2.5a) gives

$$D_c^{O*} = 2.2751 \cdot 10^{-5}\ \text{m}^2/\text{s}\ \ \exp\left(\frac{-14342\ \text{K}}{T^*\ (\text{K})}\right). \tag{2.5b}$$

For the concentration of O^{2-} at the oxide surface (assuming an initial oxide layer), we use the value from Gharagozloo and Kanouff (2013) given by $C_a^* = 6 \cdot 10^{28}$ ions/m^3. However, it should be noted that for $C_a^* = 6 \cdot 10^{28}$ ions/m^3, a quasi-steady approximation is not valid as will be seen in §§§ 2.2.1.6.

It is to be noted that GK give two expressions for the diffusion coefficient D_c^{O*}, one theoretical (given above by (2.5)) and the other from empirical data fitting by Lay (1970). The empirical diffusivity of oxygen in uranium dioxide is given as:

$$D_c^{O*} = 5 \cdot 10^{-5}\ \text{m}^2/\text{s}\ \ \exp\left(\frac{-119244\ \text{J/mol}}{R_g^* T^*}\right) \tag{2.6}$$

where R_g^* is the universal gas constant in units of J/(mol K) and T^* is the temperature in Kelvin. In their paper (Gharagozloo and Kanouff, 2013), they state, "*the theoretical chemical diffusion coefficient is consistently a factor of 1.75 less than*

---

[c] Although the recently published value of the lattice constant (a^*) by Leinders et al. (2015) is more accurate, we use $a^* = 3.8682\,\text{Å}$ from Gharagozloo and Kanouff (2013) to reproduce the GK results.

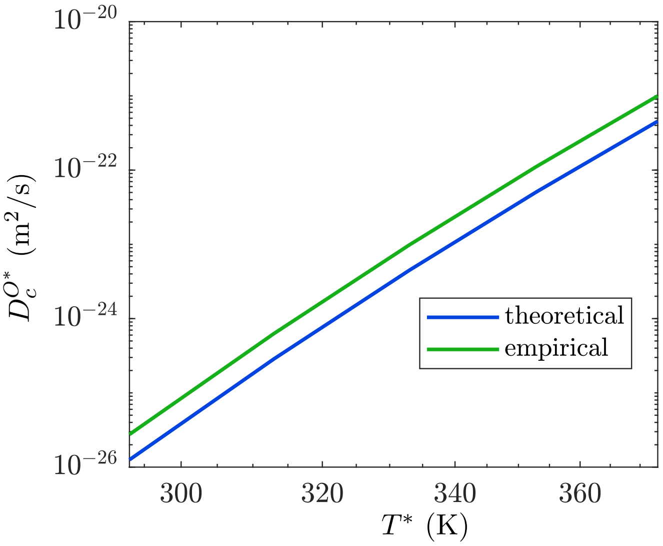

(a) $T^* = 20$ to 100°C

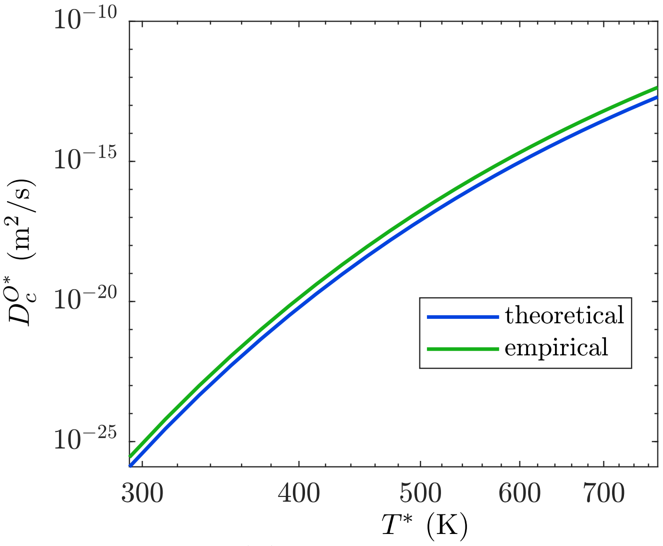

(b) $T^* = 20$ to 500°C

Figure 2.4: The temperature dependence of the theoretical and empirical chemical diffusivities given by (2.5) and (2.6) respectively, ranging from approximately 10^{-26} m^2/s at room temperature (e.g. 20 °C) to 10^{-13} m^2/s at 500°C.

the published measured chemical diffusion coefficient in the temperature range studied.". Whereas, using the same two expressions and a lattice constant of $a^* = 3.8682$ Å, we find a difference of a factor approximately equal to 4.38.

2.1.1.1 Calculation of oxide thickness

The metal-oxide interface velocity has been calculated by GK as the ratio of the flux of diffusing species to their number concentration at the oxide-metal interface that is involved in the phase transition from metal to metal oxide.

However, it is not clear as to how the density change is handled in GK, as mass conservation of the whole system is not considered: *"The outer oxide surface velocity is calculated by dividing the flux by twice the number concentration of* $UO_{2.09}$ *in solid uranium dioxide minus the metal-oxide interface velocity to account for the change in density between uranium and uranium dioxide"*.

The change in the oxide thickness at any given time step was then calculated by summing the velocities of the oxide-metal and the gas-oxide interfaces and multiplying by the time-step (see p. 2945 Gharagozloo and Kanouff, 2013).

2.1.2 Comparison of results of the quasi-steady formulation

We proceed with our quasi-steady formulation and compare the results with that of the quasi-steady model of GK. We assume that the oxygen ions diffusing into the uranium metal immediately react to form uranium dioxide. Therefore, the oxide-metal interface moves downwards as the reaction progresses. A slight hyper-stoichiometry ($\approx 5\%$) of uranium dioxide is considered which implies that 2.09 oxygen ions are required to oxidise 1 uranium atom/ion to produce 1 molecule of uranium dioxide. Over an area (ΔA^*) and time (Δt^*), there is a total number of $J_c^* \Delta A^* \Delta t^*$ oxygen ions diffusing into the underlying metal layer. These oxygen ions (O^{2-}) react with $J_c^* \Delta A^* \Delta t^*/2.09$ uranium atoms, which removes a volume of $J_c^* \Delta A^* \Delta t^*/(2.09\, N_M^*)$ from the metal, where N_M^* is the number density of uranium. If the velocity of the interface separating the metal from the oxide is v^*, then the volume of metal lost is $v^* \Delta A^* \Delta t^*$. For consistency of these two views we require a velocity of

$$v^* = \frac{\mathrm{d}z_1^*}{\mathrm{d}t^*} = \frac{J_c^*}{2.09\, N_M^*} = -\frac{D_c^{O*}}{2.09\, N_M^*} \left(\frac{C_a^*}{z_s^*(t^*) - z_1^*(t)} \right) . \tag{2.7}$$

Note that $z_1^* < 0$ and the oxide-metal interface velocity $v^* < 0$, resulting in the expected downward propagation of the interface into the metal.

The number concentration of uranium in the uranium lattice is

$$N_M^* = \left(\frac{\rho_M^*}{M_U^*}\right) N_A = 4.8235 \cdot 10^{28} \text{ atoms/m}^3, \tag{2.8}$$

where $\rho_M^* = 19.06$ g/cm^3 is the density of uranium, $M_U^* = 238$ g/mol is the molecular weight of U and $N_A = 6.023 \cdot 10^{23}$ is the Avogadro's number. Typical values for the dimensional physical constants are given in Table A.1.

2.1.2.1 Density changes at the interface

As the density of uranium dioxide ($\rho_O^* = 10.97$ g/cm^3) is less compared to that of uranium ($\rho_M^* = 19.06$ g/cm^3), the material volume increases as the metal is converted to oxide. Therefore, the gas-oxide interface moves upwards to accommodate the increased volume. The gas-oxide (or 'upper') interface velocity is computed by considering a mass balance of the system.

Let the initial total mass of the system be M_0^* and mass of the system at time t^* be $M_0^* + M_{\text{abs}}^*$, where M_{abs}^* is the mass of oxygen absorbed in time t^*. As the molecular weight of oxygen (32 g/mol) is smaller than the molecular weight of uranium (238 g/mol), the increased mass due to absorption of oxygen will be neglected in what follows, although we address this issue in Appendix B.

As shown in Figure 2.3, we assume an initial state with a metal layer of thickness $(z_1^*(t^* = 0) - (-z_\infty^*))$ and an oxide layer of thickness δ_O^*. An initial oxide layer is considered to be representative of the actual experimental conditions wherein a 'clean uranium' (i.e. uranium without an overlying oxide layer) has not been observed. This is due to the fact that uranium is very reactive with oxygen or water vapour. In the initial state, the total 'mass' (mass per unit area of the sample) is given by

$$M_0^* = \rho_M^*(z_1^*(0) + z_\infty^*) + \rho_O^*(\delta_O^*)\,, \tag{2.9}$$

where the density of the metal is denoted as ρ_M^* and the density of the oxide is ρ_O^*.

At a later time t^*, the total mass of the system becomes

$$M_0^* + M_{\text{abs}}^* = \rho_M^*(z_1^*(t^*) + z_\infty^*) + \rho_O^*(z_s^*(t^*) - z_1^*(t^*)), \tag{2.10}$$

where $z_1^*(t^*)$ and $z_s^*(t^*)$ represent the positions of the oxide-metal and the gas-oxide interfaces at time t^* and $z = -z_\infty^*$ represents the metal truncation or the far-field boundary. Equating (2.9) and (2.10) (i.e. by neglecting M_{abs}^*), we obtain

$$z_1^*(t^*)\left(1-\frac{\rho_M^*}{\rho_O^*}\right)+\frac{\rho_M^*}{\rho_O^*}z_1^*(0)+\delta_O^*=z_s^* \tag{2.11}$$

Differentiating the above equation with respect to time yields

$$\frac{\mathrm{d}z_s^*}{\mathrm{d}t}=-\frac{\mathrm{d}z_1^*}{\mathrm{d}t}\left(\frac{\rho_M^*-\rho_O^*}{\rho_O^*}\right) \tag{2.12}$$

or

$$\frac{\mathrm{d}z_1^*}{\mathrm{d}t^*}=-\frac{\rho_O^*}{\rho_M^*}\frac{\mathrm{d}(z_s^*-z_1^*)}{\mathrm{d}t^*}\,, \tag{2.13}$$

which relates the velocity of the surface (or the gas-oxide interface), $\mathrm{d}z_s^*/\mathrm{d}t^*$ with the velocity of the oxide-metal interface, $\mathrm{d}z_1^*/\mathrm{d}t^*$.

Defining the dimensional oxide layer thickness as $L^*(t^*) = z_s^*(t^*) - z_1^*(t^*)$, we can write (2.13) as

$$\frac{\mathrm{d}z_1^*}{\mathrm{d}t^*}=-\frac{\rho_O^*}{\rho_M^*}\frac{\mathrm{d}L^*}{\mathrm{d}t^*}. \tag{2.14}$$

Now substituting the oxide-metal interface velocity given by (2.7) in the above equation, we obtain

$$\frac{\mathrm{d}L^*}{\mathrm{d}t^*}=\frac{D_c^{O*}C_a^*}{2.09\,N_M^*}\frac{\rho_M^*}{\rho_O^*}\frac{1}{L^*}\,, \tag{2.15}$$

which on integrating with respect to the initial condition $L^*(t^*=0)=\delta_O^*$ gives

$$L^*=\sqrt{\left(\frac{2\rho_M^*}{\rho_O^*}\right)\left(\frac{D_c^{O*}C_a^*}{2.09\,N_M^*}\right)t^*+\delta_O^{*2}}. \tag{2.16}$$

Equation (2.16) gives an analytical expression for the dimensional thickness of the oxide layer as a function of time t^*. This analytical expression has not been derived by Gharagozloo and Kanouff (2013), and their results arise from a numerical solution.

We can now reproduce the GK results using (2.16), as shown in Figure 2.5. Interestingly, the results for $\rho_M^*/\rho_O^* = 1$ reproduce those of GK figure 3(a), even though the authors claim to include the effect of density change arising from

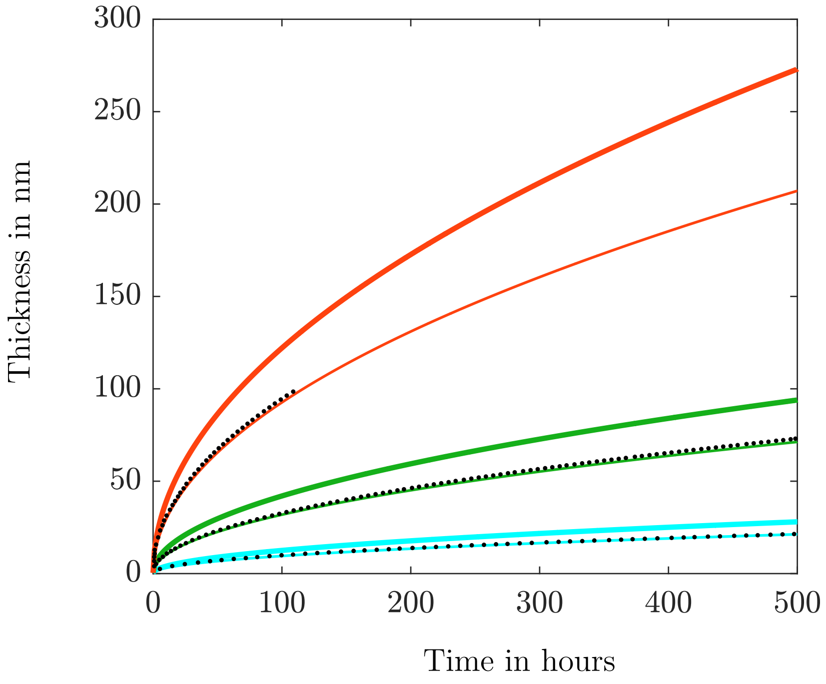

Figure 2.5: The development of the oxide layer thickness over 500 hours at three different temperatures of 100°C (cyan), 125°C (green), 150°C (red). Here thinner lines show the oxide thickness for no density change $\rho^*_M/\rho^*_O = 1$ whilst the thicker lines assume that $\rho^*_M/\rho^*_O \approx 1.74$. The GK results extracted from figure (3a) of Gharagozloo and Kanouff (2013) are represented as data points (black) for the three temperatures.

volume expansion ($\rho^*_M/\rho^*_O = 1.7375$). It is to be noted that we have used the same values of $C^*_a = 6 \cdot 10^{28}$ ions/m^3 and the lattice constant $a^* = 3.8682\,\text{Å}$ from Gharagozloo and Kanouff (2013) to calculate the oxide thickness.

2.1.3 Accuracy of the quasi-steady approximation

The GK approach assumes a linear profile (2.3) for the oxygen ions concentration in the uranium dioxide layer. In §§§ 2.2.1.6, we will show that the accuracy of this assumption is governed by the dimensionless ratio,

$$\lambda = \frac{C^*_a}{2.09\, N^*_M}\,, \tag{2.17}$$

which is referred to as the Stefan number. It is defined as the ratio of the surface (number) concentration of the diffusing oxygen ions to the (number) concentration of oxygen ions at the oxide-metal interface involved in the phase transition from metal to oxide.

For $C_a^* = 6 \cdot 10^{28}$ ions/m^3 as stated in GK, $\lambda \approx 0.6$. We will show that, for the GK model which assumes a linear concentration gradient, quasi-steady diffusion is a good first approximation to the unsteady diffusion model only when $\lambda \ll 1$.

2.2 Unsteady chemical diffusion: a Stefan problem

A chemical diffusion problem involving a phase change is analogous to the classical Stefan problem which involves phase transitions as a result of transfer of heat, and consists in solving a system of partial differential equations with one or more moving boundaries. In a classical Stefan problem, the Stefan number is defined as the ratio of the sensible to the latent heat (see Rubenstein, 2000; Gupta, 2017). In this section, we solve for the unsteady chemical diffusion problem governed by Fick's second law, where diffusion is considered to be rate-limiting, thus neglecting the details of the reactions themselves that result in a phase change (or density change) as metal (U) is converted to oxide ($UO_{2.09}$). That is, a Stefan problem deals with sharp interfaces between the different phases, where the phase boundary/interface is not known a priori. We then compare the solution obtained from solving the one-dimensional governing equations for unsteady diffusion to that obtained for the quasi-steady diffusion case, which enables us to find the range of parameter values for which quasi-steady diffusion is a good approximation. We consider two scenarios: (i) neglecting the density change as uranium is converted to uranium oxide, (ii) including the density change due to the reaction.

2.2.1 Neglecting density/volumetric changes: $\rho_M^* = \rho_O^*$

If we neglect the density change associated with the transition from uranium to uranium oxide, then the gas-oxide interface can be considered to be fixed at $z^* = z_s^*(t^* = 0) = 0$. In the oxide phase we recover a standard diffusion problem:

$$\frac{\partial c^*}{\partial t^*} = D_c^{O*} \frac{\partial^2 c^*}{\partial z^{*2}} \qquad \text{for} \qquad z_1^*(t) < z^* < 0, \tag{2.18}$$

repeating the notation of the previous section, with c^* the (number) concentration of oxygen ions in the oxide phase, D_c^{O*} the constant diffusivity of oxygen ions in the oxide phase and z^* is the spatial coordinate wherein the initial surface is located at $z_s^*(t^*=0)=0$.

The boundary conditions are

$$c^* = C_a^*(t^*) \qquad \text{on} \quad z^* = 0, \tag{2.19a}$$

$$c^* = 0 \qquad \text{on} \quad z^* = z_1^*(t^*), \tag{2.19b}$$

$$\frac{\mathrm{d}z_1^*}{\mathrm{d}t^*} = -\lambda^* D_c^{O*} \frac{\partial c^*}{\partial z^*} \qquad \text{on} \quad z^* = z_1^*(t^*)\,, \tag{2.19c}$$

where $C_a^*(t^*)$ is the time-varying surface concentration of oxygen ions, and $z_1^*(t^*)$ represents the oxide-metal interface at time t^*. In this approach, an unsteady surface concentration of oxygen ions can be allowed for, by taking the surface concentration to be a function of time, i.e. $C_a^* = C_a^*(t^*)$ until equilibrium is attained. Here, equation (2.19c) is the unsteady diffusion analogue of (2.7) and is a standard Stefan condition at the oxide-metal interface; it gives the velocity of oxide-metal interface that is proportional to the flux of the diffusing ions.

The parameter λ^* follows from (2.17) as

$$\lambda^* = \frac{1}{2.09\, N_M^*}\,, \tag{2.20}$$

where N_M^* is the (number) concentration of uranium and $\lambda = \lambda^* C_a^*$.

The initial condition for the concentration of the diffusing species is given by

$$c^*(z^*, t^*=0) = 0\,, \tag{2.21}$$

which is an obvious choice when there is no oxide formed, that is when $\delta_O^* = 0$. But any initial distribution can be considered. For example, the initial condition assumed by GK is

$$c^*(z^*, t^*=0) = C_a^* \frac{z^* + \delta_O^*}{\delta_O^*}\,, \tag{2.22}$$

which follows from a linear concentration profile $c^* = A^* z^* + B^*$ (obtained from a quasi-steady approximation), where A^* and B^* are constants that are determined from the boundary conditions.

2.2.1.1 Nondimensionalisation

We nondimensionalise using a constant (steady-state) surface concentration of oxygen ions C_a^*, an arbitrary length-scale L_{ref}^* and the diffusion time scale L_{ref}^{*2}/D_c^{O*}, resulting in

$$\frac{\partial c}{\partial t} = \frac{\partial^2 c}{\partial z^2} \quad \text{for} \quad z_1(t) < z < 0\,, \tag{2.23}$$

and subject to

$$c = C_a(t) \quad \text{on} \quad z = 0\,, \tag{2.24a}$$

$$c = 0 \quad \text{on} \quad z = z_1(t)\,, \tag{2.24b}$$

$$\frac{\mathrm{d}z_1}{\mathrm{d}t} = -\lambda \frac{\partial c}{\partial z} \quad \text{on} \quad z = z_1(t)\,. \tag{2.24c}$$

Here,

$$\lambda = \lambda^* C_a^* = \frac{C_a^*}{2.09\, N_M^*} \tag{2.25}$$

is a Stefan number, $z_1(t) = z_1^*/L_{ref}^*$ is the relative interface position, and $\delta_O = \delta_O^*/L_{ref}^*$ is a relative measure of the initial oxide thickness (if any). The dimensionless concentration of the diffusing species at the gas-oxide interface (or the oxide surface) is defined by $C_a(t)$, where $C_a \to 1$ as $t \to \infty$ by virtue of the nondimensionalisation via the value C_a^*.

We note that the neglect of any density change between the metal and the oxide implies that the 'upper' surface of the oxide remains stationary at $z = 0$. In this formulation both the concentration $c(z,t)$ and the oxide-metal interface location $z_1(t)$ are unknown and will be determined as part of the solution process.

2.2.1.2 A coordinate transformation for the moving boundary:

We use a boundary-fixing transformation to fix the moving boundary $z = z_1(t)$ in the computational ζ-coordinate defined in (2.26). We can therefore find a solution analytically in the transformed domain which is discussed in §§§ 2.2.1.3. To obtain a numerical solution, the discretisation of the oxide phase by finite difference schemes becomes difficult in the presence of a moving boundary and we must account for the changing domain associated with the diffusion equation. This again calls for a coordinate (or boundary-fixing) transformation. A numerical solution is presented in §§§ 2.2.1.4 in order the verify the accuracy of our numerical scheme (by comparing with the exact analytical solution); this is done so that an extension can be made to numerically solve the density change case (where an analytical solution is not available, such as with unsteady surface conditions or initial oxide present). Numerical simulations are also useful to investigate the influence of different initial conditions and the parameter λ on the oxide growth. It is to be noted that there is no advection of the material for the uniform density case ($\rho_M^* = \rho_O^*$).

The space and time coordinates are transformed from (z, t) to (ζ, t). We define the new coordinate ζ as

$$\zeta = \frac{z}{z_1(t)}\,, \tag{2.26}$$

which leads to the oxide layer now being spanned by $\zeta \in [0, 1]$, with $\zeta = 0$ denoting the gas-oxide interface and $\zeta = 1$ denoting the oxide-metal/internal interface. This transformation fixes the internal interface at the expense of a more complicated governing equation, as determined by the transformations

$$\frac{\partial}{\partial z} \to \frac{1}{z_1(t)}\frac{\partial}{\partial \zeta}\,, \tag{2.27a}$$

$$\frac{\partial}{\partial t} \to \frac{\partial}{\partial t} - \zeta\frac{\dot{z}_1(t)}{z_1(t)}\frac{\partial}{\partial \zeta}\,, \tag{2.27b}$$

where the dot notation above a variable indicates differentiation with respect to the nondimensionalised time.

We model only the oxide phase, as it is assumed that there is no concentration gradient in the metal phase (reaction time scale ≪ diffusion time scale). The governing equation in the oxide phase (2.23) therefore becomes

$$z_1^2\frac{\partial \bar{c}}{\partial t} - \zeta z_1 \dot{z}_1\frac{\partial \bar{c}}{\partial \zeta} = \frac{\partial^2 \bar{c}}{\partial \zeta^2} \quad \text{for} \quad 0 < \zeta < 1\,, \tag{2.28a}$$

where $\bar{c}$ denotes the transformed variable for the concentration of oxygen ions (diffusing species) in the oxide phase.

This transformed version of the diffusion equation is solved subject to the similarly transformed boundary conditions:

$$\bar{c} = C_a(t) \quad \text{on} \quad \zeta = 0\,, \tag{2.28b}$$

$$\bar{c} = 0 \quad \text{on} \quad \zeta = 1\,, \tag{2.28c}$$

$$z_1 \frac{\mathrm{d}z_1}{\mathrm{d}t} = -\lambda \frac{\partial \bar{c}}{\partial \zeta} \quad \text{on} \quad \zeta = 1\,. \tag{2.28d}$$

The interface position now appears explicitly in the governing equation (2.28a), and furthermore appears as z_1^2 or the derivative of this quantity with respect to time. This suggests a further simplification in the form,

$$L(t) = z_s - z_1(t)\,, = -z_1(t)\,, \tag{2.29a}$$

$$S(t) = L^2(t)\,, \tag{2.29b}$$

since $z_s = 0$ and $L(t)$ is now the dimensionless thickness of the oxide layer. This approach leads to the full problem defined by

$$S\frac{\partial \bar{c}}{\partial t} - \frac{\zeta \dot{S}}{2}\frac{\partial \bar{c}}{\partial \zeta} = \frac{\partial^2 \bar{c}}{\partial \zeta^2} \quad \text{for} \quad 0 < \zeta < 1\,, \tag{2.30a}$$

$$\bar{c} = C_a(t) \quad \text{on} \quad \zeta = 0\,, \tag{2.30b}$$

$$\bar{c} = 0 \quad \text{on} \quad \zeta = 1\,, \tag{2.30c}$$

$$\frac{\mathrm{d}S}{\mathrm{d}t} = -2\lambda \frac{\partial \bar{c}}{\partial \zeta} \quad \text{on} \quad \zeta = 1\,. \tag{2.30d}$$

Again a variety of initial conditions could be applied, but an obvious one is $\bar{c} = S = 0$ at $t = 0$. This corresponds to a sample that is purely metal, with no oxide layer – a condition that is difficult to impose without the coordinate transformation, as the domain of solution is vanishingly small at small times. This problem (2.30) is well-known in fluid dynamics as a ‘one-phase’ Stefan problem (in phase-transition problems such as ice melting or water freezing) and there exists an exact analytical solution for the same which is presented in the next section.

2.2.1.3 An exact analytical solution

In the case of $C_\mathrm{a} = 1$ and $\delta_O = 0$, there is an exact solution due to Neumann (cf. Gupta, 2017) which is obtained by seeking a solution in the form

$$S(t) = (z_s - z_1(t))^2 = t d_0^2\,, \tag{2.31}$$

$$\bar{c}(\zeta, t) = \bar{c}(\zeta)\,, \tag{2.32}$$

where $S(t)$ is the square of the oxide thickness and d_0 is a constant to be determined. In this case (2.30) reduces to

$$\frac{\partial^2 \bar{c}}{\partial \zeta^2} + \frac{\zeta d_0^2}{2} \frac{\partial \bar{c}}{\partial \zeta} = 0 \quad \text{for} \quad 0 < \zeta < 1 \,, \tag{2.33a}$$

$$\bar{c} = 1 \quad \text{on} \quad \zeta = 0 \,, \tag{2.33b}$$

$$\bar{c} = 0 \quad \text{on} \quad \zeta = 1 \,, \tag{2.33c}$$

$$d_0^2 = -2\lambda \frac{\partial \bar{c}}{\partial \zeta} \quad \text{on} \quad \zeta = 1 \,, \tag{2.33d}$$

for which a solution is

$$\bar{c} = 1 + \alpha \,\mathrm{erf}\left(\frac{d_0 \zeta}{2}\right) . \tag{2.34}$$

Here α is such that

$$1 + \alpha \,\mathrm{erf}\left(\frac{d_0}{2}\right) = 0 \,, \tag{2.35}$$

in order to satisfy the interface Dirichlet condition. Finally the Stefan condition provides

$$d_0^2 = -2\lambda\alpha \frac{d_0}{2} \frac{2}{\sqrt{\pi}} \exp(-d_0^2/4) \,. \tag{2.36}$$

We can determine α in terms of d_0 directly from (2.35), leaving d_0 (for any given value of λ) to be found as the root of a transcendental equation:

$$\frac{d_0 \sqrt{\pi}}{2\lambda} \mathrm{erf}\left(\frac{d_0}{2}\right) \exp(d_0^2/4) = 1 \,. \tag{2.37a}$$

Having determined d_0, the concentration profile in the oxide layer is

$$\bar{c} = 1 - \frac{\mathrm{erf}(d_0 \zeta/2)}{\mathrm{erf}(d_0/2)} \,, \tag{2.37b}$$

and the dimensionless thickness of the oxide layer is

$$L = S^{1/2} = d_0 t^{1/2} \,. \tag{2.37c}$$

2.2.1.4 A numerical formulation for the moving boundary problem

It has been seen in §§§ 2.2.1.3 that an analytical solution to (2.30) is possible for trivial initial conditions. For general initial conditions and unsteady surface conditions, however, we introduce a numerical formulation in this section. We wish to solve (2.30) numerically for any given initial conditions for $\bar{c}(\zeta, t)$ and $S(t)$, taking full account of the nonlinear terms $S\bar{c}_t$ and $\dot{S}\bar{c}_\zeta$. To achieve this, we employ a finite-difference scheme on the mesh $\{\zeta_j, t^k\}$ (where j and k denote the indices of the spatial and temporal nodes respectively), using Newton iteration at each time level. Before discretising the system we first decompose the solution $(\bar{c}, S)$ into a current guess plus a correction via (dropping the overbar denoting the transformed variable for clarity)

$$c = c_g^i + \tilde{c}\,, \tag{2.38a}$$

$$S = S_g^i + \tilde{s}\,. \tag{2.38b}$$

Here i is an index that counts the number of iterations at a given fixed time level, where the $(i = 0)$ first guess at any time level simply uses the solution at the previous time level.

Substitution of (2.38) into (2.30) and considering only the linear corrections under the assumption that the corrections $(\tilde{c}, \tilde{s})$ are small, leads to (on dropping the i superscript for clarity):

$$\tilde{s}\frac{\partial c_g}{\partial t} + S_g\frac{\partial \tilde{c}}{\partial t} - \frac{\zeta}{2}\left\{\dot{\tilde{s}}\frac{\partial c_g}{\partial \zeta} + \dot{S}_g\frac{\partial \tilde{c}}{\partial \zeta}\right\} - \frac{\partial^2 \tilde{c}}{\partial \zeta^2} = \frac{\partial^2 c_g}{\partial \zeta^2} - S_g\frac{\partial c_g}{\partial t} + \frac{\zeta}{2}\left\{\dot{S}_g\frac{\partial c_g}{\partial \zeta}\right\}, \tag{2.39a}$$

subject to the boundary conditions:

$$\tilde{c} = C_a(t) - c_g \quad \text{on} \quad \zeta = 0\,, \tag{2.39b}$$

$$\tilde{c} = -c_g \quad \text{on} \quad \zeta = 1\,, \tag{2.39c}$$

$$\frac{\mathrm{d}\tilde{s}}{\mathrm{d}t} + 2\lambda\frac{\partial \tilde{c}}{\partial \zeta} = -\frac{\mathrm{d}S_g}{\mathrm{d}t} - 2\lambda\frac{\partial c_g}{\partial \zeta} \quad \text{on} \quad \zeta = 1\,. \tag{2.39d}$$

We approach this with a standard Crank-Nicolson finite-difference scheme. The spatial and temporal discretisation of (2.39) is undertaken in the standard manner using a second-order scheme. The diffusion equation (2.39a) is solved at the spatial node ζ_j and temporal half-step $t^{k+1/2}$, using a central-differencing stencil. The Dirichlet boundary conditions (2.39b) and (2.39c) are imposed at the first/last spatial node and current time level t^{k+1}, whilst (2.39d) is solved at $t^{k+\frac{1}{2}}$ using a three-point backward-differenced expression for the ζ-derivative to maintain a second-order accuracy. After each solution of (2.39) to find the corrections $(\tilde{c}, \tilde{s})$, the current guess is updated using $c_g^{i+1} = c_g^i + \tilde{c}$ and $S_g^{i+1} = S_g^i + \tilde{s}$ before we compute new corrections $(\tilde{c}, \tilde{s})$. A solution is judged to have been obtained for $t = t^{k+1}$ when the largest absolute value of $\tilde{c}_j^{k+1}$ and $\tilde{s}^{k+1}$ is below a set tolerance (typically 10^{-8}).

2.2.1.5 Convergence of the numerical scheme

The second-order convergence of the Crank-Nicolson scheme can be verified for the one-moving boundary Stefan problem. The error (ϵ) between the numerical solution of (2.39) for the oxide thickness and the analytical solution (2.37c), for different spatial $(\Delta\zeta)$ and time steps (Δt) is depicted in the log-log plot of ϵ versus $(\Delta t, \Delta\zeta)$ in Figure 2.6, wherein the finite difference scheme shows second-order convergence, i.e. $\epsilon = \mathcal{O}((\Delta t)^2, (\Delta\zeta)^2)$.

Clearly a numerical approach is not needed here for trivial initial conditions due to the availability of an analytical solution, but the methodology has been introduced and validation of the numerical scheme has been performed for later use in solving more complex (or general) problems.

2.2.1.6 Comparison with the quasi-steady solution

We can now compare the unsteady Stefan solution for the one-moving boundary problem with the corresponding solution obtained using the quasi-steady approximation, where the (nondimensional) oxide thickness,

$$L = \sqrt{2\lambda t} \tag{2.40}$$

is obtained by nondimensionalising the quasi-steady solution (2.16) for the case of equal densities $(\rho_M^*/\rho_O^* = 1)$ and no initial oxide layer $(\delta_O^* = 0)$.

In the limit of $\lambda \ll 1$, since $\mathrm{erf}(x) \sim 2x/\sqrt{\pi}$ for small x, we recover

$$d_0^2 = 2\lambda + \cdots , \tag{2.41}$$

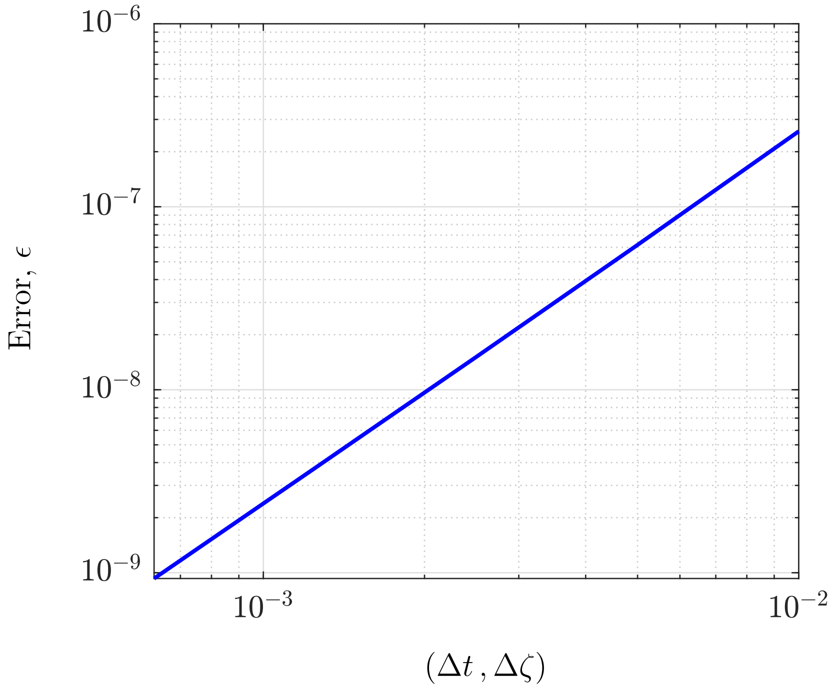

Figure 2.6: Error (ϵ) between the numerical (2.39) and analytical (2.37c) solutions for oxide thickness for different spatial step sizes and time steps (with $\Delta t = \Delta\zeta$ for each numerical simulation). The gradient of the log-log plot is found to be approximately 2.03, hence satisfying second-order convergence. Other parameters include an ad hoc choice of the Stefan number of $\lambda = C_a^*/(2.09\,N_M^*) \approx 0.05$.

from (2.37a), which yields

$$L = d_0\sqrt{t} \sim \sqrt{2\lambda t} + \cdots\,. \tag{2.42}$$

The corresponding concentration profile in the oxide layer is then

$$\bar{c} = 1 - \zeta + \cdots\,, \tag{2.43}$$

from (2.37b). The quasi-steady solution is therefore valid in the asymptotic limit of small Stefan number ($\lambda \ll 1$). As noted earlier, for the parameters used by Gharagozloo and Kanouff (2013), the Stefan number $\lambda \approx 0.6$ and hence the quasi-steady approximation may not be valid in this case. However, GK have not formulated their model in a rigorous manner, and the oxide layer thickness given by (2.40) has not been derived, nor any asymptotic predictions made.

Figure 2.7 shows the solution for the growth coefficient (d_0) of the Stefan model obtained numerically from (2.37a) over a range of values of λ. Also shown in this

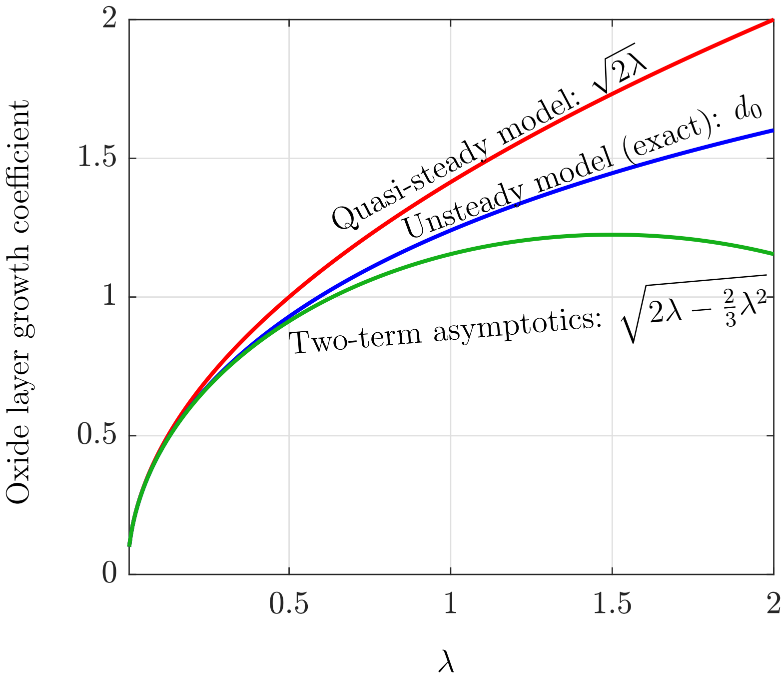

Figure 2.7: The relative oxide layer thickness (for $\rho_M^* = \rho_O^*$) is predicted to grow like $\sqrt{2\lambda t}$ in the quasi-steady model, and (more accurately) as $d_0\sqrt{t}$ in the unsteady Stefan model for equal densities. Here we compare the growth coefficients d_0 (exact solution (2.37a)), $\sqrt{2\lambda}$ (quasi-steady solution) and $\sqrt{2\lambda - 2/3\lambda^2}$ (two-term asymptotic solution (2.47)) over a range of λ. For the GK parameters, $\lambda \approx 0.6$ leading to an (approximate) error of 9% associated with the quasi-steady approximation. For larger λ (i.e. larger C_a^*), the error obviously increases.

same figure is the corresponding growth coefficient ($\sqrt{2\lambda}$) from the analysis of our quasi-steady model and the growth coefficient from the two-term asymptotic solution (2.47) that is derived in the next section. Again we see that the quasi-steady solution is consistent with the Stefan solution in the limit of small λ. At $\lambda \approx 0.6$ (appropriate to the parameters chosen by GK) the error is approximately 9% in the growth coefficient (that is, $\sqrt{2\lambda}$ compared to d_0), with the quasi-steady solution over-predicting the thickness of the oxide layer.

2.2.1.7 Two-term asymptotic expansion for the unsteady Stefan problem

We perform an asymptotic analysis in the limit of the Stefan parameter $\lambda \ll 1$ for the unsteady Stefan problem involving one unknown interface or boundary that is determined as part of the solution. In the limit of $\lambda \ll 1$, we can write an asymptotic expansion in powers of λ, the Stefan parameter which is a ratio of the atmospheric (number) concentration of the diffusing species to the number of diffusing ions required to convert a unit volume of metal atoms (or ions) to metal oxide (i.e. $\lambda = C_a^*/(2.09\, N_M^*)$). We seek an asymptotic solution in the form:

$$\bar{c} = \bar{c}_0 + \lambda \bar{c}_1 + \lambda^2 \bar{c}_2 + \dots\,, \tag{2.44a}$$

$$d_0^2 = D_0 + D_1 \lambda + D_2 \lambda^2 + \dots\,, \tag{2.44b}$$

where the coefficients at different orders, viz. $\bar{c}_0, \bar{c}_1,\ D_0, D_1, \dots$ are determined by substituting the above asymptotic expansions for $\bar{c}$ and d_0 in the governing equation and the boundary conditions (2.33), and then equating the coefficients of like powers of λ. Through this process, we obtain

$$\left.\begin{aligned} \bar{c}_0 &= 1 - \zeta\,, \\ D_0 &= 0 \end{aligned}\right\} \quad \text{at} \quad \mathcal{O}(\lambda^0)\,, \tag{2.45a}$$

$$\left.\begin{aligned} \bar{c}_1 &= \frac{\zeta^3}{6} - \frac{\zeta}{6}\,, \\ D_1 &= 2 \end{aligned}\right\} \quad \text{at} \quad \mathcal{O}(\lambda)\,. \tag{2.45b}$$

and,

$$D_2 = -2/3 \quad \text{at} \quad \mathcal{O}(\lambda^2)\,. \tag{2.45c}$$

Therefore, the two-term asymptotic expansions for the concentration ($\bar{c}$) and the square of the oxide thickness ($S(t) = L(t)^2$) can be written as

$$\bar{c} = (1 - \zeta) + \lambda \left(\frac{\zeta^3}{6} - \frac{\zeta}{6} \right) + \dots \tag{2.46}$$

$$S(t) = d_0^2 t = 2\lambda t - \frac{2}{3}\lambda^2 t + \dots\,. \tag{2.47}$$

Obviously the quasi-steady model as suggested by GK predicts the oxide thickness only up to the leading order of the full asymptotic solution.

2.2.2 Including density changes ($\rho_M^* \neq \rho_O^*$)

As noted above, there is a density change associated with the phase transition from metal to oxide (mass densities of U and UO_2 are $\rho_M^* = 19.06$ g/cm^3 and $\rho_O^* = 10.97$ g/cm^3). This implies that a stationary sample surface is not possible, whilst still conserving mass. To accommodate this density change we must also allow z_s^* to be time varying. Now considering a mass balance of the entire domain at any time t^* (see Figure 2.3 for the schematic of the system), we have (as before; see equation (2.10))

$$\begin{aligned} M_0^* + M_{\text{abs}}^* &= M_t^* \,, \\ \Rightarrow (z_s^*(0) - z_1^*(0))\rho_O^* + (z_1^*(0) + z_\infty^*)\rho_M^* + M_{\text{abs}}^* &= (z_s^*(t^*) - z_1^*(t^*))\rho_O^* \\ &\quad + (z_1^*(t^*) + z_\infty^*)\rho_M^* \,, \end{aligned} \tag{2.48a}$$

and neglecting M_{abs}^*, we have

$$\delta_O^*\rho_O^* + z_1^*(0)\rho_M^* = (z_s^*(t^*) - z_1^*(t^*))\rho_O^* + z_1^*(t^*)\rho_M^* \,. \tag{2.48b}$$

Here M_0^* is the mass per unit area of the system at the initial state ($t^* = 0$), M_{abs}^* is the mass per unit area of the diffusing species absorbed into the system in the time interval t^*, M_t^* is the mass per unit area of the system at time t^* and δ_O^* is the initial oxide thickness. We have assumed that M_{abs}^* is negligible compared to the total mass of the system in what follows.

A consequence of including the change in density is that the oxide surface and therefore the oxide layer must have an upward (ie. away from the internal/oxide-metal interface) velocity of $\dot{z}_s^*$, such that

$$\dot{z}_s^* = \dot{z}_1^* \left(1 - \frac{\rho_M^*}{\rho_O^*}\right) \,, \tag{2.49}$$

which is obtained by differentiating (2.48b) with respect to time. This surface velocity (z_s^*) is positive, since $\rho_M^*/\rho_O^* > 1$ and z_1^* is a decreasing function of time (associated with the downward propagating internal interface).

The (dimensional) diffusion problem in the oxide layer is now

$$\frac{\partial c^*}{\partial t^*} + \frac{\mathrm{d}z_s^*}{\mathrm{d}t^*}\frac{\partial c^*}{\partial z^*} = D_c^{O*}\frac{\partial^2 c^*}{\partial z^{*2}} \,, \tag{2.50a}$$

where the advection term associated with the 'upward' movement of the oxide layer is $\dot{z}_s^* \frac{\partial c^*}{\partial z^*}$ with $\dot{z}_s^*$ given by (2.49). This is to be solved in the domain

$$z_1^*(t^*) < z^* < z_s^*(t^*)\,. \tag{2.50b}$$

Conditions at the (now moving) surface and interface follow from the previous section:

$$\begin{aligned} c^* &= C_a^*(t^*) && \text{on} \quad z^* = z_s^*(t^*), \\ c^* &= 0 && \text{on} \quad z^* = z_1^*(t^*), \\ \frac{\mathrm{d}z_1^*}{\mathrm{d}t^*} &= -\lambda^* D_c^* \frac{\partial c^*}{\partial z^*} && \text{on} \quad z^* = z_1^*(t^*)\,. \end{aligned} \tag{2.50c}$$

We choose appropriate initial conditions that will be specified in §§§ 2.2.2.2 after a coordinate transformation of the governing equations and boundary conditions.

2.2.2.1 Nondimensionalisation

Nondimensionalising (2.50) similar to that in §§§ 2.2.1.1 gives

$$\frac{\partial c}{\partial t} + \frac{\mathrm{d}z_s}{\mathrm{d}t}\frac{\partial c}{\partial z} = \frac{\partial^2 c}{\partial z^2} \quad \text{for} \quad z_1(t) < z < z_s(t)\,, \tag{2.51a}$$

$$c = C_a(t) \quad \text{on} \quad z = z_s(t)\,, \tag{2.51b}$$

$$c = 0 \quad \text{on} \quad z = z_1(t)\,, \tag{2.51c}$$

$$\frac{\mathrm{d}z_1}{\mathrm{d}t} = -\lambda \frac{\partial c}{\partial z} \quad \text{on} \quad z = z_1(t)\,. \tag{2.51d}$$

Similarly, nondimensionalising (2.49) gives

$$\dot{z}_s(t) = \dot{z}_1(t)(1-\gamma)\,, \tag{2.51e}$$

where λ is the Stefan number and $\gamma = \rho_M^*/\rho_O^*$ is the relative density of the metal with respect to the metal oxide.

2.2.2.2 A coordinate transformation for the two moving boundaries

In this case where we do not neglect the density change due to the conversion of uranium ($\rho_M^* = 19.06$ g/cm^3) to uranium dioxide ($\rho_O^* = 10.97$ g/cm^3), the upper boundary (oxide-gas interface) and consequently the oxide layer advects with time as opposed to just the internal (or oxide-metal) interface in the uniform density (i.e. $\rho_M^* = \rho_O^*$) Stefan problem. We apply a similar coordinate transformation to map the oxide layer to a fixed domain, such that the boundary-fixing coordinate,

$$\zeta = \frac{z_s(t) - z}{z_s(t) - z_1(t)} \,. \tag{2.52}$$

This leads to the oxide layer now spanned by $\zeta \in [0, 1]$, with $\zeta = 0$ denoting the gas-oxide interface and $\zeta = 1$ denoting the oxide-metal interface. The governing equations, boundary and initial conditions are now transformed to the fixed ζ coordinate, with the transformations given by

$$\frac{\partial}{\partial z} \to -\left(\frac{1}{z_s(t) - z_1(t)}\right)\frac{\partial}{\partial \zeta} \,, \tag{2.53a}$$

$$\frac{\partial}{\partial t} \to \frac{\partial}{\partial t} + \left(\frac{\dot{z}_s - \zeta(\dot{z}_s - \dot{z}_1)}{z_s(t) - z_1(t)}\right)\frac{\partial}{\partial \zeta} \,, \tag{2.53b}$$

where the dot notation indicates differentiation with respect to the nondimensionalised time.

The transformed governing equation is now

$$(z_s - z_1)^2 \frac{\partial \bar{c}}{\partial t} + (z_s - z_1)\left\{\dot{z}_s - \zeta(\dot{z}_s - \dot{z}_1)\right\}\frac{\partial \bar{c}}{\partial \zeta} - (1 - \gamma)\dot{z}_1(z_s - z_1)\frac{\partial \bar{c}}{\partial \zeta} = \frac{\partial^2 \bar{c}}{\partial \zeta^2} \quad \text{in} \quad 0 < \zeta < 1 \,. \tag{2.54}$$

where $\bar{c}$ denotes the transformed variable for the concentration of the diffusing species.

The transformed governing equation is further simplified using (2.49) whilst we define $S(t) = L(t)^2$, where $L(t) = z_s(t) - z_1(t)$ is the (dimensionless) oxide thickness. Then (2.54) simplifies to

$$S\frac{\partial \bar{c}}{\partial t} - \frac{\zeta}{2}\dot{S}\frac{\partial \bar{c}}{\partial \zeta} = \frac{\partial^2 \bar{c}}{\partial \zeta^2} \quad \text{in} \quad 0 < \zeta < 1 \,. \tag{2.55a}$$

subject to the boundary conditions:

$$\bar{c} = C_a(t) \quad \text{on} \quad \zeta = 0 \,, \tag{2.55b}$$

$$\bar{c} = 0 \quad \text{on} \quad \zeta = 1 \,, \tag{2.55c}$$

$$\dot{S} = -2\gamma\lambda\frac{\partial \bar{c}}{\partial \zeta} \quad \text{on} \quad \zeta = 1 \,, \tag{2.55d}$$

and appropriate initial conditions; for example, from the exact solution for the unsteady one-moving boundary Stefan problem given by (2.37b), we assume

$$\bar{c} = 1 - \frac{\operatorname{erf}(d_0\zeta/2)}{\operatorname{erf}(d_0/2)} \quad \text{at} \quad t = 0\,. \tag{2.55e}$$

We consider that no oxide is present initially:

$$S = 0 \quad \text{at} \quad t = 0\,. \tag{2.55f}$$

We should note that the governing equation is the same as that for the uniform density case, however the Stefan boundary condition at the oxide-metal interface differs by a factor of γ (where γ is the relative density of metal to metal oxide) owing to the change in density as a result of the phase transition. Therefore, the procedure for the numerical formulation of the Stefan problem considering density change follows the same as that for the uniform density case (refer §§§ 2.2.1.4 for the numerical solution procedure).

2.3 Numerical results for the chemical diffusion models

The evolution of the oxide thickness with time obtained for the unsteady formulation (2.55) with a constant surface concentration (i.e. $C_a \equiv 1$) is plotted for different values of the parameters such as λ $(=\frac{C_a^*}{2.09N_M^*})$, (dimensionless) initial oxide thickness δ_O and γ $(=\rho_M^*/\rho_O^*)$; $\gamma \approx 1.7375$ corresponds to metal and oxide densities of $\rho_M^* = 19.06$ g/cm^3 and $\rho_O^* = 10.97$ g/cm^3. However, we consider γ to be an arbitrary parameter in Figure 2.8 to illustrate the influence of the volumetric/density change (attributed to phase transition) on the oxide growth kinetics. It can be seen that the oxide formed at any particular time is thicker where the change in density (as U is converted to UO_2) is considered (i.e. $\gamma = 1.7375$ instead of $\gamma = 1$), which is in accordance with what we might expect physically, as the oxide layer advects 'upwards' to accommodate the increased volume resulting from the phase conversion. However, it should also be noted that there will be a reduction in the diffusive flux with the thickening of the oxide layer.

A comparison of the oxide growth with time for different values of $\lambda \ll 1$ is shown in Figure 2.9, where the (nondimensionalised) quasi-steady solution (2.16)

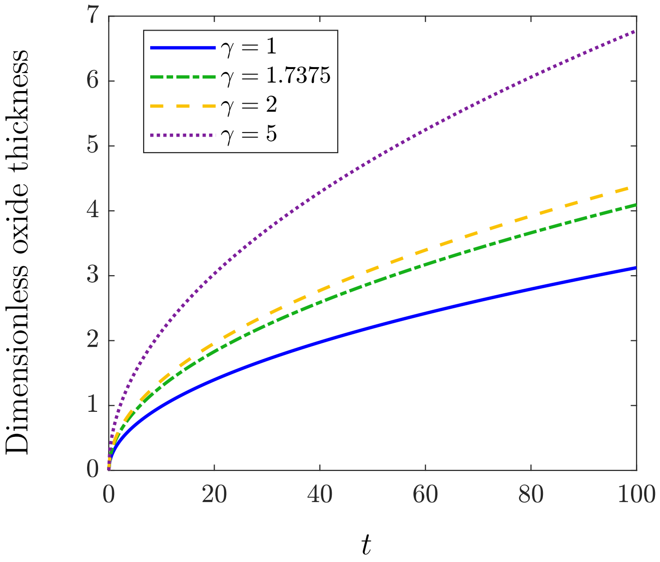

Figure 2.8: The evolution of the dimensionless oxide layer thickness ($L(t)$) with time obtained by solving the unsteady Stefan problem (2.55) for different γ values. Other parameters include: $C_a(t) \equiv 1\,, \lambda \approx 0.05\,, S(t=0) = \delta_O^2 = 0$.

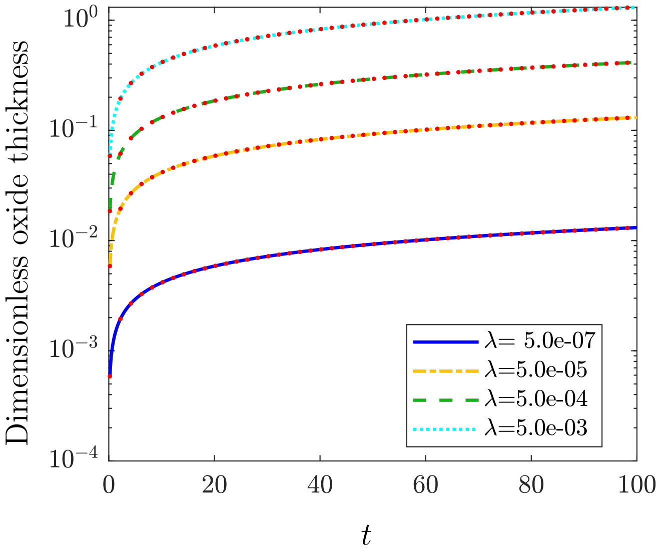

Figure 2.9: Comparison of the unsteady evolution of (nondimensional) oxide thickness with time (obtained by solving (2.55)) for different values of $\lambda = C_a^*/(2.09N_M^*) \ll 1$ with the quasi-steady solution (2.16) (red dotted lines). Other parameters include: $\gamma = 1.7375\,, S(t=0) = \delta_O^2 = 0$.

is plotted as red dotted lines. A good agreement between the unsteady and the quasi-steady solutions can be observed for these low λ values corresponding to significantly lower surface concentration (C_a^*) of the diffusing species compared to the metal concentration (N_M^*). For C_a^* values comparable to the metal concentration, the quasi-steady diffusion is a poor approximation to the unsteady problem and the same is depicted in Figure 2.10. It can be clearly observed that for $\lambda \approx 0.6$ (as considered by GK), the quasi-steady formulation over-predicts the oxide thickness.

Time-varying boundary conditions such as that shown in Figure 2.11 only affect the transient kinetics and not the long-time behaviour. Similarly, the effect of the initial parameters such as the (nondimensional) initial oxide thickness (δ_O) is only significant at small times, and do not influence the long-time oxide growth, and the same is depicted in Figure 2.12.

The evolution of the dimensional oxide thickness with dimensional time is plotted in Figure 2.13 for a range of temperature values. The influence of temperature on the oxide growth kinetics occurs via the dimensional diffusion coefficient (D_c^{O*}) given by (2.5a). Note that, a lattice constant of $a^* = 5.4713\,\text{Å}$ (Leinders et al., 2015) is used instead of $a^* = 3.8682$ Å (Gharagozloo and Kanouff, 2013). Also, a surface concentration of $C_a^* = 5 \cdot 10^{27}$ ions/m^3 (for which $\lambda \approx 0.05$) is considered in this figure instead of the GK value of $C_a^* = 6 \cdot 10^{28}$ ions/m^3 ($\lambda \approx 0.6$). To re-dimensionalise the unsteady Stefan solution, a reference diffusivity of $D_{ref}^* = D_c^{O*}$ is used where the theoretical diffusivity D_c^{O*} given by (2.5) is an exponential function of temperature; then correspondingly a reference length scale of $L_{ref}^* = (t^* D_{ref}^*/t)^{1/2}$ is used, where $t = t_\infty$[d] is taken to be equivalent to $t^* = 500$ hours. A good agreement between the unsteady and quasi-steady (represented as black dots) solutions can be observed for different temperatures. As we may expect, higher diffusivities corresponding to higher temperatures result in an increased oxide thickness.

---

[d] t_∞ is the nondimensional time up to which the simulation is run.

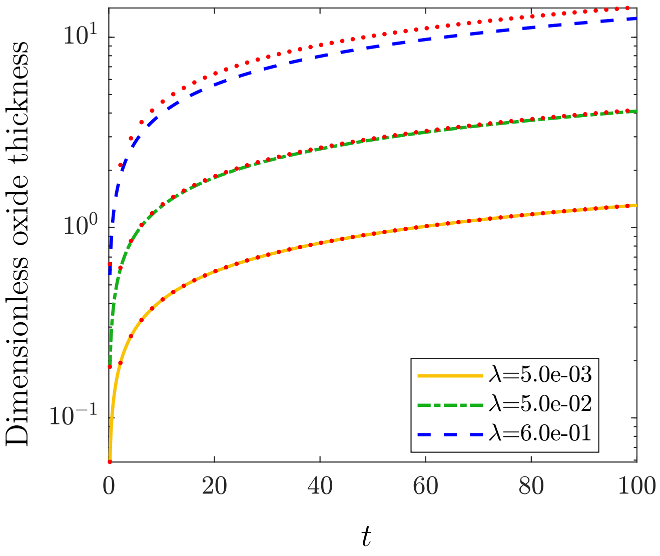

Figure 2.10: Comparison of the unsteady Stefan solution (2.55) for the (nondimensional) oxide thickness with the quasi-steady solution (2.16) (red dotted lines) for higher values of λ than those in figure 2.9. Other parameters include: $\gamma = 1.7375\,, S(t=0) = \delta_O^2 = 0$.

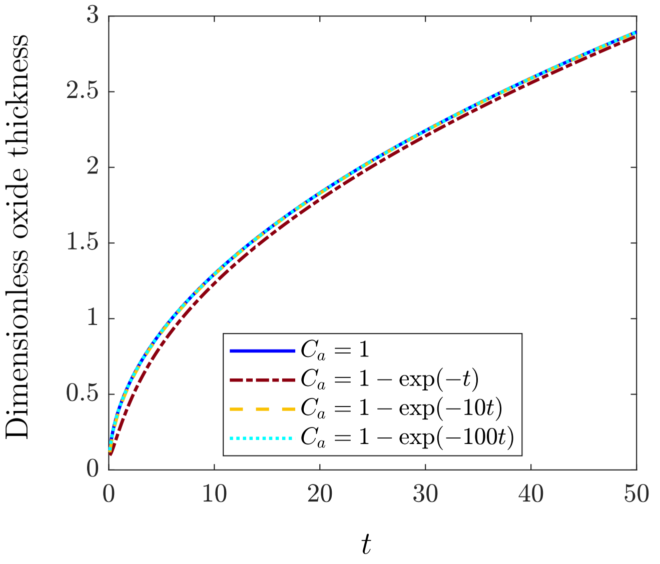

Figure 2.11: The evolution of relative oxide layer thickness with time for time-varying surface concentration of the diffusing species ($C_a(t)$), obtained by solving (2.55). Other parameters include: $\lambda \approx 0.05\,, \gamma = 1.7375$ and $\delta_O^2 = 0$.

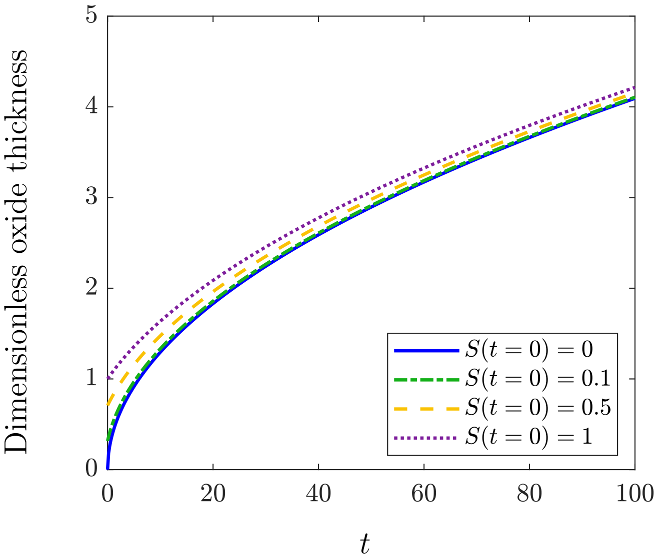

Figure 2.12: The evolution of the relative oxide layer thickness with time obtained by solving (2.55) for different initial oxide thicknesses given by δ_O where $S(t=0) = \delta_O^2$. Other parameters include: $\lambda \approx 0.05\,, \gamma = 1.7375$.

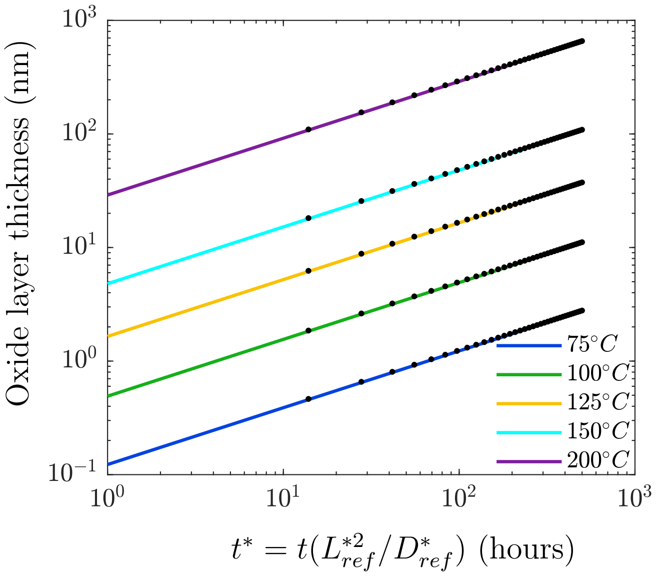

Figure 2.13: Comparison of the unsteady Stefan solution obtained by solving (2.55) with the quasi-steady solution (2.16) (represented as black dots) for the evolution of the (dimensional) oxide layer thickness with (dimensional) time at various temperatures. Other parameters include: $C_a^* = 5 \cdot 10^{27}$ ions/m^3 ($\lambda \approx 0.05$), $\gamma = \rho_M^*/\rho_O^* = 1.7375$ and $\delta_O^* = 0$.

2.4 Ionic diffusion: influence of a self-induced electric field

It has been well established (see review by Ritchie, 1984) that diffusion of oxygen ions through uranium dioxide (oxide layer) is the rate-determining step in the oxidation of uranium in a dry-air environment. However, the rate of chemical diffusion (i.e. due to a chemical potential gradient) alone does not account for the oxidation rate observed in the uranium oxidation experiments (Gharagozloo and Kanouff, 2013). As mentioned previously in Chapter 1, there are two driving forces for the diffusion of oxygen ions (O^{2-}) through the oxide layer, viz., the chemical and electrical potential gradients. Numerous studies (Evans, 1960; Ritchie, 1984; McEachern and Taylor, 1998) have indicated that an electric potential gradient across the oxide layer predominantly influences the diffusion of oxygen ions at low temperatures compared to chemical potential/concentration gradient.

A self-induced electric field is established when electrons from metal atoms pass through the oxide layer to the adsorbed oxygen atoms on the oxide surface, either due to quantum tunneling or thermionic emissions (at high temperatures). The redistribution of charges from the metal to the adsorbed oxygen atoms sets up an electrostatic potential that results in a diminishing electric field as the oxide layer grows. It should be noted that quantum tunnelling of electrons occurs only when the thickness of the oxide layer is less than 40 Å (Mott, 1940).

To take into account this additional driving force (i.e. due to an electric potential gradient) for the diffusion of oxygen ions, we formulate an ionic diffusion model in this section. As already discussed in Chapter 1, we neglect the spatial variations in the electric field strength (or space charges) and consider a *homogeneous* field E_0^*, where the electric field strength can be weak ($E_0^* < 10^4$ V/cm), moderate ($E_0^* = 10^4 - 10^6$ V/cm) or strong ($E_0^* > 10^6$ V/cm; see Fromhold and Cook, 1967). We will show later how these values of E_0^* are derived based on physical parameter values; however, it should be noted that these are only order of magnitude estimates. We identify different regimes of behaviour of our ionic diffusion model based on the relative influence of the electric field to temperature on the oxide growth. Two additional regimes associated with the Stefan parameter, namely the quasi-steady and unsteady behaviours for the ionic diffusion model will also be discussed in the forthcoming sections. Based on these identified regimes, we categorise our study into the following: (i) unsteady ionic diffusion in (a) moderate and (b) strong electric fields; (ii) quasi-steady ionic diffusion in (a) moderate and (b) strong electric fields.

It has been proposed by Fromhold and Cook (1967) that electric fields larger than 10^6 V/cm have a significant influence on the ionic current (or flux) of the diffusing species (with a nonlinear dependence on the field via the diffusion coefficients) compared to fields in the range of $10^4 - 10^6$ V/cm; hence the categorisation of the study based on the aforementioned electric field regimes.

2.4.1 Unsteady ionic diffusion in a moderate electric field

In this section, we formulate a Stefan problem for the diffusion of the oxidising species (O^{2-}) under the influence of a self-induced moderate electric field.

2.4.1.1 Problem formulation

As discussed previously (see § 2.2), the (dimensional) equation governing the diffusion of any species can be written using Fick's second law as (neglecting any material advection associated with a density change caused by the oxidation reaction):

$$\frac{\partial c^*}{\partial t^*} = -\frac{\partial J^*}{\partial z^*}\,, \tag{2.56}$$

where J^* is the (dimensional) flux of the diffusing species. If the density change associated with the metal to metal oxide transition is taken into account, then the governing equation becomes

$$\frac{\partial c^*}{\partial t^*} + \frac{\mathrm{d}z_s^*}{\mathrm{d}t^*}\frac{\partial c^*}{\partial z^*} = -\frac{\partial J^*}{\partial z^*}\,. \tag{2.57}$$

Here $\frac{\mathrm{d}z_s^*}{\mathrm{d}t^*}\frac{\partial c^*}{\partial z^*}$ denotes the additional advective flux. Note that the advection velocity is constant in the oxide layer and is equal to the velocity of the gas-oxide interface (or surface of the oxide), since the transition from U to UO_2 occurs at an interface of infinitesimal thickness.

In a moderate electric field, the form of the diffusive flux is such that

$$J^* = -D_c^{O*}\frac{\partial c^*}{\partial z^*} + \mu_q^* E^* c^*\,, \tag{2.58}$$

where D_c^{O*} is the diffusion coefficient of oxygen ions (O^{2-}) in uranium dioxide and μ_q^* is the electrical mobility of the charged particle ($q^* = -2e^*$ for O^{2-}, where $e^* = 1.6022 \cdot 10^{-19}$ Coulombs is the magnitude of electronic charge) and E^* is the electric field normal to the surface. Here, the flux of the diffusing species has a linear dependence on the electric field. The electrical mobility is related to the diffusion coefficient by the Sutherland-Einstein relation (also called the Einstein–Smoluchowski relation; Ferrari, Goldstein, and Lebowitz, 1985) given by

$$\mu_q^* = \left(\frac{q^*}{k_b^* T^*}\right) D_c^{O*}\,, \tag{2.59a}$$

for an absolute temperature T^*, with k_b^* denoting the Boltzmann constant. The theoretical diffusion coefficient is (as before, see (2.5a)) defined as

$$D_c^{O*} = 4a^{*2}\nu^* \exp\left(-\frac{W^*}{k_b^* T^*}\right)\,, \tag{2.59b}$$

where a^* is the uranium dioxide lattice constant, ν^* is the vibrational frequency, and W^* is the energy barrier height.

The second term on the right-hand side of (2.58) arises from the drift velocity (v_d^*) of a charged particle in a steady electric field:

$$v_d^* = \mu_q^* E^*\,. \tag{2.60}$$

In a moderate electric field, the nonlinear effects of the electric field on the diffusion coefficient and the electrical mobility are negligible. In this ‘linear’ (i.e. the ionic flux varies linearly with the electric field[e]) model, we also assume that changes in the electric potential/field occur over sufficiently small times, so that we can treat their contribution via an electrostatic formulation. Therefore, the scalar component of the steady electric field normal to the oxidising surface is defined in terms of the electric potential V^* as

$$E^* = -\frac{\mathrm{d}V^*}{\mathrm{d}z^*}\,. \tag{2.61}$$

In general, the electric field is related to the space charge distribution through

---

[e] Henceforth, we refer the ionic diffusion model for a moderate electric field as the ‘linear’ ionic model, whereas the ionic diffusion model for a strong electric field is referred to as the nonlinear ionic model.

the Poisson's equation which is given as

$$\frac{\mathrm{d}E^*}{\mathrm{d}z^*} = \frac{\rho^*(z^*;t^*)}{\epsilon^*}\,, \tag{2.62}$$

where ρ^* is the charge density in the medium (oxide) and ϵ^* is the permittivity. We assume that there are negligible space charges (Fromhold and Cook, 1967) set up in the medium (which implies that $\rho^*/\epsilon^* = 0 \Rightarrow \mathrm{div}E^* = 0$[f]), and therefore the contribution to the electric field is only due to the surface charge distribution, giving rise to a quasi-steady electric field denoted by E_0^*. This approximation is called the '*homogeneous field approximation*' since the electric field remains constant over the entire oxide thickness; however the electric field implicitly varies with time due to the growth of the oxide layer with time. The homogeneous electric field is thus

$$E_0^* = -\frac{\Delta V^*}{L^*(t^*)} = -\frac{V_M^*}{L^*(t^*)}\,, \tag{2.63}$$

where $\Delta V^* = V_M^*$ is the Mott potential given by (1.8) across the oxide layer of thickness $L^*(t^*)$. The Mott potential (V_M^*) is constant, whilst the electric field (E_0^*) decreases with the growth of the oxide, i.e. E_0^* implicitly varies with time.

The (dimensional) governing equation for the diffusion of a charged species in a moderate homogeneous electric field ('linear' ionic model) is therefore

$$\frac{\partial c^*}{\partial t^*} + \frac{\mathrm{d}z_s^*}{\mathrm{d}t^*}\frac{\partial c^*}{\partial z^*} = D_c^{O*}\frac{\partial^2 c^*}{\partial z^{*2}} - \mu_q^* E_0^* \frac{\partial c^*}{\partial z^*} \quad \text{for} \quad z_1^*(t^*) < z^* < z_s^*(t^*)\,, \tag{2.64}$$

where the velocity of the upper interface, $\dot{z}_s^* = 0$ if we neglect any density changes associated with the conversion from U to UO_2. The boundary and initial conditions are as given before (see (2.50c)).

2.4.1.2 Nondimensionalisation

We nondimensionalise using a reference length scale L_{ref}^*, time scale L_{ref}^{*2}/D_c^{O*}, and the constant surface concentration C_a^* as the concentration scale to arrive at the following nondimensional equation:

$$\frac{\partial c}{\partial t} + \dot{z}_s\frac{\partial c}{\partial z} = \frac{\partial^2 c}{\partial z^2} - \left(\frac{\Gamma_0}{z_s(t) - z_1(t)}\right)\frac{\partial c}{\partial z} \quad \text{for} \quad z_1(t) < z < z_s(t)\,, \tag{2.65}$$

---

[f] We consider only variation along the z-coordinate and therefore $\mathrm{div}E^* = \frac{\mathrm{d}E^*}{\mathrm{d}z^*}$.

where $\Gamma_0 = -(V_M^* q^*)/(k_b^* T^*) < 0$ is a nondimensional parameter that gives the relative importance of the electric field to the temperature effects in driving diffusion.

The governing equation (2.65) is subject to an appropriate initial concentration distribution $c(z, t = 0)$, with boundary conditions at the oxide-metal and the gas-oxide interfaces given by $c(z = z_1(t), t) = 0$ and $c(z = z_s(t), t) = 1$ respectively, whilst the Stefan boundary condition

$$\frac{\mathrm{d}z_1}{\mathrm{d}t} = -\lambda\gamma\frac{\partial c}{\partial z} \quad \text{at} \quad z = z_1(t)\,, \tag{2.66}$$

where $\lambda = C_a^*/(2.09\, N_M^*)$ and $\gamma = \rho_M^*/\rho_O^*$.

2.4.1.3 Coordinate transformation

As before (refer coordinate transformation for two moving boundaries in §§§ 2.2.2.2), we transform the system from (z, t) to (ζ, t) coordinates (i.e. from the moving physical domain to a fixed computational domain), wherein

$$\zeta \equiv \frac{z_s(t) - z}{z_s(t) - z_1(t)}\,. \tag{2.67}$$

The transformed governing equation is now

$$(z_s(t) - z_1(t))^2\frac{\partial \bar{c}}{\partial t} - \zeta(z_s(t) - z_1(t))(\dot{z}_s - \dot{z}_1)\frac{\partial \bar{c}}{\partial \zeta} = \frac{\partial^2 \bar{c}}{\partial \zeta^2} + \Gamma_0\frac{\partial \bar{c}}{\partial \zeta}\,, \tag{2.68}$$

where $\bar{c}$ is the transformed variable representing the concentration of the diffusing species.

We now define $L = (z_s(t) - z_1(t))$ and $S = L^2$ as before, which yields

$$S\frac{\partial \bar{c}}{\partial t} - \left[\frac{\zeta}{2}\dot{S} + \Gamma_0\right]\frac{\partial \bar{c}}{\partial \zeta} = \frac{\partial^2 \bar{c}}{\partial \zeta^2}\,, \tag{2.69}$$

a nondimensional form of the transformed governing equation. Note that the transformed governing equation is the same for systems with or without a density change as the parameter $\gamma = \rho_M^*/\rho_O^*$ only affects the Stefan condition.

Transformed boundary and initial conditions: The transformed nondimensionalised governing equation (2.69) is subject to the same boundary conditions as before (see (2.55b) and (2.55c)). The Stefan boundary condition is also the same as for the simple chemical diffusion given by (2.55d).

We choose an initial concentration profile given by an exact analytical solution for the one-moving-boundary Stefan problem (chemical diffusion; see (2.37b)), which is:

$$\bar{c} = 1 - \frac{\operatorname{erf}(d_0\zeta/2)}{\operatorname{erf}(d_0/2)} \quad \text{for} \quad t = 0\,, \tag{2.70}$$

where $S(t) = d_0^2 t$ and d_0 is determined from (2.36).

We will discuss the numerical results after presenting the model formulations for the unsteady ionic diffusion in a strong electric field and the quasi-steady formulations.

2.4.2 Unsteady ionic diffusion in a strong electric field

2.4.2.1 Problem formulation

In the case of a sufficiently 'strong' electric field ($E_0^* > 10^6$ V/cm), there is a nonlinear dependence of the diffusion coefficient and electrical mobility on the electric field strength (Fromhold and Cook, 1967), and we must account for this effect in the governing equation. The (dimensional) governing equation remains (considering the change in density as the metal is converted to oxide; see (2.57)):

$$\frac{\partial c^*}{\partial t^*} + \dot{z}_s^* \frac{\partial c^*}{\partial z^*} = -\frac{\partial J^*}{\partial z^*} \quad \text{for} \quad z_1^*(t^*) < z^* < z_s^*(t^*)\,, \tag{2.71a}$$

where $\dot{z}_s^*\, \partial c^*/\partial z^*$ is the advection term with $\dot{z}_s^*$ denoting the 'upward' velocity of the surface (or the oxide layer).

In (2.71a), the diffusive flux J^* is given by

$$J^*(z^*, t^*) = -\bar{D}_c^{O*} \frac{\partial c^*}{\partial z^*} + \bar{\mu}_q^* E_0^* c^*\,, \tag{2.71b}$$

where $\bar{D}_c^{O*}$ and $\bar{\mu}_q^*$ are the nonlinear diffusion coefficient and electrical mobility that are defined as (Fromhold and Cook, 1967):

$$\begin{aligned} \bar{D}_c^{O*} &= D_c^{O*} \cosh\left(\frac{q^* E_0^* a^*}{k_b^* T^*}\right) , \\ \bar{\mu}_q^* &= \mu_q^* \left(\frac{k_b^* T^*}{q^* E_0^* a^*}\right) \sinh\left(\frac{q^* E_0^* a^*}{k_b^* T^*}\right) \end{aligned} \tag{2.71c}$$

Here D_c^{O*} and μ_q^* are related via (2.59a), and we recall that a^* is the uranium dioxide lattice constant, q^* is the charge on the diffusing species, k_b^* is the Boltzmann constant and T^* denotes temperature in Kelvin. Here, the diffusion coefficient and electrical mobility have a nonlinear dependence on the electric field via the 'cosh' and 'sinh' terms, whereas the electric field has an insignificant influence on the diffusion coefficient and mobility of the ions in a moderate electric field ($E_0^* < 10^6$ V/cm). In Figure 2.14, it can be seen that temperature also plays a role in determining the influence of the electric field strength on these quantities. The dimensionless parameter $q^* E_0^* a^*/(k_b^* T^*)$ for $E_0^* = 10^4\,, 10^5\,, 10^6$ V/cm and $T^* = 300$ K are respectively $4.233 \cdot 10^{-4}$, $4.233 \cdot 10^{-3}$ and $4.233 \cdot 10^{-2}$.

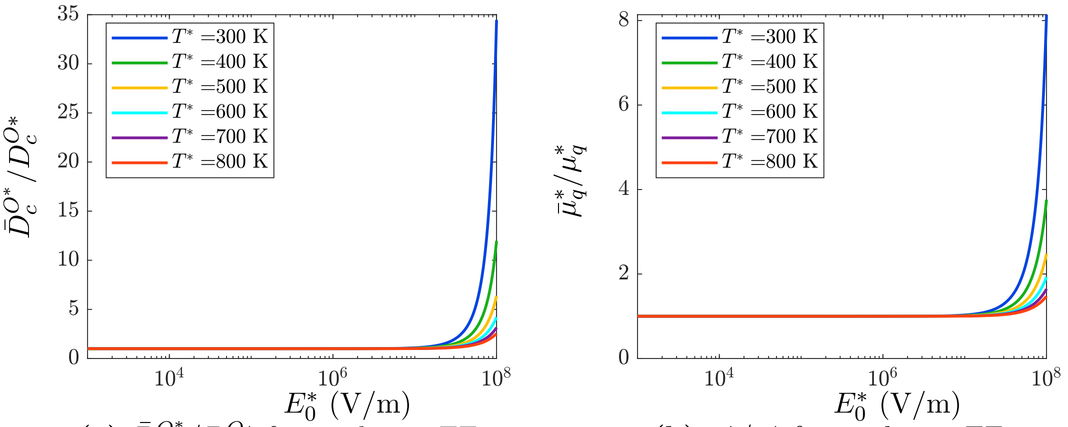

(a) $\bar{D}_c^{O^*}/D_c^{O*}$ for moderate EF ($E_0^* = 10^6 - 10^8$ V/m)

(b) $\bar{\mu}_q^*/\mu_q^*$ for moderate EF ($E_0^* = 10^6 - 10^8$ V/m)

Figure 2.14: The diffusivity ratio $\bar{D}_c^{O^*}/D_c^{O*}$ and mobility ratio $\bar{\mu}_q^*/\mu_q^*$ are plotted against the electric field strength E_0^* for different temperatures. The parameters include: $a^* = 5.4713$ Å, $\nu^* = 19 \cdot 10^{12}$ Hz, $W^* = 1.24$ eV, $k_b^* = 1.3806 \cdot 10^{-23}$ J/K.

2.4.2.2 Nondimensionalisation

We nondimensionalise (2.71) in a similar manner to the linear ionic model (see §§§ 2.4.1.2) and obtain

$$\frac{\partial c}{\partial t} + \dot{z}_s \frac{\partial c}{\partial z} = \cosh\left(\frac{\Gamma_0 \delta}{z_s(t) - z_1(t)}\right) \frac{\partial^2 c}{\partial z^2} - \delta^{-1} \sinh\left(\frac{\Gamma_0 \delta}{z_s(t) - z_1(t)}\right) \frac{\partial c}{\partial z}\,, \quad \text{(2.72a)}$$

where $\delta = (a^*/L^*_{ref})$ is the nondimensional lattice parameter and $\Gamma_0 = -\frac{(q^* V^*_M)}{(k^*_b T^*)}$ is a nondimensional parameter that gives the relative importance of the electric field to temperature effects in driving diffusion. This governing equation is subject to the boundary conditions

$$c(z = z_1(t), t) = 0\,, \quad c(z = z_s(t), t) = 1\,, \quad \text{(2.72b)}$$

and the Stefan condition:

$$\frac{\mathrm{d}z_1}{\mathrm{d}t} = -\lambda\gamma \cosh\left(\frac{\Gamma_0 \delta}{z_s - z_1}\right) \left.\frac{\partial c}{\partial z}\right|_{z=z_1(t)}\,, \quad \text{(2.72c)}$$

where $\lambda = C^*_a/(2.09\, N^*_M)$ and $\gamma = \rho^*_M/\rho^*_O = 1.7375$. The initial conditions remain the same as before (refer § 2.4.1.3). It has to be noted that in the limit of $z_1(t) \to z_s(t)$ (i.e. for very thin films), the governing equation (2.72a) is singular as $E^*_0 \to \infty$; however for practical applications, we note that an oxide-free state has not been observed even in ultra-high vacuum conditions (Banos and Scott, 2020).

2.4.2.3 Coordinate transformation

Applying the usual coordinate transformation (for two moving boundaries) given by (2.53) to governing equation (2.72a), we obtain

$$S\frac{\partial \bar{c}}{\partial t} - \frac{\zeta}{2}\dot{S}\frac{\partial \bar{c}}{\partial \zeta} = \cosh\left(\frac{\Gamma_0 \delta}{S^{1/2}}\right) \frac{\partial^2 \bar{c}}{\partial \zeta^2} + \frac{S^{1/2}}{\delta} \sinh\left(\frac{\Gamma_0 \delta}{S^{1/2}}\right) \frac{\partial \bar{c}}{\partial \zeta}\,, \quad \text{(2.73a)}$$

where $S(t) = L(t)^2 = (z_s(t) - z_1(t))^2$. The transformed form of the Stefan condition (2.72c) is then

$$\frac{\mathrm{d}S}{\mathrm{d}t} = -2\lambda\gamma \cosh\left(\frac{\Gamma_0 \delta}{\sqrt{S}}\right) \left.\frac{\partial \bar{c}}{\partial \zeta}\right|_{\zeta=1}. \quad \text{(2.73b)}$$

It is worth noting that $\Gamma_0 \ll 1$ recovers the linear (or moderate electric field) model (2.69).

2.4.2.4 Numerical scheme

The solution procedure used is the same as before (see §§§ 2.2.1.4). Applying Newton iteration (where the dimensionless oxide thickness is decomposed as $L = L_g + \tilde{l}$, whilst $c = c_g + \tilde{c}$) to (2.73a) yields (dropping the overbar denoting the transformed variable for clarity)

$$\begin{aligned}
L_g^2 \frac{\partial \tilde{c}}{\partial t} - \cosh\left(\frac{\Gamma_0 \delta}{L_g}\right) \frac{\partial^2 \tilde{c}}{\partial \zeta^2} - L_g \left[\frac{1}{\delta} \sinh\left(\frac{\Gamma_0 \delta}{L_g}\right) + \zeta \dot{L}_g\right] \frac{\partial \tilde{c}}{\partial \zeta} - \zeta L_g \frac{\partial c_g}{\partial \zeta} \dot{\tilde{l}} \\
+ \left[2 L_g \frac{\partial c_g}{\partial t} + \left\{\frac{\Gamma_0}{L_g} \cosh\left(\frac{\Gamma_0 \delta}{L_g}\right) - \frac{1}{\delta} \sinh\left(\frac{\Gamma_0 \delta}{L_g}\right) - \zeta \dot{L}_g\right\} \frac{\partial c_g}{\partial \zeta} \right. \\
\left. + \left(\frac{\Gamma_0 \delta}{L_g^2}\right) \sinh\left(\frac{\Gamma_0 \delta}{L_g}\right) \frac{\partial^2 c_g}{\partial \zeta^2}\right] \tilde{l} \\
= -L_g^2 \frac{\partial c_g}{\partial t} + L_g \left[\frac{1}{\delta} \sinh\left(\frac{\Gamma_0 \delta}{L_g}\right) + \zeta \dot{L}_g\right] \frac{\partial c_g}{\partial \zeta} + \cosh\left(\frac{\Gamma_0 \delta}{L_g}\right) \frac{\partial^2 c_g}{\partial \zeta^2}\,, \quad (2.74)
\end{aligned}$$

where we have used the binomial expansions to reduce $(1 + \tilde{l}/L_g)^{-1}$ to $(1 - \tilde{l}/L_g)$ and therefore

$$\cosh\left(\frac{\Gamma_0 \delta}{L_g + \tilde{l}}\right) = \cosh\left(\frac{\Gamma_0 \delta}{L_g}\right) - \left(\frac{\Gamma_0 \delta}{L_g^2}\right) \sinh\left(\frac{\Gamma_0 \delta}{L_g}\right) \tilde{l}\,, \quad (2.75a)$$

and similarly,

$$\sinh\left(\frac{\Gamma_0 \delta}{L_g + \tilde{l}}\right) = \sinh\left(\frac{\Gamma_0 \delta}{L_g}\right) - \frac{\Gamma_0 \delta}{L_g^2} \cosh\left(\frac{\Gamma_0 \delta}{L_g}\right) \tilde{l}\,. \quad (2.75b)$$

It is to be noted that only linear corrections are considered and we know that $\tilde{l} \ll L_g$.

Similarly, applying Newton iteration to the Stefan boundary condition at $\zeta = 1$, we obtain

$$\begin{aligned}
2 \frac{\mathrm{d}(L_g \tilde{l})}{\mathrm{d}t} - \left[2\lambda\gamma \left(\frac{\Gamma_0 \delta}{L_g^2}\right) \sinh\left(\frac{\Gamma_0 \delta}{L_g}\right) \frac{\partial c_g}{\partial \zeta}\right] \tilde{l} + 2\lambda\gamma \cosh\left(\frac{\Gamma_0 \delta}{L_g}\right) \frac{\partial \tilde{c}}{\partial \zeta} \\
= -\frac{\mathrm{d}L_g^2}{\mathrm{d}t} - 2\lambda\gamma \cosh\left(\frac{\Gamma_0 \delta}{L_g}\right) \frac{\partial c_g}{\partial \zeta}\,. \quad (2.76)
\end{aligned}$$

Now, a second-order Crank-Nicolson scheme is applied to (2.74) at the spatial node ζ_j and temporal half-step $t^{k+1/2}$, and similarly for the boundary conditions (refer §§§ 2.2.1.4 for the numerical procedure). A tolerance of 10^{-8} is set for the linear corrections. A comparison of the different results is presented in § 2.5.

2.4.3 Quasi-steady diffusion in a strong electric field

In this section, we review (and interpret) the quasi-steady approximation made in the work of Gharagozloo and Kanouff (2013). This will allow us to contrast their approach with the full solution of the unsteady ionic diffusion problems (2.72) and (2.69), to assess the range of parameters for which the GK analysis is valid.

Mathematically, the quasi-steady diffusion can be written as

$$\frac{\partial J^*}{\partial z^*} = 0\,, \tag{2.77}$$

which results in $J^* = J_0^*$, a constant-in-space (but implicitly time-varying) flux of O^{2-} in the oxide layer. A nonlinear flux of the diffusing ions dependent on the electric field is of the form given in (2.71b). Solving the quasi-steady ionic diffusion model (2.77) (with the appropriate flux J^* given by (2.71b)) for c^* gives

$$c^*(z^*) = \frac{J_0^*}{E_0^*\bar{\mu}_q^*} + A^* \exp\left(\frac{E_0^*\bar{\mu}_q^* z^*}{\bar{D}_c^{O*}}\right)\,, \tag{2.78}$$

where A^* is a constant of integration. We determine A^* and J_0^* from the boundary conditions $c^*(z_1^*) = 0$ and $c^*(z_s^*) = C_a^*$, which then gives

$$c^*(z^*) = \frac{C_a^*}{1-\exp\left(E_0^*\bar{\mu}_q^*(z_s^*-z_1^*)/\bar{D}_c^{O*}\right)}\left[1-\exp\left(\frac{E_0^*\bar{\mu}_q^*(z^*-z_1^*)}{\bar{D}_c^{O*}}\right)\right]\,, \tag{2.79a}$$

and therefore

$$J_0^* = E_0^*\bar{\mu}_q^*\left\{\frac{C_a^*}{1-\exp(E_0^*\bar{\mu}_q^*(z_s^*-z_1^*)/\bar{D}_c^{O*})}\right\}\,. \tag{2.79b}$$

The above expressions for the constant flux J_0^* and concentration $c^*(z^*)$ are analogous to those derived by Fromhold and Cook (1967).

The previously discussed Stefan condition still applies to determine the rate of advancement of the oxide-metal interface. On defining $L^* = z_s^*(t^*) - z_1^*(t^*)$, we obtain

$$\frac{\mathrm{d}L^*}{\mathrm{d}t^*} = -\lambda^*\gamma J_0^* = -\lambda^*\gamma E_0^*\bar{\mu}_q^* \left\{ \frac{C_a^*}{1-\exp(E_0^*\bar{\mu}_q^* L^*/\bar{D}_c^{O*})} \right\}, \tag{2.80}$$

where $E_0^* = -V_M^*/L^*$, $\lambda^* = 1/(2.09\, N_M^*)$ and $\gamma = \rho_M^*/\rho_O^*$.

2.4.3.1 Nondimensionalisation

Using the same characteristic scales (length-scale L_{ref}^*, time scale L_{ref}^{*2}/D_c^{O*}, and concentration scale C_a^*) to nondimensionalise (2.80), we obtain

$$\frac{\mathrm{d}L}{\mathrm{d}t} = -\gamma\frac{\lambda}{\delta}\sinh\left(\frac{\Gamma_0\delta}{L}\right)\left[\frac{1}{1-\exp(L\delta^{-1}\tanh(\Gamma_0\delta/L))}\right], \tag{2.81}$$

subject to $L(t=0) = \delta_O^*/L_{ref}^* = 1$, where δ_O^* is the initial oxide thickness. Here, we have assumed that $L_{ref}^* = \delta_O^*$, however any arbitrary reference length scale can be considered. The diffusivity and mobility are given by (2.71c) and have been substituted to arrive at the above equation. Here, $\delta = a^*/L_{ref}^*$, $\lambda = C_a^*/(2.09\, N_M^*)$ and $\Gamma_0 = -V_M^* q^*/k_b^* T^*$.

2.4.4 Quasi-steady diffusion in a moderate electric field

For a sufficiently small Γ_0 (i.e. $\Gamma_0 \ll 1$), the nonlinear diffusivity and mobility given by (2.71c) become (2.59). In this 'moderate' electric field, $(\bar{D}_c^{O*}, \bar{\mu}_q^*)$ in (2.80) are replaced with (D_c^{O*}, μ_q^*) and $\exp(\Gamma_0) \approx (1+\Gamma_0)$, in which case the Stefan condition at the oxide-metal interface becomes

$$\frac{\mathrm{d}L^*}{\mathrm{d}t^*} = -\lambda^*\gamma J_0^* = \frac{\lambda^* C_a^*\gamma D_c^{O*}}{L^*}, \tag{2.82}$$

where (D_c^{O*}, μ_q^*) are given by (2.59).

Nondimensionalising using the same characteristic scales as before, we obtain

$$L\frac{\mathrm{d}L}{\mathrm{d}t} = \lambda\gamma, \tag{2.83}$$

which on integration gives

$$S(t) = L(t)^2 = 2\lambda\gamma t + \delta_O^2, \tag{2.84}$$

where the initial (dimensionless) oxide thickness is given by $\delta_O = \delta_O^*/L_{ref}^*$. Therefore in the limit of vanishingly small ionic forcing, the result is consistent with the chemical diffusion problem (2.16), as we should expect. The validity of the quasi-steady approximation to model the ionic diffusion for a moderate electric field is analysed in §§§ 2.4.4.1, where it is required that the surface concentration of the diffusing species should be much less than the concentration of the diffusing species at the oxide-metal interface involved in the phase transition (i.e. $\lambda \ll 1$).

A comparison of our numerical results with those of GK, and with the published experimental results will be presented in Chapter 6.

2.4.4.1 Asymptotic Analysis for the Ionic Diffusion Model with a Linear Forcing

The quasi-steady results from (2.84) can be arrived at from the general formulation (equations (2.69) for a moderate electric field) in the limit $\lambda \ll 1$.

The nondimensional transformed governing equation for ionic diffusion in the presence of a moderate electric field that involves density change accompanying a phase transition is given by (see equation (2.69))

$$S\frac{\partial \bar{c}}{\partial t} - \left[\frac{\zeta}{2}\dot{S} + \Gamma_0\right]\frac{\partial \bar{c}}{\partial \zeta} = \frac{\partial^2 \bar{c}}{\partial \zeta^2}\,, \tag{2.85}$$

subject to appropriate initial conditions and the boundary conditions:

$$\bar{c}(\zeta = 0, t) = 1\,, \quad \bar{c}(\zeta = 1, t) = 0, \tag{2.86}$$

whilst the Stefan condition is

$$\frac{\mathrm{d}S}{\mathrm{d}t} = -2\gamma\lambda \left.\frac{\partial \bar{c}}{\partial \zeta}\right|_{\zeta=1}. \tag{2.87}$$

Seeking asymptotic solutions of the form

$$\bar{c} = C_0(\zeta) + \lambda C_1(\zeta) + \dots\,, \tag{2.88a}$$

and

$$d_0^2 = D_0\lambda + D_1\lambda^2 + \dots\,, \tag{2.88b}$$

where $S = d_0^2 t$. Substituting these expansions in the governing equation above, we obtain

$$\frac{\partial^2(C_0 + \lambda C_1 + \dots)}{\partial \zeta^2} + \left[\frac{\zeta}{2}(D_0\lambda + D_1\lambda^2 + \dots) + \Gamma_0\right]\frac{\partial(C_0 + \lambda C_1 + \dots)}{\partial \zeta} = 0\,. \tag{2.89}$$

Similarly, the boundary conditions become

$$C_0 + \lambda C_1 + \dots = 1 \quad \text{on} \quad \zeta = 0\,, \tag{2.90a}$$

$$C_0 + \lambda C_1 + \dots = 0 \quad \text{on} \quad \zeta = 1\,, \tag{2.90b}$$

$$D_0\lambda + D_1\lambda^2 + \dots = -2\gamma\lambda(C_{0\zeta} + \lambda C_{1\zeta} + \dots)|_{\zeta=1} \quad \text{on} \quad \zeta = 1\,. \tag{2.90c}$$

Equating the coefficients of different powers of λ, we obtain at $\mathcal{O}(\lambda^0)$:

$$C_{0\zeta\zeta} + \Gamma_0 C_{0\zeta} = 0\,,^{\text{g}}\,, \tag{2.91}$$

subject to

$$C_0 = 1 \quad \text{on} \quad \zeta = 0\,, \tag{2.92a}$$

$$C_0 = 0 \quad \text{on} \quad \zeta = 1\,. \tag{2.92b}$$

The Stefan condition arises at $\mathcal{O}(\lambda)$:

$$D_0 = -2\gamma C_{0\zeta}|_{\zeta=1}\,. \tag{2.93}$$

Solving (2.91) subject to the boundary conditions (2.92), we obtain the leading-order concentration profile of oxygen ions across the uranium dioxide layer:

$$C_0 = 1 - \left(\frac{1 - e^{-\Gamma_0\zeta}}{1 - e^{-\Gamma_0}}\right) = \frac{e^{-\Gamma_0\zeta} - e^{-\Gamma_0}}{1 - e^{-\Gamma_0}}\,. \tag{2.94}$$

The Stefan condition (2.93) then determines

$$D_0 = 2\gamma\Gamma_0\left(\frac{e^{-\Gamma_0}}{1 - e^{-\Gamma_0}}\right)\,, \tag{2.95}$$

which when substituted in (2.88b) gives the leading-order coefficient for square of the oxide thickness.

---

[g] Here, the subscript $_\zeta$ represents differentiation with respect to ζ.

Now solving the problem at $\mathcal{O}(\lambda)$, we have the governing equation:

$$C_{1\zeta\zeta} + \frac{\zeta}{2} D_0 C_{0\zeta} + \Gamma_0 C_{1\zeta} = 0\,, \tag{2.96}$$

subject to the boundary conditions:

$$C_1 = 0 \quad \text{on} \quad \zeta = 0\,, \tag{2.97a}$$

$$C_1 = 0 \quad \text{on} \quad \zeta = 1\,. \tag{2.97b}$$

The Stefan condition at $\mathcal{O}(\lambda^2)$ provides the first-order correction to the square of the oxide growth-coefficient:

$$D_1 = -2\gamma C_{1\zeta}|_{\zeta=1}\,. \tag{2.97c}$$

Substituting the value of D_0 and $C_{0\zeta}$, and solving the governing equation (2.96) subject to boundary conditions (2.97a) and (2.97b), we obtain

$$C_1 = -\frac{\gamma e^{-\Gamma_0}}{(1-e^{-\Gamma_0})^3}\left[\left(1-e^{-\Gamma_0}\right)\left(\frac{\zeta^2}{2}\Gamma_0 + \zeta\right) + e^{-\Gamma_0}\left(\frac{\Gamma_0}{2}+1\right)\left(e^{-\Gamma_0\zeta}-1\right)\right]. \tag{2.98}$$

The coefficient D_1 is then determined as

$$D_1 = \frac{2\gamma^2 e^{-\Gamma_0}}{(1-e^{-\Gamma_0})^3}\left[(1-e^{-\Gamma_0})(1+\Gamma_0) - \frac{e^{-2\Gamma_0}}{\Gamma_0}\left(\frac{\Gamma_0}{2}+1\right)\right]. \tag{2.99}$$

The asymptotic expansion for the concentration of oxygen ions in the uranium dioxide layer given by

$$\bar{c}(\zeta) = C_0 + \lambda C_1 + \lambda^2 C_2 + \dots\,, \tag{2.100}$$

therefore becomes

$$\begin{aligned}\bar{c}(\zeta) = \left(\frac{e^{-\Gamma_0\zeta} - e^{-\Gamma_0}}{1-e^{-\Gamma_0}}\right) - \lambda\frac{\gamma e^{-\Gamma_0}}{(1-e^{-\Gamma_0})^3}\Bigg[&\left(1-e^{-\Gamma_0}\right)\left(\frac{\zeta^2}{2}\Gamma_0+\zeta\right)\\ &+ e^{-\Gamma_0}\left(\frac{\Gamma_0}{2}+1\right)\left(e^{-\Gamma_0\zeta}-1\right)\Bigg] + \dots\,.\end{aligned} \tag{2.101}$$

Similarly, the square of the oxide thickness ($S(t)$) is

$$S = d_0^2 t = D_0 \lambda t + D_1 \lambda^2 t + \dots\,, \tag{2.102a}$$

which implies

$$S(t) = 2\gamma\Gamma_0\lambda \left(\frac{e^{-\Gamma_0}}{1 - e^{-\Gamma_0}}\right) t + \lambda^2 \frac{2\gamma^2 e^{-\Gamma_0}}{(1 - e^{-\Gamma_0})^3} \left[(1 - e^{-\Gamma_0})(1 + \Gamma_0) - \frac{e^{-2\Gamma_0}}{\Gamma_0}\left(\frac{\Gamma_0}{2} + 1\right)\right] t + \dots\,. \tag{2.102b}$$

To determine the effectiveness of this perturbation expansion, we compare the asymptotic and numerical solutions for different values of λ in § 2.5.

2.5 Results for the ionic diffusion model

In this section, we discuss the numerical results obtained for the different regimes of the ionic diffusion model. Validation of the numerical results is done for the unsteady linear ionic diffusion model using an asymptotic solution that has been derived in §§§ 2.4.4.1. Furthermore, a detailed discussion of the comparison with experimental results will be presented in Chapter 6 to analyse the effectiveness of the model.

The dependence of the diffusivity and mobility of the oxygen ions (in the oxide layer) on the oxide thickness ($L^*(t^*)$) and implicitly on the electric field via $E_0^* = -V_M^*/L^*(t^*)$ is shown in Figure 2.15a and Figure 2.15b, respectively. Negative values for the ion mobility signify that the transport of oxygen ions (anions; O^{2-}) is in the opposite direction to that of the electric field. As can be seen in Figure 2.15a, the diffusivity at very small times (i.e. when $L^*(t^*) \sim a^*$) differs by at least 25 orders of magnitude to its value at later times (for e.g., when $L^*(t^*) \sim 500\,a^* \approx 274$ nm). Similarly, the mobility of ions at very small times differs by at least 24 orders of magnitude to its value at later times. Thus the nonlinear influence of the strong field on these quantities is only significant at very small times when the oxide thickness is of comparable magnitude to the lattice constant, and this effect subsides at later times.

Similarly, in Figure 2.16, the temperature dependence of the diffusivity and mobility of ions is depicted at different times (or different oxide thicknesses). This

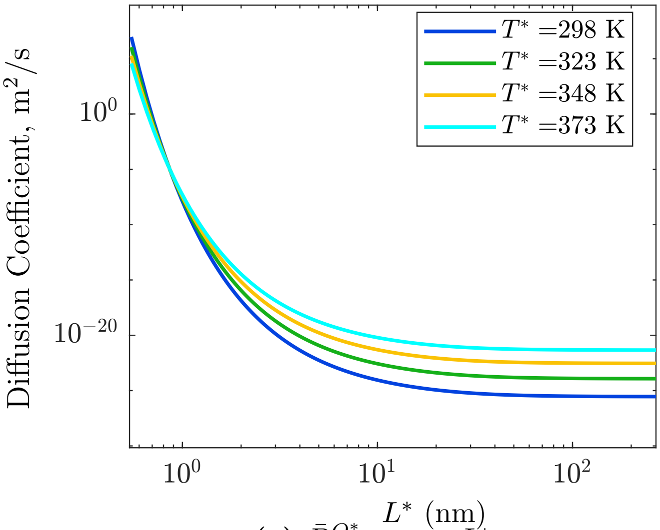

(a) $\bar{D}_c^{O*}$ versus L^*.

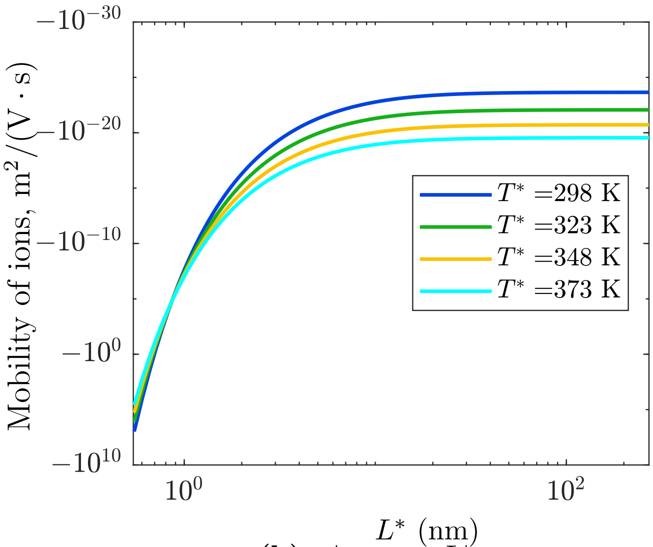

(b) $\bar{\mu}_q^*$ versus L^*.

Figure 2.15: The dependence of the diffusion coefficient, $\bar{D}_c^{O*}$ and electrical mobility ($\bar{\mu}_q^*$) of O^{2-} ions on the oxide thickness, $L^*(t^*)$ (and implicitly on the homogeneous electric field, $E_0^* = -V_M/L^*(t^*)$) for various temperatures (refer equations (2.71c) for $\bar{D}_c^{O*}$ and $\bar{\mu}_q^*$). Negative values for $\bar{\mu}_q^*$ indicate that the movement of ions is in the opposite direction to E_0^*. Parameters chosen are: $a^* = 5.4713$ Å, $\nu^* = 19$ THz, $W^* = 1.24$ eV, $k_b^* = 1.3806 \cdot 10^{-23}$ J/K, $V_M^* = -0.97$ V (as defined in (1.8)).

figure lends further support to the earlier statement about the influence of the electric field strength on the diffusivity and ion mobility. It is evident from the figure that the nonlinear effect of the field ('strong' field) is only felt when the oxide thickness is of comparable magnitude to the lattice constant. At a later instant in time, that is when $L^* \gg a^*$, $\bar{D}_c^{O*} \to D_c^{O*}$ and the same is shown in the figure. As is apparent, the influence of the temperature compared to the electric field strength on the diffusivity and mobility becomes predominant only at later times (for e.g. when $L^* \sim 5a^*$). It can be seen that the influence of the electric field strength is dominant compared to temperature effects at earlier times (i.e. when $L^* \sim a^*$).

The numerical solution for the oxide thickness obtained from the linear unsteady ionic diffusion model (2.69) is validated against the asymptotic solution (2.102b) as shown in Figure 2.17. As can be seen in the figure, the leading-order (i.e. one-term) asymptotic solution captures the behaviour of the full numerical problem for a sufficiently small λ. Here, subfigure 2.17a shows the plot of oxide thickness with time for $\lambda = 0.5952$ corresponding to a surface concentration of $C_a^* = 6 \cdot 10^{28}$ ions/m^3 that has been assumed by Gharagozloo and Kanouff (2013). From this figure, it is appropriate to conclude that the quasi-steady approximation is not valid for the O^{2-} surface concentration considered by GK.

Similarly, a comparison of the numerical solution (solid lines) for the linear unsteady problem with the asymptotic solution (2.101) (dashed lines) for a sufficiently small value of $\lambda = 0.01$ is shown in Figure 2.18. A good agreement between the numerical and asymptotic solutions can be observed.

In Figure 2.19, the growth of the (dimensionless) oxide with time for the quasi-steady and unsteady models in both moderate (linear; denoted as Lin. in the figure) and strong (nonlinear; denoted as NL) electric fields are plotted. As may be expected, chemical diffusion is the slowest which is reflected in the oxide growth being the slowest compared to the ionic diffusion models. However, the difference in the oxide growth at any particular time between the density change ($\gamma = 1.7375$) and no density change ($\gamma = 1$) cases is the smallest for the chemical diffusion model compared to the ionic diffusion models. The difference in the oxide growth between $\gamma = 1.7375$ and $\gamma = 1$ is more pronounced in the quasi-steady ionic diffusion model compared to unsteady ionic model. It is also evident from the figure that both the linear and nonlinear ionic models result in the same behaviour at sufficiently large times. Also note that the quasi-steady model

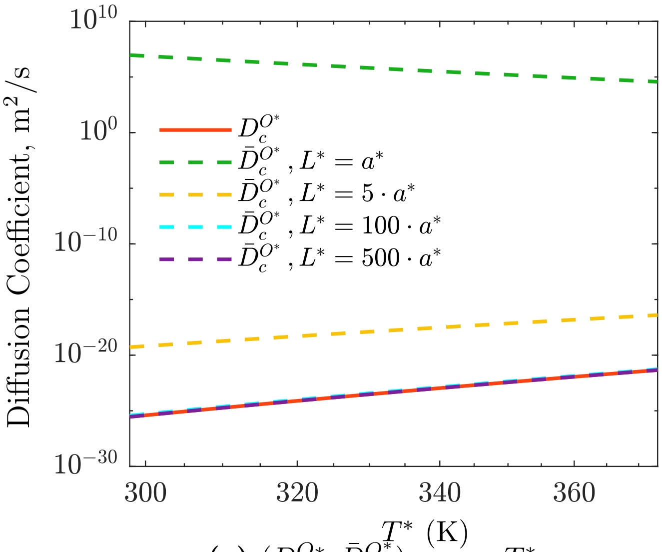

(a) $(D_c^{O*}, \bar{D}_c^{O^*})$ versus T^*.

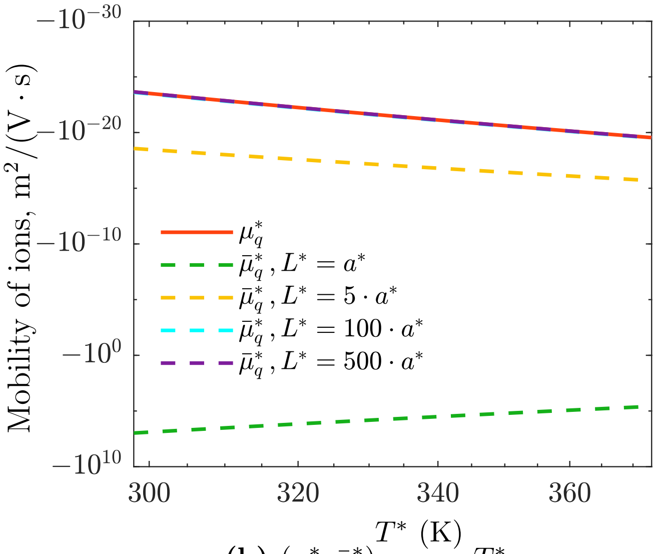

(b) $(\mu_q^*, \bar{\mu}_q^*)$ versus T^*.

Figure 2.16: The temperature dependence of the diffusion coefficients $(D_c^{O*}, \bar{D}_c^{O^*})$ and electrical mobilities $(\mu_q^*, \bar{\mu}_q^*)$ of ions in moderate (as defined by (2.59)) and strong electric fields (as defined by (2.71c)) respectively, wherein $E_0^* = -V_M/L^*(t^*)$. Parameters chosen are: $a^* = 5.4713$ Å, $\nu^* = 19$ THz, $W^* = 1.24$ eV, $k_b^* = 1.3806 \cdot 10^{-23}$ J/K, $V_M^* = -0.97$ V (as defined in (1.8)).

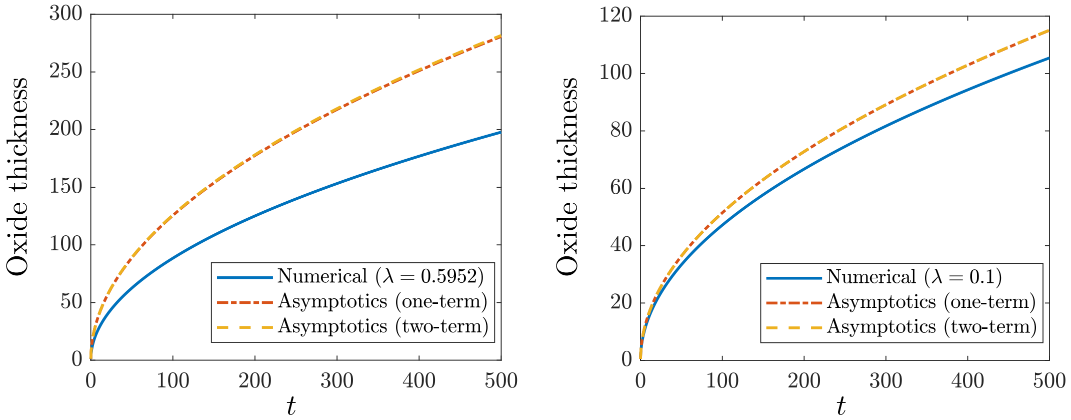

(a) $\lambda \approx 0.6$ **(b)** $\lambda = 0.1$

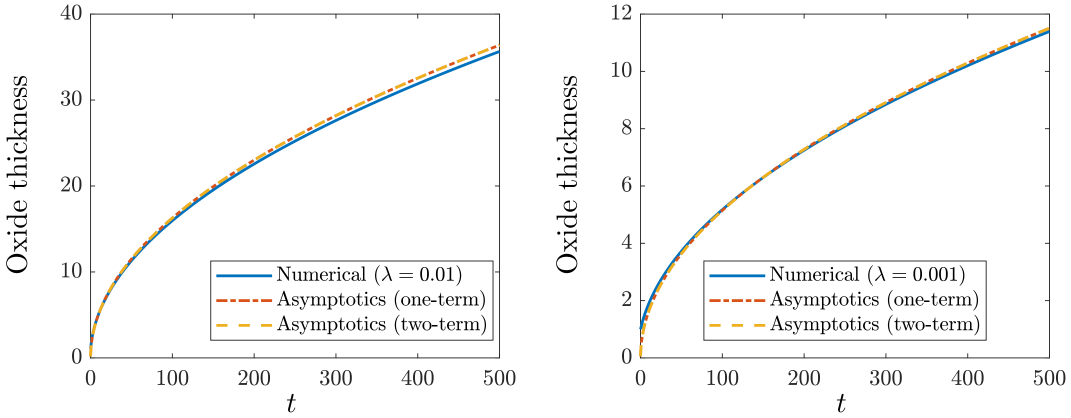

(c) $\lambda = 0.01$ **(d)** $\lambda = 0.001$

Figure 2.17: Validation of the numerical results (obtained from the solution of the unsteady moderate electric field Stefan model (2.69)) against the asymptotic solution (see (2.102b)). Other parameters include: $\gamma = 1.7375$, $\delta = 0.1$, $\Gamma_0 = -76.2$ corresponding to $T^* = 22$°C, $V_M^* = -0.97$ V.

over-predicts the oxide thickness compared to the unsteady model.

The influence of surface concentration of the diffusing species (C_a^*) via the nondimensional Stefan parameter $\lambda = C_a^*/(2.09\, N_M^*)$ (ratio of the surface concentration of the diffusing species C_a^* to its concentration at the oxide-metal interface required for the conversion of one cubic meter of metal with a concentration N_M^*) on the oxide growth kinetics in a quasi-steady model (with moderate electric field) is plotted in Figure 2.20. As may be anticipated, an increase in λ results in an increase in the oxide thickness at any particular time. Similarly, the same plot for the unsteady ionic diffusion model is shown in Figure 2.21.

Similarly, increasing the magnitude of the nondimensional parameter Γ_0, which gives the relative influence of the electric field to the temperature effects, results in

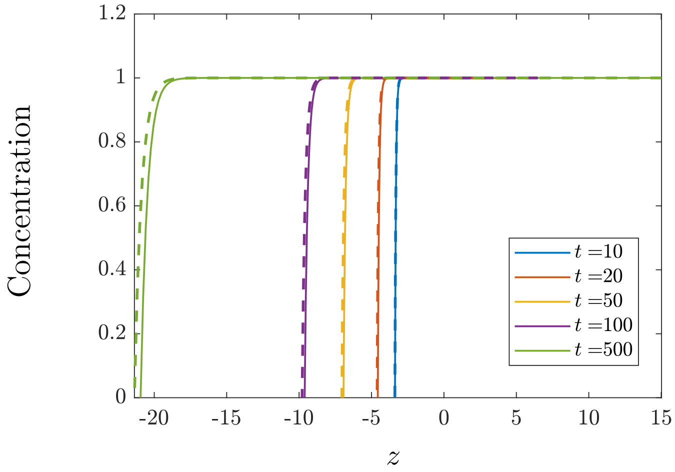

Figure 2.18: Validation of the numerical solution (solid lines) for the concentration profiles obtained from the linear ionic model (2.69) with the asymptotic (dashed lines) solution for the same (given by (2.101)). The parameters include: $\lambda = 0.01$, $\gamma = 1.7375$, $\delta = 0.1$, $\Gamma_0 = -76.2$ corresponding to $T^* = 22^\circ$ C and $V_M^* = -0.97$ V.

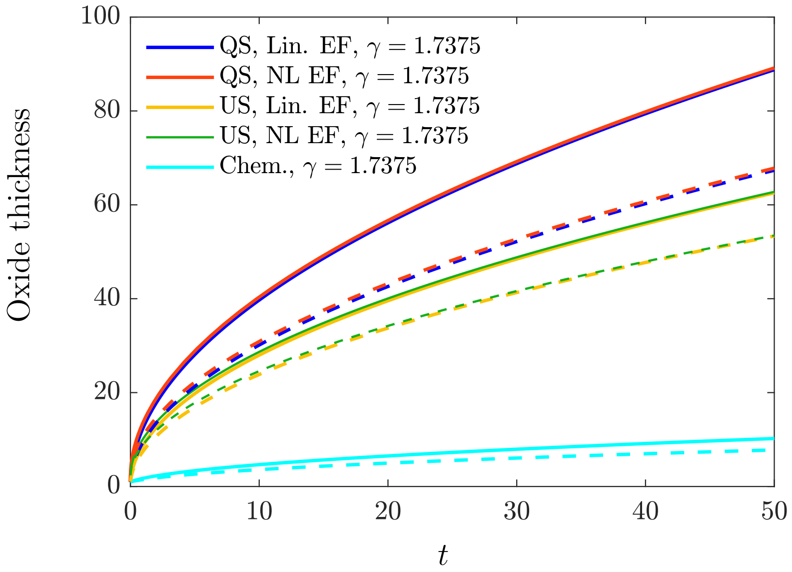

Figure 2.19: Evolution of oxide thickness (nondimensional) with time for the quasi-steady (denoted as QS) and unsteady (denoted as US) models showing the influence of density/volumetric changes ($\gamma = 1.7375$ for density change (solid lines) and $\gamma = 1$ for no density change (dashed lines)). Other parameters include: $\lambda \approx 0.6$, $\Gamma_0 = -76.2$ corresponding to $T^* = 22$ °C and $V_M^* = -0.97$ V (as defined in (1.8)).

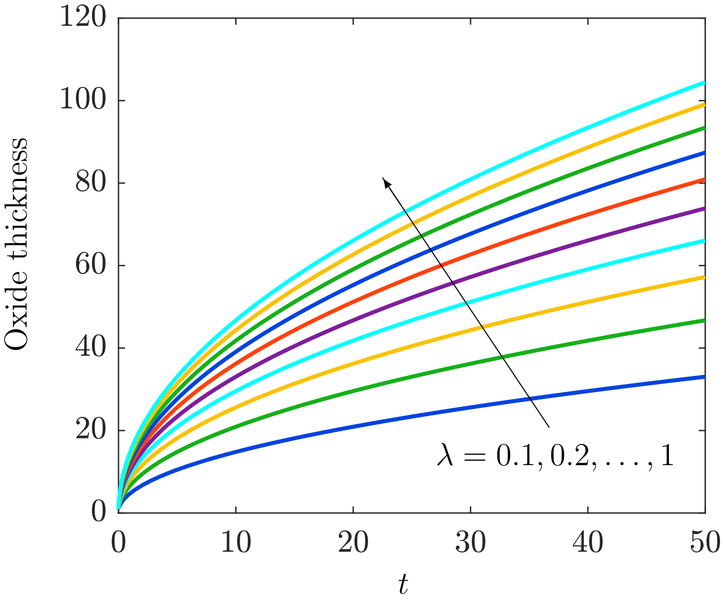

Figure 2.20: Effect of varying $\lambda = C_a^*/(2.09N_M^*)$ on the evolution of oxide thickness with time for the quasi-steady model with moderate electric fields (solution obtained by solving (2.84)). Other parameters include: $\gamma = 1.7375$, $\delta = 0.1$, $L(t = 0) = 1$, $\Gamma_0 = -62.8$ corresponding to $T^* = 85$ °C and $V_M^* = -0.97$ V.

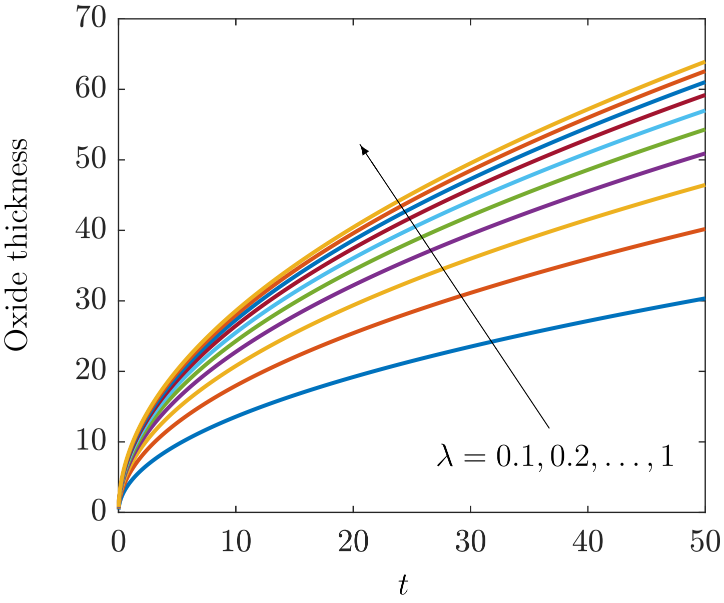

Figure 2.21: Effect of varying $\lambda = C_a^*/(2.09N_M^*)$ on the evolution of oxide thickness with time for the unsteady linear ionic model given by (2.69). Other parameters include: $\gamma = 1.7375$, $L(t = 0) = 1$, $\Gamma_0 = -62.8$ corresponding to $T^* = 85$ °C and $V_M^* = -0.97$ V.

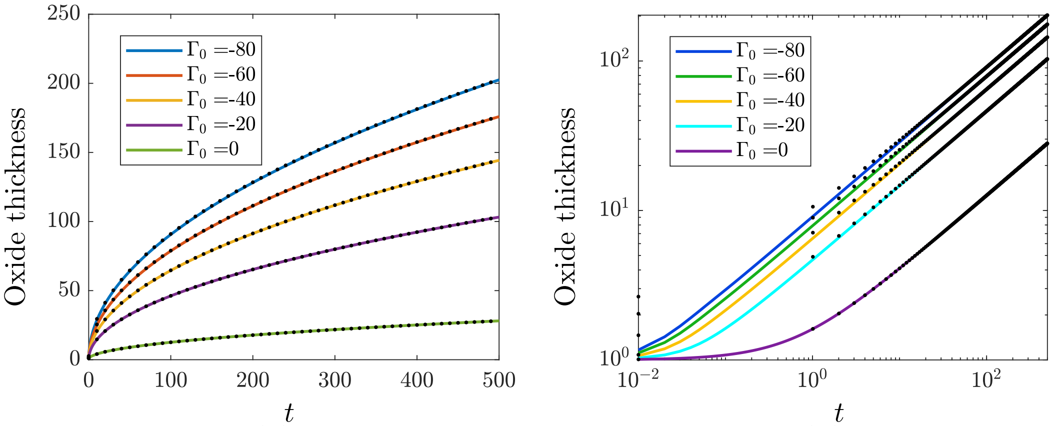

(a) **(b)**

Figure 2.22: Effect of the electric field forcing, as measured by $\Gamma_0 = -q^* V_M^* / (k_b^* T^*)$ on the oxide growth kinetics for the unsteady Stefan model with strong (represented as black dots; obtained by solution of (2.73)) and moderate (as lines; obtained by solution of (2.69)) electric fields. Other parameters include: $\gamma = 1.7375$, $\delta = 0.1$ and $\lambda = C_a^* / (2.09\, N_M^*) = 0.5952$. The same figure on a log-log axis (b) shows the difference in oxide thickness between moderate and strong fields at small times.

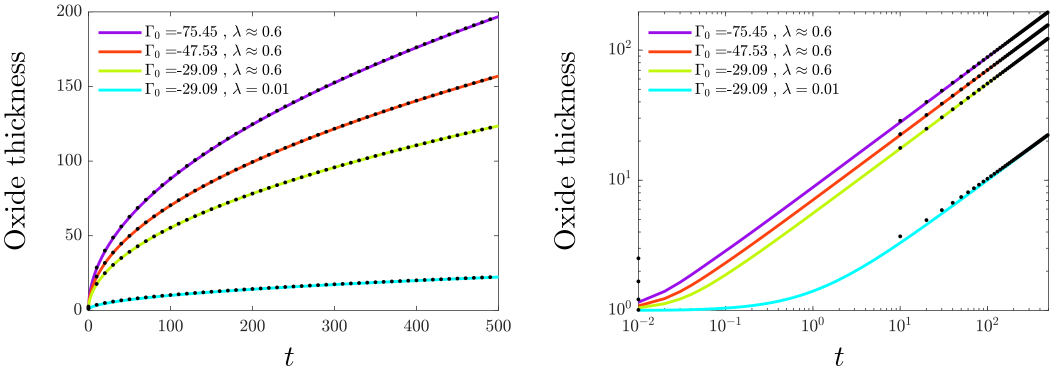

(a) **(b)**

Figure 2.23: Evolution of oxide thickness with time for the unsteady Stefan model with strong (denoted as black dots; obtained by solution of (2.73)) and moderate (as lines; obtained by solution of (2.69)) electric fields for different values of Γ_0 $(=-75.45\,, -47.53\,, -29.09$ corresponding to temperatures $T^* = 25°\,, 200°$, $500°$ C and $V_M^* = -0.97$ V) and λ. The other parameters include: $\gamma = 1.7375$, $\delta = 0.1$, $L(t = 0) = 1$. The same figure on a log-log axis (b) shows the difference in oxide thickness between moderate and strong fields at small times.

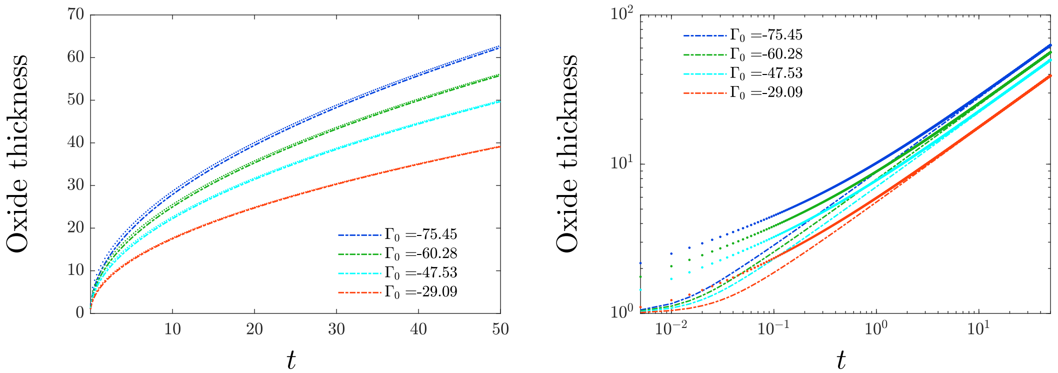

(a) **(b)**

Figure 2.24: The growth of oxide thickness for small time ($t \leq 50$) for the unsteady Stefan model with strong (denoted as dots; obtained by solution of (2.73)) and moderate (as dashed lines; obtained by solution of (2.69)) electric fields for different values of Γ_0 ($=-75.45\,,-47.53\,,-29.09$ corresponding to temperatures $T^* = 25^\circ\,,200^\circ$, 500° C and $V_M^* = -0.97$ V). The other parameters include: $\gamma = 1.7375$, $\delta = 0.1$, $L(t=0) = 1$.

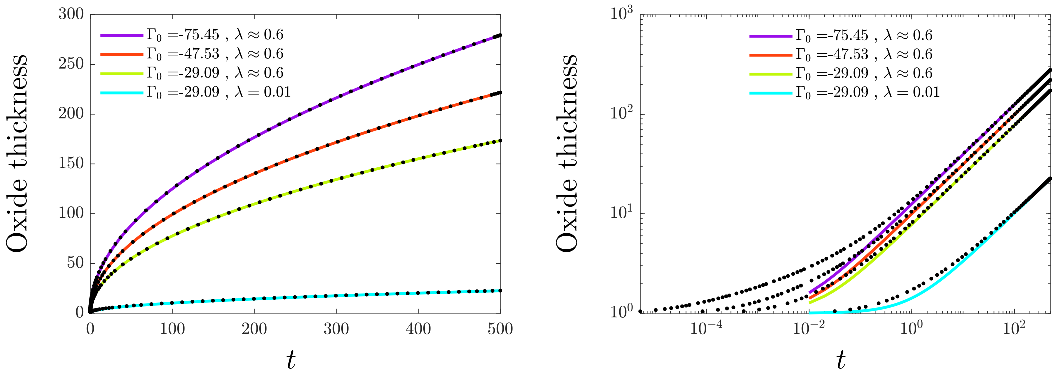

(a) **(b)**

Figure 2.25: Evolution of oxide thickness with time for the quasi-steady Stefan model with strong (denoted as black dots; obtained by solution of (2.81)) and moderate (as lines; obtained by solution of (2.84)) electric fields for different values of Γ_0 ($=-75.45\,,-47.53\,,-29.09$ corresponding to temperatures $T^* = 25^\circ\,,200^\circ\,,500^\circ$ C and $V_M^* = -0.97$ V) and λ. The other parameters include: $\gamma = 1.7375$, $\delta = 0.1$, $L(t=0) = 1$.

an increased oxide thickness. The (nondimensional) oxide thickness as a function of (nondimensional) time for different values of Γ_0 in the unsteady ionic diffusion model is plotted in Figure 2.22. Here, it can be seen that both the nonlinear (strong electric field; as black dots) and linear (moderate electric field; as lines) models essentially lead to the same behaviour (to the graphical accuracy known), with differences between the linear and nonlinear models only apparent at very small times.

The combined influence of Γ_0 and λ on the oxide growth with time for the unsteady ionic diffusion model is plotted in Figure 2.23, where the values of $\Gamma_0 = -75.45\,, -47.53,\ -29.09$ correspond to the dimensional temperature values $T^* = 25^\circ\,, 200^\circ,\ 500^\circ$ C and $V_M^* = -0.97$ V. The same plot at small times (i.e. $t \leq 50$) is shown in Figure 2.24. It can be seen that there is a larger deviation of the behaviour of the nonlinear model from the linear ionic model at very small times (for e.g. $t \leq 1$), with the deviation more pronounced at lower temperatures. This corroborates our earlier statement that the nonlinear influence of the strong field on the oxidation kinetics is only significant at very small times when the oxide thickness is of comparable magnitude to the lattice constant, and this effect subsides at later times. The oxide thickness for the quasi-steady model with different values of Γ_0 and λ is shown in Figure 2.25. A similar behaviour to the unsteady model is observed, but an increased oxide thickness at any particular time is predicted compared to the unsteady model.

2.6 Discussion on dry-air oxidation

Diffusion of O^{2-} due to a concentration gradient alone does not account for the observed experimental oxidation rate. A self-induced electric potential gradient due to the rearrangement of charges provides an additional driving force for the migration of O^{2-} to then react with the metal, which results in an increase in the oxidation rate. We have formulated a one-phase unsteady Stefan model for this 'ionic diffusion' problem that involves two main parameters: Γ_0 and λ. Here, Γ_0 measures the importance of the additional ionic component due to the self-induced electric field. If Γ_0 is sufficiently large, we are in the "strong-field" regime in which the diffusivity and mobility of the O^{2-} ions are nonlinearly affected by the field. At lower Γ_0, we find a "moderate-field" regime. The moderate-field regime is the most relevant and the strong-field effects are only found at very early times (very thin oxides; $L^*(t^*) < 100\,a^*$ for example) as has been shown through the results (see figures 2.15 and 2.16 for example). This brief period of a strong field has little lasting effect on the evolution of the oxide growth and the moderate-field approach is sufficient to describe the oxidation kinetics for practical timescales. When Γ_0 is sufficiently small, we recover the Stefan problem without the ionic (electric field) effects, and therefore chemical diffusion is dominant at these small values of Γ_0. The value of the other nondimensional parameter λ that gives the ratio of the surface concentration of the diffusing species to its concentration at the oxide-metal interface involved in the phase transition, determines if quasi-steady approximation can be made. When λ is sufficiently small, we recover a quasi-steady theory compatible with the GK model. However, the parameter values taken by GK are out of the regime of validity of the quasi-steady approximation; therefore the results reported by Gharagozloo and Kanouff (2013) should be treated with some caution.

Comparison of the dimensional numerical results with the published experimental results of various authors is presented in Chapter 6.

In the next chapter, we derive a mixed-phase (diffuse-interface) model for dry-air oxidation where we have a finite width of the 'interface' (called "reaction fronts") between the different homogeneous/pure phases, instead of an infinitesimally thin interface (or "sharp interface") assumed in the Stefan model.

Chapter 3

Mixed-phase model: dry-air oxidation of uranium

The models we have discussed so far treat the material as being composed of discrete layers separated by an interface. At such an interface, the transition between (for example) U and UO_2 is assumed to occur over an infinitesimal length scale. This simplification allows us to formulate the corrosion problem as a classical Stefan problem, where we track the movement (or velocity) of the interface using a Stefan condition.

As the underpinning chemistry and physics become complex in more challenging corrosion environments, it is unclear how to construct an analogous Stefan problem (or even if one exists). For example, in Chapter 4 we examine a corrosion problem in water vapour that requires three material phases, one of which is generated as a reaction intermediate in a complex two-step reaction process, and two diffusing species. We need to be able to address these complex situations and to do this we propose an alternative approach based on a mixed-phase (or diffuse-interface) model. This approach removes the assumption of discrete layers, and allows instead for smooth continuous transitions in the material (e.g. from U to UO_2); this approach will be critical in later chapters but here we take the opportunity to reformulate the dry-air oxidation problem in this manner to ensure that there is consistency with our earlier treatments.

To this end, we now represent the distribution of the phases (U/UO_2) as a continuum instead of discrete layers. In this approach, the composition of the material (e.g. the volume fractions of UO_2 and U) become continuous functions of position and time across the whole material domain. The reactions in this approach will still be found to occur in spatially localised regions (also called "reaction fronts"). These reaction fronts separate regions of homogeneous material composition where diffusion dominates over chemical reactions.

The pioneering work that provides a theoretical understanding of the reaction fronts in reaction-diffusion systems with second-order reaction kinetics was done by Gálfi and Rácz (1988), where they considered a one-dimensional model of the form

$$\frac{\partial a}{\partial t} = D_a \frac{\partial^2 a}{\partial z^2} - kab\,, \qquad \frac{\partial b}{\partial t} = D_b \frac{\partial^2 b}{\partial z^2} - kab\,. \tag{3.1}$$

Here, both species A (with concentration a) and B (with concentration b) are diffusing with diffusivities $D_a\,, D_b$ respectively; kab is the (dimensional) reaction rate for the reaction $A+B \to C$ where C is the inert solid product. They showed that at large times and for $D_a = D_b$, the reaction rate has the (dimensional) form

$$kab \sim kt^{-2/3} F\left(\frac{z - z_f}{t^{1/6}}\right)\,, \tag{3.2}$$

where F is some functional form and z_f is the propagating reaction front location at any time t. Later, Koza (1996) considered the same system, but with $D_a \neq D_b$ (and also for the case where one of the diffusivities is zero) and showed that the exponents in the asymptotic form (3.2) is true for any reaction-diffusion system with second-order kinetics irrespective of the diffusivities of the reactants. These length scales have also been confirmed by the computational work of Jiang and Ebner (1990) and the theoretical analysis of Koza (1997). In addition, the conclusions of these theoretical studies have been validated through the experiments of Léger, Elezgaray, and Argoul (1997). The more recent theoretical work of Bazant and Stone (2000) investigated generalised higher-order reaction kinetics with reaction rate $ka^m b^n$, where $m\,, n \geq 1$ ($m\,, n$ being the reaction orders for the diffusing and non-diffusing reactants respectively). They demonstrated the following form for the reaction rate:

$$ka^m b^n \sim kt^{-\nu_1} F\left(\frac{z - z_f}{t^{\nu_2}}\right)\,, \tag{3.3}$$

where $\nu_1 = m/(m+1)$ and $\nu_2 = (m-1)/(2\cdot(m+1))$. Note that ν_1 and ν_2 are only dependent on the reaction order of the diffusing reactant.

Now, we return to our uranium oxidation problem, which has the additional complexities of a non-constant diffusion coefficient that is a function of the material composition, and advection accompanying the reaction and diffusion processes.

3.1 Problem formulation

We consider the diffusion of oxygen ions (O^{2-}) in the bulk material, with a phase change from U to UO_2 determined by the overall reaction $U^{4+} + 2\,O^{2-} \rightarrow UO_2$. Here, we have neglected the hyper-stoichiometry in the representation of the oxide (i.e. UO_2 instead of $UO_{2.09}$) for simplicity. The hyper-stoichiometry is however incorporated in the numerical simulations. To describe the evolution of the system we will make use of (where the asterisk denotes a dimensional quantity) the following three quantities:

$c^*(z^*, t^*)$ the number concentration of O^{2-},

$M^*(z^*, t^*)$ the number concentration of U,

$O^*(z^*, t^*)$ the number concentration of UO_2.

The only diffusing species is O^{2-} with a concentration c^* that has constant diffusivities $D_c^{M^*}$ and $D_c^{O^*}$ in a pure metal and pure oxide respectively. Here, a lower-case letter for the concentration denotes the diffusing species (c^*) whilst upper-case letters denote the nondiffusing phases (M^*, O^*). Note that the concentrations of the O^{2-} diffusing species, metal and the oxide are tracked in this model, as opposed to tracking only the diffusing species in the Stefan model.

We consider a fixed control volume ΔV^* with a constant cross-sectional area ΔA^*. Applying particle conservation of an individual species in the control volume, we have that the change in the quantity (or total number) of a particular species in the control volume during the time interval Δt^* is given by the summation of the net influx of the species and the formation (or depletion) of the species within the control volume in the same time interval. The net influx (through advection and/or diffusion) is the difference between the influx and efflux of the species via the control surfaces. Formation or depletion (source or sink) of the species occurs due to chemical reactions within the control volume.

Taking the limits $\Delta V^* \rightarrow 0$ ($\Delta z^* \rightarrow 0$ in the one-dimensional case) and $\Delta t^* \rightarrow 0$, we have the governing equation for the diffusing species (oxygen ions) as

$$\frac{\partial c^*}{\partial t^*} = -\frac{\partial F_c^*}{\partial z^*} + r_c^* \,, \tag{3.4}$$

where the flux F_c^* is taken to be the sum of the diffusive and advective components:

$$F_c^* = v^* c^* - D_c^* \frac{\partial c^*}{\partial z^*} \,. \tag{3.5}$$

Here D_c^* is a diffusion coefficient that is a function of the material composition (that is, its value will vary locally according to the amount of U and UO_2 present) and in general varies with z^* and t^*, and $v^*(z^*, t^*)$ is the advection velocity that arises due to phase/volumetric changes as the relatively more dense metal is converted to a less dense oxide. Similarly, the governing equations for the nondiffusing phases $M\,, O$ are respectively written as

$$\begin{aligned} \frac{\partial M^*}{\partial t^*} &= -\frac{\partial F_M^*}{\partial z^*} + r_M^* \,, \\ \frac{\partial O^*}{\partial t^*} &= -\frac{\partial F_O^*}{\partial z^*} + r_O^* \,, \end{aligned} \tag{3.6}$$

where the fluxes include only the respective advective components: $F_M^* = v^* M^*$ and $F_O^* = v^* O^*$.

The governing equations for c^*, M^* and O^* are then

$$\frac{\partial c^*}{\partial t^*} + \frac{\partial (v^* c^*)}{\partial z^*} = \frac{\partial}{\partial z^*}\left(D_c^* \frac{\partial c^*}{\partial z^*} \right) + r_c^* \,, \tag{3.7a}$$

$$\frac{\partial M^*}{\partial t^*} + \frac{\partial (v^* M^*)}{\partial z^*} = r_M^* \,, \tag{3.7b}$$

$$\frac{\partial O^*}{\partial t^*} + \frac{\partial (v^* O^*)}{\partial z^*} = r_O^* \,, \tag{3.7c}$$

where the effective diffusion coefficient in the material is assumed to be the weighted sum of the diffusivities in the pure phases. Zhu et al. (2001) calculated the effective diffusivity in a composite material with diffuse interfaces, using a spectral method. They had formulated a continuum description of the effective diffusivity based on the discrete formulation that had been derived from the Reuss bound (lower-bound) by Nan (1993). We have used an equivalent upper-bound (Voigt model of the '*rule of mixtures*') for ease of computation using numerical schemes. Using the upper-bound of the rule of mixtures, the effective diffusivities D_h^* and D_c^* are calculated as:

$$D_c^* = \frac{O^*}{N_O^*} D_c^{O*} + \frac{M^*}{N_M^*} D_c^{M*} \,. \tag{3.7d}$$

Here $N_{O,M}^*$ are the number concentrations of the pure oxide (UO_2) and metal phases (U) with O^{2-} diffusivities D_c^{O*} and D_c^{M*} respectively; (O^*/N_O^*) and (M^*/N_M^*) represent the local volume fractions of the oxide and the metal.

The nonlinear reaction terms r_i^* where $i = (c, O, M)$ can be defined using the *rate law* for elementary chemical reactions if the reaction mechanism is known. It states that the rate of formation or depletion of an entity[a] in an *elementary* chemical reaction is proportional to the product of the concentrations of the individual reactants, each raised to the power of its respective stoichiometric coefficient in the elementary reaction. For a non-elementary reaction such as in this case, we can write the rate law or the *mean-field approximation* which has a power-law structure for the rate of formation of a product; for example, $r_P^* \propto C_A^{*\alpha} C_B^{*\beta}$ for a reaction $A + B \xrightarrow{k^*} P$ where r_P^* is the reaction rate for the formation of product P, $C_{(A,B)}^*$ are the concentrations of the species A, B and α, β are the *'kinetic orders'* of the reaction which are either written from the stoichiometry of the rate-limiting step if the reaction mechanism is known, or determined experimentally.

For the sake of simplicity, we assume the simplest form of the rate law for the overall reaction $U^{4+} + 2\,O^{2-} \xrightarrow{k^*} UO_2$; we will return in a later chapter to include higher-order kinetics in a more complex configuration. The aforementioned reaction leads to a sink of O^{2-} and U, whilst (3.7c) has a source of UO_2. The reaction terms in (3.7a) - (3.7c) are therefore

$$r_c^* = -2k^* c^* M^* \,, \quad r_M^* = -k^* c^* M^* \,, \quad r_O^* = +k^* c^* M^* \,, \tag{3.7e}$$

where k^* is a dimensional second-order reaction rate constant.

Given the number concentration of each species, we define a concentration (or density) of the mixed phase via

$$\varrho^* = M^* + O^* \,. \tag{3.7f}$$

---

[a] An entity here refers to an atom, molecule or compound involved in a chemical reaction.

Simple addition of the evolution equations for M^* (3.7b) and O^* (3.7c) is sufficient to confirm that the reaction conserves ϱ^*, given the source/sink terms defined in (3.7e):

$$\frac{\partial \varrho^*}{\partial t^*} + \frac{\partial}{\partial z^*}\left(\varrho^* v^*\right) = 0\,. \tag{3.7g}$$

The system (3.7) is closed by imposing that the bulk material consists of only the O^* and M^* phases. From particle conservation of uranium, as the metal is converted to oxide, we have:

$$O^* = (N_M^* - M^*)\frac{N_O^*}{N_M^*}\,, \tag{3.7h}$$

which implies

$$O + M = 1\,, \tag{3.7i}$$

where $O = (O^*/N_O^*)\,, M = (M^*/N_M^*)$ are the respective nondimensional concentrations or the volume fractions of the oxide and metal, and $N_{M,O}^*$ correspond to the number concentrations of pure U and UO_2 respectively.

The system of equations (3.7) are solved, subject to the initial conditions of $M^* = N_M^*$, $O^* = 0$, $c^* = 0$ that represent an unexposed initial sample of pure uranium, and with the imposition of $c^* = C_a^*$ on the surface of the material $(z^* = z_s^*(t^*))$. In general, C_a^* can be time-dependent, but we will consider a constant value in what follows. The boundary conditions considered are:

$$\left.\begin{aligned} &c^*(z = z_s^*(t^*), t^*) = C_a^*\,, \quad c^*(z^* = -z_\infty^*, t^*) = 0\,, \\ &M^*(z^* = -z_\infty^*, t^*) = N_M^*\,, \\ &O^*(z^* = -z_\infty^*, t^*) = 0 \end{aligned}\right\} \text{ for } t^* \geq 0; \tag{3.8a}$$

no boundary condition is required for the advection velocity v^* since we will transform the problem in a way which will eliminate it from the equations. The metal base/truncation boundary is represented as $z^* = -z_\infty^*$. The boundary conditions represent that the diffusing ions have a constant concentration of C_a^* at the oxide (UO_2) surface, whilst a pure metal is recovered far away from the surface at $z^* = -z_\infty^*$.

3.1.1 The dimensionless problem

We nondimensionalise using an arbitrary length scale L^*_{ref} and a diffusive timescale L^{*2}_{ref}/D^*_{ref}. The concentrations of the different species in the material are nondimensionalised using the respective pure-phase concentrations (refer A.1 for material densities or pure-phase concentrations). The quantity ϱ^* that represents the local density of the mixed phase is nondimensionalised using the pure metal density (considering that the initial phase is purely metal). We therefore have

$$\begin{gathered} t^* = \frac{L^{*2}_{ref}}{D^*_{ref}} t\,, \quad z^* = L^*_{ref} z\,, \quad v^* = \frac{D^*_{ref}}{L^*_{ref}}\, v(z,t)\,, \quad c^* = C^*_a\, c(z,t)\,, \\ M^* = N^*_M\, M(z,t)\,, \quad O^* = N^*_O\, O(z,t)\,, \quad \varrho^* = N^*_M \varrho\,, \quad k^* = \frac{D^*_{ref}}{L^{*2}_{ref} N^*_M} k\,. \end{gathered} \tag{3.9}$$

Here C^*_a is the surface concentration of the diffusing oxygen ions (O^{2-}). The reference diffusivity will be taken as $D^*_{ref} = D^{O*}_c$ (i.e. the diffusivity of O^{2-} in UO_2) in what follows. The dimensionless equations of this mixed-phase (or diffuse-interface) model are then

$$\frac{\partial c}{\partial t} + \frac{\partial}{\partial z}(vc) = \frac{\partial}{\partial z}\left(D_c(M)\frac{\partial c}{\partial z}\right) - 2kcM\,, \tag{3.10a}$$

$$\frac{\partial M}{\partial t} + \frac{\partial}{\partial z}(vM) = -kcM\frac{C^*_a}{N^*_M}\,, \tag{3.10b}$$

$$\frac{\partial O}{\partial t} + \frac{\partial}{\partial z}(vO) = kcM\,\frac{C^*_a}{N^*_O}\,, \tag{3.10c}$$

where

$$O + M = 1\,, \tag{3.10d}$$

$$D_c(M) = 1 + M(\mu - 1)\,, \tag{3.10e}$$

with $\mu = D^{M*}_c/D^{O*}_c$ (the ratio of the diffusivities in the two phases).

As noted above, on defining the mixture concentration

$$\varrho = M + O\,\frac{N^*_O}{N^*_M}\,, \tag{3.10f}$$

it is clear that

$$\frac{\partial \varrho}{\partial t} + \frac{\partial}{\partial z}(v\varrho) = 0\,, \tag{3.10g}$$

is a consequence of (3.10b) and (3.10c) as expected for a purely chemical reaction. The boundary conditions for c, M, O are

$$\left.\begin{aligned} &c(z = z_s(t), t) = 1\,, \quad c(z = -z_\infty, t) = 0\,, \\ &M(z = -z_\infty, t) = 1\,, \quad O(z = -z_\infty, t) = 0 \end{aligned}\right\} \text{ for } t \geq 0\,. \tag{3.11a}$$

The initial conditions are given as

$$M(z, t = 0) = 1\,, \quad O(z, t = 0) = 0 \quad \text{and} \quad c(z, t = 0) = 0\,, \tag{3.11b}$$

with the imposition of $c = 1$ at the surface $z = z_s(t)$ for all t.

We solve the system of equations (3.10) subject to boundary and initial conditions (3.11) for two cases, namely, with and without the consideration of density/volumetric changes. We then compare the results of this new mixed-phase dry-air problem in the limit of a large reaction rate constant or equivalently in the limit as $t \to \infty$ with the results of the Stefan formulation (see § 2.2 for the unsteady Stefan formulation). It has been formally proven by Hilhorst, Van Der Hout, and Peletier (1996) that a simpler reaction-diffusion problem of the type $A + B \to C$, where A diffuses and reacts with the substrate B, can be modelled as a Stefan problem (discrete-layer model) in the limit of a large reaction rate constant (i.e. as $k \to \infty$) or equivalently as $t \to \infty$. That is, the authors there proved that the free boundary of the reaction-diffusion problem converges pointwise to the free boundary of the Stefan problem as $k \to \infty$. Here, the term 'free boundary' refers to the unknown domain boundary (or surface boundary) that is found as part of the solution to the problem.

Solving the mixed-phase problem with density/volumetric changes leads to a more difficult computation as we have to deal with the advection terms in (3.10) that arise as a result of the expanding domain. We will investigate a method for dealing with the expanding domain based on the Howarth-Dorodnitsyn transformation. The Howarth-Dorodnitsyn transformation is generally used to reduce the compressible boundary-layer equations to a form similar to the incompressible equations. In our case, we use the transformation to fix the moving boundaries for ease of application of the numerical scheme. Since the position and velocity of the moving boundaries are not known a priori, it is simpler to discretise the domain by using a fixed computational coordinate system. This approach in formulating and solving the governing equations over a transformed fixed domain is similar to a Lagrangian approach instead of an Eulerian (control volume) approach to track the expanding material. It is essentially a trade-off between ease of application of the numerical scheme and more complicated governing equations.

3.1.2 *Case 1: Excluding density change*

We first consider the simpler case wherein there is no density/volumetric change as the metal is converted to oxide, that is, $N_M^* = N_O^*$ and $v = 0$. Hence the whole domain is fixed in space, with no expansion of the material. The dimensionless problem (3.10) reduces to

$$\frac{\partial c}{\partial t} = \frac{\partial}{\partial z}\left(D_c(M)\frac{\partial c}{\partial z}\right) - 2kcM\,, \tag{3.12a}$$

$$\frac{\partial M}{\partial t} = -kcM\frac{C_a^*}{N_M^*}\,, \tag{3.12b}$$

$$\frac{\partial O}{\partial t} = kcM\frac{C_a^*}{N_O^*}\,, \tag{3.12c}$$

with

$$O + M = 1\,, \tag{3.12d}$$

$$D_c(M) = 1 + M(\mu - 1)\,, \tag{3.12e}$$

and

$$\varrho = M + O = 1\,. \tag{3.12f}$$

The system of equations (3.12) has been solved subject to boundary and initial conditions (3.11) by the method of lines in MATLAB using the ODE solver `ode15s`[b] which is straightforward.

---

[b] The `ode15s` solver is a variable time-step, variable-order, stiff differential equations solver which has been used instead of `ode45` solver as the latter was extremely slow requiring a large number of time steps that resulted in the solution array exceeding the "maximum array size preference" for integrating the differential equations (say) up to a nondimensional time of

The results are presented with discussion in § 3.2.

3.1.3 *Case 2: Including density change:* a solution strategy for the moving domain

Considering that at time $t = 0$ the bulk material occupies a domain $z \in [-z_\infty, z_s(0)]$, and as the reaction proceeds, the change in density due to the phase transition (metal → metal oxide) leads to a moving surface with a domain $z \in [-z_\infty, z_s(t)]$; here $z_s(t)$ defines the surface location of the expanding material, where the expansion is due to a reduction in the (number) density (or concentration) as the metal is converted to oxide (refer Table A.1 for pure-phase densities). In the case of a mixed phase where there is a continuous variation in the composition of the material, this results in an advection velocity that depends on the material composition (i.e. $v(z,t)$). To cope with the spatially varying advection velocity (and the changing domain size) we will use a (ζ, t) coordinate system where the ζ coordinate is obtained via a Howarth-Dorodnitsyn transformation that moves with the bulk material:

$$\zeta = \int_{-z_\infty}^{z} \varrho \, \mathrm{d}z \,, \tag{3.13}$$

where ϱ is defined in (3.10f). Here a position defined by $\zeta = \mathit{constant}$ maintains a constant number of uranium atoms/ions (in both U and UO_2) below it as the reaction proceeds. The physical domain $[-z_\infty, z_s(t)]$ is thus mapped to $[0, \zeta_s]$ in the transformed coordinates.

The surface of the material is located at a fixed value of $\zeta = \zeta_s$, where

$$\zeta_s = \int_{-z_\infty}^{z_s(t)} \varrho \, \mathrm{d}z \,. \tag{3.14a}$$

As the total number of uranium atoms is conserved, if the initial state is purely metal represented by $c = O = 0$ and $M = 1$, with the sample surface at the nondimensional location of $z = z_s(0) = 0$ then

$$\zeta_s = \int_{-z_\infty}^{0} \varrho \, \mathrm{d}z \tag{3.14b}$$

$t = 500$ with both relative and absolute error tolerances 10^{-6}, $\Delta z = 0.02$, $\mu = 1$ and $k = 1$.

for all time.

Transformation rules: In terms of this new coordinate system the solution is for (c, M, O, v) as functions of ζ and t, where

$$\frac{\partial}{\partial t} \to \frac{\partial}{\partial t} - \varrho v \frac{\partial}{\partial \zeta}\,, \tag{3.15a}$$

$$\frac{\partial}{\partial z} \to \varrho \frac{\partial}{\partial \zeta}\,, \tag{3.15b}$$

with the first of these following from an integration over z of (3.10g) (assuming that $v = 0$ on $z = -z_\infty$):

$$\int_{-z_\infty}^{z} \left(\frac{\partial \varrho}{\partial t}\right)\bigg|_z \mathrm{d}z + \varrho v = 0 \tag{3.16a}$$

which gives

$$-\varrho v = \int_{-z_\infty}^{z} \left(\frac{\partial \varrho}{\partial t}\right)\bigg|_z \mathrm{d}z = \frac{\partial}{\partial t}\bigg|_z \int_{-z_\infty}^{z} \varrho \,\mathrm{d}z\,. \tag{3.16b}$$

Note that the operators $(\partial/\partial t)|_z$ and $\int \mathrm{d}z$ commute with each other as z is independent of time in the Eulerian coordinates.

In this new (ζ, t) coordinate system, equations (3.10a)–(3.10c) now reduce to

$$\frac{\partial c}{\partial t} = \varrho \frac{\partial}{\partial \zeta}\left(\varrho D_c \frac{\partial c}{\partial \zeta}\right) - 2kcM - \varrho \frac{\partial v}{\partial \zeta} c\,, \tag{3.17a}$$

$$\frac{\partial M}{\partial t} = -kcM \frac{C_a^*}{N_M^*} - \varrho \frac{\partial v}{\partial \zeta} M\,, \tag{3.17b}$$

$$\frac{\partial O}{\partial t} = kcM \frac{C_a^*}{N_O^*} - \varrho \frac{\partial v}{\partial \zeta} O\,, \tag{3.17c}$$

where D_c, which is a function of the metal concentration, is determined from (3.10e). Here the advection terms (proportional to v) are removed in the new (ζ) coordinate, but the expansion of the bulk material during the phase change leads to additional source/sink terms proportional to v_ζ.

From the last two equations, or equivalently (3.10g), together with the requirement of $O + M = 1$ leads to

$$\varrho \frac{\partial v}{\partial \zeta} = kcM \frac{C_a^*}{N_M^*} \left(\frac{N_M^*}{N_O^*} - 1 \right) . \tag{3.18}$$

So we can determine the velocity field of the mixed-phase material explicitly in terms of the reacting material and the associated change in (number) density between the phases. Hence we are left to solve

$$\frac{\partial c}{\partial t} = \varrho \frac{\partial}{\partial \zeta} \left(\varrho D_c \frac{\partial c}{\partial \zeta} \right) - kcM \left(2 + c \left(\frac{C_a^*}{N_O^*} - \frac{C_a^*}{N_M^*} \right) \right) , \tag{3.19a}$$

$$\frac{\partial M}{\partial t} = -kcM \frac{C_a^*}{N_M^*} \left(1 + M \left(\frac{N_M^*}{N_O^*} - 1 \right) \right) , \tag{3.19b}$$

$$\frac{\partial O}{\partial t} = kcM \frac{C_a^*}{N_O^*} \left(1 - O \left(1 - \frac{N_O^*}{N_M^*} \right) \right) , \tag{3.19c}$$

with the effective diffusivity D_c given by (3.10e), subject to the following initial and boundary conditions. The initial conditions are associated with an initial state entirely in the U phase:

$$M(\zeta, t = 0) = 1 , \quad O(\zeta, t = 0) = 0 , \quad c(\zeta, t = 0) = 0 , \tag{3.20a}$$

and the boundary conditions for the diffusing species are

$$c(\zeta = \zeta_s, t) = 1 , \quad c(\zeta = 0, t) = 0. \tag{3.20b}$$

The system (3.19) subject to initial and boundary conditions (3.20) is solved by the method of lines in MATLAB using `ode15s` which is found to be more efficient than `ode45`. The solution of the mixed-phase model is validated against the Stefan model for large k and/or large t and is presented in § 3.2.

Inverting the coordinate transformation provides the solution in the physical space:

$$z = -z_\infty + \int_0^\zeta \frac{1}{\varrho} \, \mathrm{d}\zeta . \tag{3.21}$$

3.2 Results for the mixed-phase dry-air model

The numerical results for the mixed-phase dry-air oxidation model for both the cases that include and exclude density changes are discussed in this section. The results are then compared either with the analytical solution (see §§§ 2.2.1.3) for the case excluding density change or with the Stefan solution in the limit of a suitably large reaction rate constant ($k \to \infty$) or equivalently in the large-time limit ($t \to \infty$). It will be seen in this section that the mixed-phase model is consistent with the Stefan model in the appropriate limits. To calculate the oxide thickness, we define the center of the reaction front as the location ($z = z_1(t)$) where the reaction rate,

$$\mathcal{R}(z,t) = kcM \tag{3.22}$$

is maximised. The oxide thickness is then calculated as the distance (in the z coordinate) from the surface location $z_s(t)$ to the location of the reaction front center, $z_1(t)$; that is the oxide thickness $\Delta_O = z_s(t) - z_1(t)$. As a reminder, a reaction front in a mixed-phase model is a region where there is a transition from one phase to the other. The reaction rate (3.22) is plotted in Figure 3.1 and the location of the maximum reaction rate is at $z_1(t) = -0.4247$ for $t = 5$.

3.2.1 Dry-air oxidation without density change

Subfigure 3.2(a) shows the evolution of oxide thickness with time for the rate constant values $k = 1\,, 10\,, 100$; subfigure 3.2(b) depicts the same plot on a log-log axes. It can be seen that the mixed-phase model agrees with the discrete-layer/Stefan model at a suitably large t or k. The numerical solution is calculated using the method of lines which has been implemented using MATLAB (`ode15s` solver).

We define a quantity $\lambda = C_a^*/(2\,N_M^*)$ for the sake of comparison with the Stefan solution (obtained from solving (2.51)). Now, the evolution of the oxide thickness with time is plotted in Figure 3.3 for different values of λ. Smaller values of λ result in a reduction in oxide thickness (at fixed values of time) as we may expect. Here, the analytical solution (given by (2.37c)) with the appropriate surface concentration of the diffusing species is compared with the solution obtained by solving (3.12). A good agreement between the two solutions

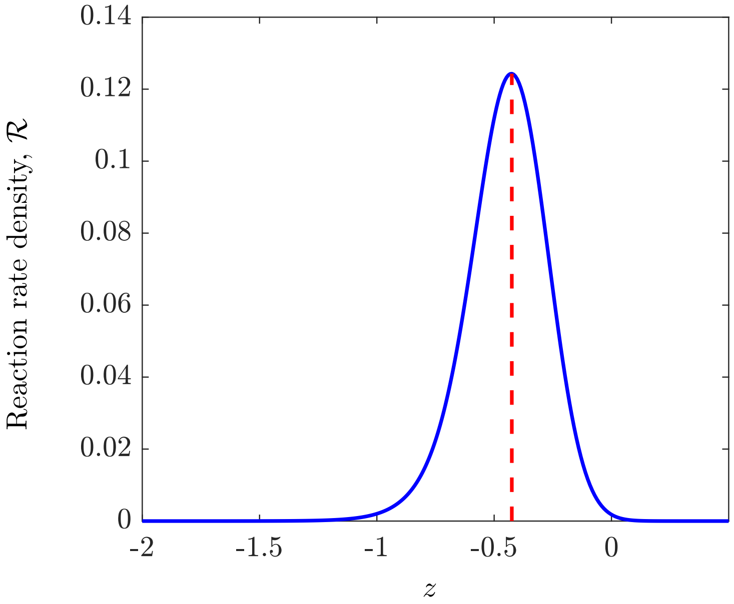

Figure 3.1: Variation of the reaction rate (3.22) with the z coordinate at a nondimensional time $t = 5$. The center of the reaction front ($z = z_1(t)$) is defined as the location of the maximum reaction rate. Parameters include: $C_a^* = 5 \times 10^{27}$ ions/m^3, $\mu = 1\,, k = 5\,, z_s(t = 5) = 0.4997\,, z_1(t = 5) = -0.4247\,, z_\infty = -5$ and the number densities of the metal and the oxide are given in Table A.1.

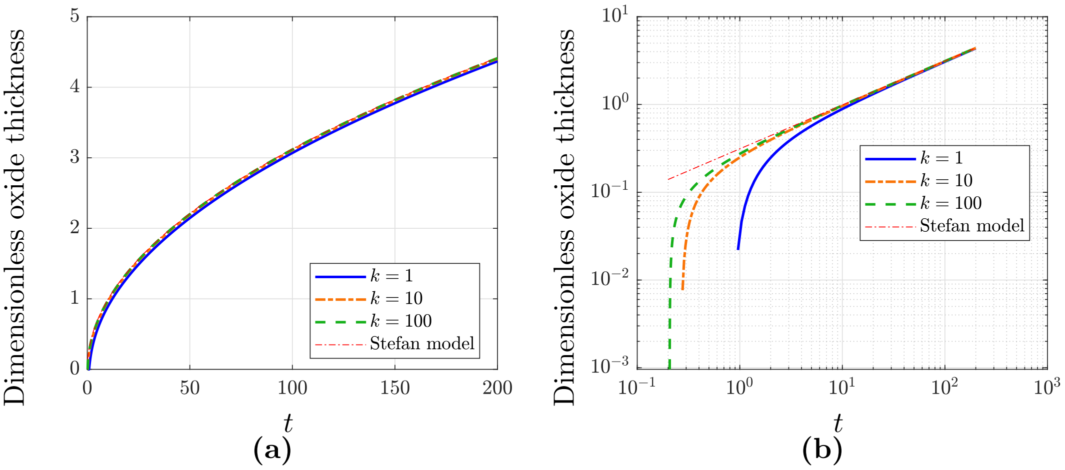

(a) **(b)**

Figure 3.2: Evolution of oxide thickness (Δ_O) with time for the mixed-phase (without density change) model (given by (3.12)) and Stefan model (obtained from the solution of (2.51)) for dry-air oxidation. Other parameters include: $\lambda = C_a^*/(2\,N_M^*) = 0.05$ and $\mu = 1$.

can be observed.

Figure 3.4 depicts the influence of the diffusivity ratio $\mu = D_c^{M*}/D_c^{O*}$ on the oxide growth. It can be seen that an increase in the diffusivity ratio μ results

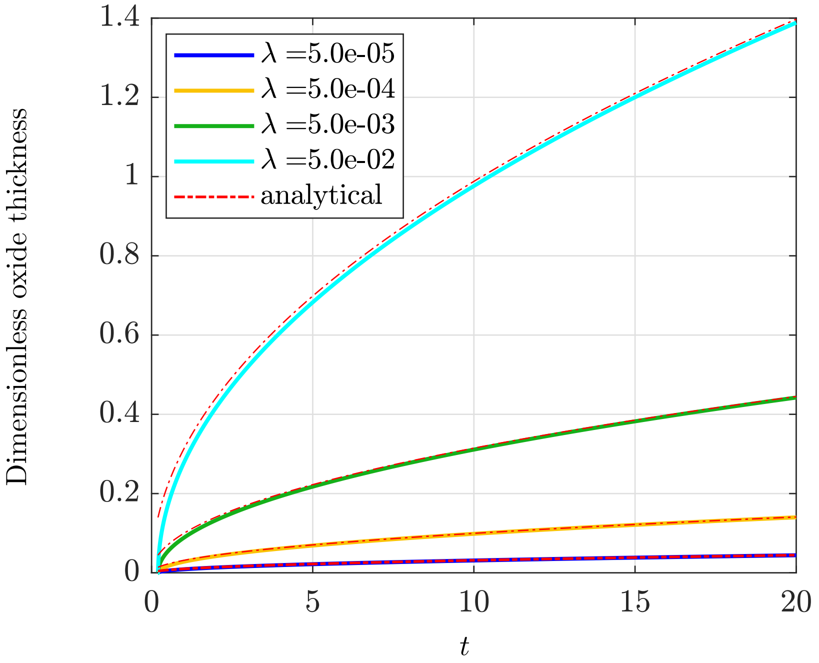

Figure 3.3: Comparison of the mixed-phase (without density change) (defined by (3.12)) and analytical (given by (2.37c)) solutions for the oxide growth with time for different values of $\lambda = C_a^*/(2\,N_M^*)$. Other parameters include: $k = 500\,, \mu = 1$.

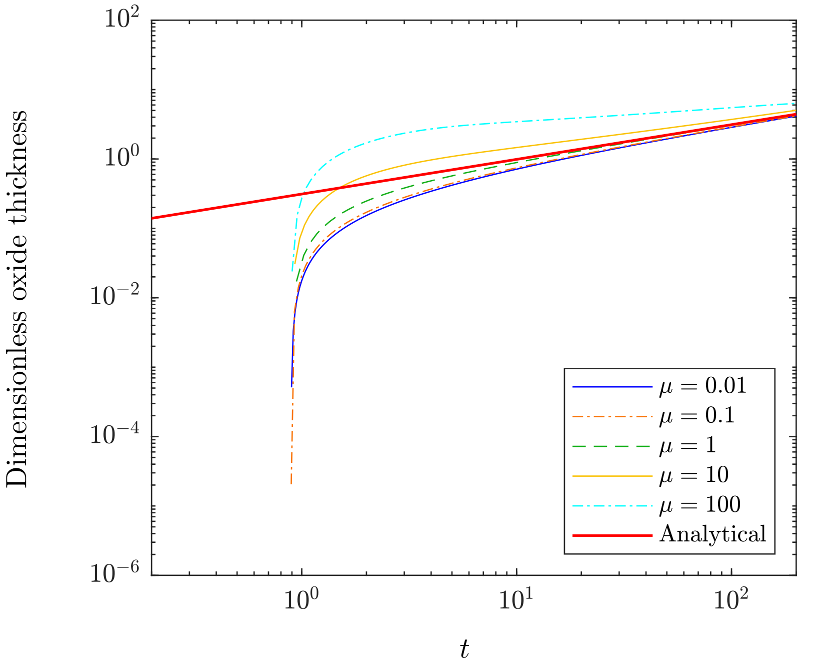

Figure 3.4: Evolution of the oxide thickness with time obtained by solving (3.12) (no density change) for different values of the diffusivity ratio, $\mu = D_c^{M*}/D_c^{O*}$. Other parameters include: $k = 500\,, \lambda = 0.05$.

in an initial increase in the oxide thickness as more metal is converted to oxide, and vice-versa. However, at a suitably large time (not depicted in the figure), the solution obtained from the mixed-phase model approaches the Stefan solution which is independent of μ.

3.2.2 Dry-air oxidation with density change

For the case including density change in the mixed-phase model, we solve the system (3.19) subject to the appropriate boundary and initial conditions and the results are presented in this section. A good agreement between the mixed-phase and the Stefan solutions for different values of the diffusivity ratio μ and a suitably large rate constant $k = 500$ can be observed in Figure 3.5.

Similarly, Figure 3.6 shows the oxide growth with time for different rate constant values k where the solutions obtained from the mixed-phase model (3.19) and the Stefan model are compared. As it can be seen, the solution from the mixed-phase model approaches the Stefan solution as $k \to \infty$ or as $t \to \infty$.

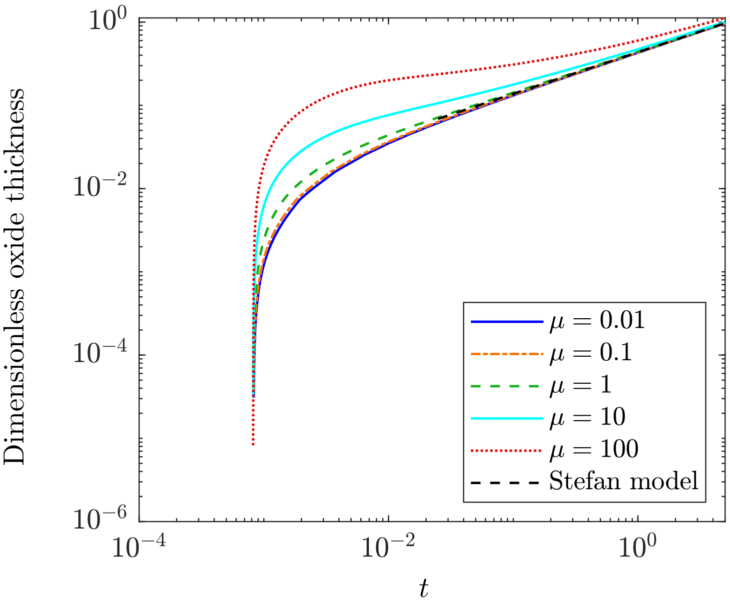

Figure 3.5: Comparison of the oxide growth with time for the mixed-phase model (3.19) and the Stefan model including density change for different values of the diffusivity ratio $\mu = 0.01\,, 0.1\,, 1\,, 10\,, 100$. Other parameters include: $k = 500\,, \lambda = 0.05$.

Figure 3.7 depicts the concentration profiles for the different diffusing and nondiffusing species at times $t = 5$ and $t = 50$, and a reaction front propagating to the left with time as more metal is consumed to produce the oxide. The

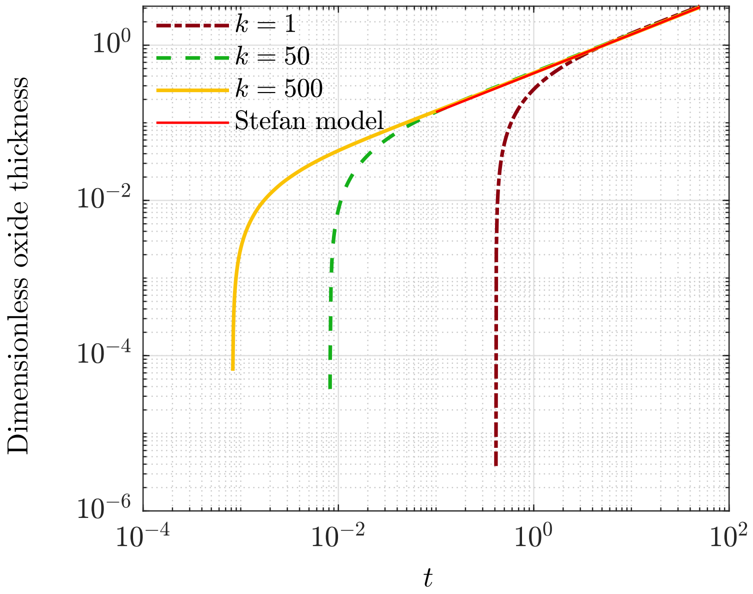

Figure 3.6: Evolution of the oxide thickness with time obtained by solving mixed-phase sytem (3.19) for different rate constant values k and its comparison with the Stefan model. Other parameters include: $\lambda = 0.05\,, \mu = 1$.

steep transition region in the concentration profiles where the metal is converted to oxide phase is called the 'reaction front'. The width of the reaction front is a function of the reaction rate constant. Higher values of the rate constant results in a thinner reaction front as is depicted in Figure 3.8. We will return to investigate the details of the reaction fronts in the next chapter.

Having verified our mixed-phase formulation (which can handle an expanding or advecting medium) by comparing with the discrete-layer Stefan model for the oxidation kinetics of uranium in dry air, we now extend our model to study the more complex oxidation of uranium in water vapour, which is presented in Chapter 4.

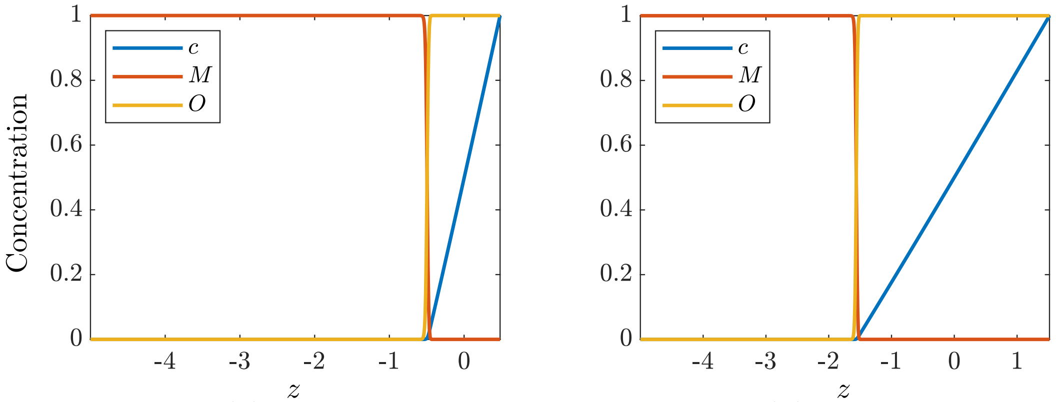

(a) $t = 5$ **(b)** $t = 50$

Figure 3.7: Concentration profiles of the diffusing and nondiffusing species at different times (a) $t = 5$ and (b) $t = 50$ showing the reaction front propagating to the left. The parameters include: $\lambda = 0.05\,, \mu = 1\,, k = 500$. The plot shows the material domain extending from $-z_\infty = -5$ to $z_s(t)$ with $z_s(t = 5) = 0.48$ and $z_s(t = 50) = 1.52$.

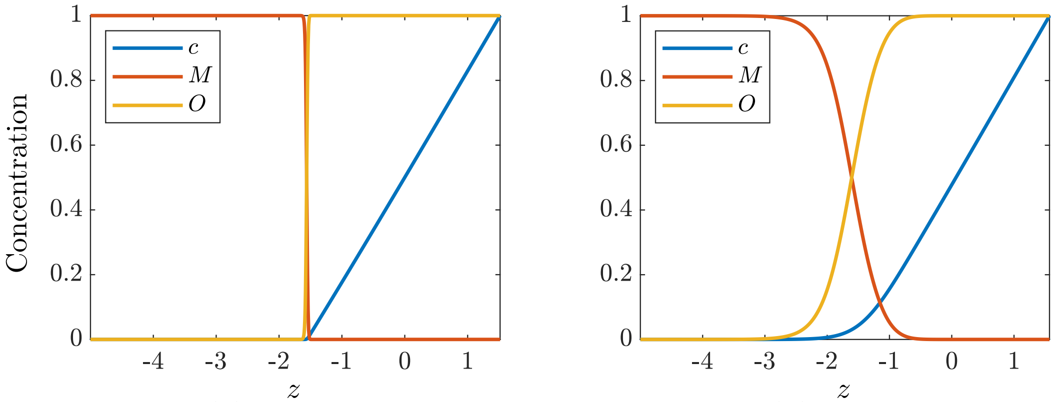

(a) $k = 500$ **(b)** $k = 1$

Figure 3.8: Concentration profiles of the diffusing and nondiffusing species at time $t = 50$ for different rate constant values (a) $k = 500$ and (b) $k = 1$. Other parameters include: $\lambda = 0.05\,, \mu = 1$ with $-z_\infty = -5\,, z_s(t = 50) = 1.52$ and the location of the reaction front, $z_1(t = 50) = -1.55$ for $k = 500\,, z_1(t = 50) = -1.42$ for $k = 1$.

Chapter 4

Early-stage corrosion of uranium in water vapour

This chapter forms the basis of material published in the paper, "Asymptotics of coupled reaction-diffusing fronts with multiple static and diffusing reactants: uranium oxidation in water vapor" by Natchiar, Hewitt, Monks and Morall in SIAM Journal on Applied Mathematics (Monisha Natchiar et al., 2020).

4.1 Introduction

In this chapter, we discuss our mathematical model for the early-stage oxidation of uranium by water vapour which has been derived based on a reaction mechanism proposed by Glascott and Findlay (2019) (outlined in § 1.2.6). Here, '*early-stage*' oxidation refers to oxidation before cracking and spalling of the surface oxide; note that early-stage behaviour is not the same as small time behaviour. Recent atom-probe tomography studies by Martin et al. (2016) has confirmed that oxidation in a water-vapour environment occurs via a different reaction mechanism compared to that in dry air/oxygen. In the water-vapour oxidation of uranium, uranium hydride (UH_3) is formed as an intermediate, which further reacts to form the uranium oxide (UO_2) product. As already discussed in Chapter 1, in a water-vapour environment, hydroxide ions (OH^-) from water vapour ($H_2O_{(v)}$) constitute the diffusing species as opposed to oxygen ions (O^{2-}) in a dry-air environment. However, the modelling approach for water-vapour oxidation remains the same as that of the mixed-phase dry-air model (see §§ 3.1.3).

The system is modelled as a diffuse-interface (or mixed-phase) model that includes density changes, as the underpinning chemistry/physics of water-vapour oxidation is too complex to model it as a (discrete-layer) Stefan problem. The density/phase changes in the mixed-phase model give rise to a moving domain as a result of advection or material expansion. We therefore adopt the same solution strategy as tested and verified in §§ 3.1.3 to solve the problem in this moving domain. In addition, we neglect the elaborate surface processes such as adsorption, desorption and the surface reactions and replace them with approximate simple Dirichlet boundary conditions at the surface. An asymptotic analysis is performed to deduce the behaviour at large times or for high reaction rate constants. We know from Chapter 3 that the "reaction fronts" are localised for sufficiently large reaction rate constants and/or large times, and therefore we can recover an equivalent "discrete-layer" model through an asymptotic analysis. The numerical results obtained are discussed in §§ 4.2.4 and their comparison with the large-time asymptotic predictions are discussed in §§ 4.2.6. The parameter space is explored and the effect of different parameters such as the diffusivities, material densities and the rate constants of the reactions on the oxidation kinetics is discussed.

4.2 A diffuse-interface model

Similar to the mixed-phase model for dry-air oxidation, in a mixed-phase (diffuse-interface) model for water-vapour oxidation, we represent the distribution of phases (nondiffusing species) as a continuum instead of discrete layers. In this chapter, we use the term '*species*' to denote both the diffusing and nondiffusing components in the system, whereas the term '*phase*' is used exclusively for the nondiffusing components. Here, the physical variables such as concentration, advection velocity, and so on are continuous functions of position and time in the entire material domain. The dimensionless concentrations or volume fractions determine the material composition; for example, a nondimensional concentration of $M = 1$ denotes a pure metal phase. This model can therefore take into account transition regions (also called *reaction fronts* where reaction terms balance with the diffusion term; see Bazant and Stone, 2000) between the different pure phases. That is, here *reaction fronts* separate regions of homogeneous compositions referred to as the 'diffusion' layers, rather than the *sharp interfaces* between the pure phases that are a characteristic feature of the Stefan model. In this alternative approach, we consider that there are ‘mixed’ regions which are a more realistic representation (see the experimental studies of Martin et al., 2016) than the discrete-phase Stefan model.

4.2.1 Formulation

In accordance with the reaction scheme discussed in § 1.2.6, we will consider the diffusion of hydroxide ions (OH^-) through the surface oxide, followed by reaction of the hydroxide ions with the hydride (UH_3) to form uranium dioxide (UO_2) and hydrogen radicals ($H^\bullet$). The further diffusion of hydrogen radicals into the metal (U) regenerates the hydride phase. The reaction-induced phase changes are associated with density changes and therefore volume expansion in the material, thus contributing to a local time-varying advection velocity $v^*(z^*, t^*)$. To describe the evolution of such a system, we will denote the (number) concentrations of the species, with lower-case letters representing the diffusing and upper-case letters the nondiffusing species, as (where the asterisk denotes a dimensional quantity):

$$c^* \equiv [\mathrm{OH}^-], \quad h^* \equiv [\mathrm{H}^\bullet],$$
$$O^* \equiv [\mathrm{UO_2}], \quad H^* \equiv [\mathrm{UH_3}], \quad M^* \equiv [\mathrm{U}]\,.$$

The mathematical description of the oxidative corrosion of uranium by water vapour can then be written as a system of one-dimensional coupled reaction-diffusion-advection partial differential equations:

$$\frac{\partial c^*}{\partial t^*} + \frac{\partial}{\partial z^*}(v^* c^*) = \frac{\partial}{\partial z^*}\left(D_c^* \frac{\partial c^*}{\partial z^*}\right) + r_c^*\,, \tag{4.1a}$$

$$\frac{\partial h^*}{\partial t^*} + \frac{\partial}{\partial z^*}(v^* h^*) = \frac{\partial}{\partial z^*}\left(D_h^* \frac{\partial h^*}{\partial z^*}\right) + r_h^*\,, \tag{4.1b}$$

$$\frac{\partial O^*}{\partial t^*} + \frac{\partial}{\partial z^*}(v^* O^*) = r_O^*\,, \tag{4.1c}$$

$$\frac{\partial H^*}{\partial t^*} + \frac{\partial}{\partial z^*}(v^* H^*) = r_H^*\,, \tag{4.1d}$$

$$\frac{\partial M^*}{\partial t^*} + \frac{\partial}{\partial z^*}(v^* M^*) = r_M^*\,, \tag{4.1e}$$

subject to the boundary conditions:

$$c^*(z_s^*, t^*) = C_a^*, \quad c^*(-z_\infty^*, t^*) = 0, \quad h^*(z_s^*, t^*) = 0, \quad h^*(-z_\infty^*, t^*) = 0,$$
$$O(-z_\infty^*, t^*) = 0, \quad H(-z_\infty^*, t^*) = 0, \quad M(-z_\infty^*, t^*) = N_M^*, \quad v^*(-z_\infty^*, t^*) = 0\,, \tag{4.2}$$

and appropriate initial conditions which will be discussed after nondimensionalising the above system of equations.

Here for example, $c^*(z^*, t^*)$ is the local concentration of OH$^-$ ions, $v^*(z^*, t^*)$ is the local advection velocity, $D^*_{c,h}(z^*, t^*)$ are the effective diffusivities of species OH$^-$, H$^\bullet$ respectively and r^*_i denotes the local reaction rate of species i, with $i = c, h, O, H, M$. The material domain ranges from $z^* = -z^*_\infty$ (representing a position far into the metal i.e. the bottom truncation of the domain) to $z^* = z^*_s$ (at the material surface exposed to water vapour that dissociates into H$^+$ and OH$^-$). The surface concentration of OH$^-$ is taken to be C^*_a. The effective diffusivities are functions of the local material composition and given by (4.3).

It is worth noting that the hydrogen radical concentration at the surface is zero as we assume that they instantaneously recombine to form gaseous hydrogen at the surface. The boundary conditions at $z^* = -z^*_\infty$ represent far-field conditions away from the oxide surface and into the metal. The initial conditions that have been considered are representative of the experimental observations and will be discussed later. For example, a thin (of the order of a few nm) oxide layer has always been observed in the experiments (see Baker, Less, and Orman, 1966a; Martin et al., 2016 and Banos and Scott, 2020) irrespective of the method of preparation of the sample.

Effective diffusivities D^*_c and D^*_h: The effective diffusivities in the material are assumed to be the weighted sum of the diffusivities in the pure phases[a] (similar to that in (3.7d)):

$$\begin{aligned} D^*_c &= M D^{M*}_c + O D^{O*}_c + H D^{H*}_c \,, \\ D^*_h &= M D^{M*}_h + O D^{O*}_h + H D^{H*}_h \,, \end{aligned} \tag{4.3}$$

where $D^{j^*}_i$ represents the dimensional diffusivity of species i in phase j, and M , O, H are the volume fractions of the metal, oxide and hydride respectively. We also assume that the effective diffusivities of OH$^-$ and H$^\bullet$ are independent of c, h at the (small) concentration levels of interest.

Based on the proposed reaction scheme (refer § 1.2.6), we apply the *rate law* for

---

[a] Here 'pure' phases mean the pure metal, oxide and hydride phases with (number) concentrations given by N^*_M , N^*_O , N^*_H respectively (see §§§ 4.2.1.1).

elementary chemical reactions, also called the *mean-field approximation*[b] to write the reaction rates of the different species as:

$$r_c^* = -2k_{cH}^*\, c^{*2} H^*\,, \tag{4.4a}$$

$$r_h^* = 5k_{cH}^*\, c^{*2} H^* - 3k_{hM}^* h^{*3} M^*\,, \tag{4.4b}$$

$$r_H^* = k_{hM}^*\, h^{*3} M^* - k_{cH}^* c^{*2} H^*\,, \tag{4.4c}$$

$$r_M^* = -k_{hM}^*\, h^{*3} M^*\,, \tag{4.4d}$$

$$r_O^* = k_{cH}^*\, c^{*2} H^*\,. \tag{4.4e}$$

Here, k_{cH}^* and k_{hM}^* represent the *rate constants* of the elementary reactions that vary with temperature as defined by the Arrhenius equation[c]. However, there is not much information available in the literature on these rate constant values; we will return to this issue of practically relevant values later in Chapter 5. The reaction rate r_i^* is negative if there is depletion (*sink* term) and positive if there is formation (*source* term) of species i. The coefficients in the reaction (source/sink) terms arise from the stoichiometry of the elementary reaction steps, where for example, 2 molecules/ions of OH^- react with 1 molecule of UH_3 in a reaction with rate constant k_{cH}^* to produce 5 hydrogen radicals and 1 UO_2 molecule.

We assume that the recombination of hydrogen radicals to form hydrogen gas (H_2) occurs only at the material surface and hence is not accounted for in the bulk reactions. This assumption finds support in the literature (Ao et al., 2016) as hydrogen is known to exist only in three forms in the oxide (UO_2), viz., as hydride ion, proton in hydroxide ion or as hydrogen radical. In accordance with the proposed reaction scheme and for the sake of simplicity, we assume that hydrogen exists in the form of radicals, the recombination of which can happen only at the active sites on the oxide surface. Furthermore, we neglect the surface reaction of water vapour with the oxide lattice (rate constant k_s^* in § 1.2.6) as a simplistic first approach. Also, we neglect the reaction of surface hydroxide ions with the electrons to form hydrogen gas (rate constant k_e^*).

---

[b] Refer § 3.1 for a detailed explanation of the mean-field approximation, which has been used for the dry-air problem.

[c] The Arrhenius equation is defined as $k^* = A^* \exp(-E_a^*/(R_g^* T^*))$, where k^* is the dimensional rate constant at temperature T^* for a reaction with activation energy E_a^*, A^* is the frequency factor that gives the frequency of collisions, and R_g^* is the universal gas constant.

4.2.1.1 Nondimensionalisation

The pure-phase number concentrations of U, UO_2 and UH_3 are respectively,

$$\begin{aligned} N_M^* &= 4.8235 \cdot 10^{28} \text{ no. of U atoms/m}^3\,, \\ N_O^* &= 2.4471 \cdot 10^{28} \text{ no. of UO}_2 \text{ molecules/m}^3\,, \\ N_H^* &= 2.7366 \cdot 10^{28} \text{ no. of UH}_3 \text{ molecules/m}^3\,. \end{aligned} \tag{4.5}$$

The concentrations of the nondiffusing phases are nondimensionalised via

$$H^* = N_H^*\, H(z,t)\,, \quad M^* = N_M^*\, M(z,t)\,, \quad O^* = N_O^*\, O(z,t)\,. \tag{4.6}$$

For the diffusing phases, we nondimensionalise using the surface concentration C_a^* of OH^-, which is assumed to be known from the external gas state:

$$c^* = C_a^*\, c(z,t)\,, \quad h^* = C_a^*\, h(z,t)\,. \tag{4.7}$$

Now using a reference length scale L_{ref}^* and diffusion coefficient D_{ref}^*, we introduce further dimensionless quantities:

$$z^* = L_{ref}^*\, z\,, \quad t^* = \frac{L_{ref}^{*2}}{D_{ref}^*}\, t\,, \quad v^* = \frac{D_{ref}^*}{L_{ref}^*} v(z,t)\,. \tag{4.8}$$

The resulting dimensionless form of (4.1) is now

$$\frac{\partial c}{\partial t} + \frac{\partial}{\partial z}(vc) = \frac{\partial}{\partial z}\left(D_c \frac{\partial c}{\partial z}\right) + r_c\,, \tag{4.9a}$$

$$\frac{\partial h}{\partial t} + \frac{\partial}{\partial z}(vh) = \frac{\partial}{\partial z}\left(D_h \frac{\partial h}{\partial z}\right) + r_h\,, \tag{4.9b}$$

$$\frac{\partial H}{\partial t} + \frac{\partial}{\partial z}(vH) = r_H\,, \tag{4.9c}$$

$$\frac{\partial M}{\partial t} + \frac{\partial}{\partial z}(vM) = r_M\,, \tag{4.9d}$$

$$\frac{\partial O}{\partial t} + \frac{\partial}{\partial z}(vO) = r_O\,. \tag{4.9e}$$

Note that the term ‘concentration’ will henceforth be used to refer to the ‘number concentration’ of the respective species.

The nondimensional system (4.9) is now subject to source/sink terms of the form:

$$r_c = -2\left\{\frac{k^*_{cH}C^*_a N^*_H L^{*2}_{ref}}{D^*_{ref}}\right\} c^2 H\,, \tag{4.9f}$$

$$r_h = 5\left\{\frac{k^*_{cH}C^*_a N^*_H L^{*2}_{ref}}{D^*_{ref}}\right\} c^2 H - 3\left\{\frac{k^*_{hM}C^{*2}_a N^*_M L^{*2}_{ref}}{D^*_{ref}}\right\} h^3 M\,, \tag{4.9g}$$

$$r_H = \left\{\frac{k^*_{hM}C^{*2}_a N^*_M L^{*2}_{ref}}{D^*_{ref}}\right\}\left(\frac{C^*_a}{N^*_H}\right) h^3 M - \left\{\frac{k^*_{cH}C^*_a N^*_H L^{*2}_{ref}}{D^*_{ref}}\right\}\left(\frac{C^*_a}{N^*_H}\right) c^2 H\,, \tag{4.9h}$$

$$r_M = -\left\{\frac{k^*_{hM}C^{*2}_a N^*_M L^{*2}_{ref}}{D^*_{ref}}\right\}\left(\frac{C^*_a}{N^*_M}\right) h^3 M\,, \tag{4.9i}$$

$$r_O = \left\{\frac{k^*_{cH}C^*_a N^*_H L^{*2}_{ref}}{D^*_{ref}}\right\}\left(\frac{C^*_a}{N^*_O}\right) c^2 H\,, \tag{4.9j}$$

where the bracketed terms are all dimensionless ratios, and we can introduce the associated dimensionless parameters:

$$\epsilon = \frac{C^*_a}{N^*_M}\,, \quad k_{cH} = \left\{\frac{k^*_{cH}C^*_a N^*_H L^{*2}_{ref}}{D^*_{ref}}\right\}\,, \quad k_{hM} = \left\{\frac{k^*_{hM}C^{*2}_a N^*_M L^{*2}_{ref}}{D^*_{ref}}\right\}\,. \tag{4.9k}$$

Here ϵ is a small parameter in the model which is the ratio of the surface concentration of the diffusing species to the concentration of the pure metal phase; k_{cH} and k_{hM} are the nondimensional reaction rate constants of the reactions between OH^- and UH_3 (reaction 1), and between U and $H^\bullet$ (reaction 2) respectively. These are essentially Damköhler numbers for each reaction, based on the reference length scale and diffusivity.

With these definitions, (4.9f) - (4.9j) become

$$r_c = -2k_{cH}\, c^2 H\,, \tag{4.9l}$$

$$r_h = 5k_{cH}\, c^2 H - 3k_{hM}\, h^3 M\,, \tag{4.9m}$$

$$r_H = \epsilon(k_{hM}\, h^3 M - k_{cH}\, c^2 H)\left(\frac{N^*_M}{N^*_H}\right)\,, \tag{4.9n}$$

$$r_M = -\epsilon k_{hM}\, h^3 M\,, \tag{4.9o}$$

$$r_O = \epsilon k_{cH}\left(\frac{N^*_M}{N^*_O}\right) c^2 H\,. \tag{4.9p}$$

Since H, M, O are in essence the volume fractions of the nondiffusing phases, we have $H+M+O=1$ and therefore the advection velocity resulting from material expansion can be determined from the addition of equations (4.9c), (4.9d) and (4.9e):

$$\frac{\partial v}{\partial z} = \epsilon k_{hM} h^3 M \left(\frac{N_M^*}{N_H^*} - 1 \right) + \epsilon k_{cH} c^2 H \left(\frac{N_M^*}{N_O^*} - \frac{N_M^*}{N_H^*} \right) . \tag{4.9q}$$

For ambient conditions we expect $\epsilon \ll 1$; that is, we expect the surface concentration of the diffusing OH^- species (C_a^*) to be much less than the pure metal concentration N_M^*. The atmospheric concentration of water vapour is found from the saturation vapour pressure of water (P_s^*) at a particular temperature using the ideal gas law. We use the (dimensional) Arden Buck equation (Buck, 1981) to calculate the saturation vapour pressure of water P_s^* (in kPa) as a function of temperature T^* (in °C):

$$P_s^* = 0.61121 \text{ kPa} \exp \left[\left(18.678 - \frac{T^*}{234.5 \text{ °C}} \right) \left(\frac{T^*}{257.14 \text{ °C } + T^*} \right) \right] . \tag{4.10}$$

For example, at 22°C, the saturation vapour pressure calculated using (4.10) is $P_s^* = 2.6442$ kPa. Therefore at 60% RH[d], the water vapour pressure is calculated to be 1.5865 kPa, for which the concentration of water vapour using the ideal gas law is given as

$$\frac{n^*}{V^*} = \frac{P^*}{R^* T^*} = \frac{1.5865 \cdot 10^3 \text{ Pa}}{8.314 \text{ J/mol K } \cdot 295 \text{ K}} = 0.6468 \text{ mol/m}^3 \approx 11.6 \text{ g/m}^3 . \tag{4.11}$$

Thus at 22°C and 60% RH, there is approximately 11.6 g/m^3 of water vapour in air, which is equivalent to approximately 0.65 mol/m^3 of water vapour. We take this value to be the atmospheric concentration of pure $H_2O_{(v)}$ in our model, assuming that the concentration of dry air (i.e. O_2, N_2) is zero. If we naively assume that the surface concentration of OH^- matches the atmospheric concentration of water vapour, then a molar density for U of $8 \cdot 10^4$ mol/m^3, leads to

$$\epsilon \approx 8.13 \cdot 10^{-6} \ll 1 . \tag{4.12}$$

---

[d] Note that the percentage of relative humidity is only used to obtain a representative amount of water vapour under ambient conditions. It should not be assumed that a moist air environment (water vapour including dry-air/oxygen) has been considered in this model.

This suggests that, even allowing for more complex adsorption mechanisms, the relative concentration of OH^- may still be much less than unity for ambient conditions. Hence ϵ is a small parameter in the model, which can be made use of whilst numerically solving the system (4.9). Figure 4.1 shows ϵ as a function of temperature for increasing (bottom to top) values of relative humidity[e]. Note that Figure 4.1 follows the familiar pattern of the Psychrometric Chart widely used by engineers to analyse the thermodynamic and physical properties of vapour-gas mixtures.

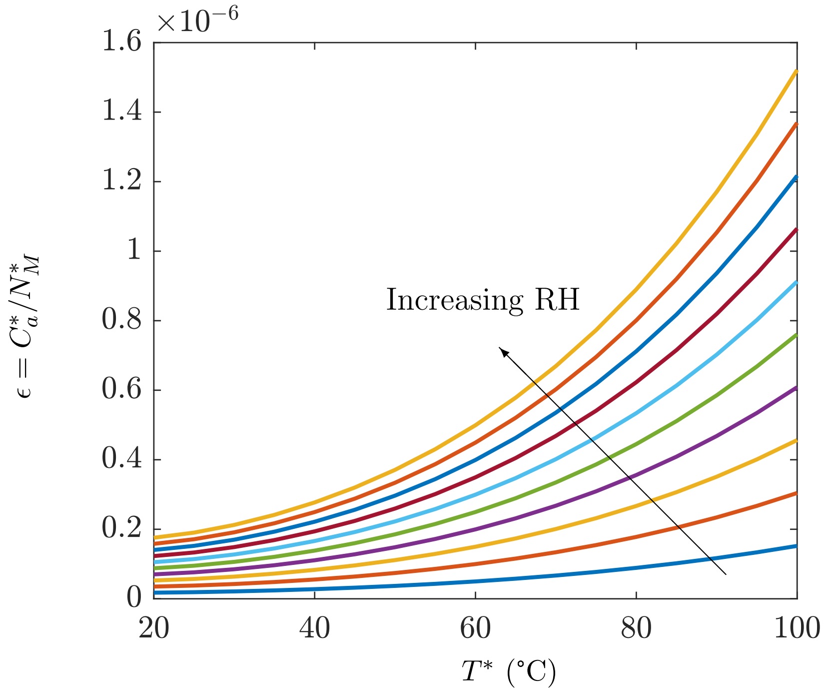

Figure 4.1: Variation of the relative surface concentration of OH^-, $\epsilon = C_a^*/N_M^*$ as a function of temperature and relative humidity calculated using (4.10) and (4.11); we have assumed the surface concentration of OH^- to be equal to the atmospheric concentration of water vapour. The relative humidity is varied from 0.1 to 1 in steps of 0.1 (bottom to top).

4.2.2 Model reduction

4.2.2.1 Choice of reference length scale (L_{ref}^*)

As the choice of length scale is arbitrary, we can choose L_{ref}^* to make the rate constant $k_{hM} = 1$, such that k_{cH} remains as the only rate constant parameter

---

[e] Although the terminology relative humidity has been retained, it should not be assumed that dry air (O_2,N_2, etc.) is present. It has only been used for ease of comparison.

in the model in addition to the diffusivity parameters. However, this reduction in the number of parameters by one does not remove C_a^* from the problem; C_a^* remains hidden in the other reaction rate constant k_{cH}. The choice of L_{ref}^* that makes $k_{hM} = 1$ is

$$L_{ref}^* = \left(\frac{D_{ref}^*}{k_{hM}^* C_a^{*2} N_M^*} \right)^{\frac{1}{2}} , \tag{4.13}$$

which in turn leads to

$$k_{cH} = \frac{k_{cH}^* N_H^*}{k_{hM}^* C_a^* N_M^*} . \tag{4.14}$$

4.2.2.2 Slow timescale

We can make use of the multiple time scales occurring in the model to further reduce the model. Considering ϵ to be a small parameter in the model, we introduce a long time scale (or slow-time variable)

$$\tau = \epsilon t , \tag{4.15}$$

such that $\tau = \mathcal{O}(1)$, and hence

$$\frac{\partial}{\partial t} \to \epsilon \frac{\partial}{\partial \tau} . \tag{4.16}$$

The dimensionless system (4.9) is then transformed to give a nonlinear (moving-boundary) problem defined by

$$\epsilon \left(\frac{\partial c}{\partial \tau} + \frac{\partial}{\partial z} (Vc) \right) = \frac{\partial}{\partial z} \left(D_c \frac{\partial c}{\partial z} \right) - 2k_{cH}\, c^2 H , \tag{4.17a}$$

$$\epsilon \left(\frac{\partial h}{\partial \tau} + \frac{\partial}{\partial z} (Vh) \right) = \frac{\partial}{\partial z} \left(D_h \frac{\partial h}{\partial z} \right) + 5k_{cH}\, c^2 H - 3k_{hM}\, h^3 M , \tag{4.17b}$$

$$\frac{\partial H}{\partial \tau} + \frac{\partial}{\partial z} (VH) = (k_{hM}\, h^3 M - k_{cH}\, c^2 H) \left(\frac{N_M^*}{N_H^*} \right) , \tag{4.17c}$$

$$\frac{\partial M}{\partial \tau} + \frac{\partial}{\partial z} (VM) = -k_{hM}\, h^3 M , \tag{4.17d}$$

$$\frac{\partial O}{\partial \tau} + \frac{\partial}{\partial z} (VO) = k_{cH}\, c^2 H \left(\frac{N_M^*}{N_O^*} \right) , \tag{4.17e}$$

where $v = \epsilon V$ (V is the velocity measured on the slow-time scale) and k_{hM} can be set to unity by choice of L_{ref}^*.

The rescaled velocity is now determined from

$$\frac{\partial V}{\partial z} = k_{hM}\, h^3 M \left(\frac{N_M^*}{N_H^*} - 1\right) + k_{cH}\, c^2 H \left(\frac{N_M^*}{N_O^*} - \frac{N_M^*}{N_H^*}\right) . \tag{4.17f}$$

The small parameter ϵ multiplying the time derivatives in equations (4.17a) and (4.17b) implies that the diffusion is essentially quasi-steady as $\epsilon \to 0$, i.e. an $\mathcal{O}(1)$ change in the concentration of the diffusing phases $(c\,, h)$ produces only an ϵ change in the concentration of the nondiffusing phases $(O\,, H\,, M)$. Hence the model is reduced using the quasi-steady approximation by considering $\epsilon = 0$ and is solved using a numerical strategy as detailed in §§ 4.2.3.

4.2.3 Solution strategy for the moving domain

4.2.3.1 Howarth-Dorodnitsyn transformation

We now employ a coordinate transformation that is frequently used in reducing the compressible flow equations to a simpler form equivalent to that for an incompressible fluid. As was done for the dry-air mixed-phase problem (see §§ 3.1.3), the Howarth-Dorodnitsyn transformation is used here to fix the moving boundaries for ease of application of the numerical scheme.

Similar to that in §§ 3.1.3, we introduce a material coordinate which exists in the form of

$$\zeta = \int_{-z_\infty}^{z} \varrho \,\mathrm{d}z \;\in [0, \zeta_s] , \tag{4.18}$$

where the quantity ϱ, denoting the mixture concentration nondimensionalised with respect to the concentration of the metal, is defined as

$$\varrho = M + O\frac{N_O^*}{N_M^*} + H\frac{N_H^*}{N_M^*} ; \tag{4.19}$$

ζ_s is the fixed (dimensionless) size of the transformed domain (or material) that denotes the total number of uranium atoms/ions present in the oxide, hydride and metal across the whole domain. It is assumed that the expansion of the material domain is unidirectional (along increasing z coordinate which is from the metal towards the oxide surface), and therefore we assume that the advection velocity $V = 0$ on $z = -z_\infty$ that is a bottom truncation present in the metal sufficiently far away from the oxide surface.

Transformation rules: Transforming from (z, τ) to (ζ, τ) coordinate system (cf. transformation rules defined earlier in §§ 3.1.3), we have

$$\frac{\partial}{\partial z} \to \frac{\partial \zeta}{\partial z}\frac{\partial}{\partial \zeta} \qquad = \varrho \frac{\partial}{\partial \zeta}\,, \tag{4.20a}$$

$$\frac{\partial}{\partial \tau} \to \frac{\partial}{\partial \tau} + \frac{\partial \zeta}{\partial \tau}\frac{\partial}{\partial \zeta} = \frac{\partial}{\partial \tau} - \varrho V \frac{\partial}{\partial \zeta}\,, \tag{4.20b}$$

where (4.20b) is defined using the continuity equation (conservation of uranium atoms), similar to that derived in §§ 3.1.3.

We transform the system (4.17) using the above transformation rules and set $\epsilon = 0$ as a quasi-steady approximation for low surface concentrations ($C_a^* \ll N_M^*$), but retain k_{cH} as an $\mathcal{O}(1)$ parameter. This then makes diffusion quasi-steady which essentially means that at very low concentrations of OH^-, reactions take a 'long' time to lead to $\mathcal{O}(1)$ changes in the volume fractions (or dimensionless concentrations) of the three phases $(O\,, H\,, M)$ in the material. On this long time scale we can treat diffusion as quasi-steady.

4.2.3.2 Transformed governing equations

In terms of the (material) coordinate ζ, the final problem is now reduced to the following non-linear fixed-domain version:

$$0 = \varrho \frac{\partial}{\partial \zeta}\left(D_c\, \varrho \frac{\partial c}{\partial \zeta}\right) - 2k_{cH}\, c^2 H\,, \tag{4.21a}$$

$$0 = \varrho \frac{\partial}{\partial \zeta}\left(D_h\, \varrho \frac{\partial h}{\partial \zeta}\right) + 5k_{cH}\, c^2 H - 3h^3 M\,, \tag{4.21b}$$

$$\frac{\partial H}{\partial \tau} = (\, h^3 M - k_{cH}\, c^2 H)\left(\frac{N_M^*}{N_H^*}\right) - \varrho V_\zeta H\,, \tag{4.21c}$$

$$\frac{\partial M}{\partial \tau} = -\, h^3 M - \varrho V_\zeta M\,, \tag{4.21d}$$

$$\frac{\partial O}{\partial \tau} = k_{cH}\, c^2 H \left(\frac{N_M^*}{N_O^*}\right) - \varrho V_\zeta O\,, \tag{4.21e}$$

$$\varrho V_\zeta = h^3 M \left(\frac{N_M^*}{N_H^*} - 1\right) + k_{cH} c^2 H \left(\frac{N_M^*}{N_O^*} - \frac{N_M^*}{N_H^*}\right)\,, \tag{4.21f}$$

$$\varrho = M + O\left(\frac{N_O^*}{N_M^*}\right) + H\left(\frac{N_H^*}{N_M^*}\right)\,, \tag{4.21g}$$

$$D_c = MD_c^M + OD_c^O + HD_c^H \, , \tag{4.21h}$$

$$D_h = MD_h^M + OD_h^O + HD_h^H \, , \tag{4.21i}$$

where we solve for the nine unknowns $c\,, h\,, H\,, M\,, O\,, \varrho\,, (\varrho V_\zeta)\,, D_c$ and D_h. Here the variables $\varrho\,, (\varrho V_\zeta)\,, D_c$ and D_h can be trivially eliminated; however we retain them in the formulation to simplify the resulting numerical scheme. The parameters in the model are k_{cH}, D_c^M, D_c^H, D_c^O, D_h^M, D_h^H and D_h^O, whilst k_{hM} has been set to unity. Note that O can instead be obtained from $O = 1 - H - M$ than solving using the above specified governing equation for O.

4.2.3.3 Initial and boundary conditions

Initial conditions: We can solve (4.21) using arbitrary initial conditions for $(O\,, M\,, H)$, but we choose to impose the following smooth initial conditions:

$$\begin{aligned} O(\tau = 0) &= \frac{1}{2}\left(1 + \tanh(\zeta - (\zeta_s - \delta_O))\right) \, , \\ M(\tau = 0) &= \frac{1}{2}\left(1 - \tanh(\zeta - (\zeta_s - \delta_M))\right) \, , \\ H(\tau = 0) &= 1 - M(\tau = 0) - O(\tau = 0) \, , \end{aligned} \tag{4.22}$$

in the region $\zeta \in [0, \zeta_s]$. These initial conditions represent a slightly pre-oxidised state with an initial oxide thickness δ_O and an initial hydride thickness $\delta_H = (\delta_M - \delta_O)$, and the transition between different phases are considered to be sufficiently smooth. As (4.21a) and (4.21b) are quasi-steady, the initial profiles for $(c\,, h)$ are determined by the choices (4.22). Note that a smoothly-varying initial oxide and hydride layers allow for the initiation of the reaction, based on our proposed reaction scheme § 1.2.6. Absence of an initial hydride layer would result in the hydroxide ions (OH⁻) simply diffusing through the material domain without reacting, whereas an initial oxide layer is more representative of the experimental conditions.

We cannot impose arbitrary initial conditions for c and h since we have quasi-steady approximation for the diffusing species, which then prompts us to obtain initial profiles for the diffusing species (c, h) using a numerical continuation technique, where the continuation parameter (say, s) is the surface concentration of the OH⁻ diffusing species. We increment the continuation parameter s starting from $s = 0$ and obtain the initial profiles for c and h until the desired boundary condition is reached. For $s = 0$, an initial solution $c = h = 0$ across the whole domain is obtained. We increment the continuation parameter by a small value, say $\Delta s = 0.1$ and find the solution by solving equations (4.21a) and (4.21b) using a suitable iterative method such as Newton iteration in conjunction with a finite-difference scheme; this is continued until we reach the desired surface boundary condition which corresponds to $s = 1$. The solution obtained at $s = 1$ will then constitute the initial quasi-steady concentration profiles for $(c,\, h)$ across the material domain.

Boundary conditions: We have the nondimensionalised surface boundary conditions:

$$c(\zeta = \zeta_s, \tau) = 1\,, \quad h(\zeta = \zeta_s, \tau) = 0 \quad \text{for } \tau \geq 0\,. \tag{4.23a}$$

When sufficiently deep into the sample, we always recover a pure metal phase, whilst there is no diffusing species:

$$\left.\begin{aligned} c(\zeta = 0, \tau) = 0\,, &\quad h(\zeta = 0, \tau) = 0\,, \\ O(\zeta = 0, \tau) = 0\,, &\quad H(\zeta = 0, \tau) = 0\,, \\ M(\zeta = 0, \tau) = 1\,, &\quad V(\zeta = 0, \tau) = 0\,, \end{aligned}\right\} \quad \text{for } \tau \geq 0\,, \tag{4.23b}$$

representing the far-field boundary conditions. Note that the advection velocity is zero in the metal.

4.2.3.4 Remapping to the physical coordinate

Having solved in the computational ζ domain, the solution can be remapped to the physical coordinate system via

$$z = \int_0^{\zeta} \frac{1}{\varrho}\, \mathrm{d}\zeta\,. \tag{4.24}$$

4.2.3.5 Numerical solution scheme

We numerically solve the transformed system (4.21) subject to the initial and boundary conditions (4.22) and (4.23) using a combination of Newton iteration to handle the nonlinearity and a second-order semi-implicit Crank-Nicolson finite-difference scheme for the time marching, as has been used for the dry-air oxidation problem.

The governing equations, boundary and initial conditions are thus converted into a linear matrix system, wherein we solve for the linear corrections to the guess values at each time-level (see §§§ 2.2.1.4 for details). The guess values are updated iteratively until the corrections are below some specified tolerance (say 10^{-8}). The updated solution at a particular time-level then becomes the guess value for the solution at the next time-level; the process is continued until some desired time value. In what follows, superscript k denotes the previous time level. The solution at the current time-level $k+1$ is decomposed into a guess value plus a correction as (for example) $c^{k+1} = c_g + \tilde{c}$.

Applying Newton iteration to (4.21a) at the current time-level $(k+1)$ and neglecting the higher-order correction terms, we write the equation for c as:

$$\begin{aligned}
&-\varrho_g^2 D_{c_g}\frac{\partial^2 \tilde{c}}{\partial \zeta^2} - \left[2\varrho_g D_{c_g}\tilde{\varrho} + \varrho_g^2 \tilde{D}_c\right]\frac{\partial^2 c_g}{\partial \zeta^2} \\
&- \left[2\varrho_g \frac{\partial D_{c_g}}{\partial \zeta}\tilde{\varrho} + \varrho_g^2\frac{\partial \tilde{D}_c}{\partial \zeta} + \left(D_{c_g}\tilde{\varrho} + \varrho_g \tilde{D}_c\right)\frac{\partial \varrho_g}{\partial \zeta} + \varrho_g D_{c_g}\frac{\partial \tilde{\varrho}}{\partial \zeta}\right]\frac{\partial c_g}{\partial \zeta} \\
&- \left[\varrho_g^2\frac{\partial D_{c_g}}{\partial \zeta} + \varrho_g D_{c_g}\frac{\partial \varrho_g}{\partial \zeta}\right]\frac{\partial \tilde{c}}{\partial \zeta} + 2k_{cH}\left(2c_g H_g \tilde{c} + c_g^2 \tilde{H}\right) \\
&= \varrho_g^2 D_{c_g}\frac{\partial^2 c_g}{\partial \zeta^2} + \left[\varrho_g^2\frac{\partial D_{c_g}}{\partial \zeta} + \varrho_g D_{c_g}\frac{\partial \varrho_g}{\partial \zeta}\right]\frac{\partial c_g}{\partial \zeta} - 2k_{cH}\, c_g^2 H_g\,,
\end{aligned} \tag{4.25a}$$

where we apply central differences to approximate the derivatives at each nodal point (ζ_j, τ^{k+1}):

$$\frac{\partial^2 \tilde{c}}{\partial \zeta^2} \approx \frac{(\tilde{c}_{j+1} - 2\tilde{c}_j + \tilde{c}_{j-1})}{(\Delta\zeta)^2}\,, \tag{4.25b}$$

$$\frac{\partial \tilde{c}}{\partial \zeta} \approx \frac{(\tilde{c}_{j+1} - \tilde{c}_{j-1})}{\Delta\zeta}\,, \tag{4.25c}$$

and so on; $\Delta\zeta$ is the spatial step-size of the one-dimensional computational domain.

Similarly, the equation for h given by (4.21b) can be written as:

$$\begin{aligned}
&-\varrho_g^2 D_{h_g}\frac{\partial^2\tilde{h}}{\partial\zeta^2}-\left[2\varrho_g D_{h_g}\tilde{\varrho}+\varrho_g^2\tilde{D}_h\right]\frac{\partial^2 h_g}{\partial\zeta^2}\\
&-\left[2\varrho_g\frac{\partial D_{h_g}}{\partial\zeta}\tilde{\varrho}+\varrho_g^2\frac{\partial\tilde{D}_h}{\partial\zeta}+\left(D_{h_g}\tilde{\varrho}+\varrho_g\tilde{D}_h\right)\frac{\partial\varrho_g}{\partial\zeta}+\varrho_g D_{h_g}\frac{\partial\tilde{\varrho}}{\partial\zeta}\right]\frac{\partial h_g}{\partial\zeta}\\
&-\left[\varrho_g^2\frac{\partial D_{h_g}}{\partial\zeta}+\varrho_g D_{h_g}\frac{\partial\varrho_g}{\partial\zeta}\right]\frac{\partial\tilde{h}}{\partial\zeta}-\left[5k_{cH}\left(c_g^2\tilde{H}+2c_gH_g\tilde{c}\right)-3\left(h_g^3\tilde{M}+3h_g^2M_g\tilde{h}\right)\right]\\
&=\varrho_g^2 D_{h_g}\frac{\partial^2 h_g}{\partial\zeta^2}+\left[\varrho_g^2\frac{\partial D_{h_g}}{\partial\zeta}+\varrho_g D_{h_g}\frac{\partial\varrho_g}{\partial\zeta}\right]\frac{\partial h_g}{\partial\zeta}+5k_{cH}\,c_g^2H_g-3h_g^3M_g\,,
\end{aligned}\tag{4.25d}$$

and the equations for H, M, (ϱV_ζ), ϱ, D_c, D_h are respectively,

$$\begin{aligned}
\tilde{H}-\frac{\Delta\tau}{2}\Bigg[\frac{N_M^*}{N_H^*}&\left\{\left(h_g^3\tilde{M}+3h_g^2M_g\tilde{h}\right)-k_{cH}\left(c_g^2\tilde{H}+2c_gH_g\tilde{c}\right)\right\}\\
&-(\varrho V_\zeta)_g\tilde{H}-(\varrho\tilde{V}_\zeta)H_g\Bigg]=H^k-H_g\\
&+\frac{\Delta t}{2}\Bigg[\left\{\left(h_g^3M_g-k_{cH}c_g^2H_g\right)\frac{N_M^*}{N_H^*}-(\varrho V_\zeta)_gH_g\right\}\\
&+\left\{\left(h^3M-k_{cH}c^2H\right)\frac{N_M^*}{N_H^*}-(\varrho V_\zeta)H\right\}\Bigg|^k\Bigg],
\end{aligned}\tag{4.25e}$$

$$\begin{aligned}
\tilde{M}-\frac{\Delta\tau}{2}\left[-\left(h_g^3\tilde{M}+3h_g^2M_g\tilde{h}\right)-(\varrho V_\zeta)_g\tilde{M}-(\varrho\tilde{V}_\zeta)M_g\right]&=M^k-M_g\\
+\frac{\Delta t}{2}\left[\left\{-h_g^3M_g-(\varrho V_\zeta)_gM_g\right\}-\left\{h^3M+(\varrho V_\zeta)M\right\}\Big|^k\right]&,
\end{aligned}\tag{4.25f}$$

$$\begin{aligned}
(\varrho\tilde{V}_\zeta)-\left(\frac{N_M^*}{N_H^*}-1\right)\left[h_g^3\tilde{M}+3h_g^2M_g\tilde{h}\right]-k_{cH}\left(\frac{N_M^*}{N_O^*}-\frac{N_M^*}{N_H^*}\right)\left[c_g^2\tilde{H}+2c_gh_g\tilde{c}\right]\\
=-(\varrho V_\zeta)_g+\left(\frac{N_M^*}{N_H^*}-1\right)h_g^3M_g+k_{cH}\left(\frac{N_M^*}{N_O^*}-\frac{N_M^*}{N_H^*}\right)c_g^2H_g\,,
\end{aligned}\tag{4.25g}$$

$$\tilde{\varrho}-\tilde{M}-\frac{N_O^*}{N_M^*}\tilde{O}-\frac{N_H^*}{N_M^*}\tilde{H}=-\varrho_g+M_g+O_g\frac{N_O^*}{N_M^*}+H_g\frac{N_H^*}{N_M^*}\,,\tag{4.25h}$$

$$\tilde{D}_c - D_c^M \tilde{M} - D_c^O \tilde{O} - D_c^H \tilde{H} = -D_{c_g} + D_c^M M_g + D_c^O O_g + D_c^H H_g \,, \tag{4.25i}$$

$$\tilde{D}_h - D_h^M \tilde{M} - D_h^O \tilde{O} - D_h^H \tilde{H} = -D_{h_g} + D_h^M M_g + D_h^O O_g + D_h^H H_g \,, \tag{4.25j}$$

where the Crank-Nicolson scheme is used for time-marching and $\Delta\tau$ is the time step used. The equations (4.25) are solved at each of the nodal points in the one-dimensional computational grid. It should be noted that since the governing equations for c, h are quasi-steady, the corresponding discretised equations have been evaluated at just a single time-level $(k+1)$, whereas the discretised governing equations for M, H involve both k and $(k+1)$ time-levels.

Now, applying Newton iteration to the boundary conditions, we have

$$\left.\begin{array}{l} \tilde{c}(\zeta=\zeta_s,\tau) = 1 - c_g \,, \quad \tilde{h}(\zeta=\zeta_s,\tau) = -h_g \\ \tilde{c}(\zeta=0,\tau) = -c_g \,, \quad \tilde{h}(\zeta=0,\tau) = -h_g \,, \quad \tilde{V}(\zeta=0,\tau) = -V_g \\ \tilde{M}(\zeta=0,\tau) = 1 - M_g \,, \quad \tilde{H}(\zeta=0,\tau) = -H_g \,, \end{array}\right\} \text{for } \tau \geq 0 \,, \tag{4.25k}$$

and similarly for the initial conditions.

A linear matrix system $\mathbf{A}\boldsymbol{x} = \mathbf{B}$ can now be constructed, where $\boldsymbol{x}$ represents the vector of linear corrections $(\tilde{c}_j\,, \tilde{h}_j\,, \tilde{H}_j\,, \tilde{M}_j\,, (\widetilde{\varrho V_\zeta})_j\,, \tilde{\varrho}_j\,, \tilde{D}_{cj}\,, \tilde{D}_{hj})$ with the spatial nodal index, $j = 0, 1, \ldots, N$. The linear system has been solved using MATLAB® version 9.3. The MATLAB code has been optimised for speed through vectorisation, for example, and uses functions specific to sparse matrices such as `sparse` and `colamd`. The latter function has been used to reorder the matrix $\mathbf{A}$ by applying suitable column permutations so that the cost of computing and applying the L and U factors of the matrix $\mathbf{A}$ are cheaper than the traditional backslash operator (\ or `mldivide`) in order to obtain the vector $\boldsymbol{x}$. The computational time taken to run the code on a machine with 16 GB RAM, Intel i7 - 6700 CPU @ 3.4 GHz processor was $3.9 \cdot 10^4$ s for a typical problem with τ up to 10^5, $\Delta\tau = 0.5$ and $\Delta\zeta = 0.15$.

4.2.4 Numerical results

Numerical experiments were conducted for different ranges of the diffusivity and rate constant parameters and the results are reported in this section. The numerical results are obtained by solving the system (4.21) using the solution strategy detailed in §§ 4.2.3. In order to calculate the oxide and hydride thicknesses based on our numerical results, we define the location of the centre of the first reaction front (i.e. $z_1(\tau)$) as the position where the reaction rate,

$$\mathcal{R}_1(z,\tau) = k_{cH}\, c^2(z,\tau)H(z,\tau) \tag{4.26}$$

is maximised. Similarly, the centre of the second reaction front (i.e. $z_2(\tau)$) is defined as the location where the reaction rate,

$$\mathcal{R}_2(z,\tau) = h^3(z,\tau)M(z,\tau) \tag{4.27}$$

is maximised. The (dimensionless) oxide and hydride thicknesses are then calculated as

$$\Delta_O = z_s(\tau) - z_1(\tau)\,, \quad \Delta_H = z_1(\tau) - z_2(\tau) \tag{4.28}$$

respectively, where $z_s(\tau)$ is the surface location.

Typical spatial concentration (dimensionless) profiles of the diffusing (OH^- (c), $H^{\bullet}$ (h)) and the nondiffusing (U (M), UO_2 (O) and UH_3 (H)) components at a nondimensional time of $\tau = 10^4$ are shown in Figure 4.2. The initial surface is located at $z = z_s(0) = 0$ and it can be seen that $z_s(\tau) > z_s(0)$ ($\tau = 10^4$ in Figure 4.2) due to advection/material expansion that result from phase changes. In Figure 4.2, the transition from hydride to oxide phase occurs at $z \approx -75$ and will be referred to as the *reaction front 1* or RF1, and the transition from metal to the intermediate hydride phase occurs at $z \approx -100$ henceforth referred to as the *reaction front 2* or RF2. The direction of propagation of the reaction fronts is into the bulk metal and opposite to that of the surface. Reaction fronts are transition regions and hence account for the steep concentration gradients of the nondiffusing phases in these regions. They separate regions of homogeneous compositions of the nondiffusing phases constituting the 'diffusion layers' wherein diffusion is the dominant physical process, whereas reactions are the dominant physicochemical process occurring in the reaction fronts. These 'reaction fronts' are infinitely thin compared to the 'diffusion layers' at large times, and the same is verified using large-time (τ) asymptotic analysis that will be described in §§ 4.2.5. Unless otherwise specified, the numerical results presented in this section use an initial dimensionless oxide thickness of $\delta_O = 10$ and an initial hydride of $\delta_H = 5$ in the computational domain.

The choice of diffusivity of $H^{\bullet}$ in UH_3 (D_h^H) in Figure 4.2 is three orders of magnitude smaller than the other diffusivity parameters and is reflective of the actual diffusivity values that are tabulated in Table 4.1.

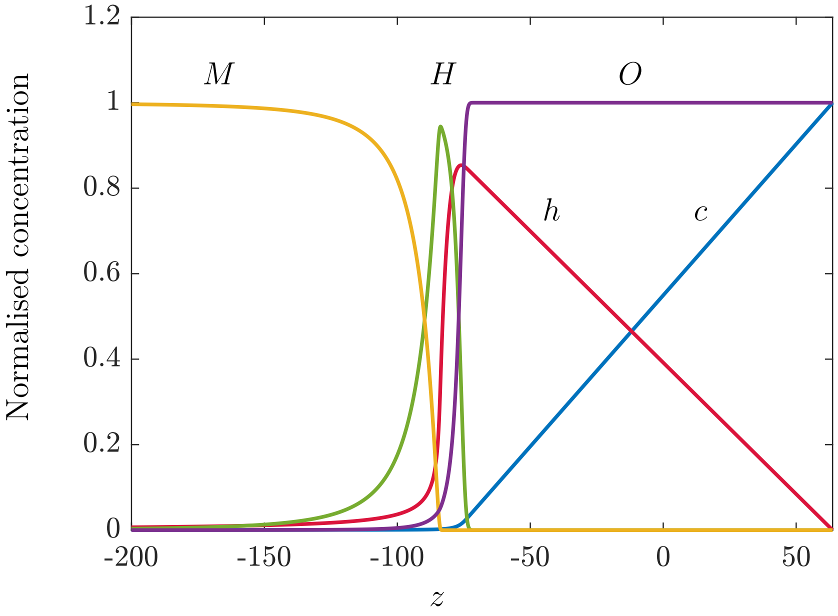

Figure 4.2: Typical dimensionless concentration profiles of the nondiffusing (O, H and M) and the diffusing (c, h) components at a nondimensional time of $\tau = 10^4$. The other dimensionless parameters chosen are: $D_c^M = D_c^O = D_c^H = D_h^M = D_h^O = 1$, $D_h^H = 10^{-3}$, $k_{cH} = 10$, and $k_{hM} = 1$. Here $z = 0$ represents the initial surface location $z_s(0)$.

Initial concentration profiles: Plots of typical initial concentration profiles of the different species as a function of the diffusivity and rate constant (k_{cH}) parameter values are shown in Figures 4.4 to 4.7. In all these figures, the initial oxide surface position is represented as $z_s(0) = 0$ whilst $z = -z_\infty$ represents the (truncated) metal base of the physical domain. Here the normalised (or nondimensional) concentration profiles across the physical domain are plotted. It will be seen via the numerical results that only three diffusivity parameters influence the kinetics of the oxidation process, which will also be verified using an asymptotic analysis presented in §§ 4.2.5.

The initial conditions depicted in Figures 4.4 to 4.7 represent quasi-steady state concentration profiles for the diffusing species OH^- (concentration c) and $H^\bullet$ (concentration h) that have been obtained using numerical continuation techniques described earlier in §§§ 4.2.3.3. It can be seen from Figure 4.4 that the rate

Table 4.1: Orders of magnitude of the diffusion coefficients (units in m^2/s) of OH^-, $H^\bullet$ and H_2 in the different phases ($U/UO_2/UH_3$) at 300 K.

Phase	Diffusing species		
	OH^-	$H^\bullet$	H_2
U	-	-	10^{-15} [a]
UO_2	10^{-16} [b]	10^{-16} [c]	-
UH_3	-	10^{-19} [d]	-

[a] Powell and Condon (1973) calculated diffusivity of H_2 in U to be $7.1658 \cdot 10^{-15}$.

[b] Marchetti et al. (2011) calculated the diffusivity of 'water species' through the grain boundaries of polycrystalline UO_2 to be $2.3 \cdot 10^{-16}$ m^2/s.

[c] Wheeler (1971); [d] Peretz et al. (1976).

constant k_{cH} significantly influences the peak value of the hydrogen radical ($H^\bullet$) concentration (henceforth referred to as h_p), whilst the concentration gradient of the hydroxyl ions (OH^-) across the oxide layer is only slightly influenced. Since the reaction time scale is much smaller than the diffusion time scale, a higher reaction rate constant k_{cH} implies that the consumption of OH^- to produce $H^\bullet$ occurs at a faster rate than the diffusion of the product $H^\bullet$, resulting in an increase in h_p with an increase in k_{cH}. Similarly in Figure 4.3, it can be seen that a lower value of $H^\bullet$ diffusivity in the hydride phase (D_h^H) results in an increase in the $H^\bullet$ concentration at the first reaction front (RF1). The diffusivity of $H^\bullet$ in the oxide phase (D_h^O), however, has a greater influence on h_p than D_h^H as shown in Figure 4.5. The $H^\bullet$ diffusivity in metal (D_h^M) has an insignificant influence on the initial h_p and is depicted in Figure 4.6; however it can be seen that D_h^M influences the concentration and depth of penetration of $H^\bullet$ into the metal with a larger D_h^M resulting in a higher $H^\bullet$ concentration within the metal and vice versa. As we may expect, a reduction in D_c^O reduces the amount of OH^- available at RF1 for the production of $H^\bullet$, which is shown in Figure 4.7. Note that the other rate constant parameter k_{hM} has been scaled out of the problem.

Contour plots of concentration: Having discussed the influence of the diffusivities and the reaction rate constants on the initial concentration profiles,

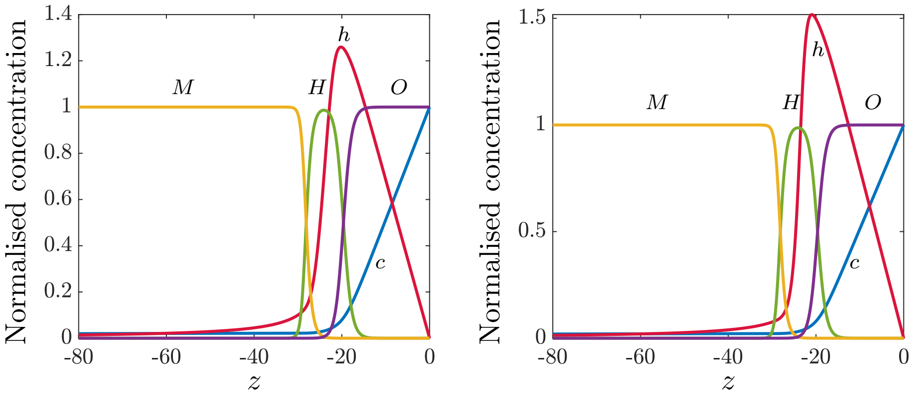

(a) $D_h^H = 0.1$ **(b)** $D_h^H = 0.001$

Figure 4.3: Initial concentration profiles of the different species across the material domain for different values of $H^\bullet$ diffusivity in the hydride phase as given by (a) $D_h^H = 0.1$ and (b) $D_h^H = 0.001$. Other parameters include $k_{cH} = 1$, $D_c = D_h^M = D_h^O = 1$, $\delta_O = 10$, $\delta_H = 5$.

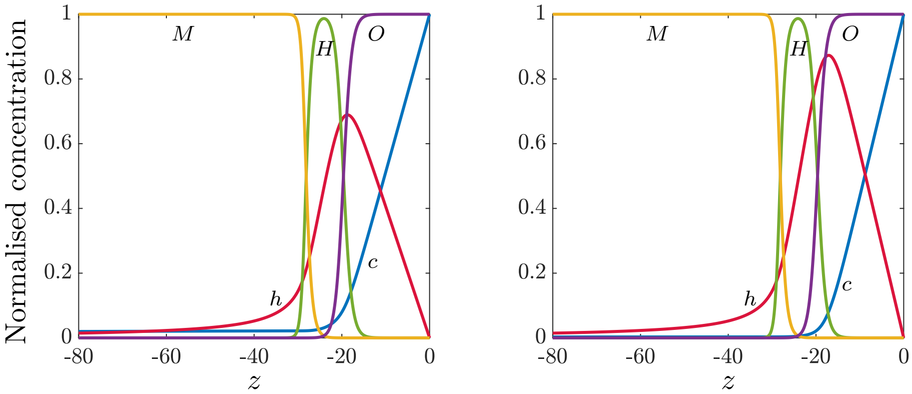

(a) $k_{cH} = 1$ **(b)** $k_{cH} = 10$

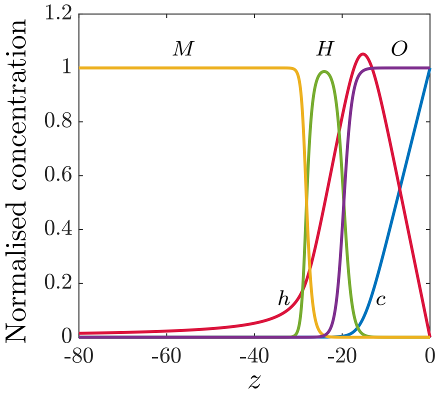

(c) $k_{cH} = 100$

Figure 4.4: Initial concentration profiles of the different species across the material domain for different values of the rate constant $k_{cH} = 1$, 10, 100 and uniform diffusivities ($D_{c,h} = 1$) are shown in subfigures (a), (b) and (c). Other parameters include $\delta_O = 10$, $\delta_H = 5$.

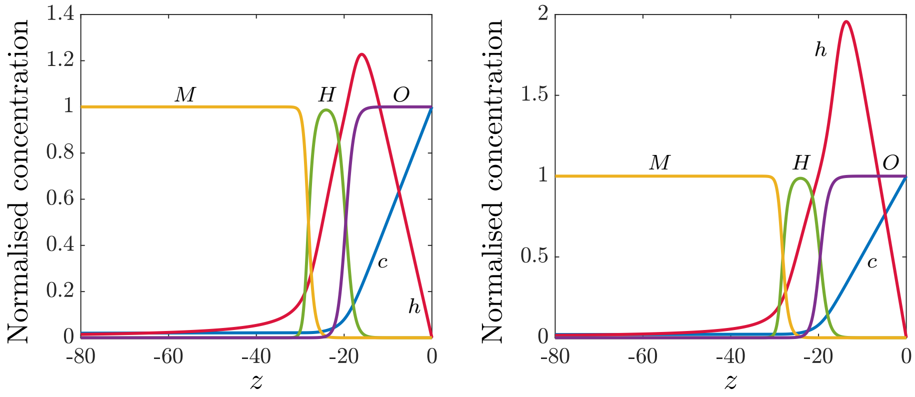

(a) $D_h^O = 0.1$ **(b)** $D_h^O = 0.01$

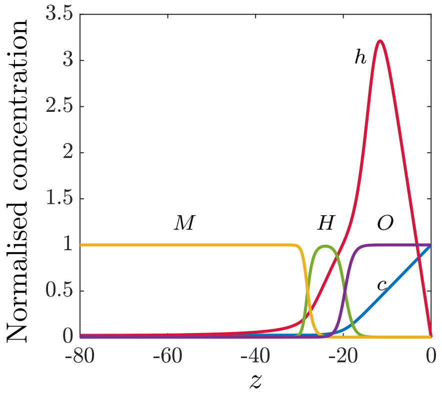

(c) $D_h^O = 0.001$

Figure 4.5: Initial concentration profiles of the different species across the material domain for various diffusivity values of H$^\bullet$ in the oxide phase as given by (a) $D_h^O = 0.1$, (b) $D_h^O = 0.01$ and (c) $D_h^O = 0.001$. Other parameters include $k_{cH} = 1$, $D_c = D_h^M = D_h^H = 1$, $\delta_O = 10$, $\delta_H = 5$.

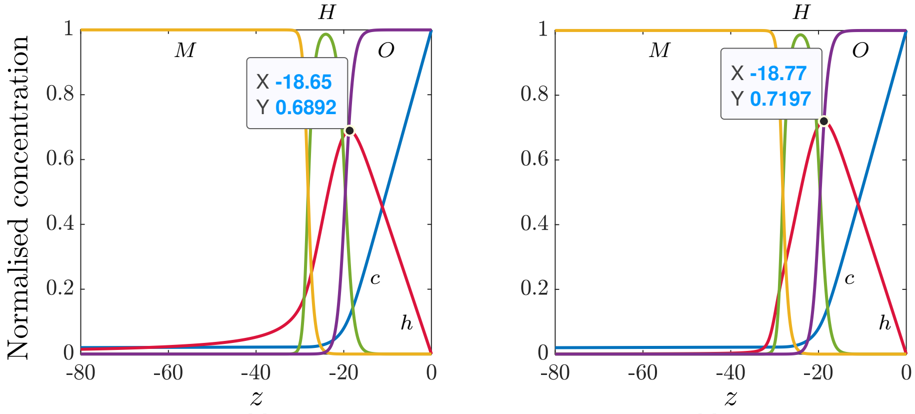

(a) $D_h^M = 1$ **(b)** $D_h^M = 0.001$

Figure 4.6: Initial concentration profiles of the different species across the material domain for various diffusivity values of H$^\bullet$ in the metal phase as given by (a) $D_h^M = 1$ and (b) $D_h^M = 0.001$. Other parameters include $k_{cH} = 1$, $D_c = D_h^O = D_h^H = 1$, $\delta_O = 10$, $\delta_H = 5$. The coordinates for the h profile are shown to indicate that D_h^M has insignificant influence on the initial profiles of the diffusing species.

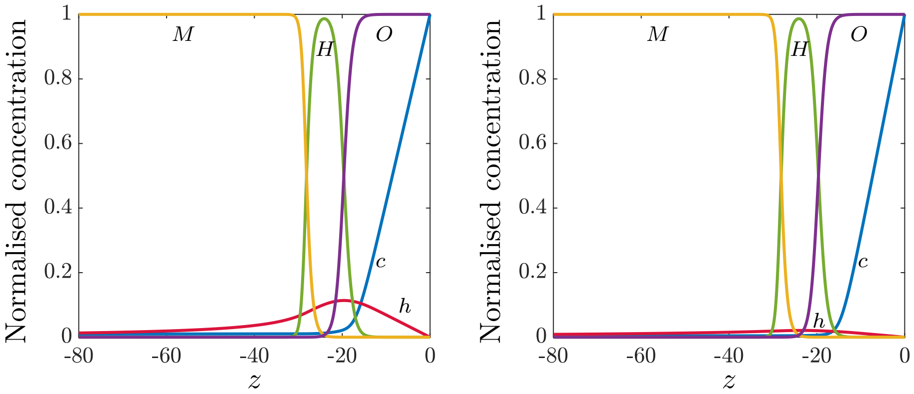

(a) $D_c^O = 0.1$ **(b)** $D_c^O = 0.01$

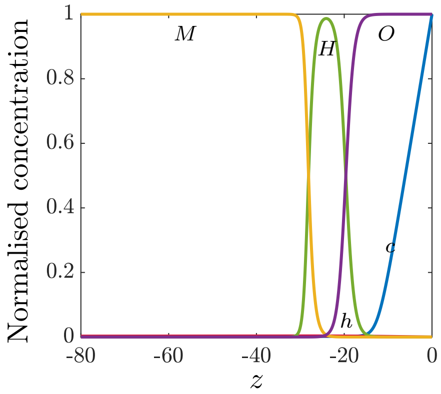

(c) $D_c^O = 0.001$

Figure 4.7: Initial concentration profiles of the different species across the material domain for various diffusivity values of OH$^-$ in the oxide phase as given by (a) $D_c^O = 0.1$, (b) $D_c^O = 0.01$ and (c) $D_c^O = 0.001$. Other parameters include $k_{cH} = 1$, $D_c = D_h^M = D_h^O = 1$, $\delta_O = 10$, $\delta_H = 5$.

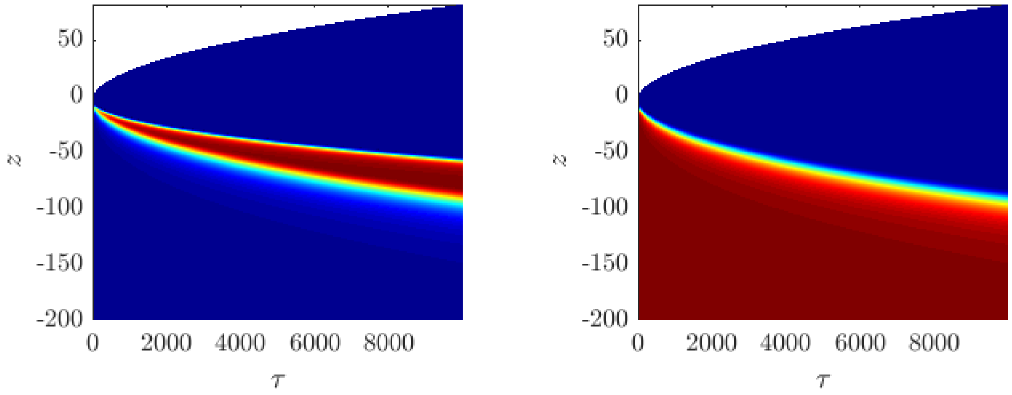

(a) Hydride (H) **(b)** Metal (M)

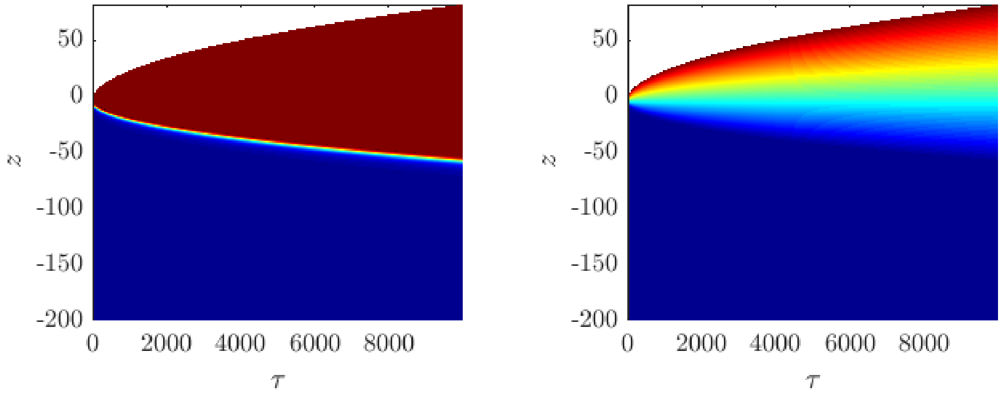

(c) Oxide (O) **(d)** OH$^-$ (c)

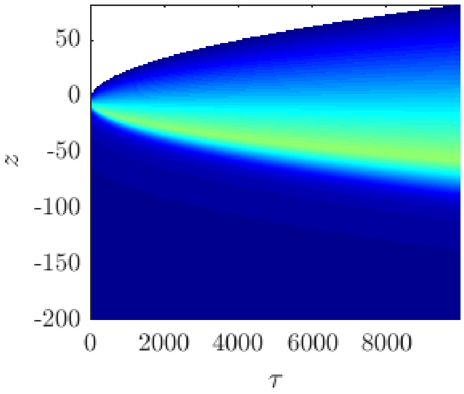

(e) H$^\bullet$ (h)

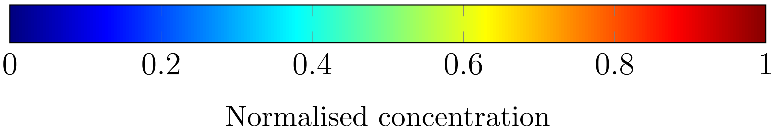

Figure 4.8: Evolution of the dimensionless concentration of UH_3, U, UO_2, OH$^-$ and H$^\bullet$ as denoted by $H\,, M\,, O\,, c$ and h respectively, in the $z-\tau$ domain up to a dimensionless time of $\tau = 10^4$. The initial surface is located at $z_s(0) = 0$. The parameters chosen are: $D_i^j = 1$, for $i = \{c, h\}$, $j = \{H, M, O\}$, $k_{cH} = 10$, initial thicknesses for oxide, $\delta_O = 4$ and hydride, $\delta_H = 1$ in the computational domain.

we now discuss the evolution of the concentrations of the different species with time. Figure 4.8 shows contours of c, h, H, M and O in the $z - \tau$ domain for an evolution of the system (4.21) with a rate constant $k_{cH} = 10$ and effective diffusivities, $D_{c,h} = 1$. Here, the slow-time variable τ is represented along the horizontal axis and the physical spatial coordinate (z) is represented along the vertical axis. A relatively slowly growing hydride layer ($\propto \tau^{1/2}$ at large times; see §§ 4.2.5) between the oxide and metal layers can be observed in subfigure 4.8a, whilst subfigure 4.8c shows the parabolic ($\propto \tau^{1/2}$) growth of the oxide layer. The (downwards) propagating reaction fronts, RF1 and RF2, are clearly visible in subfigure 4.8a indicating a sharp variation in the concentrations at the fronts. The reaction front where the metal is converted to hydride (RF2) can be observed in subfigure 4.8b, whilst subfigure 4.8c shows RF1 where the transition from the hydride to oxide phase occurs. Subfigures 4.8d and 4.8e both depict constant fluxes (i.e., a linearly varying spatial concentration profile) of the diffusing species OH^- and $H^\bullet$ respectively, where a maximum in the concentration of the hydrogen radicals is proximal to the oxide-metal boundary, and a maximum in c is at the surface. Note that the surface evolves from its initial position $z = 0 = z_s(0)$ to a higher z value owing to the expansion of the material as the metal (higher density) is converted to hydride and oxide (lower densities compared to the metal) (refer Table A.1 for $\rho^*_{M,H,O}$). Note that the material is allowed to expand freely only in the 'upward' direction as the truncated metal base is considered fixed.

Influence of k_{cH} on the oxide and hydride growth: As one of the rate constants, k_{hM} has been eliminated via our choice of an appropriate reference length scale, the influence of only the rate constant k_{cH} on the large-time growth-kinetics will be explored. We consider arbitrary values of k_{cH} in our numerical experiments, and study the evolution of the corresponding dimensionless oxide and hydride thicknesses with time. We found that k_{cH} does not have a significant influence on the overall oxidation kinetics (see Figure 4.9), whilst affecting only the growth rate of the reaction front between the oxide and hydride phases (RF1) (see Figure 4.15a). In Figure 4.9, the oxide thickness at any time τ is calculated from the surface $z_s(\tau)$ to the location of the maximal reaction rate at the first reaction front (denoted as z_1) where a rapid transition from the hydride to oxide phase occurs, i.e. $\Delta_O = z_s(\tau) - z_1(\tau)$; and similarly for the calculation of the hydride thickness, $\Delta_H = z_1(\tau) - z_2(\tau)$ where $z_2(\tau)$ is the location of the maximal reaction rate at the second reaction front. The oxide and hydride thicknesses for $k_{cH} = 1$, 10, 100 are shown in Figure 4.9, and the plots showing the evolution of the oxide thickness are found to overlap for the range of k_{cH} chosen, and similarly for the hydride thickness.

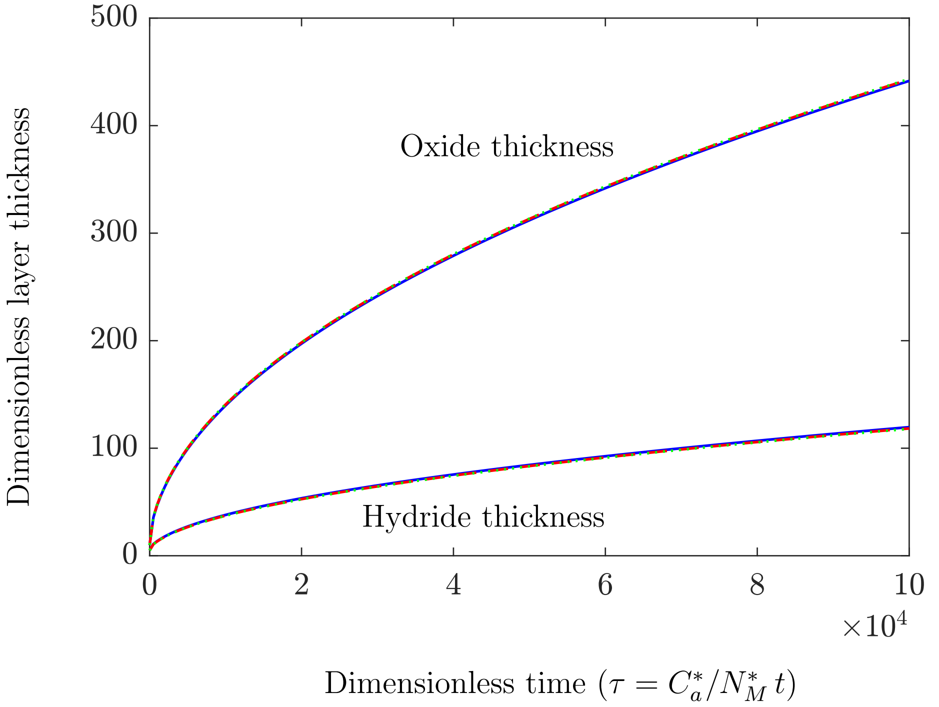

Figure 4.9: Dimensionless oxide and hydride thicknesses over a period of nondimensional time (τ) with initial oxide and hydride thicknesses of $\delta_O = 10$ and $\delta_H = 5$ respectively. Three values of the dimensionless reaction rate constant $k_{cH} = 1$ (blue solid), 10 (red dashed), 100 (green dotted) are shown. The curves for oxide (or hydride) thickness are found to overlap for different values of k_{cH} suggesting that k_{cH} has negligible influence on the overall kinetics. Other parameters include $D_c^M = D_c^O = D_c^H = D_h^M = D_h^O = D_h^H = 1$, $k_{hM} = 1$.

Concentration profiles showing the influence of k_{cH} and D_h^H: Figure 4.10 depicts the concentration profiles at a particular instant in time ($\tau = 10^4$) for different values of k_{cH} and D_h^H. As previously discussed, it can be observed that a change in k_{cH} does not substantially influence the overall kinetics (oxide and hydride thicknesses), whilst it has a profound effect on the width of the reaction front between the oxide and hydride phases (RF1). An increase in k_{cH} decreases the width of the first reaction front (RF1) correspondingly, which will be further discussed in §§ 4.2.5. However, a decrease in the diffusivity of the hydrogen radicals in the hydride phase (D_h^H) reduces the width of the intermediate hydride layer as less $H^\bullet$ diffuses to react with the metal, and the same is depicted in subfigure 4.10(d). A corresponding increase in the concentration of the hydrogen radicals in RF1 (h) can be seen with a decreased diffusivity in the hydride. A smaller D_h^H resulting in a thinner intermediate hydride layer is also shown in Figure 4.11. An elaborate quantitative description of the dependence on diffusivities will be studied via an asymptotic analysis (see §§ 4.2.5 and Figure 4.18 in particular).

Influence of the diffusivities: The quantitative dependence of the oxidation kinetics (predominantly the growth kinetics of the oxide and the hydride layers) on the diffusivity parameters will be studied in detail using a matched-asymptotic analysis (see §§ 4.2.5). We have studied the influence of the diffusion coefficients on the overall kinetics of the oxide and hydride growth through the numerical simulations. A reference diffusion coefficient of $D_{ref}^* = 10^{-16}$ m^2/s is used in the simulations; therefore for a typical concentration profile (e.g. Figure 4.2), the nondimensional diffusion coefficients are $D_c^M = D_c^O = D_c^H = D_h^M = D_h^O = 1$ and $D_h^H = 10^{-3}$ (refer Table 4.1 for observed experimental diffusivity values). There is some degree of uncertainty in the accuracy of the available diffusion coefficients, and there is not much data available on the diffusivity values D_c^{M*}, and D_c^{H*}. Through our numerical experiments, we find that D_c^{M*} and D_h^{M*} do not have any influence on the overall kinetics. We also find that D_c^{H*} does not influence the oxide growth, however it will be seen in §§§ 4.2.5.5 that for practically relevant diffusivity values, D_c^{H*} plays a crucial role in determining the hydride growth kinetics.

Influence of D_h^O: As we may expect, the diffusivity of $H^\bullet$ in the oxide phase (D_h^O) only influences the time-evolution of the hydride as it is produced when $H^\bullet$ diffuse through an already present UH_3 layer to react with the metal, whilst it does not have any influence on the oxide growth. It can be seen from Figure 4.12 that an increase in D_h^O reduces the hydride thickness, as less $H^\bullet$ will be available at RF1 to diffuse through the hydride layer and react with the metal, and vice-versa.

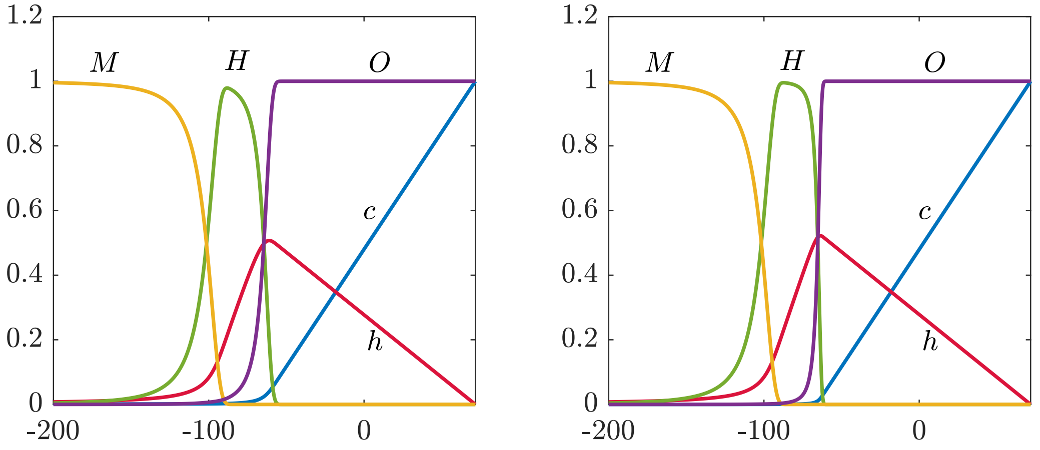

(a) $k_{cH} = 1$, $D_{c,h} = 1$.

(b) $k_{cH} = 10$, $D_{c,h} = 1$.

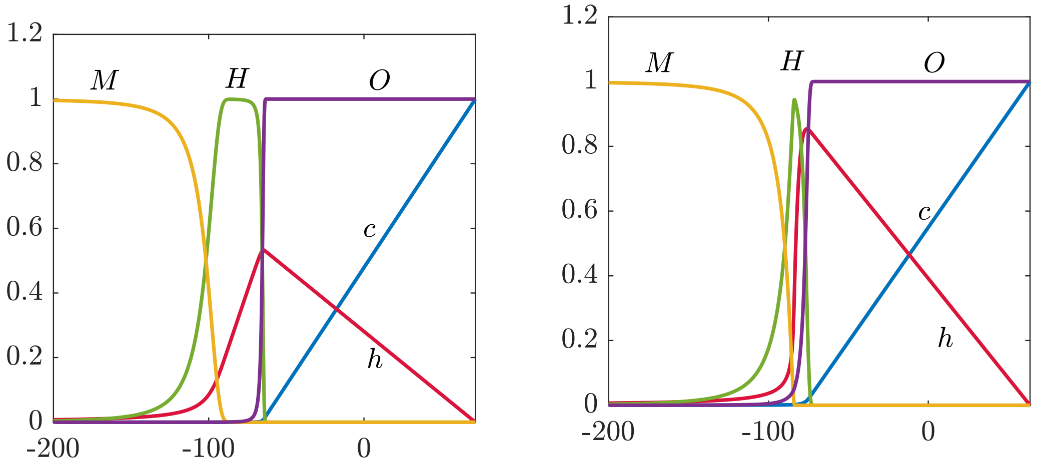

(c) $k_{cH} = 100$, $D_{c,h} = 1$.

(d) $k_{cH} = 10$, $D_h^H = 0.001$, whilst other diffusivities are equal to 1.

Figure 4.10: Concentration profiles of the different species across the material domain at $\tau = 10^4$ for different values of the rate constant $k_{cH} = 1, 10, 100$ and uniform diffusivities ($D_{c,h} = 1$) are shown in subfigures (a), (b) and (c). Subfigure (d) shows the profile for $k_{cH} = 10$ and a substantially lower value of diffusivity, $D_h^H = 0.001$. Other parameters include $\delta_O = 10$, $\delta_H = 5$.

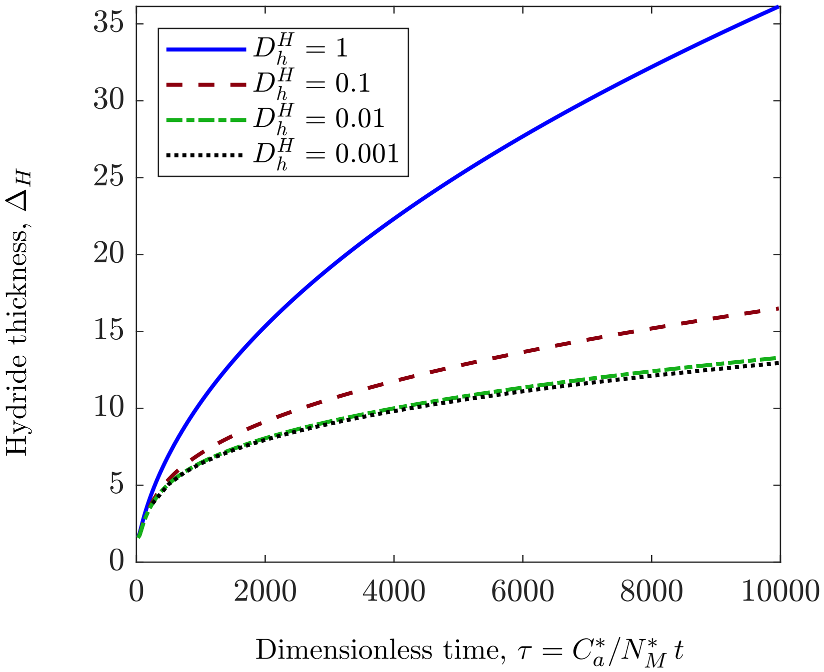

Figure 4.11: Evolution of the (dimensionless) thickness of the hydride layer over a period of nondimensional time (τ) for different values of D_h^H. The other parameters include $D_c^M = D_c^O = D_c^H = D_h^M = D_h^O = 1$, $k_{cH} = 10$, $k_{hM} = 1$ and initial conditions $\delta_H = 1\,, \delta_O = 4$.

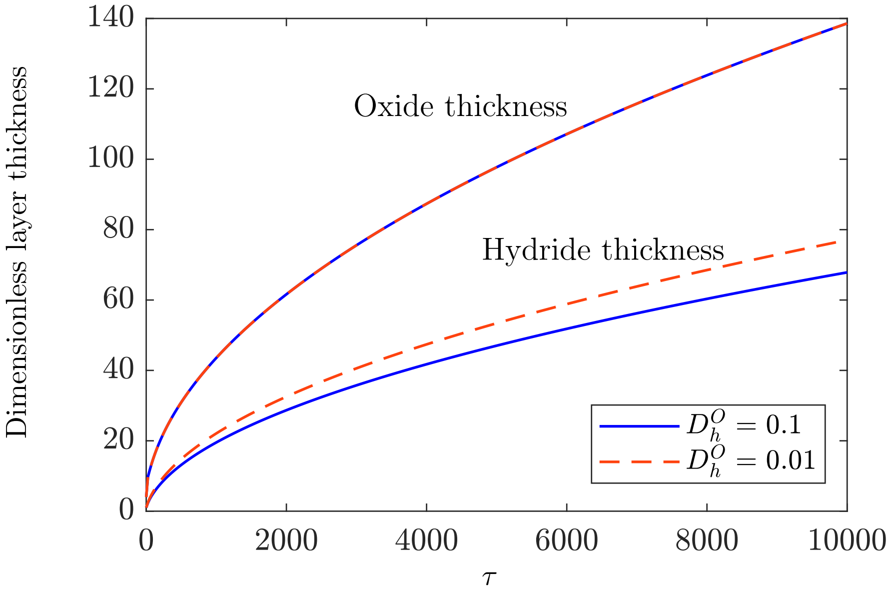

Figure 4.12: Evolution of the oxide and hydride thicknesses (dimensionless) over a period of nondimensional time (τ) for different values of the diffusivity of hydrogen radicals ($\mathrm{H}^\bullet$) in the oxide phase, $D_h^O = 0.1, 0.01$. Other parameters include $\delta_O = 4$, $\delta_H = 1$, $D_c = D_h^M = D_h^H = 1$, $k_{cH} = 1$ and $k_{hM} = 1$.

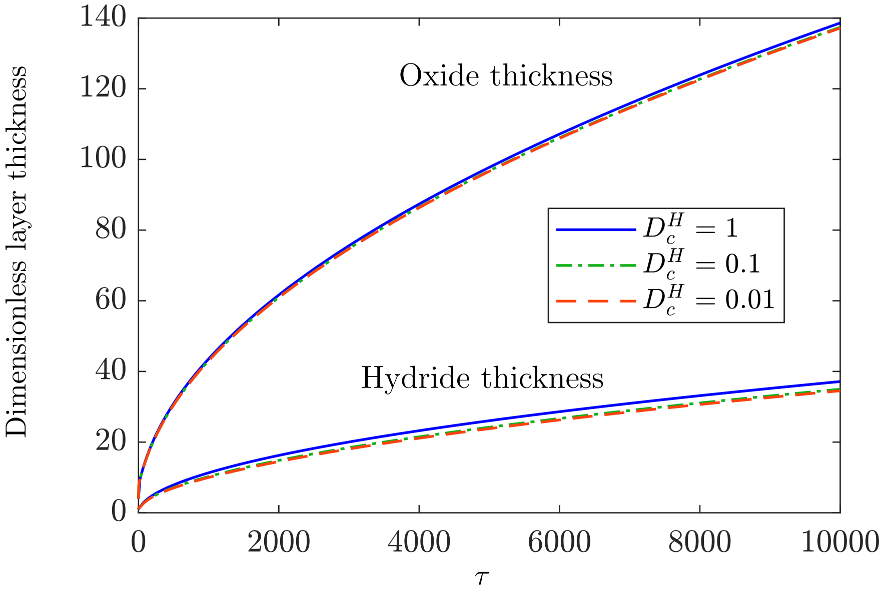

Figure 4.13: Evolution of the oxide and hydride thicknesses (dimensionless) over a period of nondimensional time (τ) for different values of the diffusivity of hydroxide ions (OH$^-$) in the hydride phase $D_c^H = 1\,, 0.1\,, 0.01$. Other parameters include $D_c^M = D_c^O = D_h = 1$, $\delta_O = 4\,, \delta_H = 1$ and $k_{hM} = 1$.

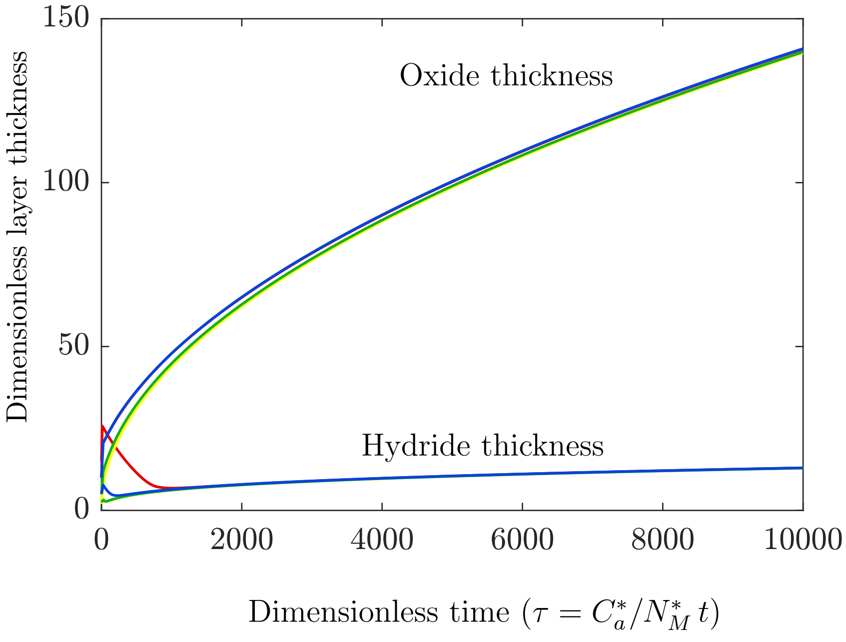

Figure 4.14: Evolution of the oxide and hydride thicknesses (dimensionless) over a period of nondimensional time (τ) for different initial oxide and hydride thicknesses: (i) $\delta_O = 10\,, \delta_H = 15$ (red), (ii) $\delta_O = 2\,, \delta_H = 4$ (yellow), (iii) $\delta_O = 5\,, \delta_H = 2.5$ (green), (iv) $\delta_O = 10\,, \delta_H = 5$ (blue). Other parameters include $D_c^M = D_c^O = D_c^H = D_h^M = D_h^O = 1$, $D_h^H = 10^{-3}$, $k_{cH} = 10$ and $k_{hM} = 1$.

Influence of D_c^H: Figure 4.13 shows the time-evolution of the oxide and hydride thicknesses for varying hydroxide (OH^-) diffusivity in the hydride phase. It appears from the figure that the diffusivity parameter D_c^H has little influence on the large-time kinetics of both the oxide and hydride growth for the chosen parameter values.

Effect of the initial conditions: The initial conditions only affect the transient growth-kinetics and not the long-time behaviour as clearly depicted in Figure 4.14. Variable initial oxide and hydride thicknesses converge to the same long-time behaviour. Here, the vertical axis denotes the dimensionless layer thickness and horizontal axis the time (τ) coordinate.

4.2.4.1 Width of the reaction fronts

Width of RF1: The width of the first reaction front (δ_1) is calculated from the numerical simulations using the second moment of $\mathcal{R}_1(z,\tau)$ defined as (Gálfi and Rácz, 1988; Polanowski and Koza, 2006)

$$\delta_1^2(\tau) = \int\limits_{-z_\infty}^{z_s(\tau)} (z - z_1(\tau))^2 \, \frac{\mathcal{R}_1(z,\tau)}{\mathcal{R}_1(\tau)} \, \mathrm{d}z \,, \tag{4.29a}$$

where $\mathcal{R}_1(z,\tau)$ is the local reaction rate in the first reaction front as defined in (4.26) and $\mathcal{R}_1(\tau)$ represents the total reaction rate of R2 (see § 1.2.6 for details of R2) defined as

$$\mathcal{R}_1(\tau) = \int\limits_{-z_\infty}^{z_s(\tau)} \mathcal{R}_1(z,\tau) \, \mathrm{d}z \,. \tag{4.29b}$$

It should be noted that the width of RF1 is defined in this way as the second moment of $\mathcal{R}_1(z,\tau)$ captures the variance of the reaction rate at RF1.

The time evolution of the width of the first reaction front for a range of k_{cH}, D_c^H and D_h^H is depicted in Figure 4.15. A decrease in the rate constant k_{cH} widens the reaction front as the transition from one phase to the other occurs on a wider spatial scale. This can be speculated as due to the reaction processes occurring at a slower rate with a decrease in k_{cH} allowing diffusion of the reactants and products, thereby increasing the width of the reaction front. Similarly, widening of the RF1 is observed with an increase in D_c^H, but D_h^H appears to not have a significant influence compared to its influence on the hydride width, which is as expected. Figure 4.15 clearly depicts that k_{cH} and D_c^H have a greater influence on the width of RF1 compared to that of D_h^H.

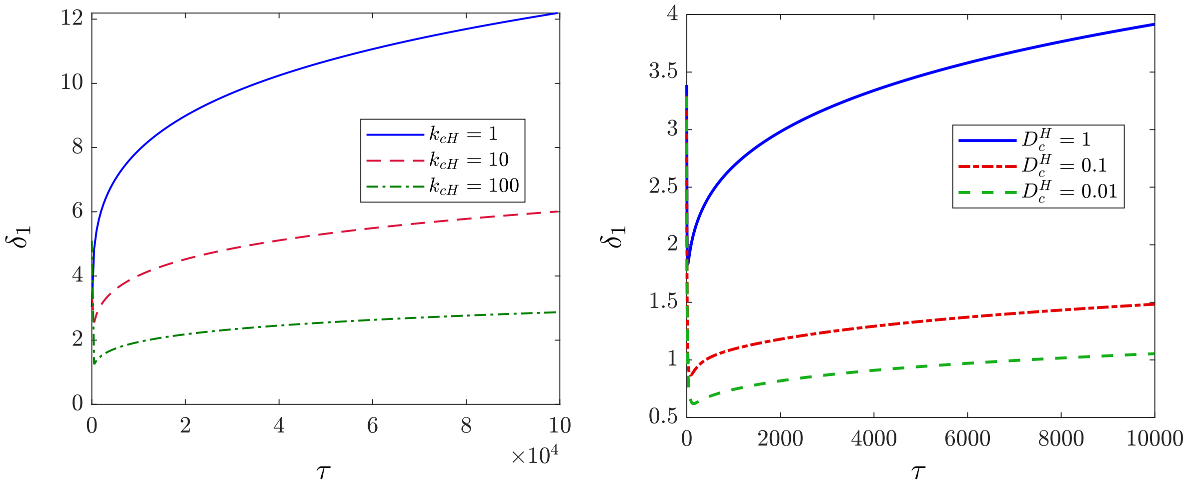

(a) Influence of k_{cH}; $D_{c,h} = 1$.

(b) Influence of D_c^H; $k_{cH} = 10, D_h = 1$.

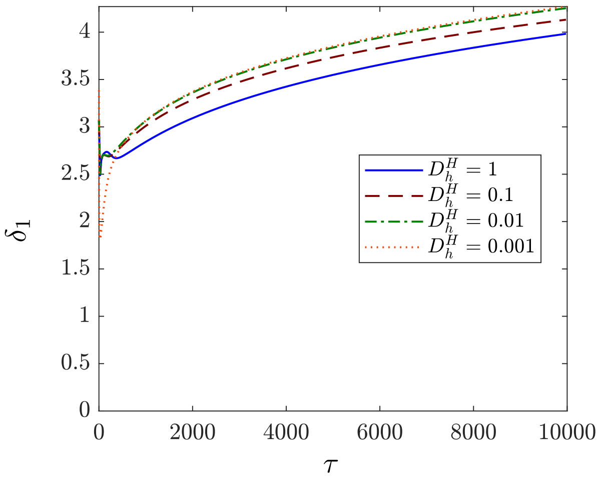

(c) Influence of D_h^H; $k_{cH} = 10$, $D_c = D_h^O = 1$.

Figure 4.15: Influence of the different parameters on the evolution of the width of RF1 obtained numerically using (4.29). Other parameters include $D_c^O = 1$ (by choice of nondimensionalisation), $D_c^M = D_h^O = 1$, initial oxide and hydride thicknesses, $\delta_O = 10$, $\delta_H = 5$.

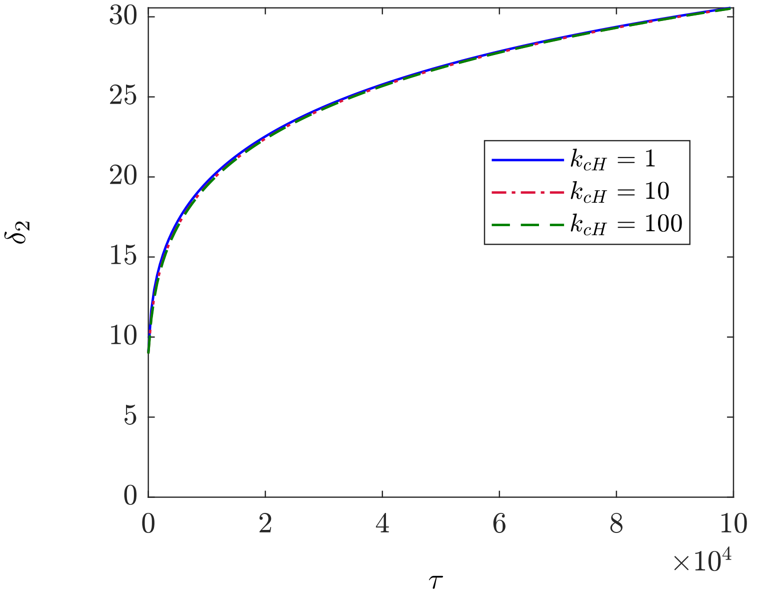

(a) Influence of k_{cH} with $D_c = D_h = 1$.

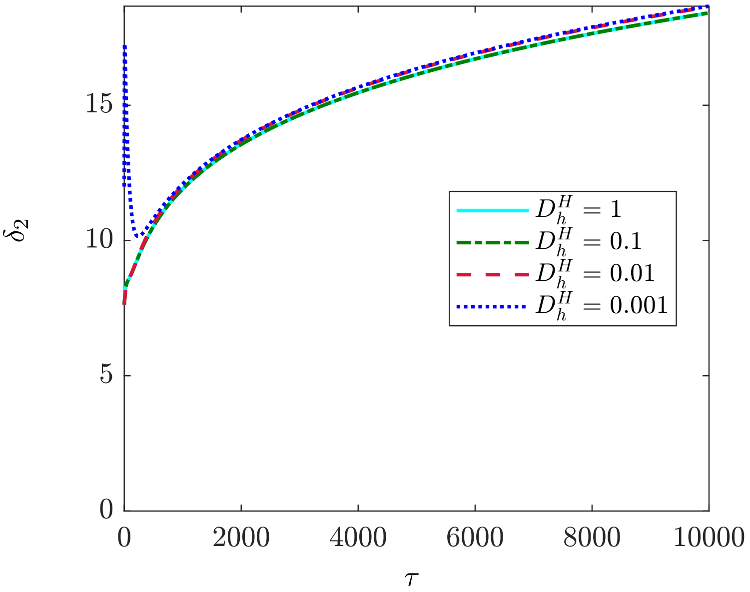

(b) Influence of D_h^H with $k_{cH} = 10\,, D_c = D_h^M = D_h^O = 1$.

Figure 4.16: Plots showing the numerical results for the width of the second reaction front as a function of time τ for different values of (a) k_{cH} and (b) D_h^H. Other parameters include initial oxide and hydride thicknesses, $\delta_O = 10$, $\delta_H = 5$.

Width of RF2: Similar to (4.29), the width of the second reaction front (δ_2) can be calculated through the second moment of $\mathcal{R}_2(z,\tau)$ defined as

$$\delta_2^2(\tau) = \int_{-z_\infty}^{z_s(\tau)} (z - z_2(\tau))^2 \, \frac{\mathcal{R}_2(z,\tau)}{\mathcal{R}_2(\tau)} \, \mathrm{d}z \,, \tag{4.30}$$

where the local reaction rate $\mathcal{R}_2(z,\tau)$ is given by (4.27) and the total reaction rate of reaction R3 (see § 1.2.6) can be found by integrating the local reaction rate across the material domain. The maximum of the reaction rates $\mathcal{R}_1(z,\tau)$ and $\mathcal{R}_2(z,\tau)$ occur within the respective reaction fronts, and the centre of RF2 (i.e. $z_2(\tau)$) is considered as the location where (4.27) is maximised.

Figure 4.16 clearly depicts that D_h^H and k_{cH} do not have any significant influence on the kinetics of the reaction between $\mathrm{H}^{\bullet}$ (hydrogen radicals) and U (uranium metal) and thence on the width of the second reaction front.

The influence of different parameters on the rate of water vapour corrosion of uranium has been studied via the numerical experiments. However, the leading-order quantitative dependencies of the oxidation kinetics on parameters such as the diffusivities, material densities and the rate constants can be investigated only via a large-time asymptotic analysis. The motivation for a large-time ($\tau \gg 1$) asymptotic analysis is threefold. We hope it will (i) explicitly reveal the dominant parameters in the model that influence the oxidation kinetics, (ii) provide an appropriate discrete-layer analogue for the mixed-phase model that investigates the complex physicochemical processes involved in the water-vapour oxidation, and (iii) serve to validate the numerical results presented in this section. The asymptotic formulation for the uranium/water-vapour oxidation is presented in the next section, whilst a validation of the numerical results against the asymptotic results will be presented in §§ 4.2.6.

4.2.5 Large-time asymptotic analysis

In this section, we discuss the large-time asymptotics (in the slow-time variable τ) of the system (4.17). In our multi-component reaction-diffusion-advection system, we assume a priori that we have three diffusion layers and two reaction fronts, and look for the large-time scaling behaviours of each of those layers. We label the diffusion layers (from the surface inwards) as *layer A* (oxide layer), *layer B* (hydride layer) and the *bulk* (unreacted metal); the reaction fronts between the diffusion layers are labelled as RF1 and RF2. A schematic of the diffusion layers and the reaction fronts with asymptotic predictions of their widths (which will be subsequently obtained) is presented in Figure 4.17.

Reaction fronts are spatially localised regions where there is occurrence of maximal reaction rates (Bazant and Stone, 2000) of the respective reactions.

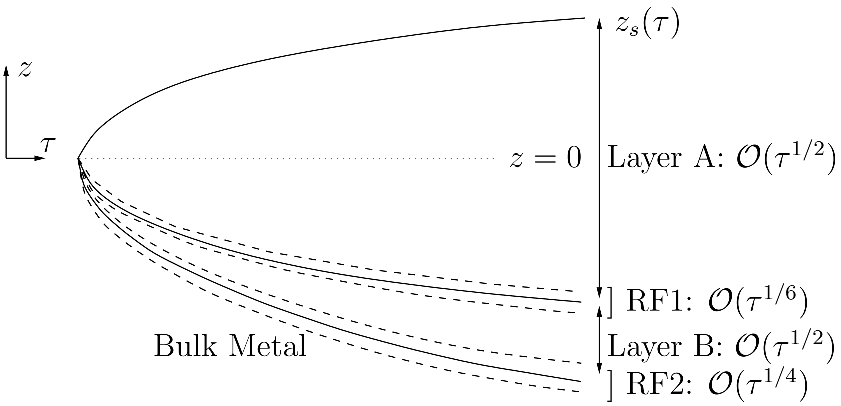

Figure 4.17: A schematic of the asymptotic regions in the general case of $D_h^H \neq 0$. The initial surface is located at $z = z_s(0) = 0$ but the medium expands as the reactions proceed, with the surface identified by $z = z_s(\tau) > 0$ for $\tau > 0$. The two reaction fronts are found at $z = z_1(\tau)$ (RF1) and $z = z_2(\tau)$ (RF2) and are separated by a diffusion layer (layer B) of thickness $\mathcal{O}(\tau^{1/2})$. The depicted scaling predictions for the reaction fronts are obtained later.

As a reminder, in RF1, hydroxide ions (c) react with uranium hydride (H) to produce uranium dioxide (O) and hydrogen radicals (h); in RF2, regeneration of the hydride occurs by the reaction of hydrogen radicals with uranium metal (M). The reaction fronts move into the bulk metal as the reactions proceed to consume the reactants at the respective fronts. Thus, there is an intricate coupling of the reaction kinetics in RF2 with that in RF1; that is, whilst the two reactions occur in spatially isolated regions, the full solution remains coupled.

In addition to the physical processes of diffusion and reaction, there is advection resulting from material expansion owing to differing densities of the nondiffusing phases. This contributes to additional complexity in solving the system.

4.2.5.1 Oxide layer: *Diffusion layer A*

It has been well-established by several authors (Gálfi and Rácz, 1988; Jiang and Ebner, 1990; Bazant and Stone, 2000; Koza, 1996) that a 'diffusion layer' (where diffusion dominates over reaction) has a square-root time dependence. Therefore an overlying oxide which has not yet cracked or spalled has a square-root dependence on time given by $\Delta_O \sim \tau^{1/2}$, where Δ_O is the dimensionless width (or thickness) of the oxide layer. In this layer, we have $H\,, M \ll 1$, and therefore the set of governing equations (4.17) (with $\epsilon = 0$) reduces to

$$\frac{\partial}{\partial z}\left(D_c \frac{\partial c}{\partial z}\right) = 0\,, \tag{4.31a}$$

$$\frac{\partial}{\partial z}\left(D_h \frac{\partial h}{\partial z}\right) = 0\,, \tag{4.31b}$$

$$O \approx 1\,, \tag{4.31c}$$

which on integration gives linear concentration profiles for c and h in the oxide layer (as $H\,, M \ll 1$ implying that $D_{c,h}$ are constant). Applying the boundary condition $c = 1$ on $z = z_s(\tau)$, and the asymptotic matching condition $c \to 0$ as $z \to z_1^+$ on (4.31a), we have

$$c \sim \frac{z - z_1(\tau)}{z_s(\tau) - z_1(\tau)} \tag{4.32}$$

at leading order, where $z_s(\tau)$ represents the time-varying surface position and $z_1(\tau)$ is the position of maximal reaction rate in *reaction front 1*. Note that we still work in the physical domain as opposed to the computational domain which was used for ease of solving the system numerically.

Now, applying the boundary condition $h = 0$ on $z = z_s(\tau)$ and the asymptotic matching condition $h = \mathcal{O}(1)$ as $z \to z_1^+$ on (4.31b), we obtain

$$h \sim \mathcal{A}(\tau)(z_s(\tau) - z)) \tag{4.33}$$

at leading order, where $\mathcal{A}(\tau) = \mathcal{O}(\tau^{-1/2})$. The solutions (4.32) and (4.33) represent the *outer solutions* of c and h in the oxide layer.

4.2.5.2 Reaction front 1 (RF1)

We have assumed a priori that the diffusion layers have a different thickness scaling compared to that of the reaction fronts. We therefore, look for a scaling of RF1 of the form: $\delta_1 \sim \tau^{\alpha}$, where δ_1 represents the width of the RF1. The scaling exponent α is such that $0 < \alpha < 1/2$, since the oxide is produced from the hydride over a spatial scale relatively thin compared to the growing oxide thickness, i.e., the reaction front is spatially localised with respect to the diffusion layers over large times (Bazant and Stone, 2000).

As the initial surface is located at $z_s(0) = 0$, we can write the location of the first reaction front as

$$z_1(\tau) = -L_A \tau^{1/2} + \cdots\,, \tag{4.34}$$

where $L_A > 0$ is defined as the growth-coefficient of the oxide layer (*layer A*) from the initial surface location $z_s(0)$.

The growth of the free surface due to volume expansion is then expressed as

$$z_s(\tau) = L_s \tau^{1/2} + \cdots \,, \tag{4.35}$$

where $L_s > 0$ denotes the growth-coefficient of the free surface (or oxide surface) from the initial surface location; growth-coefficients are constants multiplying the time-dependent terms describing the kinetics of surfaces/interfaces and are dependent on the material properties such as the material densities and diffusivities. The opposite signs of (4.34) and (4.35) signify that the direction of propagation of the surface is opposite to that of the reaction front. From (4.34) and (4.35), the definition of width (or thickness) of the oxide layer is

$$\Delta_O = z_s(\tau) - z_1(\tau) \sim (L_A + L_s)\,\tau^{1/2} \,. \tag{4.36}$$

In this inner region (RF1), we define an inner coordinate

$$X \equiv \frac{(z - z_1(\tau))}{\tau^{\alpha}} \tag{4.37}$$

in a moving reference frame, with the transformation rules

$$\begin{gathered} \partial_z \to \tau^{-\alpha}\partial_X \,, \quad \partial_{zz} \to \tau^{-2\alpha}\partial_{XX} \,, \\ \partial_\tau \to \partial_\tau + \left\{ \frac{1}{2} L_A \tau^{-\frac{1}{2}-\alpha} - \alpha X \tau^{-1} \right\} \partial_X \,, \end{gathered} \tag{4.38}$$

as $z_1(\tau) = z_s(0) - L_A \tau^{1/2}$ at leading-order.

The governing equations (4.17) (with $\epsilon = 0$) in terms of this inner coordinate are now:

$$\tau^{-2\alpha} \frac{\partial}{\partial X}\left(D_c \frac{\partial c}{\partial X} \right) = 2k_{cH}\, c^2 H \,, \tag{4.39a}$$

$$\tau^{-2\alpha} \frac{\partial}{\partial X}\left(D_h \frac{\partial h}{\partial X} \right) = -5k_{cH}\, c^2 H + 3\, h^3 M \,, \tag{4.39b}$$

$$\frac{\partial O}{\partial \tau} + \left\{ \frac{1}{2} L_A \tau^{-\frac{1}{2}-\alpha} - \alpha X \tau^{-1} \right\} \frac{\partial O}{\partial X} + \tau^{-\alpha} \frac{\partial}{\partial X}(VO) = k_{cH}\, c^2 H \left(\frac{N_M^*}{N_O^*} \right) , \tag{4.39c}$$

$$\begin{aligned}\frac{\partial H}{\partial \tau}+\left\{\frac{1}{2}L_A\tau^{-\frac{1}{2}-\alpha}-\alpha X\tau^{-1}\right\}\frac{\partial H}{\partial X}+\tau^{-\alpha}\frac{\partial}{\partial X}(VH)&\\ =(h^3M-k_{cH}\,c^2H)\left(\frac{N_M^*}{N_H^*}\right),&\end{aligned}\tag{4.39d}$$

$$\frac{\partial M}{\partial \tau}+\left\{\frac{1}{2}L_A\tau^{-\frac{1}{2}-\alpha}-\alpha X\tau^{-1}\right\}\frac{\partial M}{\partial X}+\tau^{-\alpha}\frac{\partial}{\partial X}(VM)=-h^3M\,,\tag{4.39e}$$

in RF1.

The transformed equation for advection velocity (4.17f) in this *inner region* is now:

$$\tau^{-\alpha}\frac{\partial V}{\partial X}=h^3M\left(\frac{N_M^*}{N_H^*}-1\right)+k_{cH}c^2H\left(\frac{N_M^*}{N_O^*}-\frac{N_M^*}{N_H^*}\right).\tag{4.39f}$$

In order to assume the form of the asymptotic expansions for the concentrations in RF1, we make use of the asymptotic matching principles. In the limit $z\to z_1^+$, around the neighbourhood of z_1, we can write the outer solution of c (4.32) in terms of the inner variable X as

$$c\sim\frac{X}{(L_A+L_s)}\tau^{\alpha-\frac{1}{2}}\,,\tag{4.40}$$

where (L_A+L_s) represents the overall growth-coefficient of the oxide layer as defined in (4.36).

Similarly, if we write the outer solution of h (4.33) in terms of the inner variable X as $z\to z_1^+$, we obtain

$$h\sim\mathcal{A}(\tau)\left[z_s(\tau)-z_1(\tau)-X\tau^{\alpha}\right].\tag{4.41}$$

We know from numerical simulations that the peak hydrogen radical concentration (h_p) remains constant for large times, and hence we take

$$\mathcal{A}(\tau)=\frac{h_p}{L_A+L_s}\tau^{-\frac{1}{2}}\,,\tag{4.42}$$

such that the leading-order concentration of h asymptotes to h_p in RF1. Therefore, we can write

$$h\sim h_p\left[1-\frac{X}{L_A+L_s}\tau^{\alpha-\frac{1}{2}}\right],\tag{4.43}$$

from the definition of Δ_O (see equation (4.36)).

Therefore, based on (4.40) and (4.43), we suggest asymptotic expansions in RF1 of the form:

$$c = \tau^{\alpha-\frac{1}{2}}\bar{c}_0(X) + \cdots\,, \tag{4.44a}$$

$$h = \bar{h}_0(X) + \tau^{\alpha-\frac{1}{2}}\bar{h}_1(X) + \cdots\,, \tag{4.44b}$$

$$O = \bar{O}_0(X) + \cdots\,, \tag{4.44c}$$

$$H = \bar{H}_0(X) + \cdots\,, \tag{4.44d}$$

$$M \ll 1\,, \tag{4.44e}$$

where $\bar{c}_0(X)$, $\bar{h}_0(X)$, $\bar{O}_0(X)$ and $\bar{H}_0(X)$ are the leading-order asymptotically time-invariant solutions in the inner region RF1, which are functions of the inner variable X, and $\bar{h}_1$ represents a first-order correction term of h. Hence, the asymptotic approximation of the advection velocity in RF1 can be written as

$$V = \tau^{-\gamma}\bar{V}_0(X) + \cdots\,, \tag{4.45}$$

which follows from (4.39f) for some γ.

Now, considering a non-trivial balance in (4.39a), we have that

$$\alpha = \frac{1}{6}\,, \tag{4.46}$$

which determines $\gamma = 1/2$.

The leading-order ($\mathcal{O}(\tau^{-\frac{2}{3}})$) governing equations in RF1 are thus,

$$\frac{\mathrm{d}}{\mathrm{d}X}\left(\bar{D}_c\frac{\mathrm{d}\bar{c}_0}{\mathrm{d}X}\right) = 2k_{cH}\bar{c}_0^2\bar{H}_0\,, \tag{4.47a}$$

$$\frac{\mathrm{d}}{\mathrm{d}X}\left(\bar{D}_h\frac{\mathrm{d}\bar{h}_1}{\mathrm{d}X}\right) = -5k_{cH}\bar{c}_0^2\bar{H}_0\,, \tag{4.47b}$$

$$\frac{1}{2}L_A\frac{\mathrm{d}\bar{H}_0}{\mathrm{d}X} + \frac{\mathrm{d}\big(\bar{H}_0\bar{V}_0\big)}{\mathrm{d}X} = -k_{cH}\bar{c}_0^2\bar{H}_0\frac{N_M^*}{N_H^*}\,, \tag{4.47c}$$

$$\frac{\mathrm{d}\bar{V}_0}{\mathrm{d}X} = k_{cH}\bar{c}_0^2\bar{H}_0\left(\frac{N_M^*}{N_O^*} - \frac{N_M^*}{N_H^*}\right)\,, \tag{4.47d}$$

whilst the governing equation for h containing the leading-order term yields the trivial equation

$$\frac{\mathrm{d}}{\mathrm{d}X}\left(\bar{D}_h\frac{\mathrm{d}\bar{h}_0}{\mathrm{d}X}\right) = 0\,, \tag{4.47e}$$

where

$$\bar{D}_{c,h}(X) = D^H_{c,h}\bar{H}_0 + D^O_{c,h}\left(1-\bar{H}_0\right), \tag{4.47f}$$

and $D^O_c = 1$ by our choice of a reference diffusivity ($D^*_{ref} = D^{O*}_c$). Here, $\bar{O}_0 = 1 - \bar{H}_0$ provides the oxide fraction which is also consistent with (4.39c). The neglected quantity $M = o(\tau^{-\frac{2}{3}})$.

The first-order correction term $\bar{h}_1$ is needed to determine the gradient of the h-profile in the hydride layer, which will then be used to determine the matching conditions for h in RF2.

Matching (4.47) with *layer A* (refer (4.40) and (4.43) for outer solutions of c and h), we obtain

$$\frac{\mathrm{d}\bar{c}_0}{\mathrm{d}X} \sim \frac{1}{L_s+L_A}\,, \quad \bar{h}_0 \sim h_p\,, \quad \frac{\mathrm{d}\bar{h}_1}{\mathrm{d}X} \sim -\frac{h_p}{L_s+L_A}\,, \quad \bar{H}_0 \to 0 \quad \text{as} \quad X \to +\infty\,, \tag{4.48}$$

and matching with *layer B*, we have

$$\bar{c}_0 \to 0\,, \quad \frac{\mathrm{d}\bar{h}_1}{\mathrm{d}X} \sim \mu\,, \quad \bar{H}_0 \to 1 \quad \text{as} \quad X \to -\infty\,, \tag{4.49}$$

where μ will be determined later. The above matching condition for $\bar{c}_0$ as $X \to -\infty$ essentially implies that the diffusing OH^- ions are fully consumed in RF1, which is consistent with the experimental results of Martin et al. (2016) and the theoretical reaction front solutions of Bazant and Stone (2000). The matching conditions for the advection velocity will be found subsequently.

We can solve (4.47) numerically using a shooting method to obtain the concentration profiles within the first reaction front, which will be discussed in § 4.2.7. However, the full solution within the reaction front is not essential to making progress with the asymptotic description and to obtain the matching conditions for the hydride layer. We integrate (4.47) across first reaction front to find μ and the relevant matching conditions for the advection velocity.

Integration across RF1: Now, on integrating (4.47a) across RF1, i.e. from $X \to -\infty$ to $X \to +\infty$, we obtain

$$\left[\bar{D}_c \frac{\mathrm{d}\bar{c}_0}{\mathrm{d}X}\right]_{-\infty}^{\infty} = 2\, k_{cH} \int_{-\infty}^{\infty} \bar{c}_0^2 \bar{H}_0 \, \mathrm{d}X \, . \tag{4.50}$$

Defining

$$I_{RF1} \equiv k_{cH} \int_{-\infty}^{\infty} \bar{c}_0^2 \bar{H}_0 \, \mathrm{d}X \, , \tag{4.51}$$

and using the matching constraints

$$\bar{c}_0(-\infty) = 0 \, , \qquad \left(\frac{\mathrm{d}\bar{c}_0}{\mathrm{d}X}\right)\bigg|_{\infty} = \frac{1}{(L_A + L_s)} \, , \qquad \bar{D}_c(+\infty) = D_c^O = 1 \, , \tag{4.52}$$

we obtain

$$I_{RF1} = \frac{1}{2(L_A + L_s)} \, . \tag{4.53}$$

Similarly, on integrating (4.47b) across RF1, from $X \to -\infty$ to $X \to +\infty$, we obtain

$$D_h^O \left(\frac{\mathrm{d}\bar{h}_1}{\mathrm{d}X}\right)\bigg|_{\infty} - D_h^H \left(\frac{\mathrm{d}\bar{h}_1}{\mathrm{d}X}\right)\bigg|_{-\infty} = -\frac{5}{2}\left(\frac{1}{L_A + L_s}\right) \, . \tag{4.54}$$

Substituting (4.48) in the above equation gives

$$\mu = \left(\frac{\mathrm{d}\bar{h}_1}{\mathrm{d}X}\right)\bigg|_{-\infty} = \frac{1}{2\, D_h^H}\left[\frac{5 - 2\, D_h^O h_p}{(L_A + L_s)}\right] \, , \tag{4.55}$$

thus providing the gradient for the concentration of H$^{\bullet}$ (h) in layer B.

Determination of advection velocity: Taking the same approach and integrating (4.47c), we find that

$$\frac{1}{2} L_A \left[\bar{H}_0\right]_{-\infty}^{\infty} + \left[\bar{V}_0 \bar{H}_0\right]_{-\infty}^{\infty} = -\frac{N_M^*}{N_H^*} I_{RF1} \, , \tag{4.56}$$

where $\bar{H}_0(+\infty) = 0$ and $\bar{H}_0(-\infty) = 1$. The advection velocity *'ahead'* of the front (with respect to the direction of propagation of the reaction front) is thus determined to be

$$\bar{V}_0|_{-\infty} = -\frac{L_A}{2} + \frac{N_M^*}{N_H^*}\,\frac{1}{2\,(L_A + L_s)}\,, \tag{4.57}$$

and the advection velocity '*behind*' the front (i.e., as $X \to +\infty$) is determined from the leading-order governing equation for the oxide fraction which is written from (4.39c):

$$\frac{1}{2}L_A\frac{\mathrm{d}\bar{O}_0}{\mathrm{d}X} + \frac{\mathrm{d}\big(\bar{O}_0\bar{V}_0\big)}{\mathrm{d}X} = k_{cH}\bar{c}_0^2\bar{H}_0\frac{N_M^*}{N_O^*}\,. \tag{4.58}$$

On integrating the above equation using appropriate matching constraints (where $\bar{O}_0 = 1 - \bar{H}_0$), we obtain

$$\bar{V}_0|_{\infty} = -\frac{L_A}{2} + \frac{N_M^*}{N_O^*}\frac{1}{2\,(L_A + L_s)}\,. \tag{4.59}$$

4.2.5.3 Hydride layer: *Diffusion layer B*

The hydride layer exists as an intermediate layer between the two reaction fronts, and diffusion dominates over the reaction terms in this region. At sufficiently large times, the width of the hydride layer scales with time (τ) as

$$\Delta_H \sim L_B\tau^{\frac{1}{2}}\,, \tag{4.60}$$

where Δ_H is the dimensionless width and $L_B > 0$ represents its corresponding growth-coefficient, the form of which will be derived subsequently. Since there is quasi-steady diffusion of hydrogen radicals (h) in the hydride layer, the concentration of $\mathrm{H}^{\bullet}$ remains linear in *layer B*, which can then be written in terms of the inner coordinate X as

$$h = h_p + \left(\frac{\mathrm{d}\bar{h}_1}{\mathrm{d}X}\right)\bigg|_{-\infty} X\tau^{-\frac{1}{3}} + \cdots\,. \tag{4.61}$$

The above equation on matching with RF1 gives

$$h = h_p + \frac{1}{D_h^H}\left[\frac{5\, - 2\,h_pD_h^O}{2\,(L_A + L_s)}\right](z - z_1)\tau^{-\frac{1}{2}} + \cdots\,. \tag{4.62}$$

The second reaction front is found at $z = z_2(\tau)$, where there is maximal reaction rate for the formation of uranium hydride (H) from hydrogen radicals (h). This implies that $h = o(1)$ at $z = z_2(\tau)$, and therefore (4.62) becomes

$$0 = h_p + \frac{1}{D_h^H}\left[\frac{5\ - 2\,h_p D_h^O}{2\,(L_A + L_s)}\right][-L_B] + \cdots\,, \tag{4.63}$$

where the leading-order description of $z_2(\tau)$ given by

$$z_2(\tau) = z_1(\tau) - L_B \tau^{1/2} \tag{4.64}$$

has been substituted. This results in a leading-order mathematical expression for the growth-coefficient of the hydride layer given by

$$L_B = \frac{2\,h_p (L_A + L_s) D_h^H}{5\ - 2\,h_p D_h^O}\,. \tag{4.65}$$

It should be noted that the $\sim \tau^{1/2}$ dependence of the hydride thickness is found based on the reasoning that the asymptotic expansion (4.62) disorders at the second reaction front found at $z = z_2(\tau)$.

4.2.5.4 Reaction front 2 (RF2)

At large times, we consider that the width of the second reaction front scales with time as $\delta_2 \sim \tau^\beta$ with $0 < \beta < 1/2$.

We define an *inner coordinate* (i.e., a stretched coordinate) Y in the second reaction front (RF2):

$$Y \equiv \frac{z - z_2(\tau)}{\tau^\beta}\,, \tag{4.66}$$

where $z_2(\tau)$ represents the location of maximal reaction rate in RF2.

In order to obtain matching conditions for the limit $Y \to +\infty$ (i.e. *behind* RF2), we match with the limit $X \to -\infty$ (i.e. *ahead* of RF1). This approach is valid since we have quasi-steady diffusion in the hydride layer, as explained before.

Therefore, in the second inner region (RF2), where $z = z_2 + Y\tau^\beta$, the outer asymptotic expansion for h (4.62) can be written using the inner variable Y as

$$h \sim \frac{1}{D_h^H}\left(\frac{5\,-2\,h_p D_h^O}{2\,(L_A+L_s)}\right) Y\tau^{-\frac{1}{2}+\beta}\,, \tag{4.67}$$

which gives insight into the form of the asymptotic expansions in RF2.

We now look for asymptotic expansions in RF2 of the form:

$$h = \hat{h}_0(Y)\tau^{\beta-\frac{1}{2}} + \cdots\,, \tag{4.68a}$$

$$M = \hat{M}_0(Y) + \cdots\,, \tag{4.68b}$$

$$H = \hat{H}_0(Y) + \cdots\,, \tag{4.68c}$$

$$c\,, O \ll 1\,, \tag{4.68d}$$

where the variables with the hat symbol $(\hat{\circ})$ represent the transformed variables in RF2 that are functions of the inner variable Y. The transformed advection velocity in RF2 is assumed to have a power-law scaling of the form:

$$V = \tau^{-\mu}\hat{V}_0(Y) + \ldots\,. \tag{4.68e}$$

The transformed governing equations (i.e., transformation from $(z,\tau) \mapsto (Y,\tau)$ coordinates) for $c\,, h\,, H\,, M\,, O$ and V in RF2 are given by,

$$\tau^{-2\beta}\frac{\partial}{\partial Y}\left(D_c\,\frac{\partial c}{\partial Y}\right) = 2\,k_{cH}c^2H\,, \tag{4.69a}$$

$$\tau^{-2\beta}\frac{\partial}{\partial Y}\left(D_h\,\frac{\partial h}{\partial Y}\right) = 3\,h^3M - 5\,k_{cH}c^2H\,, \tag{4.69b}$$

$$\begin{aligned}\frac{\partial H}{\partial \tau} + \left\{\frac{1}{2}(L_A+L_B)\tau^{-\frac{1}{2}-\beta} - \beta Y\tau^{-1}\right\}\frac{\partial H}{\partial Y} + \tau^{-\beta}\frac{\partial}{\partial Y}\,(VH)& \\ = \left(h^3M - k_{cH}c^2H\right)\frac{N_M^*}{N_H^*}&\,,\end{aligned} \tag{4.69c}$$

$$\frac{\partial M}{\partial \tau} + \left\{\frac{1}{2}(L_A+L_B)\tau^{-\frac{1}{2}-\beta} - \beta Y\tau^{-1}\right\}\frac{\partial M}{\partial Y} + \tau^{-\beta}\frac{\partial}{\partial Y}\,(VM) = -h^3M\,, \tag{4.69d}$$

$$\frac{\partial O}{\partial \tau} + \left\{\frac{1}{2}(L_A+L_B)\tau^{-\frac{1}{2}-\beta} - \beta Y\tau^{-1}\right\}\frac{\partial O}{\partial Y} + \tau^{-\beta}\frac{\partial}{\partial Y}\,(VH) = k_{cH}c^2H\frac{N_M^*}{N_O^*}\,, \tag{4.69e}$$

$$\tau^{-\beta}\frac{\partial V}{\partial Y} = h^3M\left(\frac{N_M^*}{N_H^*} - 1\right) + k_{cH}c^2H\left(\frac{N_M^*}{N_O^*} - \frac{N_M^*}{N_H^*}\right)\,, \tag{4.69f}$$

where

$$D_h = D_h^H H + D_h^M M + D_h^O O\,. \tag{4.69g}$$

On substituting the asymptotic expansions (4.68) in (4.69b), a dominant balance of the diffusion term on the left-hand side with the reaction term $3h^3M$ on the right-hand side provides

$$\beta = \frac{1}{4}\,. \tag{4.70}$$

Substituting (4.68) in (4.69f), we have the scaling for the advection velocity in RF2 as $\mu = 1/2$, which is derived from a balance of

$$\tau^{-\beta-\mu}\frac{\mathrm{d}\hat{V}_0}{\mathrm{d}Y} \sim \tau^{3\beta-\frac{3}{2}}\hat{h}_0{}^3\hat{M}_0\left(\frac{N_M^*}{N_H^*}-1\right)\,. \tag{4.71}$$

The leading-order ($\mathcal{O}(\tau^{-\frac{3}{4}})$) governing equations derived by substituting the asymptotic expansions (4.68) in (4.69) are now,

$$\frac{\mathrm{d}}{\mathrm{d}Y}\left(\hat{D}_h\frac{\mathrm{d}\hat{h}_0}{\mathrm{d}Y}\right) = 3\hat{h}_0^3\hat{M}_0\,, \tag{4.72a}$$

$$\frac{1}{2}(L_A+L_B)\frac{\mathrm{d}\hat{H}_0}{\mathrm{d}Y} + \frac{\mathrm{d}\left(\hat{V}_0\hat{H}_0\right)}{\mathrm{d}Y} = \frac{N_M^*}{N_H^*}\hat{h}_0^3\hat{M}_0\,, \tag{4.72b}$$

$$\frac{1}{2}(L_A+L_B)\frac{\mathrm{d}\hat{M}_0}{\mathrm{d}Y} + \frac{\mathrm{d}\left(\hat{V}_0\hat{M}_0\right)}{\mathrm{d}Y} = -\hat{h}_0^3\hat{M}_0\,, \tag{4.72c}$$

$$\frac{\mathrm{d}\hat{V}_0}{\mathrm{d}Y} = \hat{h}_0{}^3\hat{M}_0\left(\frac{N_M^*}{N_H^*}-1\right)\,, \tag{4.72d}$$

where

$$\hat{D}_h(Y) = D_h^H\hat{H}_0 + D_h^M\left(1-\hat{H}_0\right)\,, \tag{4.72e}$$

with the following constraints obtained from matching with *layer B*:

$$\left.\begin{array}{c}\dfrac{\mathrm{d}\hat{h}_0}{\mathrm{d}Y} \sim \dfrac{1}{D_h^H}\left(\dfrac{5-2h_pD_h^O}{2(L_s+L_A)}\right)\,, \quad \hat{H}_0 \to 1\,, \\ \hat{M}_0 \to 0\,, \quad \hat{V}_0 \to \hat{V}_0(\infty)\end{array}\right\} \quad \text{as} \quad Y \to +\infty\,. \tag{4.72f}$$

Similarly, matching with the unreacted metal yields

$$\hat{h}_0 \to 0\,, \quad \hat{H}_0 \to 0\,, \quad \hat{M}_0 \to 1\,, \quad \hat{V}_0 \to 0 \quad \text{as} \quad Y \to -\infty\,. \tag{4.72g}$$

The neglected quantities are determined to be $c = o(\tau^{-\frac{3}{8}})$ and $O = o(1)$ from (4.69). The advection velocity $\hat{V}_0(\infty)$ as $Y \to +\infty$ will be determined as part of the solution process. We will solve for the concentration profiles in RF2 numerically using a shooting method in § 4.2.7, but for now, we proceed with the asymptotic solution by integrating across RF2.

Integration across RF2: Integrating (4.72a) from $Y \to -\infty$ to $Y \to +\infty$, we obtain

$$\left[\hat{D}_h \frac{\mathrm{d}\hat{h}_0}{\mathrm{d}Y}\right]_{-\infty}^{\infty} = 3\int_{-\infty}^{\infty} \hat{h}_0^3 \hat{M}_0 \,\mathrm{d}Y\,. \tag{4.73}$$

If we define

$$I_{RF2} \equiv \int_{-\infty}^{\infty} \hat{h}_0^3 \hat{M}_0 \,\mathrm{d}Y\,, \tag{4.74}$$

and substituting $\hat{h}_0(-\infty) = 0$ in (4.73), we obtain

$$D_h^H \left(\frac{\mathrm{d}\hat{h}_0}{\mathrm{d}Y}\right)\Bigg|_{Y\to+\infty} = 3\, I_{RF2}\,. \tag{4.75}$$

From the matching constraints, we know that

$$\frac{\mathrm{d}\hat{h}_0}{\mathrm{d}Y}\bigg|_{Y\to+\infty} = \frac{\mathrm{d}\bar{h}_0}{\mathrm{d}X}\bigg|_{X\to-\infty} = \left[\frac{5\, - 2\,h_p D_h^O}{2\,D_h^H (L_A + L_s)}\right]\,, \tag{4.76}$$

from which I_{RF2} is determined to be

$$I_{RF2} = \frac{1}{6}\left(\frac{5\, - 2\,h_p D_h^O}{(L_A + L_s)}\right)\,. \tag{4.77}$$

Determination of the advection velocity in RF2 : Having obtained an analytical expression for I_{RF2}, the advection velocity in RF2 can be determined by integrating the governing equations in the region using the matching constraints. If we integrate the leading-order governing equation for H (4.72b) across RF2, we obtain

$$\frac{1}{2}\,(L_A + L_B)[\hat{H}_0]_{-\infty}^{\infty} + [\hat{V}_0 \hat{H}_0]_{-\infty}^{\infty} = \left(\frac{N_M^*}{N_H^*}\right) I_{RF2}\,. \tag{4.78}$$

As $\hat{H}(+\infty) = 1$ and $\hat{H}(-\infty) = 0$, we have the leading-order advection velocity in RF2 in the limit $Y \to +\infty$ given by

$$\hat{V}_0|_{\infty} = -\frac{1}{2}(L_A + L_B) + \frac{N_M^*}{N_H^*}\,\frac{1}{6}\left(\frac{5\; - 2\,h_p D_h^O}{L_A + L_s}\right)\,. \tag{4.79}$$

Similarly, from the leading-order governing equation for M, we derive the advection velocity in the limit $Y \to -\infty$ as

$$\hat{V}_0|_{-\infty} = -\frac{1}{2}\,(L_A + L_B) + \frac{1}{6}\left[\frac{5\; - 2\,h_p D_h^O}{L_A + L_s}\right]\,. \tag{4.80}$$

Since there is no advection in the metal layer, we have $\hat{V}_0(-\infty) = 0$, which implies that

$$\frac{1}{2}\,(L_A + L_B) = \frac{1}{6}\left(\frac{5\; - 2\,h_p D_h^O}{L_A + L_s}\right)\,. \tag{4.81}$$

It must be noted that the above expression has been determined by using the matching constraints $\hat{M}(-\infty) = 1$ and $\hat{M}(+\infty) = 0$.

Now, requiring that the advection velocities match across layer B as the advection velocity is spatially varying only in the reaction fronts, i.e. since $\hat{V}_0(+\infty) = \bar{V}_0(-\infty)$ (see (4.57) and (4.79)), we have

$$-\frac{(L_A + L_B)}{2} + \frac{N_M^*}{N_H^*}\frac{1}{6}\left(\frac{5\; - 2\,h_p D_h^O}{L_A + L_s}\right) = -\frac{L_A}{2} + \left(\frac{N_M^*}{N_H^*}\right)\frac{1}{2\,(L_A + L_s)}\,, \tag{4.82}$$

which provides an algebraic equation relating the three unknown coefficients L_A, L_B, L_s and the peak hydrogen radical concentration h_p as a function of the material densities and the diffusion coefficients.

We now have three algebraic equations (4.65), (4.81) and (4.82) relating the four unknown quantities. To obtain closure to the system of equations, we have $\bar{V}(+\infty) = L_s/2$ derived from (4.35) (as the surface is advected during the material expansion), and hence we find that

$$L_A + L_s = \sqrt{\frac{N_M^*}{N_O^*}} \,. \tag{4.83}$$

After some algebraic manipulations performed on (4.65), (4.81), (4.82) and (4.83), we find that

$$L_A = \sqrt{\frac{N_O^*}{N_M^*}} + \left(\frac{N_H^*}{N_M^*} - 1\right) L_B \,, \tag{4.84}$$

and

$$8D_h^O h_p = 14 + 6\frac{D_h^H}{D_h^O}\frac{N_H^*}{N_O^*} - \left\{\left(14 + 6\frac{D_h^H}{D_h^O}\frac{N_H^*}{N_O^*}\right)^2 - 160\right\}^{\frac{1}{2}} \,. \tag{4.85}$$

Substituting the above expression for $D_h^O h_p$ and (4.83) in (4.65), we obtain the growth-coefficient of the hydride layer L_B, which in turn can be substituted in (4.84) to obtain L_A. The dependence of the unknown growth-coefficients

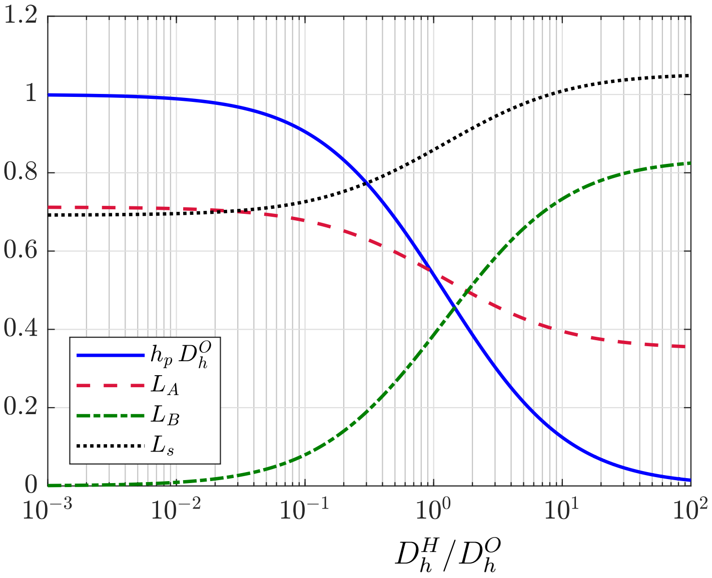

Figure 4.18: Dependence of L_A, L_B, L_s and $D_h^O\, h_p$ on the ratio of diffusivities D_h^H/D_h^O. Given $L_{A,B,s}$ the positions of the two reaction fronts and the expanding surface of the solid are known via (4.34), (4.64) and (4.35) respectively. Here these results use $N_H^*/N_O^* \approx 1.12$ and $N_M^*/N_H^* \approx 1.76$, as appropriate for the uranium oxidation example.

$L_A\,,L_B\,,L_s$ and the peak hydrogen radical concentration h_p on the diffusivity ratios and the material densities is shown in Figure 4.18. The growth-coefficients $L_A\,,L_B\,,L_s$ determine the positions of the first and second reaction fronts and the surface respectively, from which the leading-order oxide and hydride thicknesses can be found. From equations (4.65), (4.83), (4.84) and (4.85), it is evident that these coefficients depend only on the ratio of the diffusivities D_h^H/D_h^O for fixed material densities (see Table A.1) at leading-order. Furthermore, it is evident that the reaction rate constant k_{cH} does not have an impact on this leading-order description of the growth-kinetics and only influences the thickness of the first reaction front (see § 4.2.4 and Figure 4.10).

There is some degree of uncertainty in the precise values of the diffusion coefficients, and therefore we will compare the results over a range of parameters in §§ 4.2.6. However, from the literature, the expectation is for D_h^H to be small relative to D_c^O. For $D_h^H = 10^{-3}$ and $D_h^O = 1$, we find

$$L_s = 0.6921, \quad L_A = 0.7119, \quad L_B = 0.0009 \quad \text{and} \quad h_p = 0.9989\,, \tag{4.86}$$

which will be compared with the numerical results in §§ 4.2.6.

4.2.5.5 *A special case:* $D_h^H = 0\,, D_h^O \neq 0$:

As $D_h^H/D_h^O \to 0$, the leading-order thickness of the hydride layer as defined by (4.64) tends to zero, i.e. $L_B \to 0$ (where L_B is given by (4.65)). We therefore address the limiting behaviour when $D_h^H = 0$ in this subsection. It can be seen from the governing equations (4.47) that the coupling is only one way between the quantities $(\bar{c}_0\,,\bar{H}_0\,,\bar{V}_0)$ and $\bar{h}_1$. The diffusivity ratio D_h^H/D_h^O only impacts the hydrogen radical concentration, and does not influence the quantities $(\bar{c}_0\,,\bar{H}_0\,,\bar{V}_0)$ at the first reaction front. Hence we proceed to find $\bar{h}_1$ in the limit when $D_h^H = 0$.

The leading-order governing equation for h in RF1 given by (4.47b) is integrated to yield

$$\bar{D}_h \frac{\mathrm{d}\bar{h}_1}{\mathrm{d}X} = -5k_{cH}\int_{-\infty}^{X} \bar{c}_0^2 \bar{H}_0 \,\mathrm{d}X + P\,, \tag{4.87}$$

where the constant of integration P is found by matching with *layer A* (refer

(4.48) for the matching constraints):

$$P = \bar{D}_h(\infty)\left(-\frac{h_p}{L_s + L_A}\right) + 5k_{cH}\int_{-\infty}^{\infty} \bar{c}_0^2 \bar{H}_0 \, \mathrm{d}X \,, \tag{4.88a}$$

$$= D_h^O\left(-\frac{h_p}{L_s + L_A}\right) + 5I_{RF1} \,, \tag{4.88b}$$

where I_{RF1} is given by (4.53). Substituting for the constant P in (4.87) we find the gradient of h in RF1:

$$\frac{\mathrm{d}\bar{h}_1}{\mathrm{d}X} = \frac{1}{\bar{D}_h(X)}\left[\frac{5 - 2h_p D_h^O}{2(L_s + L_A)} - 5k_{cH}\int_{-\infty}^{X} \bar{c}_0^2 \bar{H}_0 \, \mathrm{d}X\right] . \tag{4.89}$$

In the general case where $D_h^H > 0$, $\bar{D}_h(-\infty) = D_h^H$ as $\bar{H}_0(-\infty) \to 1$ (see (4.47f) for $\bar{D}_h$) and the gradient of h remains finite for large negative values of X. However, in this special case where $D_h^H = 0$, $\bar{D}_h(X) \ll 1$ as $X \to -\infty$ (see equation (4.47f)) and the gradient of h becomes unbounded for large negative values of X. We address this limiting behaviour as $X \to -\infty$ in order to analyse the factors that determine the hydride thickness when $D_h^H = 0$.

For large negative values of X in RF1, we seek asymptotic expansions of the form:

$$\bar{c}(X) = a_1 X^{-\mu_1} + \cdots \,, \tag{4.90a}$$

$$\bar{H}(X) = 1 + a_2 X^{-\mu_2} + \cdots \,, \tag{4.90b}$$

$$\bar{V}(X) = a_4 - a_3 X^{-\mu_3} + \cdots \,, \tag{4.90c}$$

where the constants $a_1 \,, a_2 \,, a_3 \,, a_4 > 0$. The leading-order term for $\bar{H}(X)$ has been determined from the limit as $X \to -\infty$ and similarly, the leading-order term for $\bar{V}(X)$ (transformed advection velocity in RF1) will be $\bar{V}(-\infty)$. Substituting the above asymptotic expansions in the leading-order (in τ) governing equations (4.47) in RF1, we arrive at

$$\frac{\mathrm{d}}{\mathrm{d}X}\left(\bar{D}_c(X)[-a_1\mu_1 X^{-\mu_1 - 1} + \cdots]\right) = 2k_{cH}(a_1 X^{-\mu_1} + \cdots)^2(1 + a_2 X^{-\mu_2} + \cdots) \,, \tag{4.91a}$$

$$\begin{aligned}\frac{1}{2}L_A\left(-\mu_2 a_2 X^{-\mu_2-1}+\cdots\right)+\left(a_4-a_3X^{-\mu_3}+\cdots\right)\left(-a_2\mu_2X^{-\mu_2-1}+\cdots\right)\\ +\left(1+a_2X^{-\mu_2}+\cdots\right)\left(a_3\mu_3X^{-\mu_3-1}+\cdots\right)\\ =-k_{cH}\frac{N_M^*}{N_H^*}\left(a_1^2X^{-2\mu_1}+\cdots\right)\left(1+a_2X^{-\mu_2}+\cdots\right)\,,\end{aligned} \tag{4.91b}$$

$$a_3\mu_3X^{-\mu_3-1}=k_{cH}\left(\frac{N_M^*}{N_O^*}-\frac{N_M^*}{N_H^*}\right)\left(a_1^2X^{-2\mu_1}+\cdots\right)\left(1+a_2X^{-\mu_2}+\cdots\right)\,. \tag{4.91c}$$

Now, considering a dominant balance of the leading-order terms in (4.91a), we obtain

$$D_c^H a_1\mu_1(\mu_1+1)X^{-\mu_1-2}\sim 2k_{cH}a_1^2X^{-2\mu_1}\,, \tag{4.92}$$

which yields the scaling relation

$$-\mu_1-2=-2\mu_1\,,\quad \Rightarrow \mu_1=2\,. \tag{4.93}$$

Substituting $\mu_1=2$ in (4.92), we determine the coefficient

$$a_1=\frac{3D_c^H}{k_{cH}}\,. \tag{4.94}$$

Similarly, from (4.91c), a dominant balance between the different terms

$$a_3\mu_3X^{-\mu_3-1}\sim k_{cH}a_1^2\left(\frac{N_M^*}{N_O^*}-\frac{N_M^*}{N_H^*}\right)X^{-2\mu_1}\,, \tag{4.95}$$

yields the scaling relation

$$-\mu_3-1=-2\mu_1,\quad \Rightarrow \mu_3=3\,, \tag{4.96}$$

and therefore, we find

$$a_3=\frac{3(D_c^H)^2}{k_{cH}}\left(\frac{N_M^*}{N_O^*}-\frac{N_M^*}{N_H^*}\right)\,. \tag{4.97}$$

The leading-order term in the asymptotic expansion for $\bar{V}$ is a constant a_4 as the advection velocity is constant outside of the reaction fronts. The leading-order constant term will then be $a_4 = \bar{V}(-\infty)$ (i.e., $\bar{V} = \bar{V}(-\infty)$ as $X \to -\infty$).

Now, a dominant balance of the reaction term with the $\frac{1}{2}L_A\bar{H}_X$ term in the leading-order governing equation (see equation (4.91b)):

$$\frac{1}{2}L_A[-\mu_2 a_2 X^{-\mu_2-1}] + (-a_2 a_4)\mu_2 X^{-\mu_2-1} + a_3\mu_3 X^{-\mu_3-1} = -k_{cH}\frac{N_M^*}{N_H^*}a_1^2 X^{-2\mu_1}\,, \tag{4.98}$$

gives the scaling relation

$$-\mu_2 - 1 \sim -2\mu_1, \quad \Rightarrow \mu_2 = 3\,. \tag{4.99}$$

Now, substituting $\mu_2 = \mu_3 = 3$, $a_4 = \bar{V}(-\infty)$ from (4.57), a_3 from (4.97) and $L_s + L_A = \sqrt{N_M^*/N_O^*}$ in (4.98), and performing some algebraic manipulations we obtain

$$a_2 = 6\frac{(N_M^*/N_O^*)^{\frac{3}{2}}}{(N_M^*/N_H^*)}\frac{(D_c^H)^2}{k_{cH}}\,. \tag{4.100}$$

Having obtained the coefficients and exponents in the asymptotic expansions, we now have

$$\bar{D}_h(X) \sim D_h^O(-a_2 X^{-3})\,, \tag{4.101}$$

since $D_h^H = 0$ and a_2 is given by (4.100).

Substituting (4.101) in (4.89), we obtain

$$\frac{\mathrm{d}\bar{h}_1}{\mathrm{d}X} = \frac{1}{D_h^O(-a_2X^{-3}+\cdots)}\left\{\frac{5-2h_pD_h^O}{2(L_s+L_A)}\right. \\ \left. - 5k_{cH}\int_{-\infty}^{X}[(a_1^2X^{-4}+\cdots)(1+a_2X^{-3}+\cdots)]\,\mathrm{d}X + \cdots\right\}, \tag{4.102}$$

which on integration gives the leading-order expression for $\bar{h}_1$ as $X \to -\infty$,

$$\bar{h}_1 = -\frac{1}{a_2 D_h^O}\left(\frac{5-2h_pD_h^O}{2\sqrt{N_M^*/N_O^*}}\right)\frac{X^4}{4} + \mathcal{O}(X)\,, \tag{4.103}$$

where a_2 is given by (4.100). If $D_h^H = 0$, then $h_p = 1/D_h^O$ from (4.85). Therefore, we have

$$\bar{h}_1 = -\left[\frac{3}{8a_2 D_h^O}\sqrt{\frac{N_O^*}{N_M^*}}X^4 + \mathcal{O}(X)\right]. \tag{4.104}$$

Now, substituting (4.104) in the large-time (τ) asymptotic expansion for h given by $h = h_p + \bar{h}_1(X)\tau^{-1/3} + \cdots$ (as given by (4.44b)), we have the corresponding behaviour of h in RF1 as

$$h = h_p - \left[\frac{3}{8a_2 D_h^O}\sqrt{\frac{N_O^*}{N_M^*}}X^4 + \mathcal{O}(X)\right]\tau^{-\frac{1}{3}} + \cdots. \tag{4.105}$$

It can be seen that the expansion disorders when $|X| = \mathcal{O}(\tau^{1/12})$. In terms of the outer coordinate (z), the above expression can be written as

$$h = h_p - \left[\frac{3}{8a_2 D_h^O}\sqrt{\frac{N_O^*}{N_M^*}}(z - z_1)^4\tau^{-\frac{2}{3}} + \cdots\right]\tau^{-\frac{1}{3}} + \cdots. \tag{4.106}$$

At the (leading-order) location of the second reaction front (RF2) $z = z_2(\tau)$, we have $h = o(1)$ and therefore, the above expansion reduces to

$$0 = h_p - \left[\frac{3}{8a_2 D_h^O}\sqrt{\frac{N_O^*}{N_M^*}}(z_2 - z_1)^4\tau^{-\frac{2}{3}} + \cdots\right]\tau^{-\frac{1}{3}} + \cdots, \tag{4.107}$$

$$\Rightarrow 0 = h_p - \left[\frac{3}{8a_2 D_h^O}\sqrt{\frac{N_O^*}{N_M^*}}\,L_B^4\,\tau^{4\beta}\tau^{-1}\right] + \cdots, \tag{4.108}$$

wherein the large-time prediction of the hydride thickness is given by $(z_1(\tau) - z_2(\tau)) \sim L_B\tau^{\beta}$. The above expansion disorders at $z = z_2(\tau)$, which results in the scaling relation

$$4\beta - 1 = 0, \quad \Rightarrow \beta = \frac{1}{4}. \tag{4.109}$$

The large-time prediction for the hydride growth is thus described by

$$L_B = \left(\frac{8h_p a_2 D_h^O}{3}\sqrt{\frac{N_M^*}{N_O^*}}\right)^{\frac{1}{4}}, \tag{4.110}$$

which on substituting $h_p = 1/D_h^O$ and a_2 from (4.100) becomes

$$L_B = 2\frac{\sqrt{N_M^*/N_O^*}}{(N_M^*/N_H^*)^{\frac{1}{4}}}\frac{(D_c^H)^{\frac{1}{2}}}{(k_{cH})^{\frac{1}{4}}}\,. \tag{4.111}$$

Thus the thickness of the intermediate hydride layer is described by $\Delta_H = (z_1(\tau) - z_2(\tau)) \sim L_B \tau^{1/4}$ resulting in $\Delta_H = \mathcal{O}((k_{cH})^{-\frac{1}{4}}\tau^{\frac{1}{4}})$, whereas we found the intermediate hydride thickness to be $\mathcal{O}(D_h^H\,\tau^{1/2})$ when $D_h^H > 0$. Nevertheless, there is asymptotic scale separation even when $D_h^H = 0$ and the two reaction fronts remain spatially isolated. It should be noted that since μ_i in (4.90) are found to be integer-valued, it is appropriate to have considered asymptotic expansions in terms of X instead of $|X|$.

4.2.6 Comparison of the asymptotic solution with the numerical results

In this section, we compare the numerical results obtained by solving the system (4.21) with the asymptotic solution presented in §§ 4.2.5, thereby validating our results. To begin with, we note that the reaction front solutions to (4.47) and (4.72) are invariant under the translations $X \to X + X_1$ and $Y \to Y + Y_1$ respectively, where $X_1\,, Y_1$ are higher-order corrections to the locations of the reaction fronts. In order to compare the numerical results with the leading-order asymptotic predictions, we define the centre of reaction fronts I ($z_1(\tau)$) and II ($z_2(\tau)$) as the locations where (4.26) and (4.27) are respectively maximised. To write (4.26) and (4.27) in terms of the reaction front coordinates X and Y, we define equivalent expressions for $\bar{\mathcal{R}}_1(X)$ using $(\bar{c}_0\,, \bar{H}_0)$ and similarly for $\hat{\mathcal{R}}_2(Y)$ using $(\hat{h}_0\,, \hat{M}_0)$:

$$\bar{\mathcal{R}}_1(X) = k_{cH}\,\bar{c}_0^2(X)\bar{H}_0(X)\,, \tag{4.112a}$$

$$\hat{\mathcal{R}}_2(Y) = \hat{h}_0^3(Y)\hat{M}_0(Y)\,. \tag{4.112b}$$

Figure 4.19 shows a comparison of the numerical results for the oxide growth-coefficient $((z_s(\tau) - z_1(\tau))\,\tau^{-1/2})$ with the large-time asymptotic prediction $(L_A + L_s)$ for different values of the rate constant k_{cH} and diffusivities $(D_h^O\,, D_h^H)$. It was seen earlier through numerical simulations (see § 4.2.4) that only three diffusivity parameters affected the leading-order oxidation kinetics (albeit mostly

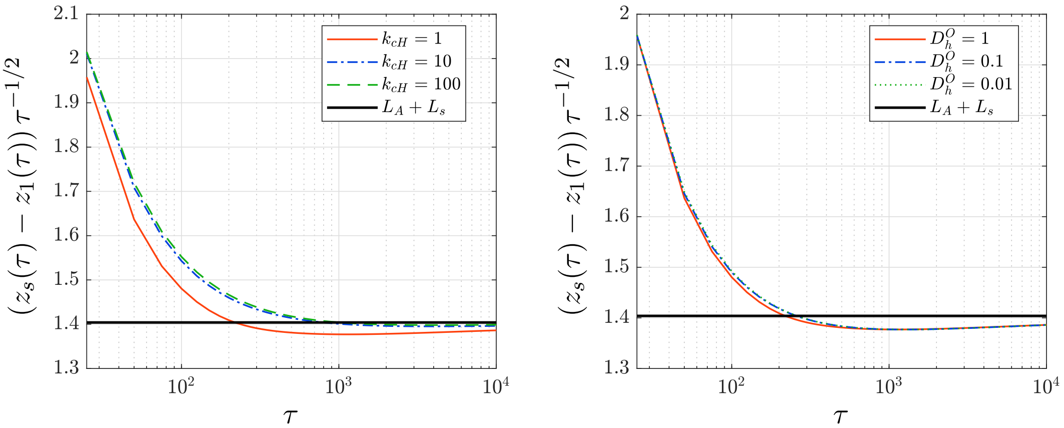

(a) Influence of k_{cH}; $D_{c,h} = 1$.

(b) Influence of D_h^O; $k_{cH} = 1, D_c = D_h^H = 1$.

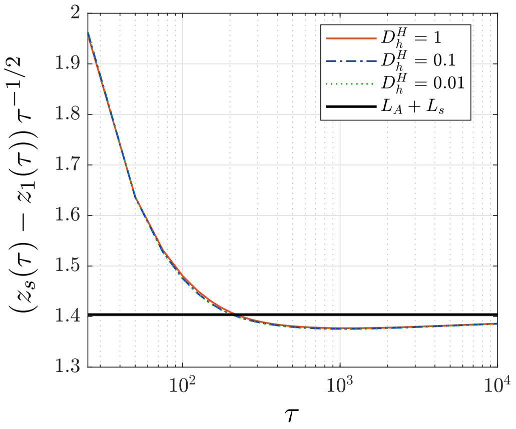

(c) Influence of D_h^H; $k_{cH} = 1$, $D_c = D_h^O = 1$.

Figure 4.19: A comparison of the numerical solution for the oxide growth-coefficient, $(z_s(\tau) - z_1(\tau))\tau^{-1/2}$ obtained by solving (4.21) with the large-time (τ) asymptotic prediction $(L_A + L_s)$. The influence of k_{cH}, D_h^O, D_h^H on the oxide growth-coefficient has been plotted. Here the black solid lines represent the asymptotic prediction $(L_A + L_s)$. The material densities are given in Table A.1. Other parameters include $D_c^O = 1$ (by choice of nondimensionalisation), $D_h^M = 1$ and initial oxide, $\delta_O = 4$ and hydride thickness, $\delta_H = 1$ for the numerical results.

the hydride growth) qualitatively, viz., $D_c^O\,, D_h^O\,, D_h^H$ and we have set $D_c^O = 1$ by virtue of the nondimensionalisation. The numerical results tend towards the predicted asymptotic value given by $L_A + L_s = \sqrt{N_M^*/N_O^*}$ (as derived in (4.83)) at large times for varying values of $k_{cH}\,, D_h^O\,, D_h^H$. The leading-order asymptotic prediction depends only on the material densities and hence remains constant for the different diffusivity and rate constant parameters. The numerical results were obtained by solving the system (4.21) via the solution scheme described in §§ 4.2.3.

Comparison between the numerical solution and the leading-order asymptotic prediction (given by $\Delta_O \sim (L_s + L_A)\tau^{1/2}$) for the oxide thickness is shown in Figure 4.20 for varying values of the initial oxide and hydride thicknesses. From the figure, it is observed that the full numerical solution agrees remarkably well with the leading-order asymptotic solution for a range of initial parameter values.

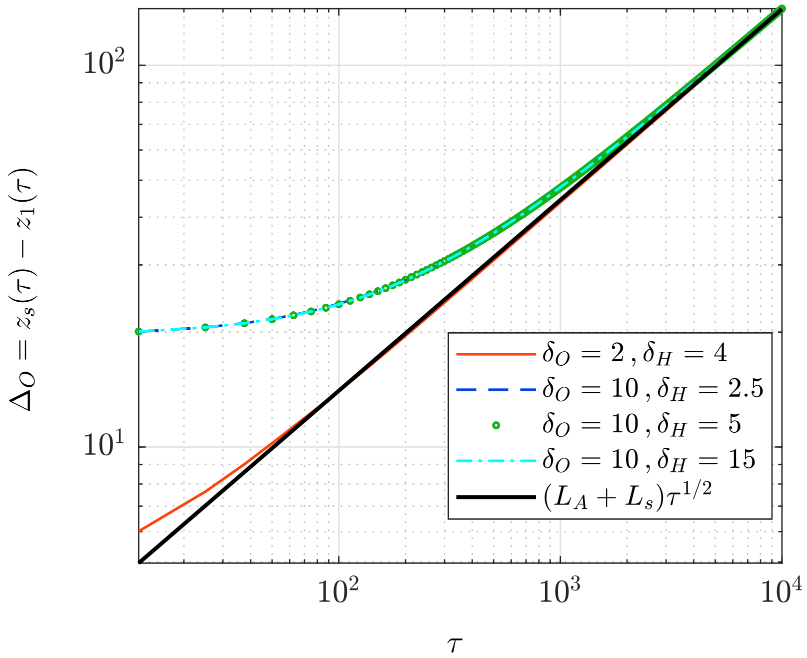

Figure 4.20: A comparison of the numerical solution for the oxide thickness ($\Delta_O = z_s(\tau) - z_1(\tau)$) obtained by solving the system (4.21) with the large-τ asymptotic prediction $(L_A + L_s)\tau^{1/2}$ for various initial oxide (δ_O) and hydride (δ_H) thicknesses. Other parameters include: $k_{cH} = 10\,, D_c = 1\,, D_h^O = D_h^M = 1\,, D_h^H = 10^{-3}$.

We now compare the numerical and asymptotic solutions for the hydride growth-coefficient for a range of diffusivity, rate constant and initial parameter

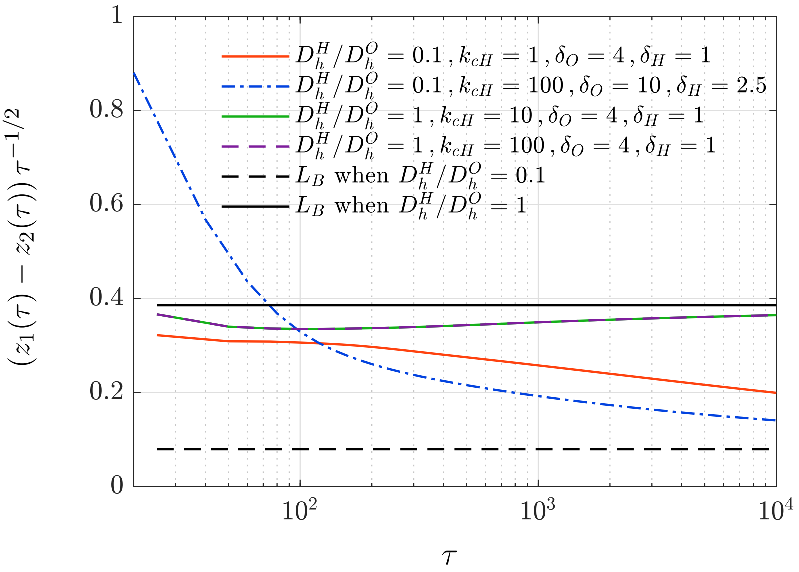

Figure 4.21: A comparison of the numerical solution for the hydride growth coefficient obtained by solving (4.21) with the large-τ asymptotic prediction for different values of the $H^{\bullet}$ diffusivity ratio D_h^H/D_h^O, rate constant k_{cH} and initial parameters $\delta_O\,, \delta_H$. Here the black solid and dashed lines represent the asymptotic predictions for the hydride-coefficient, L_B (see (4.65)) when $D_h^H/D_h^O = 0.1$ and $D_h^H/D_h^O = 1$ respectively. Other parameters include $D_c = D_h^H = D_h^M = 1$, $N_H^*/N_O^* \approx 1.12$ and $N_M^*/N_H^* \approx 1.76$.

values as shown in Figure 4.21. The numerical solution for the hydride growth-coefficient is calculated as $(z_1(\tau) - z_2(\tau))\tau^{-1/2}$, where $z_1(\tau)$ and $z_2(\tau)$ are the locations of the centres of the first and second reaction fronts respectively, whilst the leading-order asymptotic prediction for the hydride growth-coefficient is given by L_B (see equation (4.65)). Note that the comparison is only made for $D_h^H > 0$ in this figure on account of the asymptotic structure for $D_h^H > 0$ being different from that for $D_h^H = 0$ as already discussed in §§§ 4.2.5.5. It can be observed from the figure that for smaller D_h^H/D_h^O values, the numerical solution takes a much longer time (τ) to agree with the asymptotic prediction. This may be due to the higher-order correction terms becoming comparable in magnitude to the leading-order term ($\mathcal{O}(\tau^{1/2})$); therefore the leading-order solution alone does not capture the behaviour of the full numerical problem. The leading-order asymptotic coefficient for the hydride thickness (L_B) varies as $0.3859\,, 0.0796\,, 0.0092$ and $9.34 \cdot 10^{-4}$ for $D_h^H/D_h^O = 1\,, 0.1\,, 0.01\,, 0.001$ (L_B is given by (4.65)). As an example, for $D_h^H/D_h^O = 0.001$, if the coefficient of the first-order correction term ($\mathcal{O}(\tau^{1/4})$) is of the order of magnitude 10^0 (say), then we require $\tau \gg 10^{12}$ for the leading-order asymptotics ($\mathcal{O}(\tau^{1/2})$) to capture the behaviour of the full problem. In addition, as already noted, the rate constant k_{cH} and the initial parameters do not affect the leading-order kinetics, which will be further confirmed in Figure 4.22 and Figure 4.23 respectively.

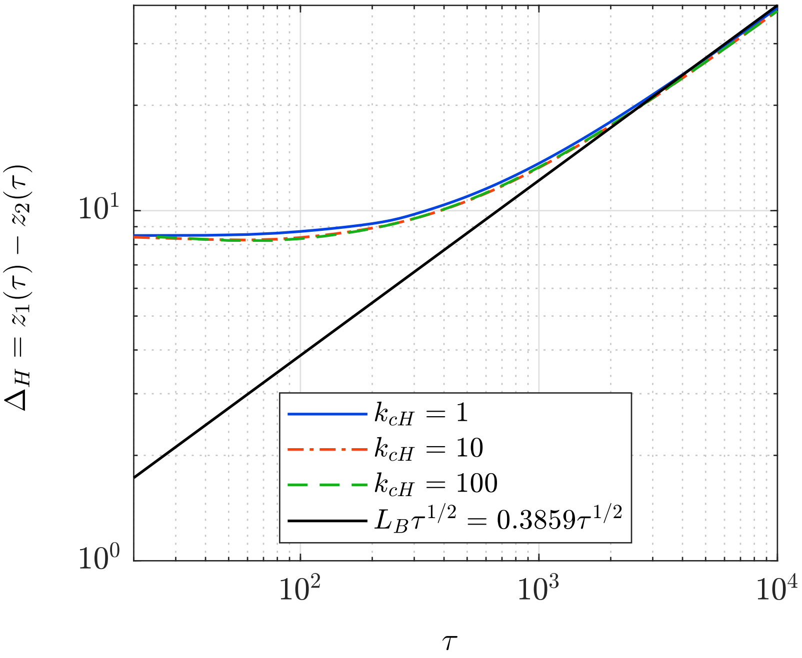

Figure 4.22: A comparison of the numerical solution for the hydride thickness, $\Delta_H = z_1(\tau) - z_2(\tau)$ obtained by solving the system (4.21) with the large-τ asymptotic prediction $L_B\tau^{1/2}$ (where L_B is given by (4.65)) for different rate constant values: $k_{cH} = 1$ (blue solid), $k_{cH} = 10$ (orange dash-dotted), $k_{cH} = 100$ (green dashed). Other parameters include $D_c = D_h = 1$, $\delta_O = 10$ and $\delta_H = 5$.

Figure 4.22 demonstrates that the rate constant k_{cH} does not have any significant influence on the leading-order oxidation kinetics. The hydride thickness is plotted against time (τ) for $k_{cH} = 1\,, 10\,, 100$. The full numerical solution is consistent with the leading-order asymptotic solution.

The hydride growth over time for different initial parameters and $D_h^H = 0.001$ is plotted in Figure 4.23a. Here, the numerical solution does not agree with the leading-order asymptotic prediction ($L_B\tau^{1/2}$ for $D_h^H > 0$) at $\tau = 10^4$ as the leading-order coefficient is found to be very small ($L_B = 9.34 \cdot 10^{-4}$ for $D_h^H = 0.001$) and any hope of recovering this behaviour would require $\tau \gg 10^{12}$ for the

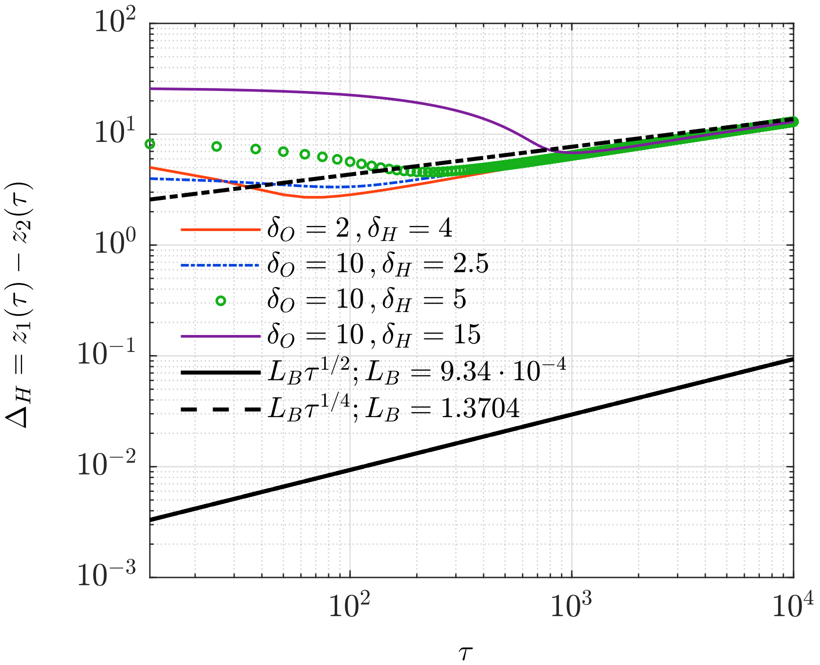

(a) For $D_h^H = 0.001\,, k_{cH} = 10$.

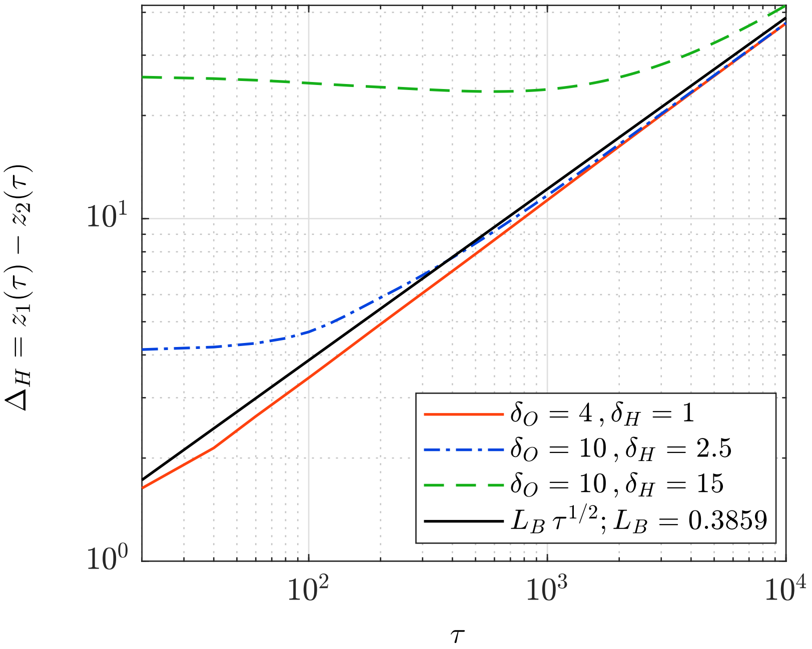

(b) For $D_h^H = 1\,, k_{cH} = 1$.

Figure 4.23: A comparison of the numerical solution for the hydride thickness, $\Delta_H = z_1(\tau) - z_2(\tau)$ obtained by solving the system (4.21) with the large-τ asymptotic prediction $L_B\tau^{1/2}$ for various initial oxide (δ_O) and hydride (δ_H) thicknesses and a $H^{\bullet}$ diffusivity in UH_3 of (a) $D_h^H = 0.001$, (b) $D_h^H = 1$. Other parameters include: $D_c = 1\,, D_h^O = D_h^M = 1$.

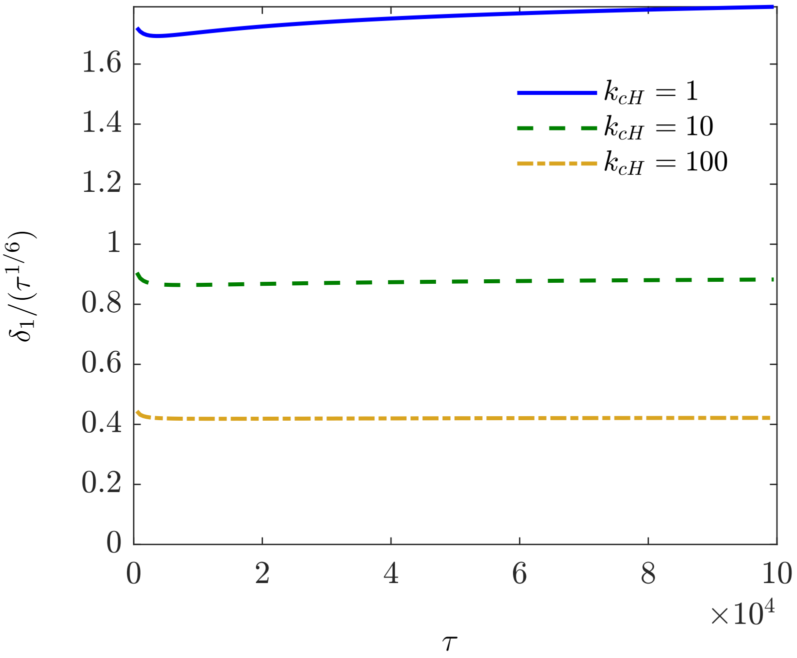

Figure 4.24: The numerical solution for the width of RF1 (δ_1) approaches the asymptotic prediction, $\delta_1 \sim \tau^{1/6}$ at large times. Here we show that the rescaled width $\delta_1/\tau^{1/6}$ approaches a constant value at a large τ for different k_{cH} values. Other parameters include uniform diffusivities $D_c = D_h = 1$, initial oxide and hydride thicknesses, $\delta_O = 10$, $\delta_H = 5$.

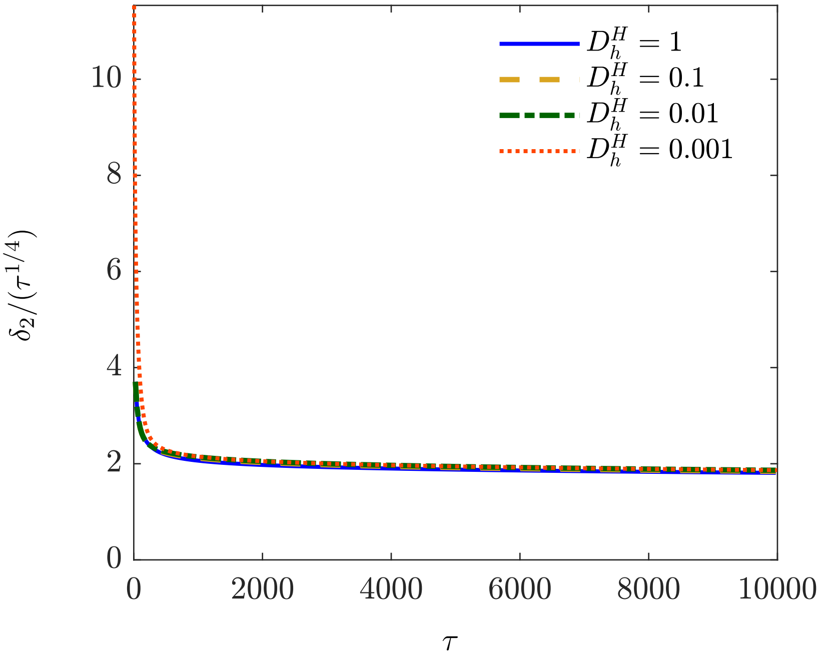

Figure 4.25: The numerical solution for the width of the RF2 (δ_2) approaches the asymptotic prediction, $\delta_2 \sim \tau^{1/4}$ at large times. Here we show that the rescaled width $\delta_2/\tau^{1/4}$ approaches a constant value at a large τ for various values of D_h^H. Other parameters include $k_{cH} = 10$, $D_c = D_h^O = D_h^M = 1$, initial oxide and hydride thicknesses, $\delta_O = 10$, $\delta_H = 5$.

numerical solution to be consistent with the leading-order prediction. However, the numerical result for the hydride width agrees with the asymptotic prediction for the limiting case wherein $D_h^H = 0$ (see §§§ 4.2.5.5 for the derivation of this limiting case). For $D_h^H = 1$ as shown in Figure 4.23b, the numerical solution agrees with the leading-order asymptotic result ($L_B \tau^{1/2}$ with $L_B = 0.3859$) for various initial parameters.

The numerical solution for the width of RF1 (see § 4.2.4.1) agrees with the asymptotic scaling $\delta_1 \sim \tau^{1/6}$ as shown in Figure 4.24, where $\delta_1/\tau^{1/6}$ tends to a constant value at large times. Similarly, for the width of RF2, $\delta_2 \sim \tau^{1/4}$ and therefore $\delta_2/\tau^{1/4}$ tends to a constant value at large times, which is depicted in Figure 4.25.

4.2.7 Determination of concentration profiles across the reaction fronts

Concentration profiles across RF1: Having solved for the unknown growth-coefficients and parameters involved in the oxidation kinetics of uranium via an asymptotic analysis, we now numerically solve for the concentration profiles within the reaction fronts using a shooting method.

In order to eliminate the rate constant k_{cH}, the governing equations (4.47) in RF1 are rescaled via the substitutions

$$X \to k_{cH}^{-\frac{1}{3}} X, \qquad \bar{c}_0 \to k_{cH}^{-\frac{1}{3}} \bar{c}_0, \qquad \bar{h}_1 \to k_{cH}^{-\frac{1}{3}} \bar{h}_1, \tag{4.113}$$

to give the nonlinear boundary value problem:

$$\frac{\partial \bar{D}_c}{\partial X}\frac{\partial \bar{c}_0}{\partial X} + \bar{D}_c \frac{\partial^2 \bar{c}_0}{\partial X^2} = 2\bar{c}_0^2 \bar{H}_0 \,, \tag{4.114a}$$

$$\frac{\partial \bar{D}_h}{\partial X}\frac{\partial \bar{h}_1}{\partial X} + \bar{D}_h \frac{\partial^2 \bar{h}_1}{\partial X^2} = -5\bar{c}_0^2 \bar{H}_0 \,, \tag{4.114b}$$

$$\frac{1}{2} L_A \frac{\partial \bar{H}_0}{\partial X} + \frac{\partial \left(\bar{H}_0 \bar{V}_0\right)}{\partial X} = -\bar{c}_0^2 \bar{H}_0 \frac{N_M^*}{N_H^*} \,, \tag{4.114c}$$

$$\frac{\partial \bar{V}_0}{\partial X} = \bar{c}_0^2 \bar{H}_0 \left(\frac{N_M^*}{N_O^*} - \frac{N_M^*}{N_H^*} \right) \,, \tag{4.114d}$$

subject to the matching boundary conditions:

$$\begin{gathered}
\bar{c}_0(-\infty) = 0, \quad \left.\frac{\partial \bar{c}_0}{\partial X}\right|_{\infty} = \frac{1}{L_s + L_A}, \\
\left.\frac{\partial \bar{h}_1}{\partial X}\right|_{\infty} = -\frac{h_p}{(L_A + L_s)}, \quad \left.\frac{\partial \bar{h}_1}{\partial X}\right|_{-\infty} = \frac{1}{2D_h^H}\left[\frac{5 - 2D_h^O h_p}{L_A + L_s}\right], \\
\bar{H}_0(+\infty) = 0, \quad \bar{H}_0(-\infty) = 1\,,
\end{gathered} \tag{4.114e}$$

where $D_c^O = 1$ (by nondimensionalisation) and the boundary conditions for $\bar{V}_0$ given by (4.57) and (4.59); whilst we require only one boundary condition each for $\bar{V}_0$ and $\bar{H}_0$, the other boundary condition will be automatically satisfied. Here, the nondimensional diffusion coefficient $\bar{D}_i$ in RF1 can be calculated using the expression

$$\bar{D}_i = (1 - \bar{H}_0)D_i^O + \bar{H}_0 D_i^H\,, \tag{4.115}$$

where species $i = \{c, h\}$.

We first solve the coupled governing equations (4.114a), (4.114c) and (4.114d) for $\bar{c}_0$, $\bar{H}_0$ and $\bar{V}_0$ in RF1 via a shooting method in MATLAB using the built-in functions `ode15i` and `fzero`. Here, $\partial \bar{c}_0/\partial X$ is taken as a new variable in order to reduce the system of equations (4.114a), (4.114c) and (4.114d) to first-order ordinary differential equations. We iterate on the boundary condition $(\partial \bar{c}_0/\partial X)|_{X\to-\infty}$ with an initial guess value of $(\partial \bar{c}_0/\partial X)|_{X\to-\infty} = 0$ until we satisfy the boundary condition $(\partial \bar{c}_0/\partial X)|_{X\to\infty} = 1/(L_A + L_s)$. The converged value using Newton-Raphson method is $(\partial \bar{c}_0/\partial X)|_{X\to-\infty} = 7.7165 \cdot 10^{-5}$ with the maximum reaction rates and leading-order coefficients for the OH^- concentration at $z = z_1(\tau)$ (or $X = 0$) tabulated in Table 4.2 for different k_{cH}. We then solve for $\bar{h}_1$ using (4.114b) from the solution obtained. The domain truncation in the numerical simulation is taken to be $X_\infty = 30$.

Figure 4.26a depicts the time-evolution of the concentration of the OH^- diffusing species at the centre of the first reaction front for $k_{cH} = 1\,, 10\,, 100$. The figure shows good agreement between the full numerical solution obtained by solving (4.21) and the large-τ asymptotic solution.

Figure 4.27 shows a comparison of the numerical and the asymptotic solutions for the concentration of the OH^- diffusing species and the UO_2 phase across the first reaction front; consistency between the numerical and asymptotic solutions

Table 4.2: Values of the leading-order coefficient for OH^- concentration at z_1 and the maximum reaction rate $\mathcal{R}_1$ for different k_{cH} obtained by solving (4.47) numerically using a shooting method. Other parameters include $D_c = D_h = 1$ and a domain truncation of $X_\infty = 30$ taken for the numerical simulation.

k_{cH}	$\bar{c}_0(X=0)$	Max. $\mathcal{R}_1$
1	0.7003	0.1527
10	0.3250	0.3291
100	0.1509	0.7090

can be observed.

Figure 4.28 shows a comparison of the full numerical and the asymptotic solutions for the concentration of $\mathrm{UO_2}$, the leading-order coefficients for the advection velocity and the reaction rate $\mathcal{R}_1$ across the first reaction front for $k_{cH} = 1\,, 10\,, 100$. The maximum reaction rate is found to increase with an increase in k_{cH} as we may expect. The asymptotic scaling laws for the advection velocity ($V \sim \tau^{-1/2}\,\bar{V}_0(X)$) and the reaction rate ($\mathcal{R}_1 \sim \tau^{-2/3} k_{cH}\bar{c}_0^2\bar{H}_0$) are consistent with the full numerical solution.

Concentration profiles across RF2: In *reaction front 2* (RF2), we similarly solve for the concentration profiles of the diffusing (h) and nondiffusing (H, M) species. The leading order governing equations are given by (4.72) with $k_{hM} = 1$. The leading order advection velocity in RF2 can be determined from

$$\frac{\partial \hat{V}_0}{\partial Y} = \hat{h}_0^3 \hat{M}_0 \left(\frac{N_M^*}{N_H^*} - 1 \right) . \tag{4.116}$$

We now solve (4.72) using a shooting method. Figure 4.26b shows a comparison between the full numerical solution and the asymptotic prediction for the time-evolution of the concentration of the $\mathrm{H}^\bullet$ diffusing species at the centre of the second reaction front (i.e., at $z = z_2(\tau)$). The numerical solution is consistent with the asymptotic scaling law $h \sim \tau^{-1/4}\hat{h}_0(Y)$. Similarly, a good agreement between the numerical and the asymptotic solutions can be observed for the concentrations of $\mathrm{H}^\bullet$ and U across RF2 that are plotted in Figure 4.29. The asymptotic scaling laws for the reaction rate and the advection velocity across RF2 are verified in Figure 4.30.

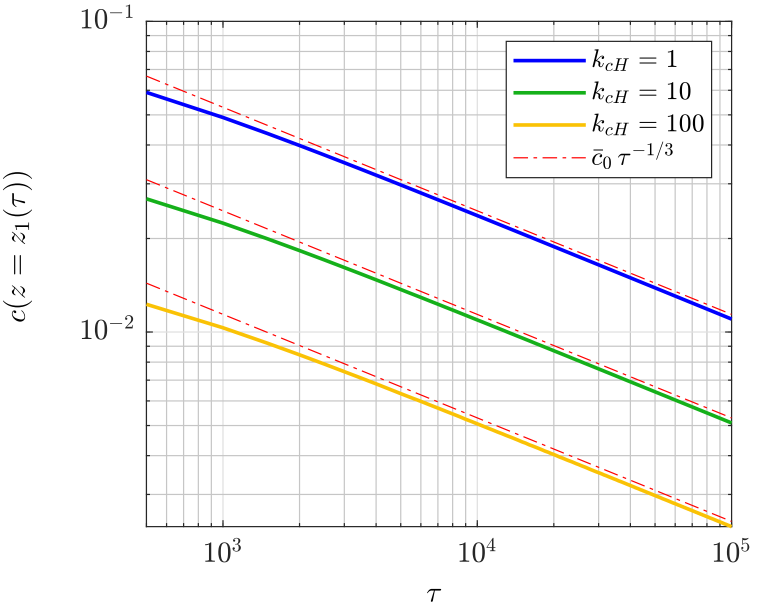

(a) Time evolution of c at $z = z_1(\tau)$.

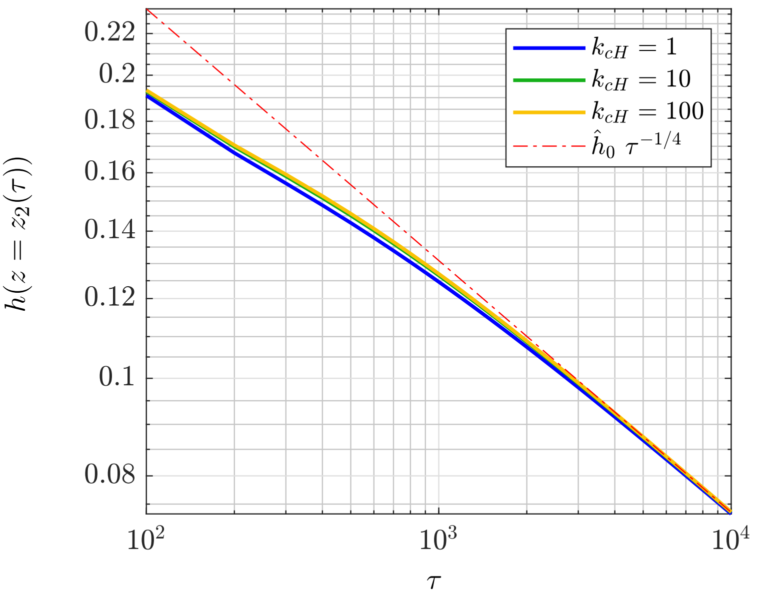

(b) Time evolution of h at $z = z_2(\tau)$.

Figure 4.26: Comparison of the numerical and asymptotic (red dashed-dotted lines) solutions for the time-evolution of the concentration of the diffusing species OH^- and $H^\bullet$ at the centre of the respective reaction fronts. The asymptotic scaling for $c(z = z_1(\tau)) \sim \bar{c}_0\,\tau^{-1/3}$ where $\bar{c}_0(X = 0) = 0.7003\,, 0.3250\,, 0.1509$ respectively for $k_{cH} = 1\,, 10\,, 100$ and a domain truncation of $X_\infty = 30$ in the numerical simulation; the asymptotic scaling for $h(z = z_2(\tau)) \sim \hat{h}_0(Y = 0)\,\tau^{-1/4}$ where $\hat{h}_0(Y = 0) = 1.1543$ with a domain truncation of $Y_\infty = 30$ in the numerical simulation. Here $X = 0$ and $Y = 0$ are centres of the respective reaction fronts where (4.26) and (4.27) are maximised. Other parameters include $D_c = D_h = 1$; initial oxide and hydride thicknesses, $\delta_O = 10$, $\delta_H = 5$ for the numerical results.

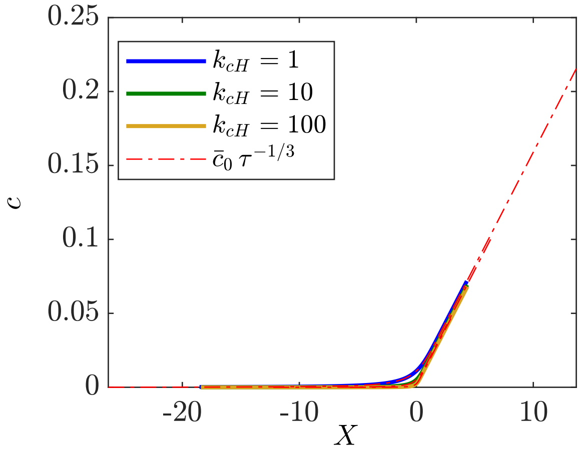

(a) Concentration of OH^- within RF1.

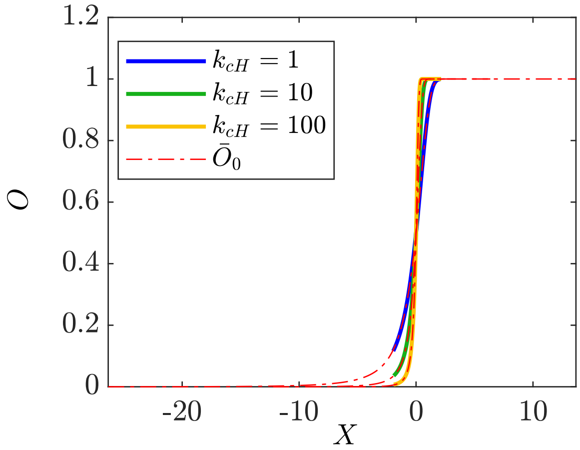

(b) Concentration of UO_2 within RF1.

Figure 4.27: A comparison of the numerical and asymptotic (red dashed-dotted lines) solutions for the concentration of the diffusing species OH^- and the oxide (UO_2) phase within the first reaction front for $k_{cH} = 1\,, 10\,, 100$. Other parameters include $D_c = D_h = 1$; initial oxide and hydride thicknesses, $\delta_O = 10$, $\delta_H = 5$ for the numerical results.

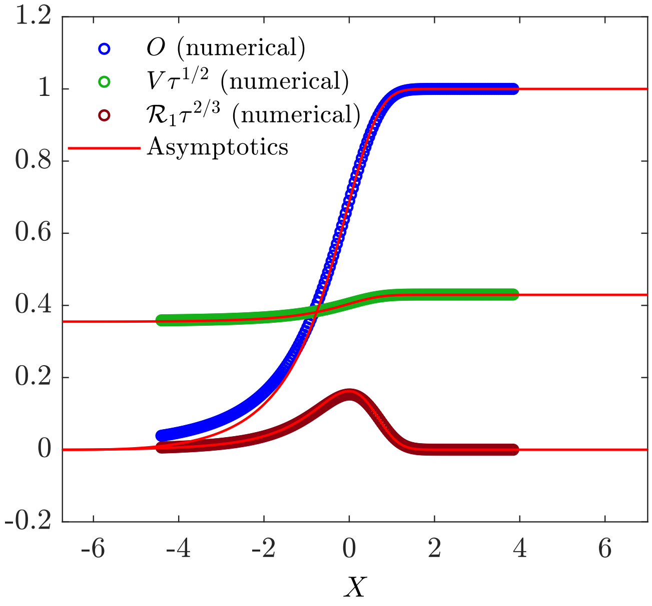

(a) $k_{cH} = 1$ (caption overleaf).

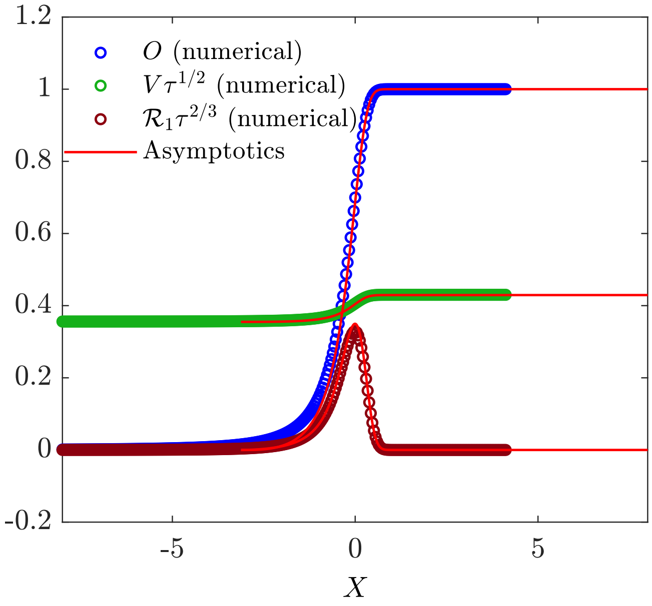

(b) $k_{cH} = 10$ (caption overleaf).

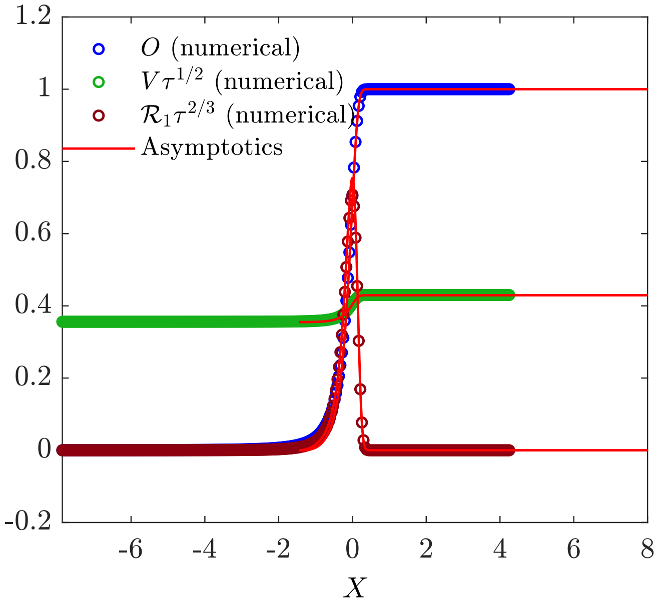

(c) $k_{cH} = 100$.

Figure 4.28: A comparison of the numerical and asymptotic solutions for the concentration of UO_2, and the quantities $V\tau^{1/2}$ (V being the advection velocity), $\mathcal{R}_1\tau^{2/3}$ across RF1. Consistency between the full numerical solution and the asymptotic scaling laws can be observed (the leading-order asymptotic coefficients are given by $\bar{V}_0(X) \sim V\tau^{1/2}$ and $\bar{\mathcal{R}}_0(X) \sim \mathcal{R}_1\tau^{2/3}$ for the advection velocity and reaction rate). Other parameters include $D_c = D_h = 1$, initial oxide and hydride thicknesses; $\delta_O = 10$, $\delta_H = 5$ for the numerical results.

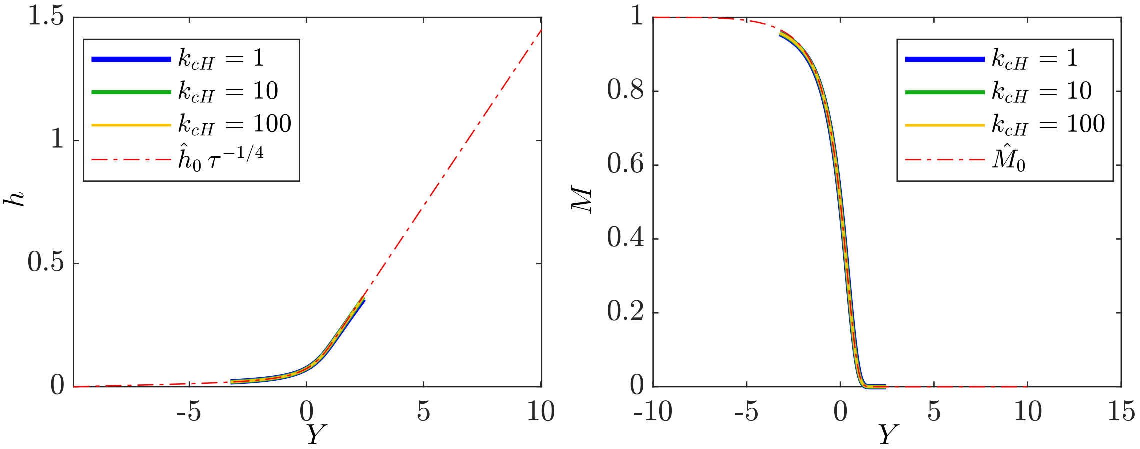

(a) Concentration of $H^{\bullet}$ across RF2. **(b)** Concentration of U across RF2.

Figure 4.29: A comparison of the numerical and asymptotic (red dashed-dotted lines) solutions for the concentrations of the diffusing species $H^{\bullet}$ and the metal U across the second reaction front. The reaction rate constant k_{cH} has no influence on the reaction kinetics in RF2. Other parameters include $D_c = D_h = 1$; initial oxide and hydride thicknesses, $\delta_O = 10$, $\delta_H = 5$ (for the numerical results).

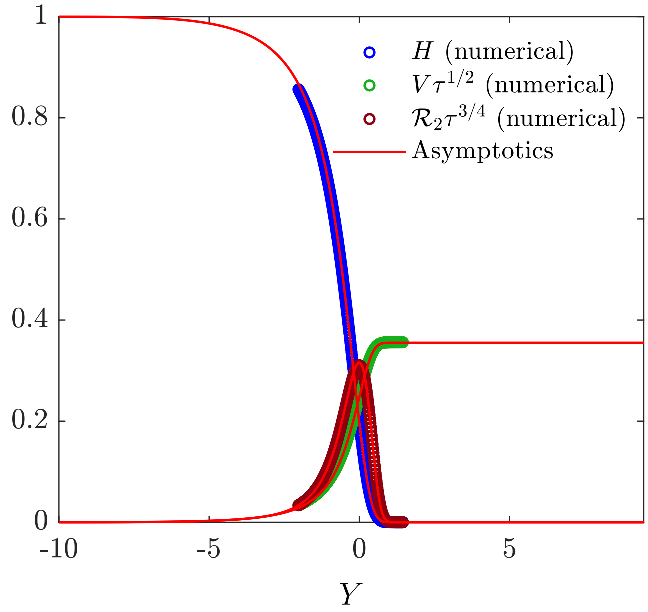

Figure 4.30: A comparison of the numerical and asymptotic solutions for the concentration of UH_3, and the quantities $V\tau^{1/2}$, $\mathcal{R}_2\tau^{3/4}$ across RF2. Consistency between the full numerical solution and the asymptotic scaling laws can be observed (the leading-order asymptotic coefficients are given by $\hat{V}_0(Y) \sim V\tau^{1/2}$ and $\hat{\mathcal{R}}_0(Y) \sim \mathcal{R}_2\tau^{3/4}$ for the advection velocity and reaction rate). Other parameters include $D_{c,h} = 1$; $\delta_O = 10\,, \delta_H = 5$ for the numerical results.

4.3 Discussion

We have formulated a one-dimensional reaction-advection-diffusion (RAD) model for the early-stage corrosion of uranium in pure water vapour. A distinguishing feature of the diffuse-interface/mixed-phase model compared to the Stefan model is the presence of (propagating) reaction fronts, which are spatially localised regions where transition from one (nondiffusing) phase to another occurs. The material advects owing to volumetric changes that result from phase transitions with a spatially and time-varying advection velocity; at any particular time, the advection velocity is however constant in each of the homogeneous phases outside of the reaction fronts. The reaction terms in the governing equations are written using the "mean-field approximation" (also called the rate law) in accordance with the proposed reaction scheme given in § 1.2.6. Note that the locations of maximum reaction rates of reactions R2 and R3 define the centres of respective fronts.

We have a small parameter $\epsilon = C_a^*/N_M^* \ll 1$ appearing in the model which has allowed us to make the quasi-steady approximation in order to further reduce the model. This gives quasi-steady diffusion of OH^- and $H^\bullet$, whilst time derivatives still appear in the governing equations for the nondiffusing phases (U, UO_2 and UH_3) (see §§§ 4.2.2.2). A solution strategy for the moving domain has been implemented through the Howarth-Dorodnitsyn transformation for the numerical simulations. In addition to solving the system numerically, we have tackled the problem using a large-time asymptotic analysis and identified four main asymptotic regions consisting of two diffusion layers and two reaction fronts. The kinetic behaviour of these four regions has been described by analytical expressions that indicate their dominant parameter dependencies.

We have found that the locations of the oxide and hydride layers (in the asymptotic large-time limit) are dominated by the diffusivity ratio D_h^H/D_h^O. The large-time (nondimensional) oxide thickness is described by $\Delta_O = (L_A + L_s)\tau^{1/2}$ with $L_A + L_s = \sqrt{N_M^*/N_O^*}$, whilst the hydride thickness $\Delta_H = L_B \tau^{1/2}$ with $L_B = 2\,h_p(L_A + L_s)D_h^H/(5 - 2\,h_p D_h^O)$ at leading order (for $D_h^H = \mathcal{O}(1)$; see Figure 4.23). The leading-order thickness of the hydride layer is thus a function of D_h^H/D_h^O. Note that the reference diffusivity D_{ref}^* is taken to be the diffusivity of OH^- in UO_2; hence $D_c^O = 1$ and does not appear as a parameter in our nondimensional asymptotic results.

The rate constant k_{cH} has been found to have little influence on the overall leading-order kinetics (note that $k_{hM} = 1$ by choice of a suitable reaction length scale). The influence of k_{cH} has only been on the solutions within the first reaction front (RF1), and does not affect the long-term evolution of the oxide and hydride growth. The widths of the first and second reaction fronts have been found to be $\delta_1 \sim \tau^{1/6}$ and $\delta_2 \sim \tau^{1/4}$ respectively.

For $D_h^H \ll 1$, however, the asymptotic prediction for the hydride thickness is $\Delta_H \sim L_B \tau^{1/4}$ with $L_B = 2\sqrt{N_M^*/N_O^*}(D_c^H)^{1/2}/((N_M^*/N_H^*)^{1/4}k_{cH}^{1/4})$; that is, the leading-order hydride thickness is dependent on the rate constant k_{cH}. For practical parameter values, the diffusivity of $H^{\bullet}$ in UH_3 is at least 10^3 times smaller than D_{ref}^* and therefore the expected observable hydride thickness in this regime is $\Delta_H = \mathcal{O}(\tau^{1/4})$.

A discussion of the dimensional results for the oxidation kinetics of uranium in water vapour, and its importance and relevance in an industrial setting will be presented in Chapter 6.

Chapter 5

Late-stage corrosion of uranium by water vapour

The material in this chapter is currently being written up for publication that is titled, "Hydride prediction during late-stage oxidation of uranium in a water-vapour environment" and is co-authored with R.E. Hewitt and P.D.D. Monks. The ensemble of 250 simulations (see for e.g. Figure 5.4) was performed by R.E. Hewitt and the table of diffusivity parameter values (see Table 5.2) was calculated by P.D.D. Monks.

5.1 Introduction

There is sufficient empirical evidence (see for e.g. Baker, Less, and Orman, 1966a; Harker, 2006; Banos and Scott, 2020) that suggests a linear regime in the water-vapour corrosion of uranium after cracking and spallation of the surface oxide. A porous oxide layer results when the surface oxide breaks away due to a build-up of internal stresses caused by the difference in densities of the metal ($\rho_M^* = 19.06$ g/cm^3) and oxide ($\rho_O^* = 10.97$ g/cm^3). The formation of low-density hydride from metal between the oxide and metal phases also contributes to the internal stresses within the oxide. This porous oxide layer allows rapid diffusion of the water vapour molecules, the dissociation of which occurs at the surface of a coherent (or adherent) oxide layer beneath the porous layer. The diffusion of OH^- through this adherent oxide layer will then constitute the rate-determining step. Experiments indicate that this adherent oxide layer has a constant thickness which depends on temperature and the material properties. In what follows, we will model diffusion through this adherent oxide layer, where its thickness is considered as a parameter in our model.

In this work, we follow the reaction scheme outlined in § 1.2.6, which proceeds with the following elementary steps within the material:

$$\mathrm{UH_3} + 2\,\mathrm{OH^-} \xrightarrow{k^*_{cH}} \mathrm{UO_2} + 5\,\mathrm{H^\bullet} + 2\,\mathrm{e^-}\,, \tag{5.1a}$$

$$\mathrm{U} + 3\,\mathrm{H^\bullet} \xrightarrow{k^*_{hM}} \mathrm{UH_3}\,, \tag{5.1b}$$

where chemical state symbols have been omitted for simplicity. A surface reaction scheme that links with the reactants and products of (5.1) is

$$2\,\mathrm{H_2O} + 2\,\mathrm{O^{2-}}_l \longrightarrow 2\,\mathrm{OH^-}_l + 2\,\mathrm{OH^-}\,, \tag{5.2a}$$

$$2\,\mathrm{e^-} + 2\,\mathrm{OH^-}_l \longrightarrow 2\,\mathrm{O^{2-}}_l + \mathrm{H_2}\,, \tag{5.2b}$$

$$2\,\mathrm{H^\bullet} \longrightarrow \mathrm{H_2}\,, \tag{5.2c}$$

where the subscript $_l$ refers to lattice-bound species. The overall reaction is therefore

$$\mathrm{U_{(s)}} + 2\,\mathrm{H_2O_{(g)}} \longrightarrow \mathrm{UO_{2(s)}} + 2\,\mathrm{H_{2(g)}}\,. \tag{5.3}$$

5.1.1 The RAD model

We begin from the one-dimensional reaction-advection-diffusion (RAD) model (4.1) given in §§ 4.2.1:

$$\frac{\partial c^*}{\partial t^*} + \frac{\partial}{\partial z^*}(v^* c^*) = \frac{\partial}{\partial z^*}\left(D^*_c \frac{\partial c^*}{\partial z^*}\right) + r^*_c\,, \tag{5.4a}$$

$$\frac{\partial h^*}{\partial t^*} + \frac{\partial}{\partial z^*}(v^* h^*) = \frac{\partial}{\partial z^*}\left(D^*_h \frac{\partial h^*}{\partial z^*}\right) + r^*_h\,, \tag{5.4b}$$

$$\frac{\partial O^*}{\partial t^*} + \frac{\partial}{\partial z^*}(v^* O^*) = r^*_O\,, \tag{5.4c}$$

$$\frac{\partial H^*}{\partial t^*} + \frac{\partial}{\partial z^*}(v^* H^*) = r^*_H\,, \tag{5.4d}$$

$$\frac{\partial M^*}{\partial t^*} + \frac{\partial}{\partial z^*}(v^* M^*) = r^*_M\,, \tag{5.4e}$$

Here $r^*_{c,h,H,M,O}$ define the reaction rate densities and v^* is a spatially-varying advection velocity induced by density reductions during the transitions from U to UH_3 and then UO_2. The concentrations being determined are both the diffusing (OH^-,$H^\bullet$) species and the bulk material volume fractions of (UH_3, U, UO_2):

$$(c^*, h^*) \equiv ([OH^-], [H^\bullet]), \quad (H^*, M^*, O^*) \equiv ([UH_3], [U], [UO_2]). \tag{5.4f}$$

The relevant diffusion coefficients are assumed to be functions of the local material composition via

$$D^*_{c,h} = M^* D^{M*}_{c,h} + O^* D^{O*}_{c,h} + H^* D^{H*}_{c,h}, \tag{5.5}$$

but independent of the relatively low concentrations of OH^- and $H^\bullet$ present in the material.

The corresponding reaction source/sink terms for the reaction scheme (5.1) are

$$(r^*_c, r^*_h) = \left(-2k^*_{cH}\, c^{*2} H^*,\ 5k^*_{cH}\, c^{*2} H^* - 3k^*_{hM} h^{*3} M^*\right), \tag{5.6a}$$

$$(r^*_H, r^*_M, r^*_O) = \left(k^*_{hM}\, h^{*3} M^* - k^*_{cH} c^{*2} H^*,\ -k^*_{hM}\, h^{*3} M^*,\ k^*_{cH}\, c^{*2} H^*\right), \tag{5.6b}$$

where k^*_{cH} and k^*_{hM} are the reaction rate constants.

To nondimensionalise this system, we use the peak (surface) concentration of OH^- denoted by C^*_a and known maximum concentrations $N^*_{H,M,O}$ for pure phases of uranium hydride ($4.54 \cdot 10^{-2}$ mol/cm^3), uranium ($8.01 \cdot 10^{-2}$ mol/cm^3) and uranium dioxide ($4.06 \cdot 10^{-2}$ mol/cm^3) respectively.

$$c^* = C^*_a\, c(z,t), \quad h^* = C^*_a\, h(z,t), \tag{5.7a}$$

$$H^* = N^*_H\, H(z,t), \quad M^* = N^*_M\, M(z,t), \quad O^* = N^*_O\, O(z,t). \tag{5.7b}$$

For the early-stage oxidation of uranium in water vapour presented in §§ 4.2.1, a length scale and time scale associated with k^*_{hM} was chosen, but here we instead choose an arbitrary reference length scale of L^*_{ref} to nondimensionalise the problem:

$$z^* = L^*_{ref}\, z, \quad t^* = \frac{L^{*2}_{ref}}{D^*_{ref}} \frac{N^*_M}{C^*_a}\, t, \tag{5.7c}$$

and a velocity scale follows directly from the ratio of length and time scales. For simplicity, the choice of L^*_{ref} will be taken as 1 nm, and $D^*_{ref} = 10^{-12}$ cm^2/s.

Under the assumption that $\epsilon = C_a^*/N_M^* \ll 1$, corresponding to peak concentrations of OH⁻ being much less than that for U, the non-dimensional RAD model reduces to quasi-steady diffusion:

$$\begin{gathered} \frac{\partial}{\partial z}\left(D_c \frac{\partial c}{\partial z}\right) = r_c\,, \quad \frac{\partial}{\partial z}\left(D_h \frac{\partial h}{\partial z}\right) = r_h\,, \\ \frac{\partial H}{\partial t} + \frac{\partial}{\partial z}(vH) = r_H\,, \quad \frac{\partial M}{\partial t} + \frac{\partial}{\partial z}(vM) = r_M\,, \quad \frac{\partial O}{\partial t} + \frac{\partial}{\partial z}(vO) = r_O\,, \end{gathered} \tag{5.8a}$$

where

$$(r_c, r_h) = \left(2k_{cH}\, c^2 H\,,\ 3k_{hM} h^3 M - 5k_{cH}\, c^2 H\right)\,, \tag{5.8b}$$

$$(r_H, r_M, r_O) = \left(\left(k_{hM} h^3 M - k_{cH} c^2 H\right) \frac{N_M^*}{N_H^*}\,,\ -k_{hM} h^3 M\,,\ k_{cH}\, c^2 H\, \frac{N_M^*}{N_O^*}\right)\,, \tag{5.8c}$$

and the dimensionless reaction coefficients are

$$k_{cH} = \frac{k_{cH}^* C_a^* N_H^* L_{ref}^{*2}}{D_{ref}^*}\,, \quad k_{hM} = \frac{k_{hM}^* C_a^{*2} N_M^* L_{ref}^{*2}}{D_{ref}^*}\,. \tag{5.8d}$$

A simple volume-fraction weighted combination of the diffusivity coefficients is employed,

$$D_{c,h} = \sum_{j=H,M,O} D_{c,h}^j j\,, \tag{5.8e}$$

where $D_{c,h}^j$ is the constant diffusivity of c, h in a region where $j = 1$. The boundary conditions are a fixed surface concentration of OH⁻ with an unreacted metal far away from the surface:

$$\left.\begin{aligned} c = 1\,, \quad h = 0 \quad &\text{at} \quad z = z_s(t) \\ c, h \to 0\,, \quad (H, M, O) \to (0, 1, 0) \quad &\text{as} \quad z \to -\infty \end{aligned}\right\} \text{for } t \geq 0\,. \tag{5.8f}$$

This model was derived for the parabolic oxidation regime, where there is no breakup of the surface oxide layer, however in the linear oxidation regime the domain is shown in Figure 5.1.

The difference lies with the upper cracked/porous oxide layer, and underlying fixed depth (Δ_{adh}^*) adherent oxide. We will discuss an approach to modelling this configuration within the confines of (5.8) below in § 5.3.

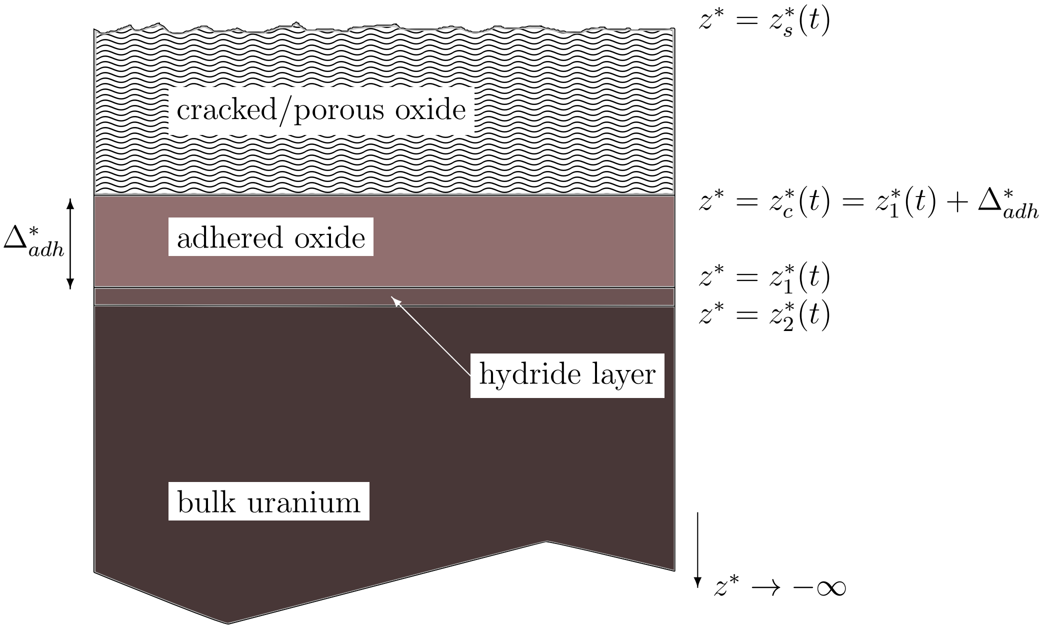

Figure 5.1: A schematic diagram of the late-stage oxidation, where a cracked/porous upper layer has developed leaving a constant thickness (Δ_{adh}^*) adhered oxide layer. Although the oxide/hydride/bulk regions are shown as distinct regions, there is a rapid (smooth) transition between each, associated with two propagating reaction fronts at $z^* = z_{1,2}^*$.

5.1.2 Typical dimensional parameter values

Solution of the RAD model above requires values for six diffusivity coefficients (D_i^{j*} with $i = \{c, h\}$, $j = \{H, M, O\}$), corresponding to the two diffusing quantities in three phases, two reaction rates (k_{cH}^*, k_{hM}^*) in (5.1), the adherent layer thickness (Δ_{adh}^*) and the peak concentration (C_a^*) of OH^-. In the discussion below we restrict ourselves to room temperature conditions.

We will start from a reference set for these values, as presented in Table 5.1, some of which can be approximated from existing work, whilst others are ad hoc choices. For the diffusion of hydrogen radicals (D_h^{j*}) there is available data that can be extrapolated down to 25°C, giving rise to the log-normal distributions outlined in Table 5.2.

For the corresponding diffusivity of OH^- (i.e. D_c^{j*}) we have little information

D_c^{j*} $\mathrm{cm^2\ s^{-1}}$	D_h^{H*} $\mathrm{cm^2\ s^{-1}}$	D_h^{M*} $\mathrm{cm^2\ s^{-1}}$	D_h^{O*} $\mathrm{cm^2\ s^{-1}}$	k_{cH}^* $\mathrm{mol^{-2}cm^6s^{-1}}$	k_{hM}^* $\mathrm{mol^{-3}cm^9s^{-1}}$
$D_{ref}^* = 10^{-12}$	$9 \cdot 10^{-16}$	$1.49 \cdot 10^{-10}$	$5 \cdot 10^{-13}$	10^8	10^{15}

Table 5.1: Representative choices for the dimensional parameters associated with diffusivity and reaction rate constants.

Diffusion coefficient ($\mathrm{cm^2/s}$)	mean	mean (log)	s.d. (log)
D_h^{H*}	$9 \cdot 10^{-16}$	-34.65	0.86
D_h^{M*}	$1.49 \cdot 10^{-10}$	-22.63	0.41
D_h^{O*}	$5 \cdot 10^{-13}$	-28.33	0.36

Table 5.2: Log-normal distributions of values for the diffusivity of (top to bottom) $H^\bullet$ in UH_3, U and UO_2 at a temperature of 25°C. Here the values are obtained from Peretz et al. (1976) for D_h^{H*}, Mallett and Trzeciak (1958) for D_h^{M*} and Wheeler (1971), UoM private communication (2020) for D_h^{O*}.

and will consider all three values to be the reference diffusivity (10^{-12} $\mathrm{cm^2/s}$). For the adherent layer thickness we appeal to Table 2 of Harker (2006) (albeit for O_2 environments). The adherent layer typically thickens at higher temperatures and herein we consider values of 30 and 50 nm for the adherent oxide thickness at room temperatures. For the reaction rate constants in (5.1) we choose ad hoc reference values of $k_{cH}^* \approx 10^8$ $\mathrm{mol^{-2}cm^6s^{-1}}$ and $k_{hM}^* \approx 10^{15}$ $\mathrm{mol^{-3}cm^9s^{-1}}$. Later results will allow for variability of all the parameters listed in Table 5.1, enabling us to characterise the sensitivity of predictions for the internal hydride layer to these reaction/diffusion parameters.

Finally for C_a^* (the peak concentration of OH^-), we first derive (see § 5.2) a simple theoretical relationship for the oxidation rate, then use this to infer a value of C_a^* consistent with available empirical data.

The recent review paper by Banos and Scott (2020) provides the following empirical fit for the (linear regime) oxidation rate of U in a water vapour environment with vapour pressure $P_{\mathrm{H_2O}}^*$:

$$1.614 \cdot 10^5 \, (P_{\mathrm{H_2O}}^*)^{\frac{1}{2}} \exp\left(-\frac{5396.8\ \mathrm{K}}{T^*}\right) \ \mathrm{mgU\ cm^{-2}\ h^{-1}}\,, \tag{5.9}$$

where $P^*_{\mathrm{H_2O}}$ is measured in millibars.

With a density for U of 19.1 g/cm^3, this reduces to

$$8.45 \cdot 10^7 \, (P^*_{\mathrm{H_2O}})^{\frac{1}{2}} \, \exp\left(-\frac{5396.8 \text{ K}}{T^*}\right) \text{ nm h}^{-1} \, . \tag{5.10}$$

Evaluated at a temperature of 25°C and a vapour pressure of 20 Torr (26.66 mbar) the material is corroded at a rate of approximately 6 nm h^{-1} with a loss of U of approximately $1.15 \cdot 10^{-2}$ mg cm^{-2} h^{-1}.

5.2 A constant-rate oxidation solution

An extensive analysis of (5.8) has been provided in Chapter 4, providing both computational results and a theoretical description (valid at large exposure times) under the assumption that the adhered oxide layer can grow without bound. Following some initial transient behaviour associated with the details of the initial state of the material, it was shown that the thickness of this adherent layer ultimately grows parabolically (as $at^{1/2}$, for some coefficient a) and that the oxide remains separated from the bulk uranium by a $\mathrm{UH_3}$ layer.

In the RAD model (5.8), the generic theoretical behaviour is that the intermediate hydride layer also thickens like $\delta t^{1/2}$ (for some constant δ) in tandem with the oxide layer. However a notable feature is that the diffusivity of $\mathrm{H}^\bullet$ in $\mathrm{UH_3}$ is small compared to that of $\mathrm{OH^-}$ in $\mathrm{UO_2}$ (i.e., $D_h^{H*}/D_c^{O*} \ll 1$; also $D_h^{H*}/D_h^{O*} \ll 1$ as in Table 5.1). It has been shown that the limit $D_h^{H*}/D_h^{O*} \ll 1$ is a special case for the RAD model; the thickness of the $\mathrm{UH_3}$ layer becomes proportional to $t^{1/4} k_{cH}^{-1/4}$ (as shown in §§§ 4.2.5.5). Of course these predictions are based on the assumption of a sufficiently long exposure of the material, whilst still neglecting the break up of any surface oxide layer.

As the oxide layer grows, diffusive flux of $\mathrm{OH^-}$ to the reaction front is reduced, and it is this fundamental mechanism that leads to an eventual parabolic behaviour for early-stage oxidation. However, the assumption of an adherent oxide layer that grows without limit is obviously expected to fail at some point. The oxide layer is known to crack and spall (Figure 5.1), the effect of which is to provide an upper limit for the adhered oxide thickness (Δ^*_{adh}). Beyond this limit, the flux of $\mathrm{OH^-}$ stops decreasing and this motivates the examination of constant-flux solutions to the same RAD model provided by (5.8). Determining the size of the adherent layer (i.e., Δ^*_{adh}) is out of the scope of this model, as it must depend upon the mechanical properties of the oxide and any stress distribution within the material; instead we seek a solution where the adherent layer thickness is specified as a parameter.

In the late-stage linear regime, we suppose that the top of the adhered oxide layer (see Figure 5.1) is given by $z_c = z^*_c/L^*_{ref} = \xi_c - Vt$, where V is the (dimensionless) propagation velocity and ξ_c an offset. The value ξ_c is determined by the full history of the evolution and remains arbitrary when considering only the late-stage linear behaviour, so we take $\xi_c = 0$ here without loss of generality. We now seek a *uniformly* translating solution to (5.8) via a ξ coordinate defined by

$$z = \xi - Vt\,, \tag{5.11}$$

where V is a constant to be found, which determines the rate of the 'shrinking core' during oxidation. The domain of solution is now $\xi \in (-\infty, 0]$, with two (now stationary in the ξ frame) reaction fronts at $\xi = \xi_{1,2}$ where the two reactions of (5.1) dominate. Here $\xi_{1,2}$ correspond to the points indicated in the dimensional schematic of Figure 5.1 as $z^*_{1,2}$.

In the translating coordinate, assuming an otherwise steady solution results in the ordinary-differential system

$$\frac{\mathrm{d}}{\mathrm{d}\xi}\left(D_c \frac{\mathrm{d}c}{\mathrm{d}\xi}\right) = r_c\,, \quad \frac{\mathrm{d}}{\mathrm{d}\xi}\left(D_h \frac{\mathrm{d}h}{\mathrm{d}\xi}\right) = r_h\,, \tag{5.12a}$$

$$V\frac{\mathrm{d}H}{\mathrm{d}\xi} + \frac{\mathrm{d}}{\mathrm{d}\xi}(vH) = r_H\,, \quad V\frac{\mathrm{d}M}{\mathrm{d}\xi} + \frac{\mathrm{d}}{\mathrm{d}\xi}(vM) = r_M\,, \quad V\frac{\mathrm{d}O}{\mathrm{d}\xi} + \frac{\mathrm{d}}{\mathrm{d}\xi}(vO) = r_O\,, \tag{5.12b}$$

where $D_{c,h}$ remain dependent on ξ through (5.8e).

A cracked/porous oxide allows direct access of water vapour to the top surface of the adhered oxide layer, leading to the boundary conditions

$$c = 1\,, \quad h = 0 \quad \text{at} \quad \xi = 0\,, \tag{5.12c}$$

$$c, h \to 0\,, \quad (H, M, O) \to (0, 1, 0) \quad \text{as} \quad \xi \to -\infty\,. \tag{5.12d}$$

This final condition requires that we recover unreacted U sufficiently deep into the metal.

Whilst solution of (5.12) will provide the local behaviour, we can predict the bulk behaviour by integration from $\xi = -\infty$ to $\xi = 0$ (assuming that the surface layer reduces to a pure oxide phase). This reveals that

$$D_c^O \frac{\mathrm{d}c}{\mathrm{d}\xi}\bigg|_{\xi=0} = 2I_1\,, \quad D_h^O \frac{\mathrm{d}h}{\mathrm{d}\xi}\bigg|_{\xi=0} = 3I_2 - 5I_1\,, \tag{5.13}$$

$$I_2 = I_1\,, \quad V = I_2\,, \quad V + v_c = I_1 N_M^*/N_O^*\,, \tag{5.14}$$

where $v_c = v(\xi = 0)$ is the advection velocity of the surface of the adherent oxide layer (as induced by the material expansion during the reaction process). The two quantities $I_{1,2}$ are related to the total consumption/production of OH^- and $\mathrm{H}^\bullet$ via:

$$I_1 = k_{cH} \int_{-\infty}^{0} c^2 H \,\mathrm{d}\xi\,, \quad \text{and} \quad I_2 = k_{hM} \int_{-\infty}^{0} h^3 M \,\mathrm{d}\xi\,. \tag{5.15}$$

Eliminating $I_{1,2}$ in (5.13) leads us to conclude that the (downward into the bulk) propagation speed V (of both reaction fronts and the constant-thickness adherent oxide layer) and (upward) advection of the adherent surface layer v_c are

$$V = \frac{D_c^O}{2} \frac{\mathrm{d}c}{\mathrm{d}\xi}\bigg|_{\xi=0}\,, \quad v_c = V\left(N_M^*/N_O^* - 1\right)\,. \tag{5.16}$$

Diffusion of OH^- in the adherent oxide layer is quasi-steady. Hence a good approximation (as confirmed in Figure 5.2) for c in the adherent layer is a simple constant-flux state:

$$c \approx 1 + \frac{\xi}{\Delta_{adh}}\,. \tag{5.17}$$

This satisfies $c(0) = 1$ and $c(-\Delta_{adh}) = 0$, where the latter state is associated with a reaction front at $\xi = \xi_1 = -\Delta_{adh}$ at which all the OH^- is consumed. In terms of the (dimensionless) adherent oxide thickness $\Delta_{adh} = \Delta_{adh}^*/L_{ref}^*$ we can therefore say that

$$V = \frac{1}{2}\frac{D_c^O}{\Delta_{adh}}\,. \tag{5.18}$$

Hence, in this regime, the reaction fronts, adherent oxide and hydride layers all

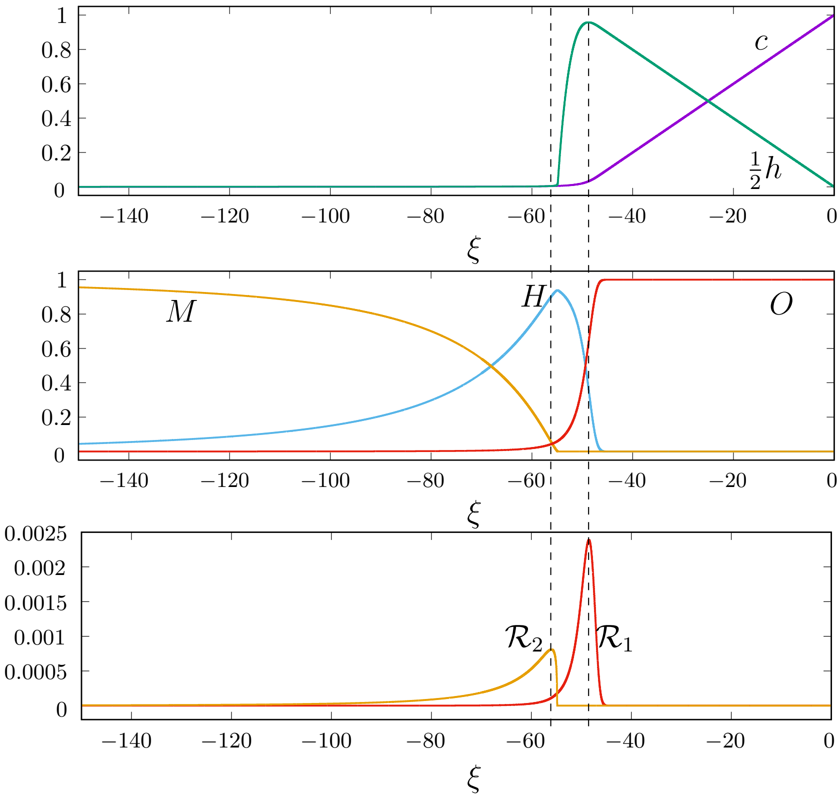

Figure 5.2: An example solution of the steady problem (5.12), for a uniformly translating reaction front state associated with the linear oxidation regime. Here the (dimensionless) adhered oxide depth is 50. Dimensionless parameters are $D_h^H = 9 \cdot 10^{-4}$, $D_h^M = 148.7$, $D_h^O = 0.497$, $D_c^j = 1$ $(j = H, M, O)$, $k_{cH} = 6.13$ and $k_{hM} = 14611$; these correspond to dimensionless versions of the reference values discussed in Table 5.1 with C_a^* chosen as described in §§ 5.1.2. The two (vertical) dashed lines indicate the reaction front positions $\xi = \xi_{1,2}$, which maximise reaction rates $\mathcal{R}_{1,2}$ defined by (5.21).

propagate into the bulk metal with a constant dimensional velocity of

$$V^* = \frac{D_c^{O*}}{2\Delta_{adh}^*} \frac{C_a^*}{N_M^*} = \epsilon \frac{D_c^{O*}}{2\Delta_{adh}^*} \,. \tag{5.19}$$

Here $\Delta_{adh}^* = L_{ref}^* \Delta_{adh}$ is a dimensional thickness of the adherent layer, D_c^{O*} is the diffusion coefficient for OH⁻ in UO_2, C_a^* is the near-surface concentration of OH⁻ and N_M^* is the number density of U.

For consistency between this constant oxidation rate solution to (5.8) and the empirical observation (5.10) we require (for example, at 25°C and a vapour pressure of 20 Torr) that $V^* = 6$ nm/h. So for given values for D_c^{O*} and Δ_{adh}^*, we can obtain a value for C_a^* from (5.19) that will give results consistent with observation.

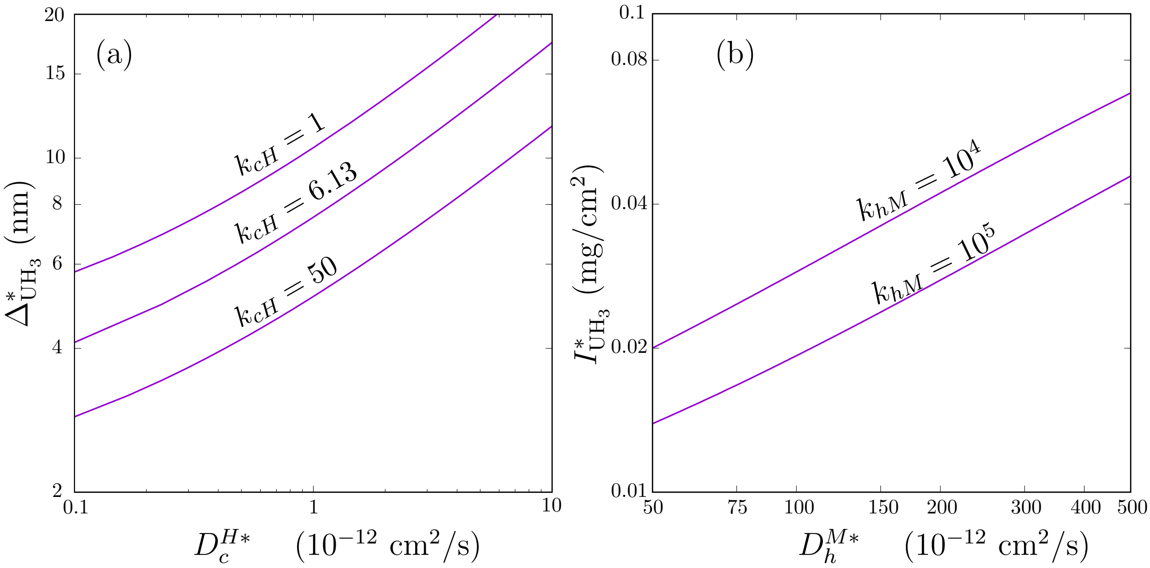

Figure 5.3: Solutions of (5.12) with $V = D_c^O/(2\Delta_{adh})$ and $\Delta_{adh} = 50$ (i.e., a 50 nm adherent layer). (a) thickness of the hydride layer (5.22), $k_{cH} \in [1, 50]$ corresponds to dimensional reaction rates in the range $k^*_{cH} \in [1.6 \cdot 10^7, 8.2 \cdot 10^8]$ $\mathrm{mol}^{-2}\,\mathrm{cm}^6\,\mathrm{s}^{-1}$. (b) mass (per unit area) of hydride (5.23), $k_{hM} \in [10^4, 10^5]$ corresponds to dimensional reaction rates in the range $k^*_{hM} \in [6.8 \cdot 10^{14}, 6.8 \cdot 10^{15}]$ $\mathrm{mol}^{-3}\,\mathrm{cm}^9\,\mathrm{s}^{-1}$. Any parameters not shown are fixed at the values specified in Table 5.1.

The expression (5.19) can also be obtained simply by considering the surface flux of oxygen required to produce UO_2 at the correct rate, without recourse to any detailed RAD model. A more interesting (and a much more sensitive metric to assess the model) is the corresponding prediction for the hydride layer thickness, which we will obtain from numerical solution of (5.12).

From (5.13) we can confirm that the hydride layer should be of constant thickness (in the linear regime), by noting that the flux of OH^- into the bulk is balanced by the outward flux of $\mathrm{H}^\bullet$:

$$D_c^O \left.\frac{\mathrm{d}c}{\mathrm{d}\xi}\right|_{\xi=0} + D_h^O \left.\frac{\mathrm{d}h}{\mathrm{d}\xi}\right|_{\xi=0} = 0\,. \tag{5.20}$$

So any internal bulk hydride owes its origin to the initial transient/parabolic stage, and once in the linear oxidation phase its volume remains constant.

5.2.1 Numerical solutions of the constant-rate oxidation regime

The constant-rate oxidation system (5.12) can be computed by a shooting method. At fixed values of the dimensionless parameters k_{cH} , k_{hM} and D_i^j with $i = \{c, h\}$, $j = \{H, M, O\}$, we can obtain solutions that correspond to a dimensionless adherent layer thickness of Δ_{adh}, by taking $V = D_c^O/(2\Delta_{adh})$ as given by (5.18).

Figure 5.2 presents the solution obtained for $\Delta_{adh} = 50$ (with other parameter values taken to be the reference values discussed in §§ 5.1.2). The figure shows (dimensionless) concentrations of the diffusing species c, h, material volume fractions H, M, O and the two reaction terms

$$\mathcal{R}_1(\xi) = k_{cH} c^2 H \,, \quad \mathcal{R}_2(\xi) = k_{hM} h^3 M \,. \tag{5.21}$$

Unlike the parabolic response at earlier times, in the linear oxidation regime described here a key feature is that these reaction fronts maintain a *constant* separation in line with (5.13). A natural thickness measure for the UH_3 layer is therefore

$$\Delta^*_{\mathrm{UH}_3} = L^*_{ref}(\xi_1 - \xi_2) \,, \tag{5.22}$$

where the asterisk again signifies a dimensional quantity and $\xi_{1,2}$ are the locations of the respective maxima of $\mathcal{R}_{1,2}$.

Figure 5.2 also demonstrates that the return to an unreacted U state (i.e. $M = 1$) can occur relatively slowly depending on the precise parameter values chosen. As an additional measure we therefore also consider the total mass of UH_3 (per unit area of material), as obtained from depth integration of the volume fraction:

$$I^*_{\mathrm{UH}_3} = L^*_{ref}\, \rho^*_H \int_{-\infty}^{0} H(\xi)\, \mathrm{d}\xi \,, \tag{5.23}$$

where ρ^*_H is the (mass) density of UH_3 (approximately 10.95 g/cm^3).

Numerical solutions of (5.12) indicate that $\Delta^*_{\mathrm{UH}_3}$ is most sensitive to D_c^H (relative diffusivity of OH^- in UH_3) then k_{cH} (the dimensionless reaction rate constant for UH_3 and OH^-). This is consistent with the asymptotic behaviour described in §§§ 4.2.5.5, where again D_c^H and the first reaction rate dominated the hydride thickness for large times in the parabolic regime (in cases of $D_h^H \ll 1$, as is the case here).

An examination of $I^*_{\mathrm{UH_3}}$ shows that it is most sensitive to the values of D_h^M (relative diffusivity of H$^\bullet$ in U) and k_{hM} (the dimensionless reaction rate constant for U and H$^\bullet$). For smaller relative diffusivity coefficients or faster reaction rates, the return to unreacted U within the metal occurs over a smaller lengthscale (as expected).

In figures 5.3(a,b) we show the dependence of $\Delta^*_{\mathrm{UH_3}}$ and $I^*_{\mathrm{UH_3}}$ as functions of the two relevant dominant parameters (being D_c^H, k_{cH} and D_h^M, k_{hM} respectively). We return to these predictions below to compare full (unsteady) solutions to the RAD model with randomised parameter choices.

5.3 Evolution through to late-stage oxidation

To validate the conclusions drawn from (5.12) discussed above, we return to the original initial-value problem posed by (5.8) and time march the system, following the same procedure outlined in §§ 4.2.3. For a simplistic model of the cracked/porous oxide (as shown in Figure 5.1) the diffusivity of OH$^-$ and H$^\bullet$ is increased by two orders of magnitude in the region $z > z_c(t) = z_1(t) + \Delta_{adh}$ where Δ_{adh} is a specified constant. This large increase in diffusion through the non-adherent oxide leads to an approximate constant concentration of OH$^-$ in the cracked/porous region.

For early times, where the oxide thickness is less than Δ_{adh} the problem is that described in Chapter 4, but beyond the point of breakaway, which is achieved when $z_s(t) > z_c(t)$, we expect to transition to a constant flux (of OH$^-$), revealing the constant-rate oxidation state discussed in § 5.2.

As the system evolves, we will focus on analogous metrics for (now unsteady) hydride production (i.e., $\Delta^*_{\mathrm{UH_3}}$ and $I^*_{\mathrm{UH_3}}$), together with additional measures for the mass loss/gain of U/UO$_2$

$$I^*_{\mathrm{UH_3}} = L^*_{ref}\, \rho^*_H \int_{-\infty}^{0} H(z,t)\,\mathrm{d}z\,, \tag{5.24a}$$

$$I^*_{\mathrm{U}} = L^*_{ref}\, \rho^*_M \int_{0}^{-\infty} (1 - M(z,t))\,\mathrm{d}z\,, \tag{5.24b}$$

$$I^*_{\mathrm{UO_2}} = L^*_{ref}\, \rho^*_O \int_{-\infty}^{0} O(z,t)\,\mathrm{d}z\,, \tag{5.24c}$$

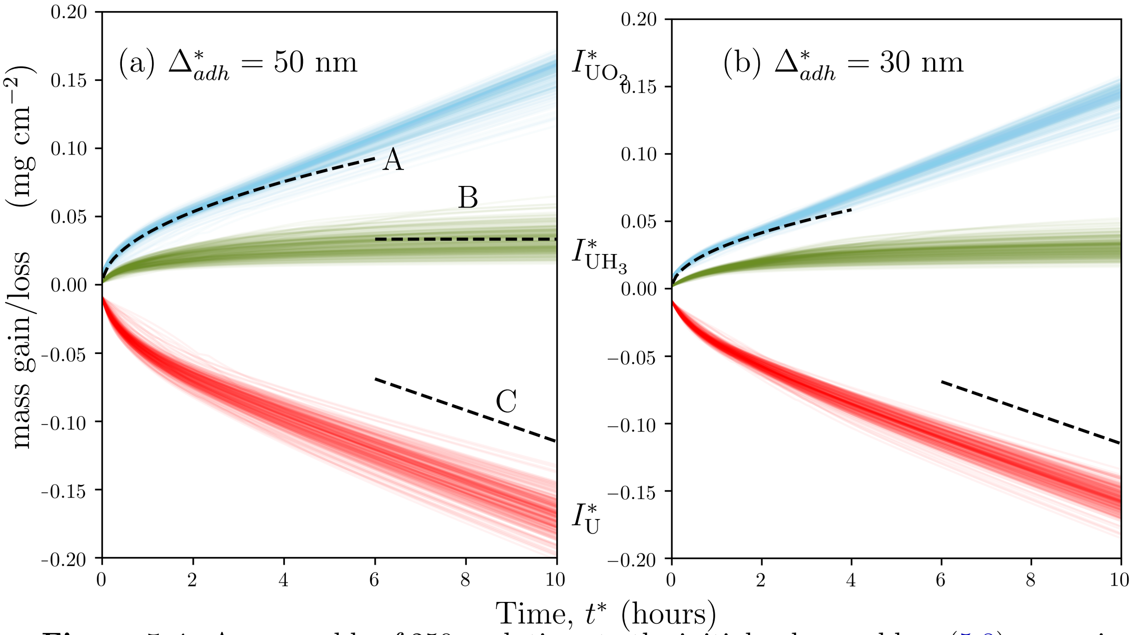

Figure 5.4: An ensemble of 250 evolutions to the initial-value problem (5.8), spanning the parameter range listed in Table 5.2 and (5.25) with an assumed adherent layer of thickness $\Delta^*_{adh} = 50$ and 30 nm. Measures of the mass gain/loss of each phase are shown ($I^*_{\mathrm{UO}_2}$ blue, $I^*_{\mathrm{UH}_3}$ green and, I^*_{U} red) as defined by (5.24). Dashed lines indicate (A) the prediction of Monisha Natchiar et al. (2020) for oxide growth in the parabolic stage, (B) the prediction for hydride production from the solution of § 5.2 and (C) the empirical rate of loss (5.9) assumed from Banos and Scott (2020).

where $\rho^*_M = 19.1\,\mathrm{g\ cm}^{-2}$ and $\rho^*_O = 10.97\,\mathrm{g\ cm}^{-2}$ are the (mass) densities for U and UO_2 respectively. Here $I^*_{\mathrm{U}} < 0$ is the mass loss of U whilst $I^*_{\mathrm{UO}_2} > 0$ is the mass gain of UO_2 (per unit area) and the definition of $I^*_{\mathrm{UH}_3}$ is consistent with that presented earlier (5.23) but using the non-translating coordinate.

We consider 250 evolutions (for an adherent oxide thickness of 50 nm) with a water vapour pressure of 20 Torr at room temperature. In each evolution the seven dimensionless parameters in (5.8) are randomised, with $D_h^{(j)}$ chosen according to Table 5.2 whilst other parameters are chosen to cover two orders of magnitude with

$$D_c^{(j)*} \in [10^{-13}, 10^{-11}]\,\mathrm{cm}^2\,\mathrm{s}^{-1}\,, \tag{5.25a}$$

$$k^*_{cH} \in [10^7, 10^9]\,\mathrm{mol}^{-2}\,\mathrm{cm}^6\,\mathrm{s}^{-1} \quad \text{and} \quad k^*_{hM} \in [10^{14}, 10^{16}]\,\mathrm{mol}^{-3}\,\mathrm{cm}^9\,\mathrm{s}^{-1}. \tag{5.25b}$$

Figure 5.4 shows the measures (5.24) over a 10 hour exposure for the 250 randomised evolutions. A parabolic phase is apparent in the first few hours, until the oxide has grown sufficiently to reach the Δ^*_{adh} limit (50 or 30 nm). Beyond

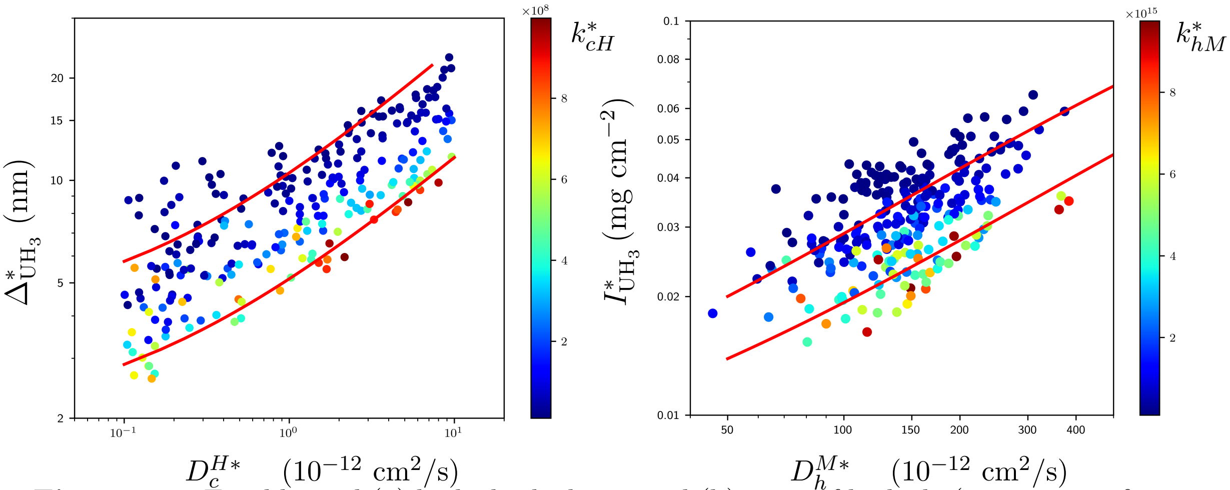

Figure 5.5: Equilibrated (a) hydride thickness and (b) mass of hydride (per sq. cm of material) after 10 hours of exposure, at room temperature and 20 Torr water vapour pressure, assuming a 50 nm adherent layer. Data are extracted from the randomised evolutions of Figure 5.4 and colours indicate the corresponding values of the reaction rates k^*_{cH} and k^*_{hM}. The solid red lines are the predictions obtained from (5.12) as presented in Figure 5.3.

this point there is a smooth transition towards a linear response for sufficiently long exposure times, and the constant-rate oxidation solution of § 5.2 becomes apparent. The mass of hydride produced is consistent with the prediction arising from (5.12) as shown by the dashed line (B) in Figure 5.4(a) as obtained using the reference values of Table 5.1. Similarly, within the first few hours the (asymptotic) prediction of oxide mass obtained from Monisha Natchiar et al. (2020) works well, taking equation (6.1) from that work and multiplying by the density of the produced oxide[a].

Using Figure 5.4 we can also compare the mass of hydride once the evolution is well into the linear regime (i.e., after 10 hours of exposure) with the predictions obtained from (5.12). The predictions of Figure 5.3 are obtained by varying only the two parameters shown in each sub-figure, whilst keeping all others at the values of Table 5.1. In this section all parameters are randomised according to Table 5.2 and (5.25), so we can now compare both approaches as shown in Figure 5.5.

Figure 5.5(a) shows the thickness of the hydride region (as measured by the spatial separation of the two peaks in reaction rates $k_{cH}c^2H$ and $k_{hM}h^3M$). The

---

[a] Note that the same has been derived in (6.1) in the next chapter.

two red lines in the figure repeat the ($k_{cH} = 1, 50$) data of Figure 5.3(a). The two parameters of D_c^{H*} (diffusion coefficient of OH^- in UH_3) and k^*_{cH} (the reaction rate constant for OH^- and UH_3 appearing in (5.1)) clearly capture the variation of hydride thickness.

Figure 5.5(b) shows the total (depth integrated) mass of hydride. The two red lines are the predictions of Figure 5.3(b) at two fixed values of the second reaction rate constant k^*_{hM} (or its dimensionless analogue k_{hM}). Again the two parameters of D_h^{M*} (diffusion coefficient for $H^\bullet$ in U) and k^*_{hM} (the reaction rate constant for $H^\bullet$ and U) capture the bulk of variability.

5.4 Conclusions

The RAD model (5.8) was presented (Monisha Natchiar et al., 2020) as a new model for uranium oxidation in a water-vapour environment, but only investigated in detail in the parabolic regime prior to cracking/spalling of the evolving surface oxide layer. This regime is mathematically interesting, with a pair of propagating reaction fronts that remain coupled via an intermediate diffusion layer of UH_3. However, clearly practical interest is mostly aimed at the later regime, where empirical evidence indicates a transition to oxidation at a constant rate for sufficient long exposure times.

Hydride production is characterised by two measures (i) $\Delta^*_{\mathrm{UH}_3}$ is the spatial separation between the two reactions of (5.1) and (ii) $I^*_{\mathrm{UH}_3}$ is the depth integrated mass (of UH_3) per unit area. When in the linear oxidation regime (e.g., after 10 hours of exposure) the first measure is dominated by the diffusivity of OH^- in UH_3 (D_c^{H*}) and the first reaction rate constant (k^*_{cH}) as confirmed by Figure 5.4(a). The second measure is dominated by the diffusivity coefficient of $H^\bullet$ in UH_3 (D_h^{M*}) and the second reaction rate constant (k^*_{hM}), as confirmed by Figure 5.4(b).

Evidence from the atom probe tomography (APT) experiments of Martin et al. (2016) points to a hydride region of approximately 5 nm thick after an hour of exposure in room conditions, so this should be considered as a lower bound to the equilibrated layer size ($\Delta^*_{\mathrm{UH}_3}$) in the linear oxidation regime. Figure 5.4 demonstrates that there are plausible choices of diffusivity coefficients and reaction rates that lead to comparable length scales. The second metric $I^*_{\mathrm{UH}_3}$ is bounded below by $\rho^*_H \Delta^*_{\mathrm{UH}_3}$ (approximately the mass associated with the hydride region per unit area) but above this it becomes a measure of the length scale over which the transition from UH_3 to U occurs. For example, Figure 5.2 shows a relatively slow recovery of M from 0 to 1 over a length scale of about 50 nm (for $L^*_{ref} = 1$ nm), this is too slow to be consistent with the concentration profiles recovered from the APT experiments. Figure 6(a) from Martin et al. (2016) suggests that the recovery to a region of unreacted metal occurs over a span of closer to 10 nm, so any experimental refinement of the values for k^*_{hM} and D^{M*}_h would have to lead to values for $I^*_{\mathrm{UH}_3}$ at the lower end of the range shown in Figure 5.4(b) for this RAD model to be consistent with observation.

We conclude by noting that this work not only assumes that the reaction scheme (5.1) holds, but also that any surface processes associated with this reaction can be largely ignored in favour of a static boundary condition for the concentration of OH^-. We also assume that any $\mathrm{H}^\bullet$ instantaneously reacts at this same location. In addition, we also impose a quasi-steady model for the diffusion of OH^- and $\mathrm{H}^\bullet$, for which we require $C^*_a \ll N^*_M$ (for example). We cannot rule out the possibility that unsteady diffusion effects may be re-introduced for $\mathrm{H}^\bullet$ in UH_3 owing to the low relative diffusivity in that region associated with $D^{H*}_h / D^*_{ref} \approx 10^{-3}$. Finally, we have taken a relatively simple linear superposition of diffusivities when dealing with the mixed-phase material (5.8e).

Chapter 6

Discussion and conclusions

6.1 Dry-air oxidation

We have formulated both chemical and ionic diffusion models for uranium oxidation in dry air, the motivation being that chemical diffusion alone does not account for the oxidation rate observed in experiments. In this section, our unsteady ionic diffusion model is compared with the results of Gharagozloo and Kanouff (2013), and with published experimental results for the oxide thickness. As we have previously remarked (see §§§ 2.1.1.1), it is not entirely clear as to how the change in density accompanying the phase transition from metal (U) to metal oxide ($UO_{2.09}$) is incorporated into the GK model. Therefore, a distinction is made between the quasi-steady limit of our model and the stated results of GK.

We recover the moderate-field regime from the strong-field model for relevant or practical timescales of interest (i.e., the nonlinear effects of a strong field are only dominant at very small timescales for which the oxide thickness $L^*(t^*) < 100\,a^*$ (see Figure 2.16); a^* being the lattice constant). We therefore mainly focus on the unsteady 'linear' ionic diffusion model (governed by the equation (2.69)) for comparisons with published results, although some comparisons are also made with the results of the nonlinear quasi-steady model. We first compare the results of our unsteady ionic model with the quasi-steady ionic model of GK, using the same parameter values specified in the published work of GK. For example, the lattice constant is $a^* = 3.8682$ Å; the surface concentration of oxygen ions is assumed to be $C_a^* = 6 \cdot 10^{28}$ ions/m^3, even though this value seems large. An accurate (order-of-magnitude) estimate of the surface concentration of oxygen ions in the dry-air oxidation of uranium remains to be found through experimental measurements and is out of the scope of the diffusion model we have presented herein.

In order to re-dimensionalise our nondimensional results, we choose the reference length scale to be the initial oxide thickness ($L^*_{ref} = \delta^*_O$)[a]; the reference diffusivity (D^*_{ref}) is the theoretical chemical diffusivity of O^{2-} given by (2.5a); the reference timescale is then taken as $L^{*^2}_{ref}/D^*_{ref}$.

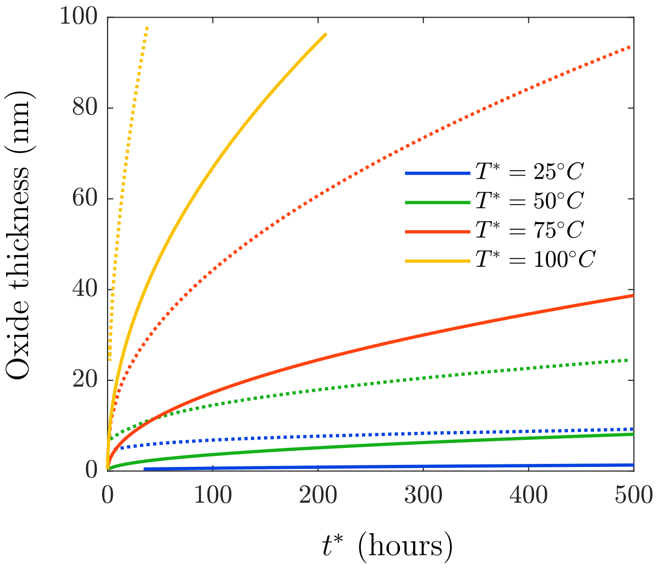

Figure 6.1: The evolution of oxide layer thickness (in nm) over 500 hours at various temperatures. Here the dotted lines represent the results extracted from figure 3(b) of Gharagozloo and Kanouff (2013) and the solid lines show the results of our unsteady ionic diffusion model. Other dimensional parameters include: $a^* = 3.8682$ Å, $D_c^{O^*}$ given by (2.5a), $q^* = -2e^*$, $\nu^* = 19$ THz and $V^*_M = -0.97$ V (as specified by Gharagozloo and Kanouff, 2013).

A comparison of our unsteady ionic model predictions with the GK results (extracted from figure 3(b) of Gharagozloo and Kanouff, 2013) is plotted in Figure 6.1 for different temperatures. The GK model (i.e. quasi-steady model) over-predicts the oxide thickness compared to our unsteady model as shown clearly, with the disagreement increasing with increasing temperatures.

The simulation results of different models are compared with the published experimental results in figures 6.2 to 6.4. The experimental results of Lin et

---

[a] For comparison with the GK results, we consider the initial oxide thickness (δ^*_O) to be one lattice constant (Gharagozloo and Kanouff, 2013).

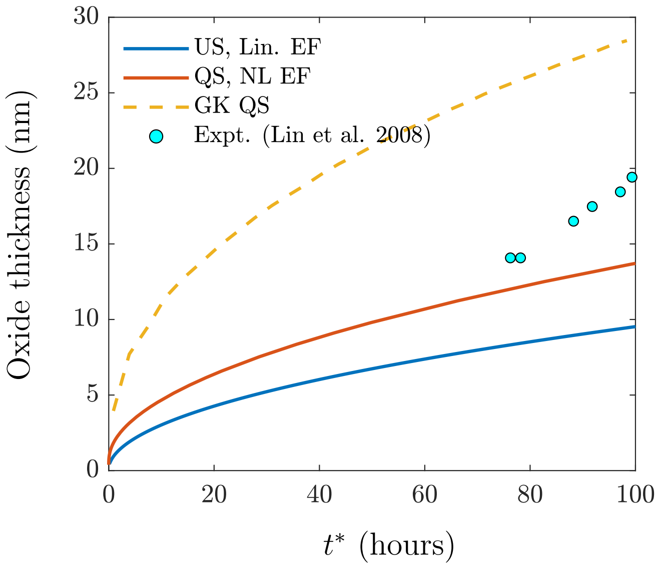

Figure 6.2: A comparison of the simulation results for the oxide thickness (in nm) over 500 hours with the experimental results of Lin et al. (2008) at 65°C. The models compared here are our unsteady (US) and quasi-steady (QS) ionic diffusion models, and the GK ionic diffusion model (GK QS, extracted from figure 4 of Gharagozloo and Kanouff, 2013). Other dimensional parameters include: $T^* = 65°\text{C}$, $C_a^*(t^*) = 6 \cdot 10^{28}$ ions/m^3, $a^* = 3.8682$ Å, $\delta_O^* = a^*$, $D_c^{O^*}$ given by (2.5a), $q^* = -2e^*$, $\nu^* = 19$ THz and $V_M^* = -0.97$ V (as specified by Gharagozloo and Kanouff, 2013).

al. (2008) at temperatures 65°C and 85°C are compared in figures 6.2 and 6.3, respectively. The simulation results of GK have been extracted from figure 4 of Gharagozloo and Kanouff (2013)[b]. In figures 6.2 and 6.3, it is found that the GK results do not agree with our quasi-steady model results for the same parameter values. Moreover, for the surface concentration, $C_a^* = 6 \cdot 10^{28}$ ions/m^3 considered here, which gives the Stefan number $\lambda = C_a^*/(2.09\, N_M^*) \approx 0.6$, the quasi-steady assumption is not appropriate and leads to an over-prediction for the oxide thickness. As discussed in §§§ 2.2.1.6, the quasi-steady approximation is valid only for $\lambda \ll 1$. Note that the notation US Lin. EF and QS NL EF in figures 6.2 and 6.3 denote the unsteady 'linear' electric field and quasi-steady 'nonlinear' electric field models respectively.

Gharagozloo and Kanouff (2013) report that their quasi-steady model results agree well with the experimental results of Lin et al. (2008) at both 65°C and 85°C. They state that the data from Lin et al. (2008) were measured using an effective

---

[b] Some inconsistencies have been found between the model formulation and the reported results of GK, therefore the simulation results have been directly extracted from the figures for comparison.

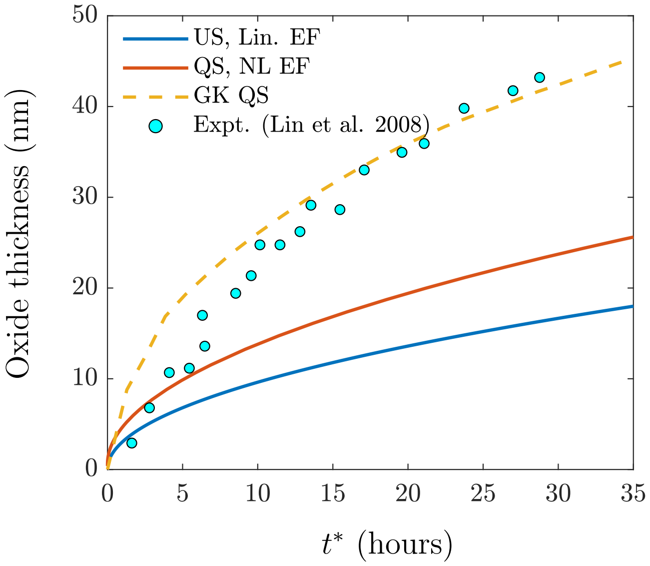

Figure 6.3: A comparison of the simulation results for the oxide thickness (in nm) over 500 hours with the experimental results of Lin et al. (2008) at 85°C. The simulation results are those of our unsteady (US) and quasi-steady (QS) ionic diffusion models, and the GK ionic diffusion model (GK QS, extracted from figure 4 of Gharagozloo and Kanouff, 2013). Other dimensional parameters include: $T^* = 85°\text{C}$, $C_a^*(t^*) = 6 \cdot 10^{28}$ ions/m^3, $a^* = 3.8682$ Å, $\delta_O^* = a^*$, $D_c^{O^*}$ given by (2.5a), $q^* = -2e^*$, $\nu^* = 19$ THz and $V_M^* = -0.97$ V (as specified by Gharagozloo and Kanouff, 2013).

ellipsometry technique for uranium sample oxidised with 99.999% pure oxygen under ultra-high vacuum, whilst they attribute the poor agreement with some of the other experimental results to measurement errors or sample preparation techniques. It can be argued that the agreement of GK results with that of Lin et al. (2008) at only 85°C and from 10 - 30 hours (see Figure 6.3) might have been fortuitous, and the conclusions of GK are thereby misleading. We also note that the quasi-steady model is a poor predictor of the oxide thickness when $\lambda = \mathcal{O}(1)$, which is the case for the values specified by GK. The unsteady model is a better model compared to the quasi-steady GK model for values of $\lambda = \mathcal{O}(1)$ and even though the quasi-steady GK model appears to agree with the experimental results of Lin et al. (2008) at 85°C in Figure 6.3, the conclusions made by GK cannot be generalised nor taken as definitive and the reasons are further elaborated below.

The oxide thickness over time obtained by solving the unsteady ionic diffusion model using the dimensional parameter values specified by Gharagozloo and Kanouff (2013) is plotted in Figure 6.4, and compared with some of the published experimental results of Adda (data taken from the review by Ritchie,

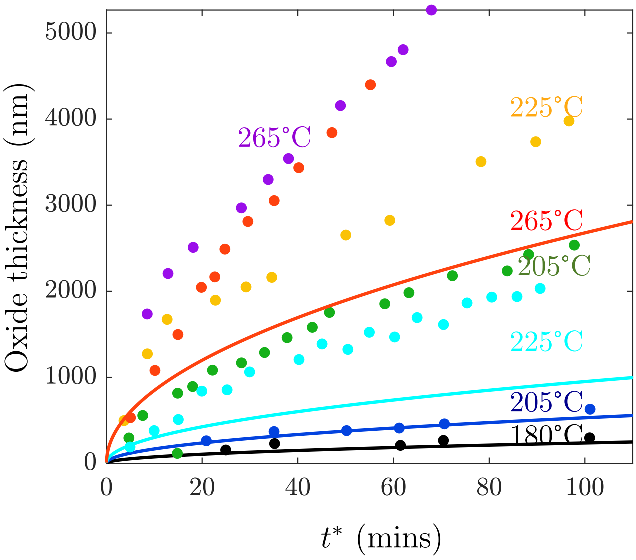

Figure 6.4: A comparison of our unsteady ionic diffusion model (solid lines) with the experimental results of Adda (represented as data points; taken from Ritchie, 1984) for oxide growth (in nm) over time (in minutes) using GK parameters at the temperatures of 180°C, 205°C, 225°C and 265°C. Data points (Adda): 180°C (black); 205°C - 'texture I' (blue), 'texture II' (green); 225 °C - 'texture I' (cyan), 'texture II' (yellow); 265°C - 'texture I' (red), 'texture II' (violet). The dimensional parameters specified by Gharagozloo and Kanouff (2013) include: $a^* = 3.8682$ Å, $\delta_O^* = a^*$, $D_c^{O^*}$ given by (2.5a), $q^* = -2e^*$, $V_M^* = -0.97$ V.

1984), wherein the uranium samples have been reported as vacuum annealed and electropolished, and subjected to 200 mm O_2/dry air. Ritchie (1984) reports an initial parabolic growth ($\propto t^{*1/2}$) followed by a linear behaviour attributed to cracking/spalling. It can be clearly observed from the figure that different samples (labelled 'texture I' and 'texture II') exhibit widely different oxidation rates at the same temperature, which Ritchie (1984) (p. 206) has ascribed to the different grain orientations of the samples. Gharagozloo and Kanouff (2013) have compared their quasi-steady model predictions with the experimental data of Adda at the temperatures of 180° and 225°C, and have reported good quantitative agreement at both temperatures. However, as clearly evident from the figure, using the same parameter values specified by GK, the full unsteady ionic model (which has been validated against an asymptotic solution in the limit $\lambda \ll 1$) does not quantitatively reproduce either of the results (texture I and II) of Adda at 225°C. Although not easily discernible in the figure, it should also be noted that the difference between the predicted and measured values of oxide thickness at approximately 100 minutes for the sample at 180°C (for example) is at least 50 nm. There are sufficient unknown parameters to artificially construct agreement with individual data sets; that is, we could fit $k_p^* t^{*1/2}$ (k_p^* being the parabolic rate constant) for ad hoc values of k_p^* without it necessarily being generalisable to describe multiple data sets over a range of conditions. This indicates that the parameters specified by GK may not be definitive; for example, the equation for D_c^{O*} given by (2.5a) need not necessarily be accurate if the diffusivity is also a function of the 'texture' (for example), which depends on the grain orientation, grain size or defect concentration that in turn affect the mechanical and electrical properties of the material. Thus, the oxidation rate may be dependent on several factors such as the grain orientation, grain size, surface/lattice defect concentration and external gas state, among others. However, the parabolic trend for the temperatures considered has been captured by the unsteady ionic diffusion model.

Although the unsteady ionic diffusion model predicts the 'parabolic' behaviour for the oxide thickness that occurs at high temperatures before cracking and spalling, the 'inverse-logarithmic' growth (as reported by Ritchie, 1984) at small times and/or low temperatures (e.g. experimental results of Larson and Taylor, see Ritchie, 1984) is not accurately captured by the model.

The presence of several degrees of freedom (for e.g., impurities present in the oxide/metal, surface and lattice defect concentration, partial pressure of oxygen gas at the surface, crystallographic orientation of the oxide surface, presence of humidity, and other experimental conditions) in uranium oxidation experiments makes it nearly impossible to conduct these experiments under precisely measurable and/or strictly controlled conditions. The thickness measurements at very small length scales (order of a few nm) in these experiments are not necessarily precise or reliable. It should be noted that only very recently (Martin et al., 2016), the presence of a discrete hydride layer of about 5 nm thickness has been explicitly detected and measured using an advanced atom probe tomography technique, albeit in uranium corrosion experiments conducted in ambient air containing water vapour. Therefore, a lack of reliable experimental results at very small lengthscales of the oxide could be a possible cause that the model is unable the reproduce the trend observed at low temperatures (100° C) and/or small times. The measurements at these small times/lengthscales will also be affected by the initial states, which may not be accurately known.

6.2 Water-vapour oxidation

In §§ 4.2.1, a one-dimensional reaction-advection-diffusion (RAD) model is presented as a new model for the early-stage (before cracking/spalling) corrosion of uranium in water vapour. For the water-vapour oxidation of uranium, the hydroxyl ions (OH^-) constitute the diffusing species whose chemical diffusivity in UO_{2+x} is many orders of magnitude larger than that of oxygen anions (O^{2-}). Diffusion is found to be the rate-determining step in oxidation by water vapour, similar to that in dry air/oxygen. In the water-vapour case, however, chemical diffusion (without the need to include ionic effects) has been found to be sufficient to account for the experimentally observed oxidation rate as reported by Baker, Less, and Orman (1966a). The RAD system evolves into pure UO_2 phase near the oxide-gas interface/surface of the material. Sufficiently far away from the surface, we recover pure metal (U). A UH_3 phase is found between the oxide and metal phases. The transition from UO_2 to UH_3 occurs rapidly in a narrow propagating reaction front (labelled RF1) where reaction R2 dominates. Similarly, transition from U to UH_3 occurs in a second narrow propagating reaction front (labelled RF2) where reaction R3 dominates (see § 1.2.6 for the proposed reaction mechanism and details of R2 and R3).

We have provided a large-time asymptotic analysis of the RAD model (in addition to solving it numerically) and found that the dimensional oxide thickness (Δ_O^*) for early-stage oxidation obeys a 'parabolic law' for sufficiently large times, with a leading-order behaviour described by $\Delta_O^* = (L_A + L_s)\left(C_a^*/N_M^* t\right)^{1/2} L_{ref}^*$ (see equations (4.36), (4.9k), (4.15) and §§ 4.2.2) which simplifies to

$$\Delta_O^* = \left(\frac{D_c^{O*} C_a^*}{N_O^*}\right)^{\frac{1}{2}} t^{*\frac{1}{2}}, \tag{6.1}$$

where t^* is the dimensional time. The leading-order oxide thickness is only influenced by the diffusivity of OH^- in UO_2 (D_c^{O*}), the (number) density of UO_2 (N_O^*) and the surface concentration of OH^- (C_a^*). For $D_h^{H*} \sim D_c^{O*}$, the dimensional hydride thickness $\Delta_H^* \sim L_B^* t^{*1/2}$ for large times (before cracking/spalling), where L_B^* is a function of the diffusivity ratio D_h^{H*}/D_h^{O*} (see Figure 4.18).

The leading-order oxide and hydride thicknesses are independent of the 'rate constants', k_{cH}^* and k_{hM}^*. These rate constants are only found to affect the solutions within the respective reaction fronts which are spatially isolated. The qualitative large-time oxidation kinetics is not affected by the details of reactions that occur within localised fronts.

However, in practice the diffusivity of $\mathrm{H}^{\bullet}$ in UH_3 is substantially smaller than OH^- diffusivity in UO_2 (i.e., $D_h^{H*} \ll D_c^{O*}$; refer Table 4.1). For this low level of relative diffusivity D_h^H, we find that the dimensional hydride thickness takes the form $\Delta_H^* \sim t^{*1/4}$ for sufficiently large times (before cracking/spalling), with the leading-order behaviour given by

$$\Delta_H^* = 2\left(\frac{D_c^{H*}}{N_O^*}\right)^{\frac{1}{2}} k_{cH}^{*-\frac{1}{4}} t^{*\frac{1}{4}}\,. \tag{6.2}$$

Therefore, for practical values of the diffusion coefficients, the hydride layer remains thin compared to the oxide phase, i.e., $\Delta_H^*/\Delta_O^* \ll 1$ over sufficiently long timescales. Also, for these practical parameter values, the hydride thickness becomes sensitive to the diffusivity of OH^- in the hydride (UH_3). The leading-order oxide thickness, however, is only sensitive to D_c^{O*} of all the diffusivity parameters, irrespective of the parameter values.

The reaction fronts remain spatially isolated and are much thinner than the leading-order oxide width for plausible timescales. The leading-order width of the reaction front RF1 is given by (refer §§§ 4.2.5.2; (4.37) in particular),

$$\delta_1^* = \alpha_1 k_{cH}^{*-\frac{1}{3}} \left(N_H^{*2} C_a^* N_M^*\right)^{-\frac{1}{6}} (D_c^{O*})^{\frac{1}{2}} t^{*\frac{1}{6}}\,, \tag{6.3}$$

where α_1 is a constant, and the width of RF2 (refer §§§ 4.2.5.4; (4.66) in particular), is

$$\delta_2^* = \alpha_2 \left(k_{hM}^* C_a^* N_M^{*2}\right)^{-\frac{1}{4}} (D_c^{O*})^{\frac{1}{2}} t^{*\frac{1}{4}} \tag{6.4}$$

for some constant α_2. The constants $\alpha_{1,2}$ can be found by solving for the local reaction front profiles in the asymptotic limit. For example, if we define δ_2^* as the width over which the volume fraction of U changes from 5% to 95% then we find that $\alpha_2 \approx 2.9$ for the set of parameter values given by $D_c^{M*} = D_c^{O*} = D_c^{H*} = 10^{-16}\ \mathrm{m}^2/\mathrm{s} = D_h^{O*} = D_h^{M*}$, whilst $\mathrm{H}^{\bullet}$ diffusivity in UH_3 is equal to $10^{-19}\ \mathrm{m}^2/\mathrm{s}$. Thus the widths of the reaction fronts depend on their respective reaction rate constants. Here, the second reaction front will remain wider compared to RF1 at sufficiently large times owing to higher-order reaction kinetics in RF2 (i.e., 4th order in RF2 compared to 3rd order in RF1). For practical parameter values, the widths of the hydride layer and the second reaction front are comparable in the asymptotic large-time limit. Our predictions of the reaction front widths are found to agree with general reaction-diffusion scales presented by Bazant and Stone (2000).

We thus have a square-root time dependence of the oxide thickness in the early stages before cracking and spalling. The overall oxidation kinetics therefore follows a parabolic law (square-root time dependence) as both the hydride layer (for practical parameter values) and the reaction fronts remain thin compared to the oxide layer at sufficiently large times. The RAD model assumes that the oxide layer grows continuously without cracking or spalling. However, it is known from experiments that cracking/spalling of the surface oxide occurs due to a build-up of internal stresses owing to the different densities of the oxide and metal, resulting in a porous/cracked oxide at the surface and an adherent layer near the metal.

After cracking/spalling, the growth is linear due to a constant width of the adherent oxide Δ^*_{adh} (which in general is found empirically to be dependent on temperature). In the linear regime, diffusion of OH^- in the adherent oxide forms the rate-determining step. Whilst new oxide is still formed at an internal interface, the oxide layer spalls near the surface after it reaches a critical thickness given by Δ^*_{adh}. We have considered Δ^*_{adh} as a parameter in our model, and examined constant-flux solutions to the same RAD model. We have shown that the adherent oxide layer moves with a constant 'downward' velocity of $(D_c^{O*}C_a^*)/(2\,\Delta^*_{adh}N_M^*)$. A constant width hydride layer consistent with the experimental observations of Martin et al. (2016) has been found in this late-stage regime. This constant hydride width depends on the details of the reactions, notably through the reaction rate constants.

6.3 Conclusions

We have modelled uranium oxidation in both dry air (or oxygen) and pure water vapour environments, where uranium dioxide (UO_{2+x}) is formed as the main corrosion product. In a water-vapour environment, an intermediate hydride (UH_3) phase exists between the oxide and metal phases in accordance with the proposed reaction scheme. The kinetics of oxidation in both these environments has been found to be determined by the diffusion of the oxidising species (O^{2-} for dry air and OH^- for water vapour). We have examined the dry-air oxidation kinetics via an unsteady ionic diffusion model (a Stefan problem), wherein a self-induced electric field contributes to the ionic flux in addition to a concentration gradient. This electric field contribution to the ionic flux increases the oxidation rate compared to chemical diffusion alone. Although we present a detailed derivation of a fully nonlinear, unsteady Stefan formulation of the ionic diffusion problem (including the effects of material expansion associated with the corrosion process), we have been unable to reproduce the agreement claimed by GK with the experimental results of Lin et al. (2008) at a temperature of 85°C. The GK model restricts attention to a quasi-steady formulation (thereby avoiding the need to solve a moving-boundary diffusion problem), but even in the quasi-steady limit the results presented by GK are not reproduced by our derivation. In support of our derivation we should note that it is shown to be consistent with a later reaction-diffusion model in the absence of ionic effects and numerical results have been validated against analytical solutions where available. There is of course sufficient freedom to modify any of the Stefan parameter, diffusion coefficient or electric field strength to recover similar agreement of the unsteady Stefan model with the results of Lin et al. (2008), but we have not taken this approach - partly due to wide variability in available data sets for dry air (see Figure 6.4).

Although the unsteady ionic diffusion model yields a 'parabolically' ($\propto t^{*1/2}$) growing oxide at high temperatures for the early-stage corrosion in dry air, it has been found that the model does not reproduce the experimental results of Larson and Taylor (data from Ritchie, 1984) at low temperature conditions (23°-100°C). Lack of reliable and precise experimental data at small times (when the oxide thickness is of the order of a few nm) and/or low temperatures (< 100°C) constrains our ability to make any conclusions regarding the oxidation rate at these conditions.

The water-vapour oxidation of uranium has been modelled using a diffuse-interface (or mixed-phase) approach instead of the discrete-layer (Stefan) approach used for modelling dry-air oxidation. A one-dimensional reaction-advection-diffusion (RAD) model for the water-vapour oxidation of uranium has been developed based on the proposed reaction scheme outlined in § 1.2.6. We have solved the water-vapour corrosion problem using both numerical simulations and a matched-asymptotic (theoretical) analysis. To solve the system numerically, a Howarth-Dorodnitsyn transformation has been used to handle the moving/advecting domain. The transformed system of equations is then solved using a second-order Crank-Nicolson scheme along with Newton iteration. We have found our numerical results to be consistent with our asymptotic solution, where both methods predict a thin propagating hydride layer that is bounded by a pair of coupled reaction fronts. Our results are based on the assumption that the surface concentration of the diffusing OH^- ions is much less than the density of the metal ($C_a^* \ll N_M^*$); that is we have quasi-steady diffusion of OH^- and $H^\bullet$, the latter being produced at the first reaction front. We have found that the oxide growth is 'parabolic', which is consistent with the observed experimental results before cracking of the surface oxide. We know from empirical measurements that $D_h^{H*} \ll D_c^{O*}$, for which the leading-order growth of the hydride layer (in the early-stage regime) is given by (6.2). We have also found that even though the oxide formation relies on the presence of an intermediate hydride layer, its thickness is not sensitively dependent on the precise size of the hydride layer; the oxide thickness only depends on the material properties and external gas/water vapour state.

A linear growth of oxide is found after cracking/spalling of the surface oxide, owing to the constant thickness of the adherent oxide (Δ_{adh}^*). In this regime (late-stage corrosion), diffusion of OH^- through the adherent oxide constitutes the rate-determining step, whence the linear growth. We have examined constant-flux solutions of the RAD model for this regime, and have found that the reaction fronts, adherent oxide and hydride layers propagate into the bulk metal with a constant velocity of $(D_c^{O*}C_a^*)/(2\Delta_{adh}^* N_M^*)$. We have considered two measures for the hydride growth in this late-stage regime, namely the hydride width (Δ_H^*) measured as the distance between the maximum reaction rates at the two fronts, and the total mass of hydride produced per unit area of the material ($I_{\mathrm{UH_3}}^*$). We found that whilst hydride width is most sensitive to the diffusivity of OH^- in UH_3 (D_c^{H*}) and the rate constant k_{cH}^*, the mass of hydride per unit area of the material is sensitive to D_h^{M*} and k_{hM}^*. There are plausible ranges of reaction rates and diffusivity coefficients that predict a hydride thickness of < 10 nm (for room temperature oxidation in a vapour pressure of 20 Torr when $\Delta_{adh}^* = 50$ nm), consistent with the experimental results of Martin et al. (2016) for oxidation at room temperature in moist air.

6.4 Future work

There are multiple directions in which this work can be extended; a couple of directions are elaborated in this section. Understanding the corrosion kinetics of uranium in moist air (containing $O_2 + H_2O_{(v)}$) is of practical interest, mainly for the safe storage of uranium in nuclear waste-disposal facilities. The presence of oxygen in a uranium-water vapour system has been reported to decrease the oxidation rate by a factor varying from 30-100 that depends on the sample properties and external gas state (Baker, Less, and Orman, 1966b). Baker et al. analysed the residual gases during the corrosion experiments in moist air and found that the partial pressure of $H_2O_{(v)}$ remained nearly constant, whilst that of O_2 decreased linearly. They also found that only small amounts of H_2 evolved during this stage. However after the pressure of O_2 dropped to zero, they found that H_2 pressure raised sharply with a concomitant decrease in the water vapour pressure. They suggested that oxygen regenerates water vapour, and does not directly contribute to the diffusing species within the oxide/material for the corrosion reaction. They ascribed the decrease in oxidation rate to surface poisoning by O_2, i.e., oxygen was suggested to retard the oxidation via a surface mechanism involving chemisorption of oxygen ions thereby resulting in a reduced number/concentration of available sites for water vapour adsorption.

Baker, Less, and Orman (1966b) also suggested that some oxygen was consumed to further oxidise the oxide product, i.e., increasing the hyper-stoichiometry of UO_{2+x} from $x = 0.09$ to $x = 0.25$. The oxidation rate has been reported to be independent of the oxygen pressure up to 100 cm Hg. It would be informative to put Baker et al.'s hypothesis to test by modelling the diffusion of both OH^- and O^{2-} in a moist air environment, and determining the rate. It has been reported that the rate of moist air oxidation although less than the water-vapour rate, is higher than that of dry-air oxidation. The oxidation rates in these environments can be found in the recent review by Banos and Scott (2020).

Secondly, heat is released during oxidation of uranium in air (Baker Jr, Schnizlein, and Bingle, 1966; Tetenbaum, Mishler, and Schnizlein, 1962; Epstein et al., 1996). If the rate of heat production outweighs the rate of heat loss to the ambient environment, this could potentially result in increasing the temperature of the material to its ignition temperature, leading to fire hazards. We could explore this scenario by coupling governing equations for heat transfer and solving for the unsteady development of temperature along with the concentration distribution within the material.

Bibliography

Ao, B., R. Qiu, H. Lu, and P. Chen (2016). "Differences in the existence states of hydrogen in UO_2 and PuO_2 from DFT + U calculations." *The Journal of Physical Chemistry C* 120.33, pp. 18445–18451.

Atkinson, A. (1985). "Transport processes during the growth of oxide films at elevated temperature." *Reviews of Modern Physics* 57.2, pp. 437–470.

Auskern, A. B. and J. Belle (1961). "Oxygen ion self-diffusion in uranium dioxide." *Journal of Nuclear Materials* 3.3, pp. 267–276.

Baker, M. M., L. N. Less, and S. Orman (1966a). "Uranium + water reaction. Part 1. Kinetics, products and mechanism." *Transactions of the Faraday Society* 62, pp. 2513–2524.

— (1966b). "Uranium + water reaction. Part 2.— Effect of oxygen and other gases." *Transactions of the Faraday Society* 62, pp. 2525–2530.

Baker Jr, L, J. G. Schnizlein, and J. D. Bingle (1966). "The ignition of uranium." *Journal of Nuclear Materials* 20.1, pp. 22–38.

Banos, A., N. J. Harker, and T. B. Scott (2018). "A review of uranium corrosion by hydrogen and the formation of uranium hydride." *Corrosion Science* 136, pp. 129–147.

Banos, A. and T. B. Scott (2020). "A review of the reaction rates of uranium corrosion in water." *Journal of Hazardous Materials*, p. 122763.

Bazant, M. Z. and H. A. Stone (2000). "Asymptotics of reaction–diffusion fronts with one static and one diffusing reactant." *Physica D: Nonlinear Phenomena* 147.1-2, pp. 95–121.

Buck, A. L. (1981). "New equations for computing vapor pressure and enhancement factor." *Journal of Applied Meteorology* 20.12, pp. 1527–1532.

Cabrera, N. F. M. N. and N. F. Mott (1949). "Theory of the oxidation of metals." *Reports on Progress in Physics* 12.1, pp. 163–184.

Castell, M. R., C. Muggelberg, G. A. D. Briggs, and D. T. Goddard (1996). “Scanning tunneling microscopy of the UO_2 (111) surface.” *Journal of Vacuum Science & Technology B: Microelectronics and Nanometer Structures Processing, Measurement, and Phenomena* 14.2, pp. 966–969.

Catlow, C. R. A. (1977). “Oxygen incorporation in the alkaline earth fluorides.” *Journal of Physics and Chemistry of Solids* 38.10, pp. 1131–1136.

Chernia, Z. (2009). “Reflectance spectroscopy in analysis of UO_2 scale: derivation of a kinetic model of uranium oxidation.” *Physical Chemistry Chemical Physics* 11.11, pp. 1729–1739.

Colmenares, C. A. (1975). “The oxidation of thorium, uranium, and plutonium.” *Progress in Solid State Chemistry* 9, pp. 139–239.

— (1984). “Oxidation mechanisms and catalytic properties of the actinides.” *Progress in Solid State Chemistry* 15.4, pp. 257–364.

Cubicciotti, D. (1952). “The reaction between uranium and oxygen.” *Journal of the American Chemical Society* 74.4, pp. 1079–1081.

Draley, J. E. and W. E. Ruther (1957). “Some unusual effects of hydrogen in corrosion reactions.” *Journal of The Electrochemical Society* 104.6, pp. 329–333.

Epstein, M, W Luangdilok, M. G. Plys, and H. K. Fauske (1996). “On prediction of the ignition potential of uranium metal and hydride.” *Nuclear Safety* 37.1, pp. 12–25.

Evans, U. R. (1960). *The corrosion and oxidation of metals: scientific principles and practical applications.* Edward Arnold, London.

Ferrari, P. A., S. Goldstein, and J. L. Lebowitz (1985). “Diffusion, mobility and the Einstein relation.” *Statistical Physics and Dynamical Systems.* Springer, pp. 405–441.

Fromhold, A. T. (1972). “Parabolic oxidation of metals in homogeneous electric fields.” *Journal of Physics and Chemistry of Solids* 33.1, pp. 95–120.

Fromhold, A. T. and E. L. Cook (1967). “Diffusion currents in large electric fields for discrete lattices.” *Journal of Applied Physics* 38.4, pp. 1546–1553.

Gálfi, L. and Z. Rácz (1988). “Properties of the reaction front in an $A + B \longrightarrow C$ type reaction-diffusion process.” *Physical Review A* 38.6, p. 3151.

Gharagozloo, P. E. and M. P. Kanouff (2013). “Ionic Diffusion Oxidation Model of Uranium.” *Journal of the American Ceramic Society* 96.9, pp. 2943–2949.

Glascott, J. and I. Findlay (2019). Private communication.

Grønvold, F. and H. Haraldsen (1948). "Oxidation of uranium dioxide (UO_2)." *Nature* 162.4106, pp. 69–69.

Gulbransen, E. A. and W. Wysong (1947). "Thin oxide films on aluminum." *The Journal of Physical Chemistry* 51.5, pp. 1087–1103.

Gupta, S. C. (2017). *The classical Stefan problem: basic concepts, modelling and analysis with quasi-analytical solutions and methods.* Vol. 45. Elsevier.

Harker, R. M. (2006). "The influence of oxide thickness on the early stages of the massive uranium–hydrogen reaction." *Journal of Alloys and Compounds* 426.1-2, pp. 106–117.

Haschke, J. M., T. H. Allen, and J. C. Martz (1998). "Oxidation kinetics of plutonium in air: consequences for environmental dispersal." *Journal of Alloys and Compounds* 271, pp. 211–215.

Haschke, J. M., T. H. Allen, and L. A. Morales (2001). "Reactions of plutonium dioxide with water and hydrogen–oxygen mixtures: Mechanisms for corrosion of uranium and plutonium." *Journal of Alloys and Compounds* 314.1, pp. 78–91.

Haycock, E. W. (1959). "Transitions from parabolic to linear kinetics in scaling of metals." *Journal of The Electrochemical Society* 106.9, p. 771.

Hedhili, M. N., B. V. Yakshinskiy, and T. E. Madey (2000). "Interaction of water vapor with UO_2 (001)." *Surface Science* 445.2-3, pp. 512–525.

Henrich, V. E. and P. A. Cox (1996). *The surface science of metal oxides.* Cambridge University Press.

Hilhorst, D., R. Van Der Hout, and L. A. Peletier (1996). "The fast reaction limit for a reaction-diffusion system." *Journal of Mathematical Analysis and Applications* 199.2, pp. 349–373.

Jiang, Z. and C. Ebner (1990). "Simulation study of reaction fronts." *Physical Review A* 42.12, p. 7483.

Jones, C. P., T. B. Scott, J. R. Petherbridge, and J. Glascott (2013). "A surface science study of the initial stages of hydrogen corrosion on uranium metal and the role played by grain microstructure." *Solid State Ionics* 231, pp. 81–86.

Kim, K. C. and D. Olander (1981). "Oxygen diffusion in UO_{2-x}." *Journal of Nuclear Materials* 102.1-2, pp. 192–199.

Kondo, T., E. D. Verink, F. H. Beck, and M. G. Fontana (1964). "Gas Chromatographic and Gravimetric Studies of Uranium Oxidation Mechanism." *Corrosion* 20.10, 314t–320t.

Koza, Z. (1996). “The long-time behavior of initially separated A + B → 0 reaction-diffusion systems with arbitrary diffusion constants.” *Journal of Statistical Physics* 85.1-2, pp. 179–191.

— (1997). “Asymptotic behaviour of initially separated A + B (static) → 0 reaction-diffusion systems.” *Physica A: Statistical Mechanics and its Applications* 240.3-4, pp. 622–634.

Lay, K. W. (1970). “Oxygen chemical diffusion coefficient of uranium dioxide.” *Journal of the American Ceramic Society* 53.7, pp. 369–373.

Léger, C., J. Elezgaray, and F. Argoul (1997). “Experimental demonstration of diffusion-limited dynamics in electrodeposition.” *Physical Review Letters* 78.26, p. 5010.

Leinders, G., T. Cardinaels, K. Binnemans, and M. Verwerft (2015). “Accurate lattice parameter measurements of stoichiometric uranium dioxide.” *Journal of Nuclear Materials* 459, pp. 135–142.

Lin, S., X. Lai, X. Lv, and H. Zhang (2008). “Study of the initial oxidation characteristics of uranium with pure oxygen below 100° C by spectroscopic ellipsometry.” *Surface and Interface Analysis* 40.3-4, pp. 645–648.

Mallett, M. W. and M. J. Trzeciak (1958). “Hydrogen-uranium relationships.” *Transactions of the American Society of Metals* 50.981-993, p. 13.

Marchetti, I., F. Belloni, J. Himbert, P. Carbol, and T. Fanghänel (2011). “Novel insights in the study of water penetration into polycrystalline UO2 by secondary ion mass spectrometry.” *Journal of Nuclear Materials* 408.1, pp. 54–60.

Martin, T. L., C. Coe, P. A. J. Bagot, P. Morrall, G. D. W. Smith, T. Scott, and M. P. Moody (2016). “Atomic-scale studies of uranium oxidation and corrosion by water vapour.” *Scientific Reports* 6, p. 25618.

McEachern, R. J. and P. Taylor (1998). “A review of the oxidation of uranium dioxide at temperatures below 400° C.” *Journal of Nuclear Materials* 254.2-3, pp. 87–121.

McGillivray, G. W., D. A. Geeson, and R. C. Greenwood (1994). “Studies of the kinetics and mechanism of the oxidation of uranium by dry and moist air A model for determining the oxidation rate over a wide range of temperatures and water vapour pressures.” *Journal of Nuclear Materials* 208.1-2, pp. 81–97.

Monisha Natchiar, S. R., R. E. Hewitt, P. D. D. Monks, and P. Morrall (2020). “Asymptotics of coupled reaction-diffusion fronts with multiple static and diffusing reactants: uranium oxidation in water vapor". *SIAM Journal on Applied Mathematics* 80.5, pp. 2249–2270.

Mott, N. F. (1940). "The theory of the formation of protective oxide films on metals, II." *Transactions of the Faraday Society* 35, pp. 472–483.

— (1947). "The theory of the formation of protective oxide films on metals.—III." *Transactions of the Faraday Society* 43, pp. 429–434.

Nan, C. W. (1993). "Physics of inhomogeneous inorganic materials." *Progress in Materials Science* 37.1, pp. 1–116.

Peretz, M., D. Zamir, G. Cinader, and Z. Hadari (1976). "NMR study of hydrogen diffusion in uranium hydride." *Journal of Physics and Chemistry of Solids* 37.1, pp. 105–111.

Polanowski, P. and Z. Koza (2006). "Reaction-diffusion fronts in systems with concentration-dependent diffusivities." *Physical Review E* 74.3, p. 036103.

Powell, G. L. and J. B. Condon (1973). "Mass spectrographic determination of hydrogen thermally evolved from uranium and uranium alloys." *Analytical Chemistry* 45.14, pp. 2349–2354.

Ritchie, A. G. (1981). "A review of the rates of reaction of uranium with oxygen and water vapour at temperatures up to 300° C." *Journal of Nuclear Materials* 102.1-2, pp. 170–182.

— (1984). "The kinetics of the initial stages of the reaction of uranium with oxygen." *Journal of the Less Common Metals* 98.2, pp. 193–214.

Rubenstein, L. I. (2000). *The Stefan Problem.* Vol. 8. American Mathematical Society.

Schnizlein, J., J. Woods, J. Bingle, and R. Vogel (1960). "Identification of the diffusing species in uranium oxidation." *Journal of The Electrochemical Society* 107, p. 783.

Senanayake, S. D. and H. Idriss (2004). "Water reactions over stoichiometric and reduced UO_2 (111) single crystal surfaces." *Surface Science* 563.1-3, pp. 135–144.

Shannon, R. D. (1976). "Revised effective ionic radii and systematic studies of interatomic distances in halides and chalcogenides." *Acta Crystallographica Section A: Crystal Physics, Diffraction, Theoretical and General Crystallography* 32.5, pp. 751–767.

Stultz, J., M. T. Paffett, and S. A. Joyce (2004). “Thermal evolution of hydrogen following water adsorption on defective UO_2 (100).” *The Journal of Physical Chemistry B* 108.7, pp. 2362–2364.

Tasker, P. W. (1979). “The surface properties of uranium dioxide.” *Surface Science* 87.2, pp. 315–324.

Tetenbaum, M., L. Mishler, and G. Schnizlein (1962). “Uranium powder ignition studies.” *Nuclear Science and Engineering* 14.3, pp. 230–238.

Totemeier, T. C. (2000). “Characterization of uranium corrosion products involved in a uranium hydride pyrophoric event.” *Journal of Nuclear Materials* 278.2-3, pp. 301–311.

Verwey, E. (1935). “Electrolytic conduction of a solid insulator at high fields The formation of the anodic oxide film on aluminium.” *Physica* 2.1-12, pp. 1059–1063.

Wheeler, V. J. (1971). “The diffusion and solubility of hydrogen in uranium dioxide single crystals.” *Journal of Nuclear Materials* 40.2, pp. 189–194.

Winer, K., C. A. Colmenares, R. L. Smith, and F. Wooten (1987). “Interaction of water vapor with clean and oxygen-covered uranium surfaces.” *Surface Science* 183.1-2, pp. 67–99.

Yasutoshi, S. (1974). “Nonstoichiometry in uranium dioxide.” *Journal of Nuclear Materials* 51.1, pp. 112–125.

Zhu, J., L.-Q. Chen, J. Shen, and V. Tikare (2001). “Computing the effective diffusivity using a spectral method.” *Materials Science and Engineering: A* 311.1-2, pp. 135–141.

Appendix A

Typical values of physical constants.

Table A.1: Model parameters.

Parameter	Symbol	Value	Units
Adsorption energy of oxygen ion	W^*_{bind}	$^\dagger 2.4$	eV
Avogadro's number	N^*_A	$6.023 \cdot 10^{23}$	1/mol
Boltzmann constant	k^*_b	$1.3806 \cdot 10^{-23}$	J/K
Charge on oxide	Z	-2	-
Density of uranium	ρ^*_M	$^\natural 19.06$	g/cm^3
Density of uranium dioxide	ρ^*_O	$^\natural 10.97$	g/cm^3
Density of uranium hydride	ρ^*_H	$^\natural 10.95$	g/cm^3
Electron affinity of oxygen	E^*	$^\dagger 2.2$	eV
Lattice constant of UO_2 at 20°C	a^*	$^\ddagger 5.4713$	Å
Mass of an oxygen atom/ion	m^*_O	$^\natural 2.6565 \cdot 10^{-26}$	kg
Molar concentration of pure uranium	n^*_M	N^*_M/N^*_A	moles/m^3

† Gharagozloo and Kanouff (2013).

‡ Leinders et al. (2015).

$^\natural$ Standard values.

Parameter	Symbol	Value	Units
Molar concentration of UO_2	n_O^*	N_O^*/N_A^*	moles/m^3
Molar concentration of UH_3	n_H^*	N_H^*/N_A^*	moles/m^3
Mass of an oxygen atom/ion	m_O^*	$^\natural 2.656 \cdot 10^{-26}$	kg
Number concentration of pure uranium	N_M^*	$4.8235 \cdot 10^{28}$	1/m^3
Number concentration of UO_2	N_O^*	$2.4471 \cdot 10^{28}$	1/m^3
Number concentration of UH_3	N_H^*	$2.7366 \cdot 10^{28}$	1/m^3
Potential barrier	W^*	$^\dagger 1.24$	eV
Vibrational frequency of ions	ν^*	$^\dagger 19$	THz
Work function	Φ_0^*	$^\dagger 3.63$	eV

Appendix B

Effect of mass absorbed in the chemical diffusion model

In instances where the Stefan condition has been reformulated in terms of the (nondimensional) rate of the oxide growth instead of the velocity of the internal interface ($\dot{z}_1(t)$) (for example in (2.55d)), the mass of oxygen absorbed has been neglected whilst considering a mass balance of the system at two different times (see §§ 2.2.2). This is under the assumption that the mass of oxygen absorbed remains negligible compared to the mass of uranium and uranium dioxide. However, weight gain has been used to quantify the rate of oxidation in quite a few experimental studies; we therefore study the influence of the absorbed mass on the oxidation rate in this section.

The (nondimensional) governing equation for the (chemical) diffusion of oxygen ions through the oxide layer is (see equations (2.51))

$$\frac{\partial c}{\partial t} + \frac{\mathrm{d}z_s}{\mathrm{d}t}\frac{\partial c}{\partial z} = \frac{\partial^2 c}{\partial z^2} \quad \text{for} \quad z_1(t) < z < z_s(t)\,, \tag{B.1a}$$

subject to boundary conditions:

$$c(z = z_s(t), t) = 1\,, \quad c(z = z_1(t), t) = 0\,, \tag{B.1b}$$

and the Stefan condition:

$$\frac{\mathrm{d}z_1}{\mathrm{d}t} = -\lambda \frac{\partial c}{\partial z}\bigg|_{z=z_1(t)}\,, \tag{B.1c}$$

and with appropriate initial conditions. Here the oxide thickness is defined as $L(t) = z_s(t) - z_1(t)$, and $z_1(t)$ denotes the location of the internal (oxide-metal) interface.

The Stefan condition (B.1c) that gives the velocity of the internal (oxide-metal) interface can be written in terms of the rate of growth of the oxide ($\dot{L}$ [a]) by considering the mass conservation of the system.

Case 1: $\dot{M}^*_{\mathbf{abs}} = 0$

If the rate of mass absorbed is assumed to be zero (i.e. $\dot{M}^*_{\text{abs}} = 0$), then the rate of growth of the oxide layer is related to the velocity of the oxide-metal interface as (see (2.49))

$$\frac{\mathrm{d}L^*}{\mathrm{d}t^*} = -\gamma \frac{\mathrm{d}z_1^*}{\mathrm{d}t^*}\,, \tag{B.2}$$

where $\gamma = \rho^*_M/\rho^*_O$ is the relative density of the metal to the oxide, and $L^* = z_s^*(t^*) - z_1^*(t^*)$ is the dimensional oxide thickness.

Case 2: $\dot{M}^*_{\mathbf{abs}} \neq 0$

In reality, the rate of mass absorbed is non-zero (i.e. $\dot{M}^*_{\text{abs}} \neq 0$), as it varies proportionally to the concentration gradient at the oxide surface. The rate of mass absorbed per unit area is then the mass flux of the diffusing species across the gas-oxide interface (or surface of the oxide), which is mathematically written as

$$\dot{M}^*_{\text{abs}} = -m^*_O D_c^{O^*} \left.\frac{\partial c^*}{\partial z^*}\right|_{z^* = z_s^*(t^*)}\,. \tag{B.3}$$

Here m^*_O is the mass of 1 oxygen atom/ion ($= 2.6565 \times 10^{-26}$ kg), c^* is the (number) concentration of the diffusing oxygen ions. The negative sign indicates that the flux is down the concentration gradient or along a negative concentration gradient (Fick's first law).

The mass flux across the surface is then related to the velocity of the interfaces (by the application of mass conservation; see figure 2.3) as

$$-m^*_O D_c^{O^*} \left.\frac{\partial c^*}{\partial z^*}\right|_{z^* = z_s^*(t^*)} = \rho^*_M \dot{z}_1{}^* + \rho^*_O \dot{L}^*\,, \tag{B.4}$$

---

[a] Here, the dot notation $\dot{\circ}$ indicates differentiation with respect to time.

where $\dot{z_1}^*(t^*)$ is the velocity of the oxide-metal interface and $\dot{L}^*(t^*) = \dot{z_s}^*(t^*) - \dot{z_1}^*(t^*)$ is the velocity of the oxide layer.
Nondimensionalising (B.4), we obtain

$$-\kappa \frac{\partial c}{\partial z}\bigg|_{z=z_s(t)} = \gamma \dot{z_1} + \dot{L}\,, \tag{B.5a}$$

where $\kappa = m_O^* C_a^* / \rho_O^*$ and $\gamma = \rho_M^* / \rho_O^*$. The above equation on transforming using (2.52) gives

$$\dot{z_1} = \frac{1}{\gamma}\left(\frac{\kappa}{L}\frac{\partial c}{\partial \zeta}\bigg|_{\zeta=0} - \dot{L}\right)\,, \tag{B.5b}$$

Now, substituting the velocity of the oxide-metal interface ($\dot{z_1}$) in terms of the rate of change of the square of oxide thickness ($\mathrm{d}S/\mathrm{d}t$) in (B.1c) and transforming to the (ζ, t) coordinates, we obtain

$$\frac{1}{\gamma}\left(\frac{\kappa}{L}\frac{\partial c}{\partial \zeta}\bigg|_{\zeta=0} - \frac{\mathrm{d}L}{\mathrm{d}t}\right) = \frac{\lambda}{L}\frac{\partial c}{\partial \zeta}\bigg|_{\zeta=1}\,, \tag{B.6a}$$

resulting in

$$\frac{\mathrm{d}S}{\mathrm{d}t} = 2\left(\kappa \frac{\partial c}{\partial \zeta}\bigg|_{\zeta=0} - \gamma\lambda \frac{\partial c}{\partial \zeta}\bigg|_{\zeta=1}\right)\,, \tag{B.6b}$$

where $S = L^2$ and $\dot{S} = 2L\dot{L}$.

In the limit of $\kappa \ll 1$ (i.e. $m_O^* C_a^* \ll \rho_O^*$), we recover '*Case 1*' where $\dot{M}^*_{\text{abs}} = 0$. Although this seems unlikely, the GK value of the surface (number) concentration of the diffusing species, $C_a^* = 6 \cdot 10^{28}$ ions per m^3 corresponds to $m_O^* C_a^* = 1593$ kg/m^3, whilst $\rho_O^* = 10970$ kg/m^3 (refer A.1). Therefore $(m_O^* C_a^*)/\rho_O^* = 0.1453$; using this argument, we provide a justification for assuming that the mass absorbed is negligible and therefore continue to neglect M^*_{abs} in our further formulations (mass absorbed in the chemical diffusion model is taken to be representative of the ionic models as well).

The cumulative mass of oxygen absorbed as a function of time and the mass absorbed (ΔM^*_{abs}) over a small time interval Δt^* have been plotted in figures B.1 and B.2. Figure B.3 shows the oxide thickness as a function of time for the cases when both inclusion and exclusion of mass of oxygen absorbed are considered.

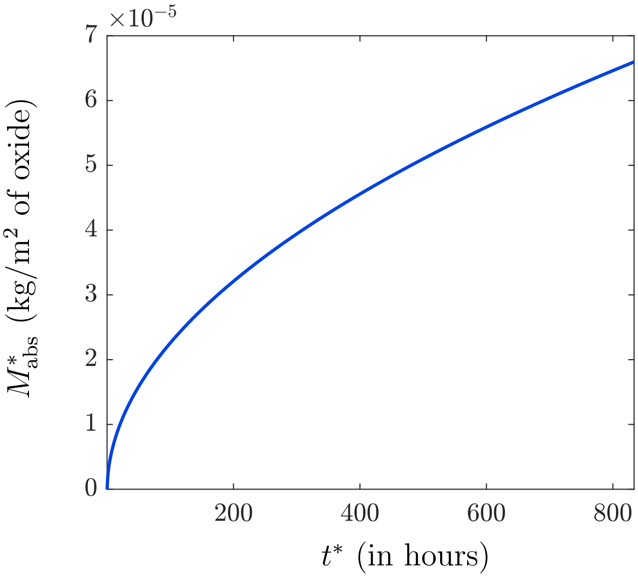

Figure B.1: Cumulative mass of oxygen ions absorbed over a period of time. $L^* = 0$ at $t^* = 0$. Parameters: $C^*_a = 6 \cdot 10^{28}$ ions per m^3, $T^* = 358$ K, $D^{O^*}_c = 1.9945 \cdot 10^{-22}$ m^2/s, $\gamma = \rho^*_M/\rho^*_O = 1.7375$ and $L^*(t^* = 0) = 0$.

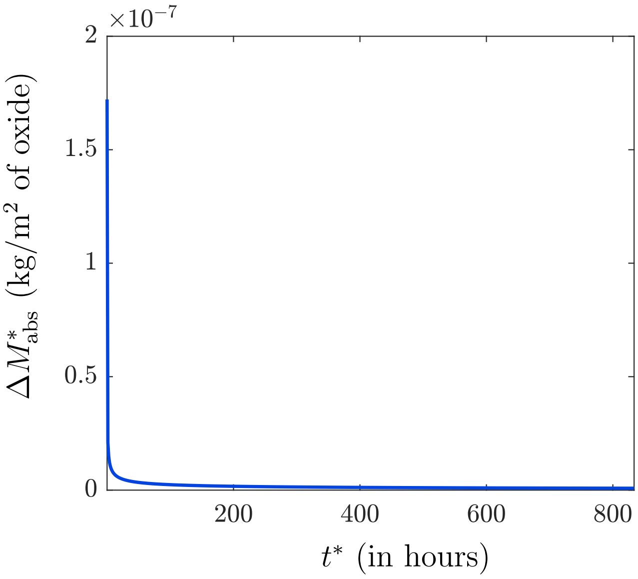

Figure B.2: Mass of oxygen absorbed ΔM^*_{abs} over a small time interval Δt^* plotted as a function of time. The parameters are those listed in figure B.1.

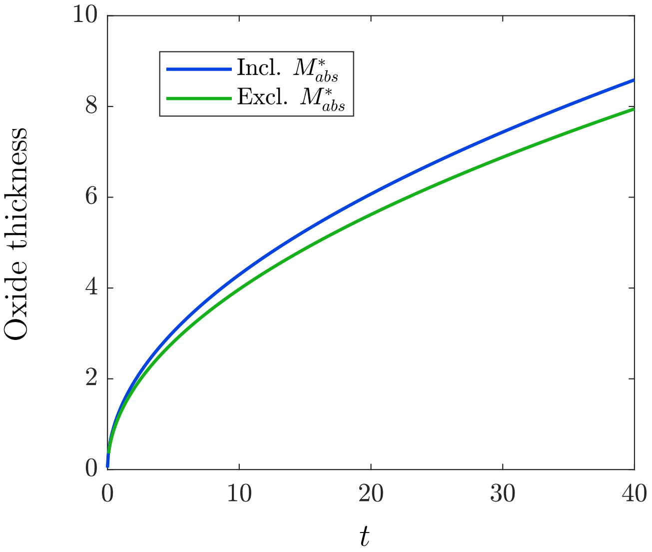

Figure B.3: A comparison of the evolution of the oxide thickness, both with/without taking account of the mass of oxygen ions absorbed (chemical diffusion with density change). Parameters: $\gamma = 1.7375\,, \lambda = 0.5952$ and $L(t = 0) = 0$.